DATA SET CATALOG #42

Mariner II Electrostatic analyzer C
62-041A-06A 1 tape

Mariner II Electrostatic analyzer D
62-041A-06C 1 tape

Table of Contents

---

1. INTRODUCTION:

The documentation for this data set was originally on paper, kept in NSSDC's Data Set Catalogs (DSCs). The paper documentation in the Data Set Catalogs have been made into digital images, and then collected into a single PDF file for each Data Set Catalog. The inventory information in these DSCs is current as of July 1, 2004. This inventory information is now no longer maintained in the DSCs, but is now managed in the inventory part of the NSSDC information system. The information existing in the DSCs is now not needed for locating the data files, but we did not remove that inventory information.

The offline tape datasets have now been migrated from the original magnetic tape to Archival Information Packages (AIP's).

A prior restoration may have been done on data sets, if a requestor of this data set has questions; they should send an inquiry to the request office to see if additional information exists.

2. ERRATA/CHANGE LOG:

NOTE: Changes are made in a text box, and will show up that way when displayed on screen with a PDF reader.

When printing, special settings may be required to make the text box appear on the printed output.

Version	Date	Person	Page	Description of Change
01				
02				

3 LINKS TO RELEVANT INFORMATION IN THE ONLINE NSSDC INFORMATION SYSTEM:

http://nssdc.gsfc.nasa.gov/nmc/

[NOTE: This link will take you to the main page of the NSSDC Master Catalog. There you will be able to perform searches to find additional information]

4. CATALOG MATERIALS:

a. Associated Documents To find associated documents you will need to know the document ID number and then click here. http://nssdcftp.gsfc.nasa.gov/miscellaneous/documents/

b. Core Catalog Materials

MARINER 2

FIELD COMPONENTS

ELECTROMETER NUMBERS

PLASMA PARAMTERS

HOUR AVERAGES OF VELOCITY

3 HOUR AVERAGE OF PLASMA PARAMETERS

62-041A-03A

62-041A-06A-D

THESE DATA SETS HAVE BEEN RESTORED. ORIGINALLY IT CONTAINED FIVE 7-TRACK, 556 BPI TAPES WRITTEN IN BINARY. THERE IS ONE RESTORED TAPE. THE DR AND DS TAPES ARE 9-TRACK, 6250 BPI. THE ORIGINAL TAPES WERE CREATED ON A 7094 COMPUTER. THE DR AND DS NUMBERS ALONG WITH THE CORRESPONDING D NUMBERS AND THE TIME SPANS ARE AS FOLLOWS:

DR#	DS#	D#	FILES	TIME SPAN	ID
DR01736	DS01736	D00982	1	08/29/62 - 11/15/62	03A
		D00186	2	08/29/62 - 12/29/62	06A
		D00187	3	08/29/62 - 12/29/62	06B
		D02887	4	08/29/62 - 12/30/62	06C
		D04893	5	08/29/62 - 12/29/62	06D

62-6414-665

[illegible] INSTRUCTIONS FOR READING AND INTERPRETING

[illegible] REDUCED DATA TAPE

1 [illegible] density = 556 bpi

Each record contains data from 21 spectra (or frames) and can be read with the following FORTRAN IV statements:

```
DIMENSION JD(21),JT(21),JFC(21),JC(21),VA(21),
VB(21),TA(21),TB(21),D(21),R(21),S(21),JH(21)

READ ( ) JD,JT,JFC,JC,VA,VB,TA,TB,D,R,S,JH
```

JD is day number at start of frame. Day 1 is Jan. 1, 1962.

JT is time in seconds from the beginning of the day at the start of frame.

JFC is frame count. An on-board counter continuously cycled from 0 to 255.

JC is a descriptive flag, which can be interpreted with the aid of Table 1 [illegible] 1 or 2. In general JC = 1, 2, or 3 for the equal-thermal-[illegible] model, = 6 or 7 for proton-only calculation, = 9 for a spectrum with apparently bad data, = 21 to 22 for the equal-temperature model, and ≥ 30 when only upper and lower limits for the temperature could be calculated.

VA is the plasma velocity, in km/sec, corresponding to the upper-limit [illegible]. VA is meaningless when JC = 9 or 30.

VB is the plasma velocity, in km/sec, corresponding to the lower-limit temperature. VB is meaningless when JC = 9 or 30. Otherwise, when JC < 30, VA = VB.

TA is the upper limit of the temperature, in 10^5 °K. TA is meaningless when JC = 6, 9, or 30.

TB is the lower limit of the temperature, in 10^5 °K. TB is meaningless when JG = 7, 9, or 30 and, otherwise, is equal to TA if JG < 30.

D is the proton density in protons/cm^3. D is meaningless when JG = 7 or 9 or when JG ≥ 30.

R is the ratio of alpha-particle density to proton density, N_α/N_p. R is meaningless when JG = 6, 7, or 9 or when JG ≥ 30.

H is 10 h, where h is the high-energy-tail parameter defined as $\log_{10}[I_{m+3}(\text{measured})/I_{m+3}(\text{calculated})]$. See Refs. 1 and 2. H is meaningless unless JG = 1, 11 or 21.

DX is the current 15-hour value of $(N_p + 3\sigma)$ used in calculating the temperature lower limits (Refs. 1 and 2). DX is meaningless when JG ≤ 30.

Samples of these reduced data are shown in Table 2. Table 2A gives all the numbers on the tape while in Table 2B the meaningless numbers have been blacked out.

The last record on the tape has one frame of good data, and the remaining 29 frames contain dummy data with JD = JT = - 1 and all other parameters = 0. This record is followed by an end-of-file.

REFERENCES

1. Neugebauer, M., and C. W. Snyder, "Mariner 2 Observations of the Solar Wind: 1. Average Properties," J. Geophys. Res., 71, 4469-4484, 1966.

2. Neugebauer, M., and C. W. Snyder, "Average Properties of the Solar Wind as Determined by Mariner 2," Jet Propulsion Lab., Tech. Rept. TR 32-991, 1966.

TABLE 1

INTERPRETATION OF JG

JG	Interpretation	Valid Parameters	Meaningless Parameters	Number of Occurrences
1	The equal-thermal-velocity (EV) calculations converged; there was a measurably large current in channel m + 3 so that h could be calculated, and |h(EV)| < |h(ET)| where the abbreviation ET represents equal-temperature calculations. The listed parameters are based on the EV model.	VA = VB, TA = TB, B,H,R	DR	13,709
2	The EV calculations converged but the current in channel m + 3 was below threshold, so h could not be calculated. The listed parameters are based on the EV model.	VA = VB, TA = TB, B,R	H,DR	6,051
3	The EV calculations converged, but since channel 8 was the peak channel, there was no channel m + 3 and h could not be calculated. The listed parameters are based on the EV model.	VA = VB, TA = TB, B,R	H,DR	97
4	Proton-only calculations, with the proton peak above the center of channel m. Spectra are in this category if either (1) neither the EV nor the ET calculations converges or (2) no measurable current in channel m + 2.	VA = VB, TA = TB, B	H,R,DR	51
7	Same as JG = 6, except that the proton peak was below the center of channel m.	VA = VB	TA,TB,B,R,H,DR	6,082
9	Spectrum no good for some reason, such as bad data.		VA,VB,TA,TB,B, H,R,DR	207
11	Both the EV and ET calculations converged and |h(ET)| < |h(EV)|. The listed parameters are based on the ET model.	VA = VB, TA = TB, B,R,H	DR	

TABLE 1 (continued)

JG	Interpretation	Valid Parameters	Meaningless Parameters	Number of Occurrences
12	Both the EV and ET calculations converged, but there was no measurable current in channel $m + 3$. Assuming I_{m+3} (measured) is just at the sensitivity threshold (digital number = 155), $\|h(ET)\| < \|h(EV)\|$. The listed parameters are based on the ET model.	VA = VB, TA = TB, D,R	H,DX	1
21	The EV calculations did not converge, while the ET calculations did converge, and there was a measurable current in channel $m + 3$. The listed parametets are based on the ET model.	VA = VB, TA = TB, D,R,H	DX	883
22	Same as JG = 21, except there was no measurable current in channel $m + 3$. The listed parameters are based on the ET model.	VA = VB, TA = TB, D,R	H,DX	200
30	No measurable current in either channel $m - 1$ or channel $m + 1$ and the spectrum had such an unusual shape that the upper and lower limits for temperature could not be found.		VA,VB,TA,TB,D,R, H,DX	28
31	No measurable current in channel $m - 1$, and the limit calculations gave $TA \geq TB > 0$.	VA ≠ VB, TA ≥ TB > 0, DX	D,R,H	10,6[illegible]
32	No measurable current in channel $m + 1$, and the limit calculations gave $TA \geq TB > 0$.	VA ≠ VB, TA ≥ TB > 0, DX	D,R,H	990
33	No measurable current in both channels $m + 1$ and $m - 1$. Set $TB = 0$. Although DX is valid, it was not used in the calculations.	VA ≠ VB, TA > TB = 0, DX	D,R,H	521

TABLE 1 (continued)

JG	Interpretation	Valid Parameters	Meaningless Parameters	Number of Occurrences
35	No measurable current in channel m + 1 and $\log_{10}(I_m/I_{m-1}) > 3.8$. Set TB = 0. DX valid, but not used.	VA ≠ VB, TA > TB = 0, DX	D,R,H	2
37	Same as 32, except for minor difference in method of calculation of TB.	VA ≠ VB, TA ≥ TB > 0, DX	D,R,H	10
41	Same as 31, except that the calculated TB was slightly larger than TA. Set TB = TA.	VA ≠ VB, TA = TB, DX	D,R,H	95
42	Same as 32, except that the calculated TB was slightly larger than TA. Set TB = TA.	VA ≠ VB, TA = TB, DX	D,R,H	3
46	Same as 31, except for minor difference in calculations of TB, which turned out to be slightly larger than TA. Set TB = TA.	VA ≠ VB, TA = TB, DX	D,R,H	191

TABLE 2A

JD	JT	JR	JG.	VA	VB	TA	TB	D	R	H	DX
242	73731	198	31	401.1	415.5	0.779	0.188	5.454	0.0241	10.53	21.305
242	73877	201	31	408.2	415.6	0.973	0.180	4.610	0.0273	6.94	21.305
242	73899	202	31	408.2	415.6	0.973	0.180	4.610	0.0273	6.94	21.305
242	73921	203	31	410.9	415.6	1.013	0.193	5.113	0.0262	7.40	21.305
242	73943	204	31	410.9	415.6	1.013	0.193	5.113	0.0262	7.40	21.305
242	74065	209	31	411.4	415.6	1.033	0.180	4.969	0.0317	4.44	21.305
242	74087	210	7	411.4	411.4	1.033	0.191	4.969	0.0317	4.44	11.174
242	74131	212	31	411.4	415.6	1.033	0.229	6.051	0.0255	6.69	21.305
242	74929	238	31	409.3	415.6	0.896	0.244	7.394	0.0205	8.49	21.305
242	74951	239	31	399.1	415.6	0.723	0.214	7.406	0.0246	13.86	21.051
242	74973	240	31	399.1	415.6	0.723	0.214	7.406	0.0246	13.86	21.051
242	77147	310	31	402.9	415.6	0.788	0.189	5.634	0.0367	9.15	21.051
242	78473	364	7	429.7	429.7	1.191	1.191	5.634	0.0367	9.15	11.174
242	78698	365	7	439.1	439.1	1.191	1.191	5.634	0.0367	9.15	11.174
242	79142	367	7	443.7	443.7	1.191	1.191	5.634	0.0367	9.15	11.174
242	79584	369	31	456.7	456.7	1.315	1.315	3.192	0.0433	86.49	11.174
242	79808	370	31	453.2	453.2	1.459	1.459	3.522	0.0439	81.97	21.305
242	80029	371	7	443.7	443.7	1.459	1.459	3.522	0.0489	81.97	21.305
242	80250	372	7	435.2	435.2	1.459	1.459	3.522	0.0489	81.97	21.305
242	80693	374	7	421.9	421.9	1.459	1.459	3.522	0.0489	81.97	21.305
242	81015	375	31	415.1	415.6	1.214	0.162	3.984	0.0517	3.07	21.051
242	81138	376	31	409.3	415.6	0.896	0.247	7.364	0.0258	9.49	21.051
242	81582	378	31	408.8	415.6	0.933	0.213	5.820	0.0334	8.21	21.051
242	81803	379	31	408.2	415.6	0.973	0.181	4.610	0.0433	6.94	21.051
242	82245	381	31	413.4	415.6	1.056	0.194	5.687	0.0318	5.93	21.051
242	82468	382	1	426.7	426.7	2.439	2.439	7.633	0.0369	7.98	21.051
242	82689	383	2	420.9	420.9	2.864	2.864	9.506	0.0360	5.40	21.051
242	82911	384	1	426.7	426.7	2.439	2.439	7.633	0.0369	7.98	21.051
242	83133	385	7	426.7	426.7	2.439	2.439	7.633	0.0369	7.98	11.174
242	83577	387	1	440.7	440.7	1.573	1.573	6.874	0.0386	15.00	11.174
242	83798	388	1	446.4	446.4	1.717	1.717	4.316	0.0424	11.10	11.174
242	84021	389	1	445.3	445.3	1.629	1.629	5.265	0.0351	12.78	11.174
242	84242	390	7	432.5	432.5	1.629	1.629	5.265	0.0351	12.78	21.305
242	84463	391	1	446.3	446.3	1.431	1.431	4.692	0.0368	16.11	21.305
242	84686	392	7	427.2	427.2	1.431	1.431	4.692	0.0368	16.11	21.305
242	84907	393	1	453.4	453.4	1.471	1.471	5.612	0.0254	13.85	21.305
242	85129	394	1	443.9	443.9	1.514	1.514	5.062	0.0592	15.24	21.051
242	85351	395	1	467.0	467.0	1.467	1.467	5.413	0.0794	7.05	21.051
242	85573	0	1	463.9	463.9	1.241	1.241	5.875	0.0693	12.30	21.051
242	85794	1	31	449.1	449.1	1.637	1.637	8.036	0.0703	75.99	21.051
242	86016	2	7	442.2	442.2	1.637	1.637	8.036	0.0703	75.99	21.051
242	86238	3	1	463.7	463.7	1.343	1.343	9.955	0.0683	11.34	21.051
243	75	4	1	481.7	481.7	0.871	0.871	10.836	0.0459	13.20	21.051
243	502	6	31	479.8	495.4	0.717	0.376	11.786	0.0239	19.20	19.622
243	724	7	1	464.7	464.7	1.018	1.018	12.625	0.0179	17.57	11.174
243	945	8	1	462.9	462.9	0.969	0.969	12.149	0.0301	19.04	11.174
243	1169	9	1	464.4	464.4	0.947	0.947	11.939	0.0291	19.04	11.174
243	1390	10	1	463.1	463.1	0.912	0.912	11.606	0.0305	21.01	11.174

TABLE 2B

JD	JT	JFC	JG	VA	VB	TA	TB	D	R	H	DX
2	72731	198	31	401.1	415.5	0.779	0.188	[illegible]	[illegible]	[illegible]	21.305
2	7 77	201	31	408.2	415.6	0.973	0.180	[illegible]	[illegible]	[illegible]	21.305
2	7 99	202	31	408.2	415.6	0.973	0.180	[illegible]	[illegible]	[illegible]	[illegible]
242	7 21	203	31	410.8	415.6	1.013	0.193	[illegible]	[illegible]	[illegible]	21.305
242	7 42	204	31	410.8	415.6	1.013	0.193	[illegible]	[illegible]	[illegible]	21.305
242	7 [illegible]	205	31	415.3	415.6	1.153	0.180	[illegible]	[illegible]	[illegible]	21.305
242	7 [illegible]	206	7	422.1	422.1	[illegible]	[illegible]	[illegible]	[illegible]	[illegible]	[illegible]
242	74707	207	31	411.3	415.6	0.970	0.225	[illegible]	[illegible]	[illegible]	21.305
242	74929	208	31	404.3	415.6	0.896	0.244	[illegible]	[illegible]	[illegible]	21.305
242	7 703	216	31	399.1	414.0	0.685	0.214	[illegible]	[illegible]	[illegible]	21.051
242	76925	217	31	399.1	414.0	0.685	0.214	[illegible]	[illegible]	[illegible]	21.051
242	77147	218	31	402.3	415.6	0.805	0.189	[illegible]	[illegible]	[illegible]	21.051
242	78476	224	7	429.7	429.7	[illegible]	[illegible]	[illegible]	[illegible]	[illegible]	[illegible]
242	78698	225	7	439.1	439.1	[illegible]	[illegible]	[illegible]	[illegible]	[illegible]	[illegible]
242	79142	227	7	443.7	443.7	[illegible]	[illegible]	[illegible]	[illegible]	[illegible]	[illegible]
242	79584	229	21	456.7	456.7	1.315	1.315	3.152	0.0433	86.49	[illegible]
242	7 708	230	21	453.2	453.2	1.459	1.459	3.522	0.0489	81.97	[illegible]
242	8 029	231	7	443.7	443.7	[illegible]	[illegible]	[illegible]	[illegible]	[illegible]	[illegible]
242	8 50	232	7	435.2	435.2	[illegible]	[illegible]	[illegible]	[illegible]	[illegible]	[illegible]
242	8 [illegible]	234	7	421.9	421.9	[illegible]	[illegible]	[illegible]	[illegible]	[illegible]	[illegible]
242	80916	235	31	415.1	415.6	1.214	0.162	[illegible]	[illegible]	[illegible]	21.051
242	81136	236	31	409.3	415.6	0.896	0.247	[illegible]	[illegible]	[illegible]	21.051
242	81582	238	31	408.8	415.6	0.933	0.213	[illegible]	[illegible]	[illegible]	21.051
242	81803	239	31	408.2	415.6	0.973	0.181	[illegible]	[illegible]	[illegible]	21.051
242	82246	241	31	413.4	415.6	1.056	0.194	[illegible]	[illegible]	[illegible]	21.051
242	82466	242	1	426.7	426.7	2.439	2.439	7.633	0.0369	7.98	[illegible]
242	82669	243	2	420.9	420.9	2.864	2.864	9.506	0.0360	[illegible]	[illegible]
242	82911	244	1	426.7	426.7	2.439	2.439	7.633	0.0369	7.98	[illegible]
242	83133	245	7	425.7	425.7	[illegible]	[illegible]	[illegible]	[illegible]	[illegible]	[illegible]
242	83577	247	1	440.7	440.7	1.573	1.573	6.874	0.0386	15.00	[illegible]
242	83796	248	1	446.4	446.4	1.717	1.717	4.316	0.0424	11.10	[illegible]
242	84021	249	1	445.3	445.3	1.629	1.629	5.265	0.0351	12.78	[illegible]
242	84242	250	7	432.5	432.5	[illegible]	[illegible]	[illegible]	[illegible]	[illegible]	[illegible]
242	84463	251	1	446.3	446.3	1.431	1.431	4.[illegible]	0.0[illegible]68	16.11	[illegible]
242	84680	252	7	427.2	427.2	[illegible]	[illegible]	[illegible]	[illegible]	[illegible]	[illegible]
242	84907	253	1	453.4	453.4	1.471	1.471	5.612	0.[illegible]64	[illegible].35	[illegible]
242	85127	254	1	[illegible]	[illegible]	1.514	1.514	5.[illegible]	0.[illegible]92	[illegible]	[illegible]
242	85351	255	1	[illegible]	[illegible]	1.467	1.467	5.[illegible]13	0.0[illegible]74	7.05	[illegible]
242	85573	0	1	463.9	463.9	1.241	1.241	5.875	0.0693	12.30	[illegible]
242	85796	1	[illegible]	[illegible]	[illegible]	[illegible]	[illegible]	[illegible]	0.0703	75.99	[illegible]
242	86019	2	[illegible]	[illegible]	[illegible]	[illegible]	[illegible]	[illegible]	[illegible]	[illegible]	[illegible]
242	86238	3	1	[illegible]	[illegible]	[illegible]	[illegible]	[illegible]	[illegible]	11.34	[illegible]
243	79	4	1	[illegible]	[illegible]	[illegible]	[illegible]	[illegible]	[illegible]	[illegible]	[illegible]
243	502	6	31	477.[illegible]	[illegible]	[illegible]	[illegible]	[illegible]	[illegible]	[illegible]	[illegible]
243	724	7	1	464.7	464.7	1.018	1.018	12.[illegible]	[illegible].0179	17.57	[illegible]
243	946	8	1	462.9	462.9	0.969	0.969	12.149	0.0301	19.04	[illegible]
243	1159	9	1	464.4	464.4	0.947	0.947	11.939	0.0291	19.04	[illegible]
243	1390	10	1	463.1	463.1	0.912	0.912	11.606	0.0305	21.01	[illegible]

TABLE OF CONTENTS

I. Initial Identification

A. DATA SET IDENTIFICATION
1. Mariner 2 62-041A-06C
2. Experimenter -Marcia Neugebauer
3. Acquisition Agent -Judith E. Devaney
4. Electrostatic Analyzer 'C'
One Hour Averages

B. TAPE IDENTIFICATION
1. Tape Number D-02887, C-02094
2. Mode- BCD, Density - 556 BPI
3. Created on IBM 7094-E
4. One File
5. One Tape
6. The Tape Can Be Read with the following Fortran Formatted read:
READ (5,1) (IH(I), V(I), N(I), I=1,6), ND
1FORMAT (6(I3,F6.1,I3),I8)
IH is the beginning hour plus 2 (e.g., if IH=2, the average is between 0000 and 0100 UT).

V is the plasma velocity. Where upper and lower limits of velocity had to be computed, the upper limit was used in the average.

N is the number of points in the average.

ND is the day number, where Jan. 1, 1962 is day number 1.

I. Initial Identification

A. DATA SET IDENTIFICATION
1. Mariner 2 62-041A-06C
2. Experimenter -Marcia Neugebauer
3. Acquisition Agent -Judith E. Devaney
4. Electrostatic Analyzer 'C'
One Hour Averages

B. TAPE IDENTIFICATION
1. Tape Number D-02887, C-02094
2. Mode- BCD, Density - 556 BPI
3. Created on IBM 7094-E
4. One File
5. One Tape
6. The Tape Can Be Read with the following Fortran Formatted read:
READ (5,1) (IH(I), V(I), N(I), I=1,6), ND
1FORMAT (6(I3,F6.1,I3),I8)

IH is the beginning hour plus 2 (e.g., if IH=2, the average is between 0000 and 0100 UT).

V is the plasma velocity. Where upper and lower limits of velocity had to be computed, the upper limit was used in the average.

N is the number of points in the average.

ND is the day number, where Jan. 1, 1962 is day number 1.

Instrument Specification Sheet

Inst. 6
Mariner 2
1962 Alpha-Rho
27 Aug 1962
Page 1 of 3

SOLAR PLASMA SPECTROMETER

COGNIZANT ORGANIZATION
Jet Propulsion Laboratory (JPL)/H. Neugebauer, Dr. C.W. Snyder, and H.R. Hertz

PURPOSE
Measure the flux and energy spectrum of the positively charged component of streams of solar plasma which may be moving radially outward from the sun.

INSTRUMENT CHARACTERISTICS AND CONFIGURATION
The instrument is a charged-particle spectrometer with a logarithmic response covering the range of energies as shown in the table below.

The plasma analyzer consists of a pair of curved plates, electrically charged with respect to each other, that selects the charged particles of desired energy; a Faraday cup which collects the charge of the particles traversing the electrostatic field between the plates; an electrometer circuit for measuring the current due to this collected charge; and a high-voltage generating system which applies voltage in sequence to the analyzer plates. The plates have an angular length of 120 degrees with radii of curvature of 3.97 and 4.50 inches.

The analyzer has, effectively, a 10-degree angular resolution and a 12 percent energy resolution. The high-voltage supply is programmed to apply 10 progressively greater deflecting voltages to the plates. The electrometer circuit, utilizing logarithmic feedback, can measure currents from 10^{-6} amp.

DETAILS OF MEASUREMENT

Type of Particle or Field
Positive ions and solar protons

Energy Range

Programmer step level	Voltage across deflection plates, v	Energy level of particles reaching cup, ev
1	60	240
2	89	356
3	132	528
4	196	784
5	290	1160
6	432	1728
7	642	2568
8	952	3808
9	1420	5680
10	2100	8400
11	−0	−
12	−0	Electrometer calibration

(JPL SPS 37-15)

ELECTRO-OPTICAL SYSTEMS, INC. Pasadena, California

18 -C-100

FOR OFFICIAL USE ONLY

1 May 1963

Instrument Specification Sheet

SOLAR PLASMA SPECTROMETER

Inst. 6
Mariner 2
1962 Alpha-Rho
27 Aug 1962
Page 2 of 3

DETAILS OF MEASUREMENT (continued)

Energy Resolution
12%

Angular Resolution
10°

ALTITUDE OR TRAJECTORY FOR MEASUREMENT
Throughout trajectory until end of communications.

LIFETIME OF MEASUREMENT
~ 129 days

TIME CORRELATION WITH OTHER MEASUREMENTS
Solar activity; Inst. 3 and Inst. 4

INSTRUMENT POWER CONSUMPTION
1 watt

WEIGHT
4.8 lbs

INSTRUMENT DATA FORMAT

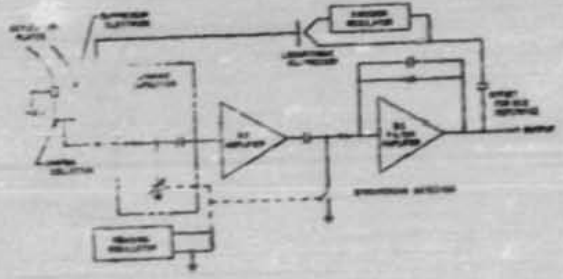

SOLAR PLASMA ELECTROMETER
(JPL Diagram)

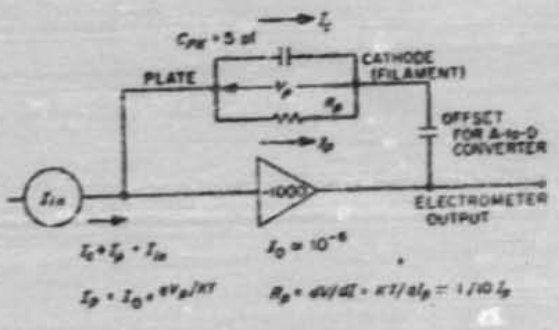

ELECTROMETER EQUIVALENT CIRCUIT
(JPL Diagram)

Instrument Specification Sheet

SOLAR PLASMA SPECTROMETER

CONSTRAINT CALIBRATION ORGANIZATION
JPL

INSTRUMENT CALIBRATION PROCEDURE

Preflight
Laboratory proton accelerator

Inflight
Figure 1 is a typical calibration curve. The linearity of the response over this dynamic range is excellent. Provision is made for a "zero current" measurement by holding both collecting plates at zero voltage, as well as for a calibrating current of 10^{-10} amps fed directly to the electrometer input through a constant-current source.

DEPOSITORY FOR DATA
JPL

five unmanned lunar and planetary exploration of space. Of particular interest in this area is the low-energy solar corpuscular radiation sometimes called solar plasma or the solar wind (Ref. 1, 2). The determination of the flux of these particles as a function of (1) their energy and direction of travel, (2) the magnetic field that accompanies them, and (3) time is an essential step in the understanding of the physics of the solar corona, the modulation of cosmic rays, the distortion of the terrestrial and lunar magnetic fields, and many solar-terrestrial phenomena such as magnetic storms, auroras, and time variation in the contents and extent of the Van Allen belts. Various theories of the solar corona have predicted the direction of travel of the interplanetary plasma to be isotropic (Ref. 3), radially away from the Sun (Ref. 4, 5), or perpendicular to the ecliptic along a field line of a solar magnetic dipole (Ref. 6). The solar plasma was predicted to contain electrons, protons, and some heavier positive ions which have velocities near 300 km/sec. The energy of most of the electrons in the plasma streams would then be a few electron volts, with positive ion energies in the kilovolt range.

Measurement of this radiation by conventional methods is made somewhat difficult by the fact that the energies of these particles may be so low as to preclude penetration of even the thinnest of the thin-walled counters. For this reason, the detector system about which the instrumentation in this report is designed was chosen to provide an unobstructed collection path for those charged particles of interest. This detector is the curved-plate electrostatic analyzer. The formulation of experiments to be conducted with these plasma analyzers and the design of the electrostatic deflection plates have been the responsibilities of M. M. Neugebauer and C. W. Snyder of the Jet Propulsion Laboratory (JPL).

The principal goals of these solar plasma experiments, in summary, were to perform interplanetary measurements to determine the extent of, and the variations in, the solar corona. A correlated engineering requirement was the development of an electronic system providing, within the minimal weight and power allocations customary in these applications, stable and reliable performance over periods of time required to traverse planetary distances. An additional goal was to provide instrumentation capable of being used in various low-current applications.

II. FUNCTIONAL DESCRIPTION

A. The Basic System

The basic electrostatic system is illustrated in Fig. 1. Charged particles entering the instrument are deflected by an electric field approximately transverse to the particle velocity. Those particles with a particular charge sign and within a certain range of energy per unit charge, and a certain range of angle of incidence are deflected through the curved tunnel onto the charge collector. Particles that enter the instrument with the wrong charge sign, energy per unit charge, or angle of incidence strike the analyzer walls and are not collected. The energy distributions of both positively and negatively charged particles entering the device can be determined by varying the sign and magnitude of the deflection voltage. The charge collection rate is measured at each energy level by a wide-range electrometer.

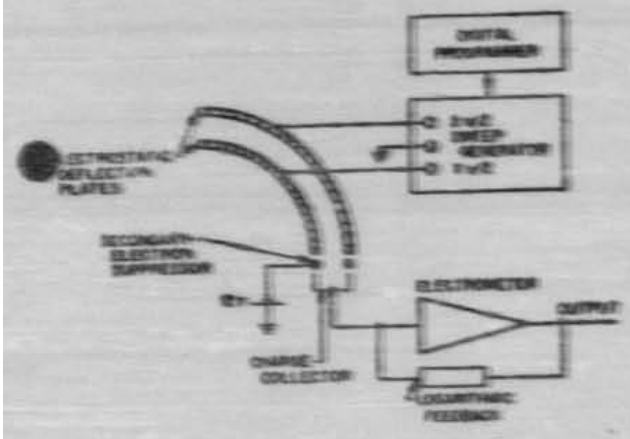

Fig. 1. Block diagram of basic solar plasma instrumentation

B. Ranger I, 2 Plasma Instrument

The primary mission of the first two Ranger spacecraft was to test the performance of those functions and parts of the spacecraft necessary for carrying out subsequent lunar and planetary missions using essentially the same spacecraft design. The secondary mission was the further determination of the nature of the particles and fields in interplanetary space. The plasma instrument, like most of the other Ranger I, 2 instruments, was directed toward the study of certain solar-terrestrial relationships, such as the correlation between geomagnetic storms and the solar wind.

One of the most important considerations in the Ranger-type spacecraft (the Mariner configuration is similar), is that the vehicle is attitude-stabilized in such a manner that the axis of symmetry (and thus the sensitive surface of the solar panels) points toward the Sun, and the plane that contains this axis and the high-gain antenna also contains the Earth (Fig. 2).

Six plasma detectors, each with an acceptance angle of approximately 15 deg, were situated on the spacecraft so as to point in six orthogonal directions: toward and away from the Sun, approximately forward and backward in the ecliptic, and approximately north and south of the ecliptic. The analyzers were assembled in pairs, and as seen in Fig. 2, the pair of analyzers pointing toward and away from the Sun was located on a boom intended to place the analyzers beyond the plasma sheath of the vehicle itself. The determination of the direction of particle travel was expected to make it possible to choose among the principal theoretical models for the interplanetary plasma.

The basic Ranger assembly is outlined in the block diagram of Fig. 3. The electrostatic drive for the deflection plates is supplied by a programmable high-voltage sweep amplifier. By having the ability to change the polarity of the deflection plate voltages, this amplifier enables the deflection system to focus either electrons or positive ions onto the collector. The sweep program was selected to provide discrimination at four electron energy levels between and including 12.7 and 110 ev. Similarly, eight positive-ion energy levels between 12.7 and 5,490 ev were to be monitored.

1. Deflection Voltage System

The high-voltage amplifier is programmed by a 4 × 12 diode matrix which consecutively gates a reference voltage to one of the 12 input resistors of the amplifier. The matrix is driven by a four-stage binary counter which accepts one pulse per 2 sec from the spacecraft Data Automation System (DAS). A reset pulse from the DAS every 120 sec recycles the counter for another measurement sequence. The measurement cycle is shown in Table 1.

The voltage drive for both pairs of deflection plates consists of an operational amplifier having wide dynamic range, augmented by two subsidiary amplifiers for generation of stable low-voltage steps. This system

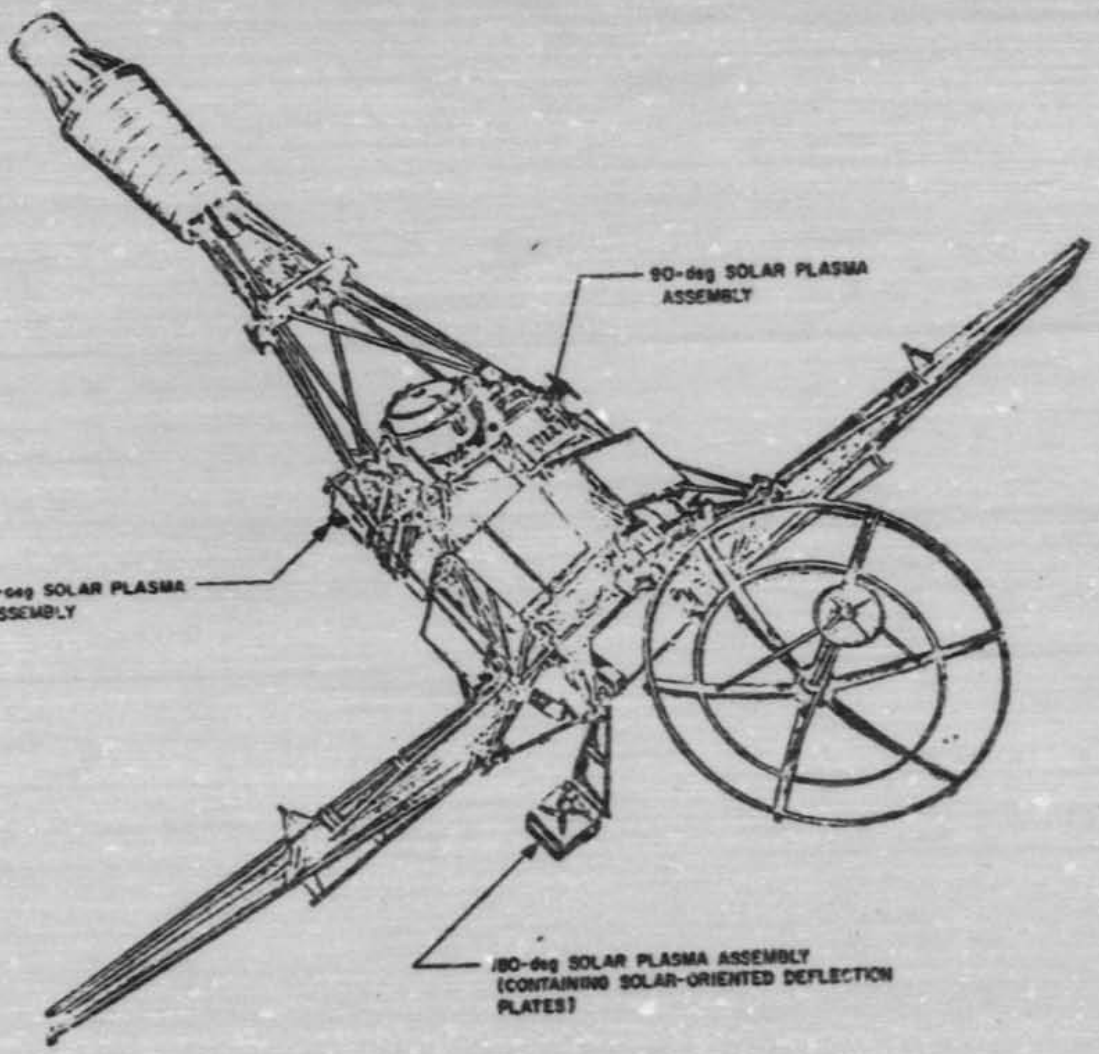

Fig. 2. Ranger 1, 2 spacecraft

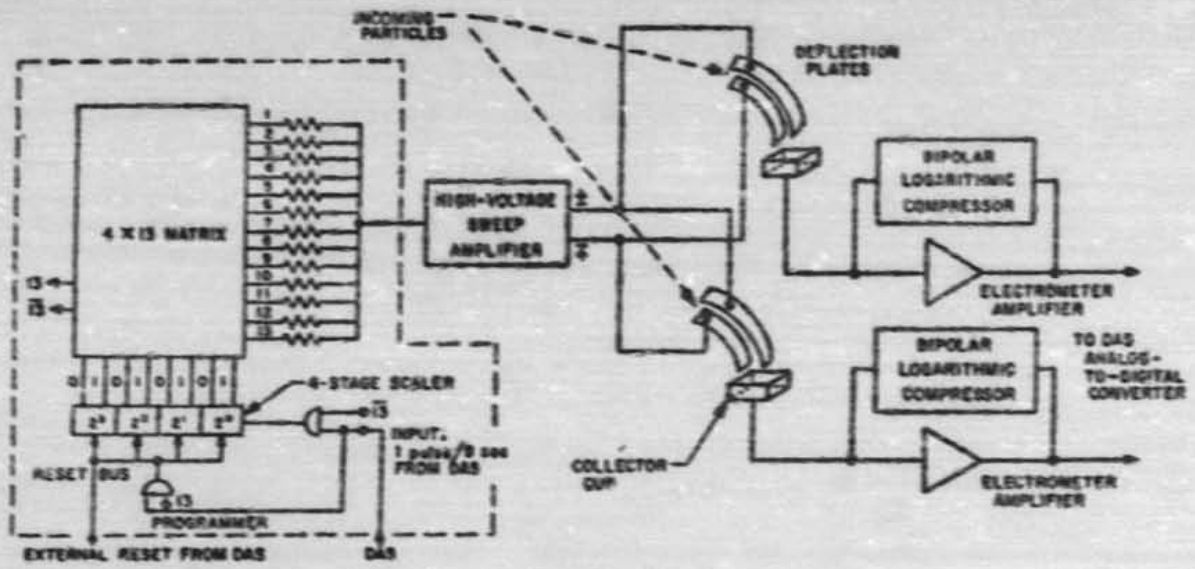

Fig. 3. Block diagram of the *Ranger* solar plasma instrument

delivers programmed voltages of +100 to −1,000 v dc and −100 to +1,000 v dc to the inner and outer plates, respectively. The differential voltages across the deflection plates and the corresponding energy levels are shown in Table 2.

Table 1. Measurement cycle for *Ranger* solar plasma instruments

Interval	Time, sec	Operation
1	0 to 9	Deflection voltages are set at step 1.
1	9 to 9.2	Outputs of all six electrometers are simultaneously converted to 8-bit digital form and stored by the DAS.
2	9 to 18	Deflection voltages are set at step 2, and data from interval 1 are commutated to the communications system at a standard telemetry transmission rate.
3 to 12	10 consecutive 9-sec intervals	Measurement procedures are the same as in the first interval. In each interval, data of the previous interval are telemetered.
13	108 to 120	Deflection voltages are set at the step 1 level, but the electrometers are not sampled in this period.

Table 2. Particle energies corresponding to voltage across *Ranger* deflection plates

Step number	Deflection plate voltage (outer minus inner), v	Particle energy, ev
1	−40	110[a]
2	−20	54.5[a]
3	−10	27.4[a]
4	− 5	13.7[a]
5	5	13.7[b]
6	10	27.4[b]
7	20	54.5[b]
8	63	172[b]
9	131	414[b]
10	365	1,000[b]
11	840	2,300[b]
12	2,000	5,490[b]

[a]Electron.
[b]Positive ion.

2. Electrometer

The current-measuring part of the instrument consists of a dual logarithmic current-to-voltage transducer and

a dynamic capacitor-modulated carrier-type dc amplifier. The logarithmic device produces compression of both electron and positive-ion currents between 10^{-13} and 10^{-6} amp; for the deflection plate geometry being used, these currents correspond to particle fluxes ranging between 3.8×10^{5} and 3.8×10^{11} cm^{-2} sec^{-1} for each energy interval. The compressed analog output is converted to 8-bit digital form for transmission accuracy.

The twin-analyzer assemblies were produced in two forms. The two assemblies mounted on the superstructure above the main, hexagonally shaped body of the spacecraft (Fig. 2) each contained deflection systems whose apertures were 90 deg apart. The combined effect of having these two similarly constructed units on diagonal corners of the spacecraft was to produce four unobstructed analyzing views orthogonal to the axis of symmetry. The third assembly (illustrated in Fig. 4), which was extended from the vehicle at the end of a boom, contained apertures 180 deg apart for looking toward and away from the Sun. A compartment containing two electrometers, which is partially obscured in Fig. 4, is shown in Fig. 5.

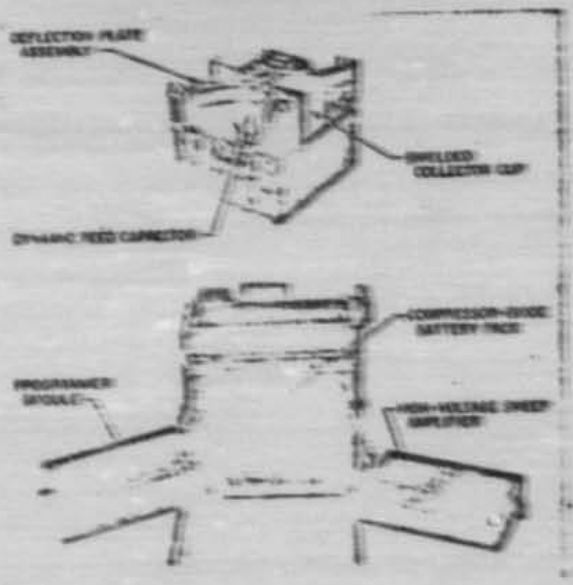

Fig. 4. 180-deg solar plasma analyzer used on the *Ranger*

Rangers 1 and *2* were to be placed in "parking" or satellite orbits by *Atlas-Agena B* launch vehicles. At the end of the parking orbits, the spacecraft were to be accelerated from orbital velocity to nearly escape velocity in a direction away from the Moon (Ref. 7). *Ranger 1* was launched at 8:04 a.m. Eastern Daylight Time on August 23, 1961. The velocity increment needed to accelerate the spacecraft into a highly eccentric orbit from the parking phase did not occur, and as a result, *Ranger 1* was placed in a low Earth orbit (Ref. 8). The solar plasma experiment produced data of little scientific or engineering value, owing to orientation problems and ionospheric interactions.

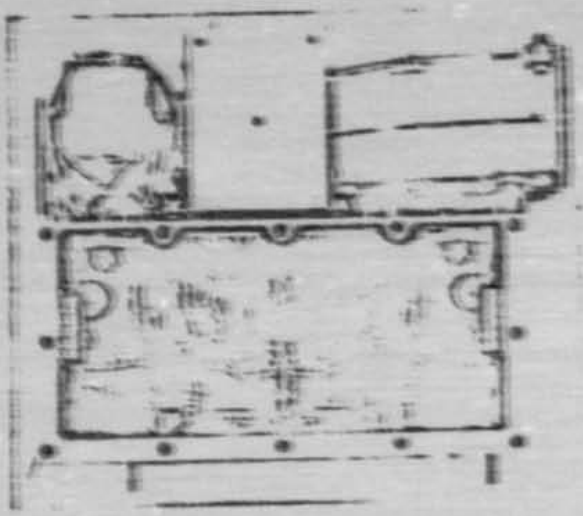

Fig. 5. Dual electrometer compartment

C. *Mariner 2 Plasma Instrument*

During the time when *Ranger 2* was being prepared for launch at the Atlantic Missile Range (AMR), a new passenger opportunity for a plasma instrument was presented. Work was proceeding at this time on the assembly of an 1,100-lb spacecraft called *Mariner* that was to be launched toward Venus in the following year by the *Atlas-Centaur* vehicle. However, after one of the two years allotted between spacecraft inception and launch had elapsed, it was established that *Centaur* would not be available for the planetary launch opportunity. A new *Mariner* spacecraft was being formulated, based upon an abbreviated schedule and the lesser weight-lifting capability of the *Atlas-Agena*. The new spacecraft was patterned after the *Ranger* system in terms of communication, guidance, control, and structure; however, the weight allocations for the components on the new spacecraft were more restrictive than those for the original *Mariner*. Scientific hardware, for example, was limited to 44 lb.

Based upon allocations of 5 pounds and 1 watt, one of the most important questions asked at this time was, "How comprehensive an experiment can be performed with one analyzer where six were required for the *Ranger 1* and 2 experiment?" Important observations made in March 1961 on *Explorer X* (Ref. 9, 10) suggested a radial flow of plasma from the Sun. With this valuable information, a single solar-oriented analyzer was proposed for *Mariner*. Subsequent approval required that the instrument be delivered within three months. The accelerated delivery requirement was considered realistic primarily because the *Mariner* package was patterned closely after the *Ranger* instrument.

The *Mariner* instrument did, however, provide a valuable opportunity for improving and updating the existing design. The electrostatic deflection plates, for instance, were extended from a 90-deg sector curve to a 120-deg curve. The ground rails separating the high-voltage plates were mechanically improved, and the collector-to-shield design was altered, thereby reducing collector-to-ground capacitance by 60%. The programming section of the instrument remained virtually unaltered, and deflection voltages were now supplied exclusively by the main high-voltage *Ranger* sweep amplifier. The new instrument was limited to positive-ion measurements of such energy levels as to make it possible to discard both positive and negative subsidiary amplifiers.

The sweep program is shown in Table 3 and the theoretical energy resolution and directionality are shown in Fig. 6, where the fraction of a beam of singly charged particles with energy E, incident at various angles on an analyzer, that reaches the collector cup is plotted vs. E/E_c. The energy E_c is that required for a trajectory with a constant radius of curvature for normally incident, singly charged particles. The value of E_c for the spacing and the 120-deg circular-sector geometry of the *Mariner* plates is four times the deflection voltage (Ref. 11, 12).

The electrometer made compressed measurements of only positive-ion current, thereby dispensing with a vacuum tube and its battery-operated filament-current supply. Other modifications of the electrometer circuit were as follows:

1. Nonlinear secondary feedback was introduced, resulting in improved low-current transient response.
2. A 10^{-10} amp in-flight calibration was added.
3. A discriminator circuit was added to prevent amplifier saturation due to negative background current.

Table 3. Solar plasma particle energies corresponding to *Mariner 2* deflection plate voltages

Programmer step level	Voltage (nominal) across deflection plates, V	Energy E_c of particles crossing aperture, ev
1	60	240
2	90	360
3	132	528
4	196	784
5	290	1,160
6	425	1,700
7	630	2,520
8	950	3,800
9	1,400	5,600
10	2,100	8,400
11	−1.4	—[a]
12	−1.4	—[b]

[a] Low-energy and background measurement.
[b] Electrometer calibration.

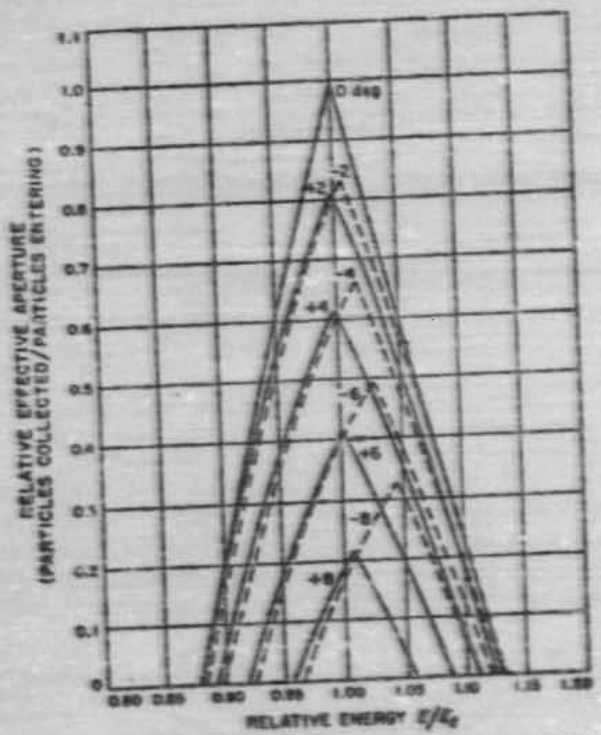

Fig. 6. Calculated *Mariner 2* solar plasma experiment response as functions of particle energy and incident angle

4. An improved dynamic-capacitor modulator was used.
5. Modulator excitation was now supplied by a self-resonant electro-acoustical oscillator.

The *Mariner* version of the plasma instrument is shown in Fig. 7 on board the *Mariner 2* spacecraft. It is shown once again in a more detailed but obscured view in Fig. 8.

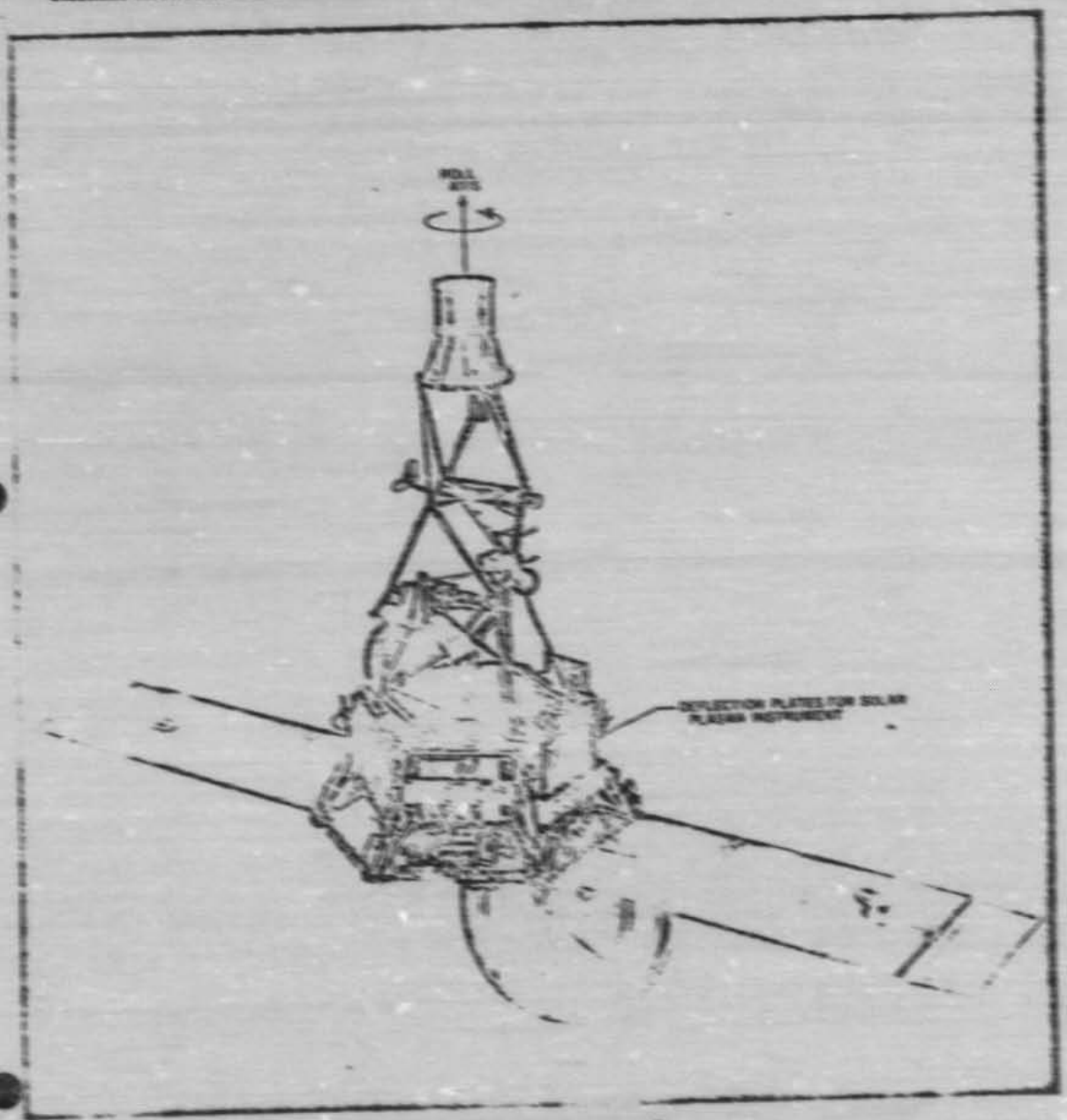

Fig. 7. *Mariner 2* spacecraft

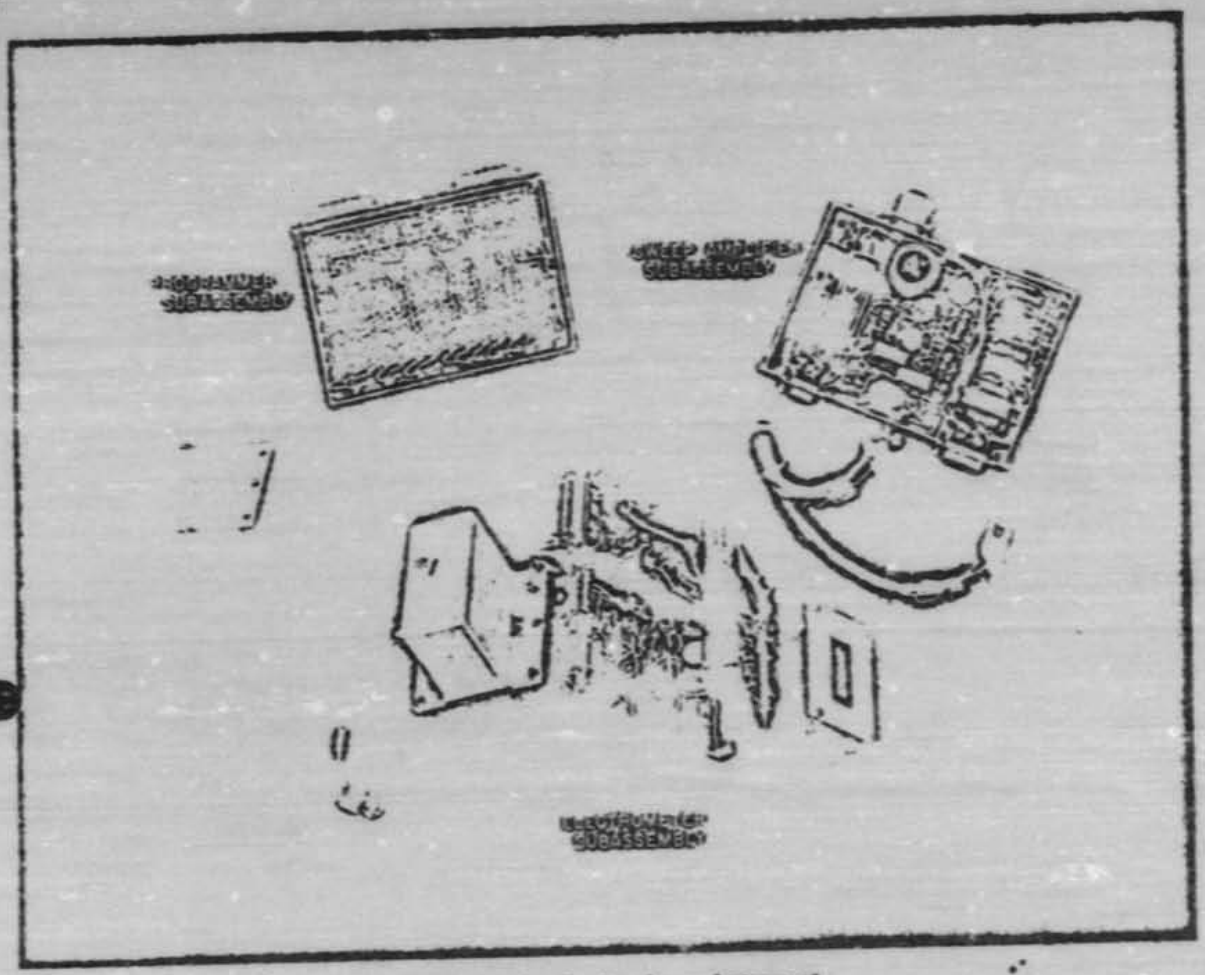

Fig. 8. Mariner 2 solar plasma instrument

III. THE ELECTROMETER SYSTEM

The basic form chosen for the electrometer system is the conventional operational amplifier configuration. The usual high-gain inverting amplifier is present but with certain external differences. The feedback element, usually a single resistor, in this case contains a more complex nonlinear circuit. The input resistor of the operational amplifier and its associated voltage source are replaced, in this application, by a current source of virtually infinite impedance. This amplifier configuration is popular in electrometer measurements because the small input (or summing-point) potential and small variations thereof minimize effects of input leakage resistance. Similarly, effects of input-to-ground capacitance upon the speed of response are also minimized.

The carrier-amplifier approach was pursued because input-modulating comparators of the dynamic capacitor variety offered such attractive prospects as high resistance, stability, and long life expectancy. Furthermore, if the modulator parameters were properly chosen, the need for a vacuum-tube input to the carrier amplifier would be eliminated. In addition, if the modulator frequency were made sufficiently high, the electrometer speed of response would not be severely limited by amplifier bandwidth, which would also be commensurately higher.

The choice of a nonlinear thermionic device for the principal feedback element was influenced by such considerations as dynamic range, simplicity, and familiarity. The dynamic current range requested by the experimenters was 7 decades--between 10^{-13} and 10^{-6} amp. The dynamic voltage range of the amplifier was forecast to be about 3 decades, limited at the high end by power supply voltage and at the low end by amplifier stability and the accuracy of analog-to-digital conversion. The more complex, though nonetheless appealing, technique of automatic switching of feedback resistors could not be used in view of project exigencies.

The stability of the static characteristic of the amplifier-compressor system was then realized to be primarily a function of the stability of the feedback tube. Regardless of this masking effect, the development of the capacitive modulator-stabilized amplifier was considered thoroughly worthwhile. The availability of a reliable modulator-amplifier combination would fulfill that perennial requirement for a system capable of providing low-threshold, fast, accurate, and long-lived measurements.

A. The Logarithmic Compressor

One of the simplest and most usable of nonlinear vacuum-tube devices is the logarithmic diode. This section of the Report describes two innovations to standard applications of logarithmic diodes as follows:

1. Emission stabilization by use of a low-voltage filament-current regulator.
2. Connection of two diodes and a battery, or its equivalent, in such a manner as to produce two distinguishable logarithmic calibration segments, i.e., one segment each for positive- and negative-polarity currents.

1. Unipolar Circuit

One of the simplest and most usable of nonlinear vacuum-tube devices is the logarithmic diode. If the voltage V_p on the diode shown in Fig. 9 were set at zero by shorting the plate to the ground-referenced side of the filamentary cathode, a current I_o would flow. This initial-velocity electron current decreases upon the application of a negative plate voltage. For this reason the second-quadrant portion of the characteristic shown in Fig. 9 is sometimes called the retarding field region. A number of subminiature electrometer tubes were inspected in this region, many of which displayed almost flawless exponential characteristics of the form $I_p = I_o\, e^{\varepsilon' V_p}$ below I_o. Many of the I_o's were in the range of 10^{-9} to 10^{-8} amp. The CK5886 subminiature pentode, a veritable work-horse of electrometer applications, was chosen, and both screen and control grids were tied to the plate

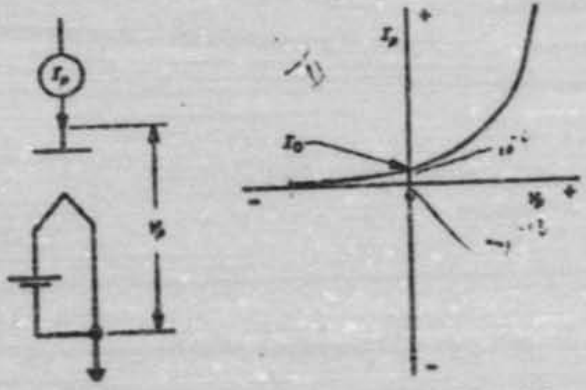

Fig. 9. Thermionic diode and associated characteristic

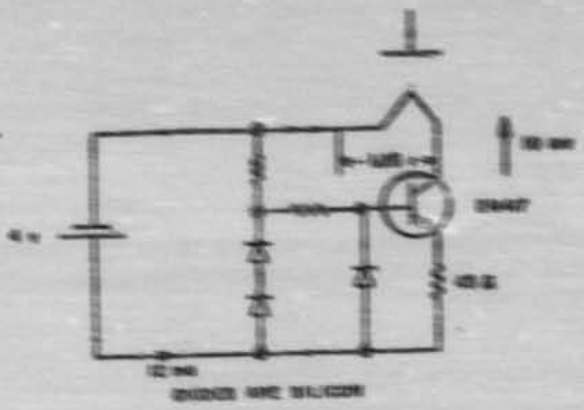

Fig. 10. Filament current regulator

to produce a diode connection. Extensive tube evaluations conducted under varying temperature conditions confirmed the desirability of having filament emission controlled with a constant-current regulator. This circuit, as shown in Fig. 10, affords low-voltage current regulation usually not available with series voltage-dropping resistors. An important feature of the regulator is that the emitter diode voltage of the germanium transistor is small enough compared with the drop across the adjacent silicon diode to permit inclusion of an important degeneration emitter in the transistor circuit. Probably more important still is the temperature tracking of the emitter diode and silicon diode voltages. The circuit has a current regulation of approximately 2% over a −30 to +75°C temperature range. Its regulation is such that current variations are 8% of input voltage variations at the nominal 4 v. Regulator performance is shown in Table 6.

During preliminary tube evaluation it was observed that drifts in plate voltage under conditions of constant plate current, but varying filament current, were often as much as three times smaller when measured with respect to the negative side of the filament than when measured with respect to the positive side. This effect, though not fully understood, is the principal reason for referencing the nonstandard negative side of the filament. Connecting the nave vacuum tube in its triode configuration makes it far less sensitive to cathode temperature changes (Ref. 10). The triode, however, is sensitive to plate voltage variations. The sensitivity of plate current to plate voltage variations for a CK5886 may be shown to be approximately 0.2 decade/2% change in V_b when

$$I_{b_1} = 10^{-10}\ \text{amp}$$

Table 6. Performance of filament current regulator

Battery voltage, v	I_f, ma		
	At +25°C	At −30°C	At +75°C
4.0	10.17	10.13	10.20
3.5	10.09	10.05	10.12
3.0	9.99	9.97	10.00
2.5	9.91	9.89	9.95
2.0	9.82	9.87	9.87

and

$$V_{b_1} = 3.5\ \text{v}.$$

Although the comparison is not exact, a similar tube, the CK5886 connected as a diode, produces the following filament-induced variation: 0.05 decade/2% change in I_b when

$$I_{b_1} = 10^{-6}\ \text{amp}$$

and

$$I_{b_2} = 20\ \text{ma}.$$

The diode connection was selected because of its 2-terminal character and its consequent amenability to being used in the feedback leg of a fast operational amplifier. The filament current regulator, in addition, reduced variations in the static characteristics of the CK5886 tube to an acceptably low level.

2. Bipolar Circuit

If it is desirable to measure currents of both polarities over similarly wide ranges, the notion of using two logarithmic diodes in opposing directions becomes very appealing. Consider what happens when two diodes are connected back-to-back, i.e., plate 1 to filament 2; plate 2 to filament 1. To satisfy the loop voltage equation, both plate voltages should be equal and of opposite polarity ($V_{b_1} = -V_{b_2}$). In the case of tubes having identical characteristics, the plate voltages become zero. For closely matched tubes, the circulating current will therefore be close to I_c, a value large enough to mask the effects of smaller external input currents. When it becomes necessary to reduce the circulating current, a biasing arrangement such as that shown in Fig. 11 may be used. The dc voltage V_c may then be made large enough to reduce the circulating current I_c to a value equal to or less than the threshold input current. The resultant characteri-

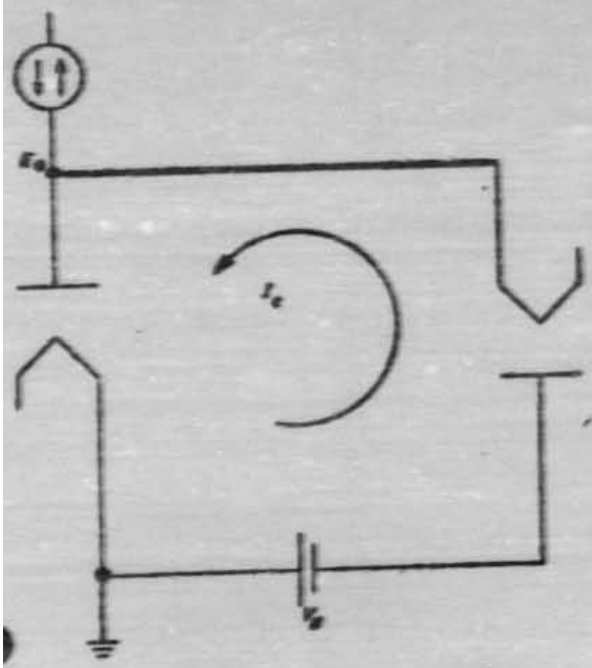

Fig. 11. Bipolar logarithmic current-to-voltage compressor

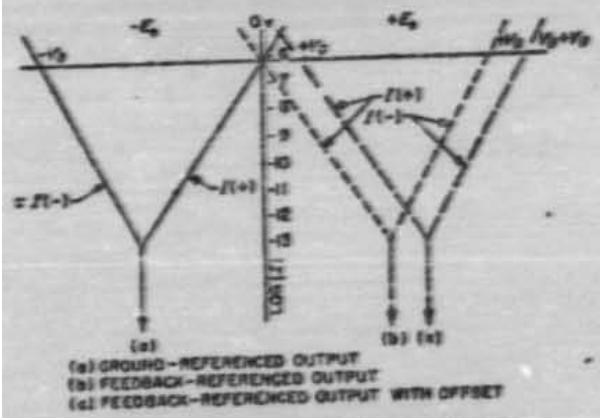

Fig. 12. Bipolar logarithmic characteristics

tic, as shown in Fig. 12a, would be produced with $V_0 = 3.75$ where both tubes have representative semilog slopes of 250 mv per current decade and I_0's of 10^{-4} amp.

To adapt this circuit to the form used on the *Ranger*, the circuit of Fig. 11 was transposed so that the input node was connected to the summing point of the inverting dc electrometer amplifier, and the formerly grounded connection was connected to the amplifier output. An ideal amplifier having zero drift, infinitesimal error potential, and zero input leakage, among other qualities, would force the input current through the feedback circuit and as a consequence produce an output characteristic (Fig. 12b) that was a mirror image of the original (Fig. 12a). To remain safely within the sampling range of the analog-to-digital converter that followed the amplifier, a small translational offset V_0 was inserted. The electrometer system with the feedback arrangement as used on the *Ranger* is shown in Fig. 13 and the corresponding translated curves are shown in Fig. 12c.

The filament supply was the most formidable problem connected with the logarithmic electron-current measurement. Although identical regulators were used, the transformer-rectifier supply used on the filament near the amplifier output could not be used for the filament at the input. For reasons of dc and ac isolation, a conventional insulated mercury-cell battery pack was used for the input filament of each of the two adjacent electrometers that appeared in each assembly. Each battery pack, capable of delivering two separate 50-mw loads for about 700 hr, weighed 3 lb. The penalties paid for the range and simplicity of this electron measurement

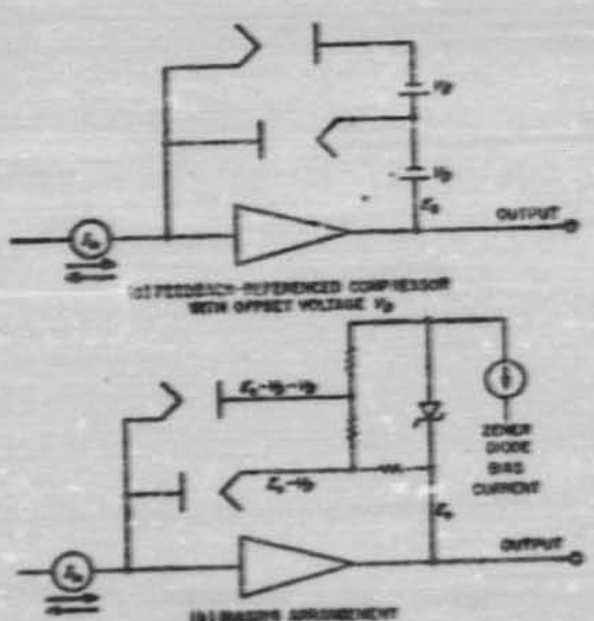

Fig. 13. Bipolar logarithmic electrometer

were in the weight of the battery pack and in the reduced gyroscope operational replacement flexibility.

2. Dynamic Equivalent Circuit

An important consideration in circuit application is the exposition of an equivalent network representing an accurate dynamic model of the logarithmic diode. This network enters into calculations for electrometer speed of response and into the formulation of feedback polynomials used in the determination of closed-loop stability.

A good approximation to the characteristic produced by the diode used in the logarithmic amplifier is (Ref. 14)

$$I_b = I e^{q(E_{cc}-E_b)/KT} \tag{3}$$

where

I_b = plate current

I = total emission current

E_{cc} = plate-to-filament voltage

E_c = contact potential

q = electron charge

K = Boltzmann constant.

Both E_c and I may be omitted by substituting I_o as the plate current at zero plate voltage (since the relation does hold for this tube):

$$I_b = I_o e^{qE_{cc}/KT} \tag{3}$$

or

$$E_{cc} = \frac{KT}{q} \ln \frac{I_b}{I_o}. \tag{3}$$

The resistance of the diode may be written

$$r_b = \frac{dE_{cc}}{dI_b} = \frac{KT}{qI_b}. \tag{4a}$$

The slope of the semilog characteristic may be written

$$M = \frac{q}{KT} = \frac{\ln (I_2/I_1)}{E_{cc_2} - E_{cc_1}} = \frac{\ln (I_2/I_1)}{E_{cc_2} - E_{cc_1}}.$$

Most of the 5886 diodes operating at filament currents of 10 ma displayed characteristics having about 200 mv per current decade. Applying this information, accordingly, to the last equation,

$$M = \frac{\ln 10}{0.200} = 11.$$

Using this approximation, the resistance may be written

$$r_b = \frac{1}{11 I_b} \tag{4b}$$

This expression is valid so long as the input current is static or varies slowly. If input current fluctuates rapidly, the equivalent instantaneous plate current will be different owing to interelectrode capacitance effects as suggested in Fig. 14. Lower-case terms are used here to denote transient or dynamic values of current, in which case i_b and i_{cc} are not necessarily equal on an instantaneous basis and may conceivably be of opposite polarity.

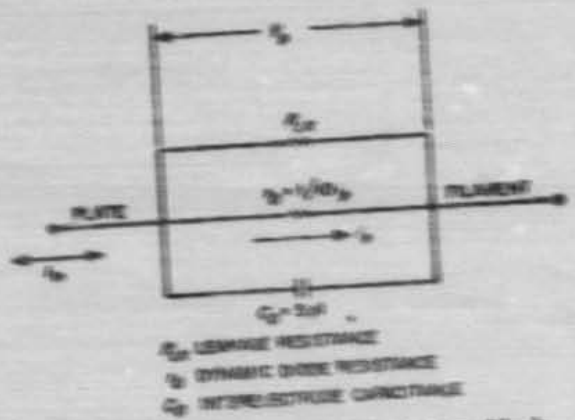

Fig. 14. Dynamic equivalent circuit of a logarithmic diode

Effects of expected extremes in ambient or mounting temperature (273 to 343°K) are attenuated to a good degree by a comparatively stable and high filament temperature (1350°K as calculated from the expression $T = q/KM$).

3. The Electrometer Amplifier

Since the instrument that was flown on Mariner 2 was a refined version of the Ranger instrument, the

discussion in this Section will bear mainly on the electrometer amplifier used in the *Mariner 2* solar plasma instrument (see Fig. 15).

1. Detailed Description

If the main feedback loop is inspected in a counterclockwise direction starting at the input, the first element of interest is the dynamic capacitor assembly. This modulator was developed for JPL through a series of contracts with the Applied Physics Corporation of Monrovia, California. The device is mechanically resonant near 2,400 cps ($Q_u \approx 200$) and is driven at this resonance by a tuned Class C amplifier (Ref. 15). The capacitive-drive oscillator loop is completed with a lead titanate vibration transducer, which is affixed to the vibrating reed element. Following the modulator are a one-stage low-noise ac preamplifier and a 3-stage ac postamplifier. The carrier signal is then half-wave demodulated with a transistor switch. Direct-coupled amplification and filtering are performed by a 4-stage Miller-type filter amplifier. The loop is then closed with a single logarithmic diode and its associated 10-ma current regulator. An offset voltage used in the flight instrument is not shown in the block diagram of Fig. 15.

Since the dynamic resistance of the feedback element may vary as many orders of magnitude as can the measurable input current, it was decided to augment the main loop with a secondary loop for purposes of nonlinear damping. The notion of an efficient single linear network correction for fast, stable operation in this system over a 7-decade current range still remains a pleasant fantasy.

/ A comparator that is referenced at a pre-saturation voltage has been provided to preclude saturation of the amplifier, an event that could occur in the presence of small negative background currents. When this reference level has been exceeded, an input current source, which doubles as a calibration current, is activated, thereby bringing the electrometer to a midrange voltage.

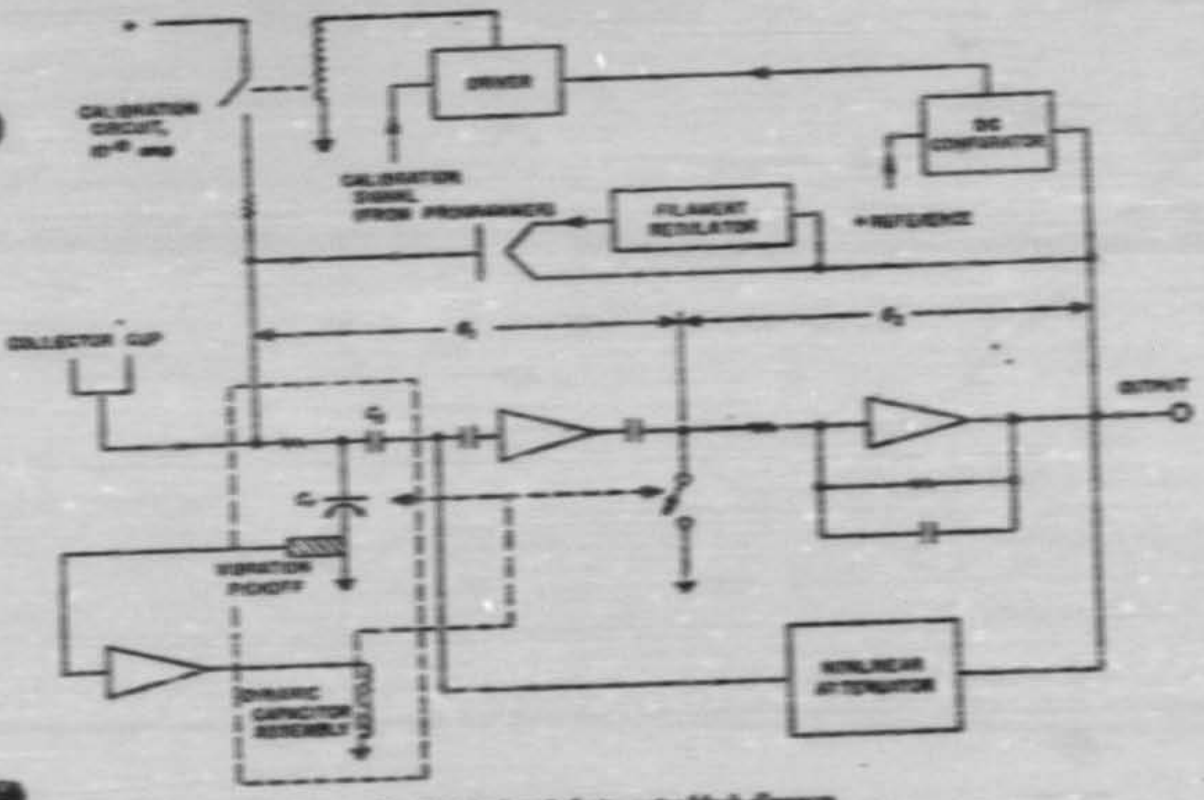

Fig. 15. *Mariner 2* electrometer block diagram

2. Design Choices

A figure of 1,000 was selected as the requirement for dc gain between the input and the output. If one neglects the effects of leakage current and resistance, the figure of 1,000 becomes the dc feedback factor. This standard of amplifier tightness limits dynamic deviations to 0.1% of the output as obtained with infinite gain.

The portion of this over-all gain incorporated into the carrier section was determined principally by considerations of noise and dc stability. The gain had to be made large enough to adequately minimize the effects of drifts in the demodulator baseline and the dc amplifier as seen at the electrometer input, but not so large as to permit input noise to drive the output stage of the ac amplifier into nonlinear operation. A representative gain of 35 for G_1 (see Fig. 15) reduced drifts from the dc section to the order of 1 mv as observed at the electrometer input. Noise at the output of the ac amplifier was about 100 mv rms within a linear dynamic capability of +2.5 and −6 v.

Since the transformer-rectifier power supply for the instrument was driven by a 50-v, 2,400-cps, square-wave source, it was certain that at least small amounts of 2,400-cps energy would be present in the carrier amplifier. The *Ranger* modulator was driven at the spacecraft power frequency, also 2,400 cps, and the ac amplifier, which was designed accordingly, was retained for the *Mariner* electrometer. The self-resonant dynamic capacitors used for *Mariner* were, therefore, ordered with mechanical resonances sufficiently displaced from 2,400 cps as to minimize internal beat-frequency signals.

The ac preamplifier presented one of the most likely areas for innovation. The question was whether the parameters of the customary vacuum-tube preamplifier could be replaced by those of a transistor. The number of stages needed for the carrier section turned out to be about the same both for a high-input impedance bootstrapped amplifier and for conventional low-input impedance common-emitter amplifiers. The low-impedance connection, as embodied in the circuit of Q1 in Fig. 16, was finally used. This circuit, as one might suspect, predated the commercial availability of field-effect transistors. The current gain of the carrier amplifier was significantly increased by a current step-up transformer ($n = 14{:}1$) interposed between the preamplifier and the dynamic capacitor. The primary impedance, which was sometimes the amplifier input impedance, was still relatively small compared with the capacitive source reactance of the dynamic capacitor. A phase-stable current gain of 14 could, therefore, be expected without increasing the noise component at the output of the carrier amplifier. Several germanium and silicon transistors were inspected in unloaded models of the preamplifier. The 2,400-cps gains of this highly degenerative circuit were experimentally confirmed to be equal, and then the output noise content was inspected. The germanium 2N417 was selected for the application because of its superior noise performance as observed through this empirical procedure. The chief safeguard against high-temperature saturation of the transistor caused by collector leakage is the diode CR2, whose I_{co} characteristic is matched to that of the transistor to at least 70°C. The preamplifier bias configuration presented an optimum thermal stability ($S_{I_c} = 1$) along with reduced gain to 1/*f* noise.

All amplifier elements within the main loop contained some local feedback. The oscillator that drove the dynamic capacitor, in fact, had a temperature-sensitive amplitude variation designed to maintain a more constant modulation conversion efficiency than would ordinarily be obtained with a constant drive voltage.

3. Gain

a. Carrier Amplifier. The first element entering into the gain equation for the carrier section is the dynamic capacitance (C_v in Fig. 17). Briefly reviewing the theory of operation of this modulator (Ref. 16), consider the elements V_{2a}, R2, and the dynamic capacitor as shown in Fig. 18a, with the output of C_v open-circuited in this example. Treating the capacitor as a parallel-plate device, its value may be written

$$C_v = \frac{\epsilon_0 A}{d} \tag{5}$$

where

A = area

d = separation between plates

ϵ_0 = dielectric constant of free space.

If one of the plates is sinusoidally driven at a frequency f such that its separation from the other plate is

$$d = d_0 \left[1 + (\Delta d/d_0) \sin \omega t\right], \tag{6}$$

the varying capacitance may then be expressed

$$C_v = \frac{\epsilon_0 A}{d_0 \left[1 + (\Delta d_0/d_0) \sin \omega t\right]} = \frac{C_0}{\left[1 + (\Delta d/d_0) \sin \omega t\right]} \tag{7}$$

where C_0 is the rest capacitance. In the general case where

$$R_1 C_0 >> 1/\omega$$

a constant charge

$$Q_0 = V_{1a} C_0 \tag{8}$$

is built up across the capacitor, C_v. The combined average, plus modulation voltage produced, is given by

$$V = \frac{Q_0}{C_v} = \frac{V_{1a} C_0 [1 + (\Delta d/d_0) \sin \omega t]}{C_v}$$

$$= V_{1a} [1 + (\Delta d/d_0) \sin \omega t] . \tag{9}$$

The conversion efficiency η_c is the figure of merit describing the efficiency of dc-to-ac conversion and is defined as follows:

$$\eta_c = \frac{V_{\text{max (open circuit)}}}{V_{1a\ (dc)}} = \frac{\Delta d}{d_0} \frac{\sqrt{2}}{2} . \tag{10}$$

Representative parameters and component values for the *Mariner 2*-type modulators are as follows:

$$C_0 = 50 \text{ pf}$$

$$C_A = 70 \text{ pf}$$

$$\eta_c = 10\%$$

and

$$f_r = 2{,}350 \text{ cps}$$

where C_A is a high-quality vacuum dielectric capacitor built into the modulator assembly, and f_r is the mechanical resonant frequency at which the reed is driven.

An ac approximation to the dynamic capacitor circuit, shown in Fig. 16b, replaces the dc source V_{1a} with the ac generator $\eta_c V_{1a}$, and replaces the nonlinear C_v with a source capacitance C_0. The feedback resistor R12 provides degeneration in the preamplifier and at the same time presents a suitably small termination to the transformer secondary. The nominal impedances of the transformer are 200 K and 1 K for the primary and secondary, respectively. The secondary impedance as shown by the Miller equivalent in Fig. 16b and c is indeed about 1 K. Under actual conditions when the preamplifier is loaded by the "Triplet" ac amplifier, the impedance may rise from 1 K to about 2.5 K with a small amount of reactive detuning present. Neglecting the effect of R_p, the open-circuit preamplifier output voltage $E_{1(oc)}$ may now be calculated from the circuit of Fig. 18c. In this circuit, the source impedance in ohms is given by

$$X_g = X_A + X_a + X_0 = 2.64 \times 10^6$$

where

$$X_a = 1.36 \times 10^6$$

$$X_A = 0.97 \times 10^6$$

$$X_0 = 0.31 \times 10^6 \qquad (C_0 = 220 \text{ pf})$$

and the primary input impedance is given by

$$R_p \cong 0.2 \times 10^6 .$$

The primary current, i_p, is given approximately by

$$i_p = \frac{\eta_c V_{1a}}{-j X_g} .$$

Therefore

$$v_p = \frac{i_p n R_{12}}{(1 - A_v)} = \frac{\eta_c V_{1a}}{-j X_g} \frac{n R_{12}}{1 - A_v}$$

and

$$E_{1(oc)} = \frac{\eta_c V_{1a} n R_{12}}{-j X_g} \frac{A_v}{1 - A_v} . \tag{11}$$

According to the equation

$$\left| \frac{E_{1(oc)}}{\eta_c V_{1a}} \right| \cong \frac{n R_{12}}{X_g}$$

the gain at 2,350 cps is calculated to be 0.25. In a test performed on the circuit of Fig. 18, the dynamic capacitor assembly was replaced by a 27-pf series capacitor, and a generator simulating the signal $\eta_c V_{1a}$ was connected to the input. The gain of this circuit vs. the frequency is shown in Fig. 19. The output impedance of the preamplifier was measured to be 5 K at 2,350 cps.

The triplet amplifier is a 3-stage, direct-coupled, feedback-biased cascade. At the carrier frequency, a substantial portion of the feedback used to bias the

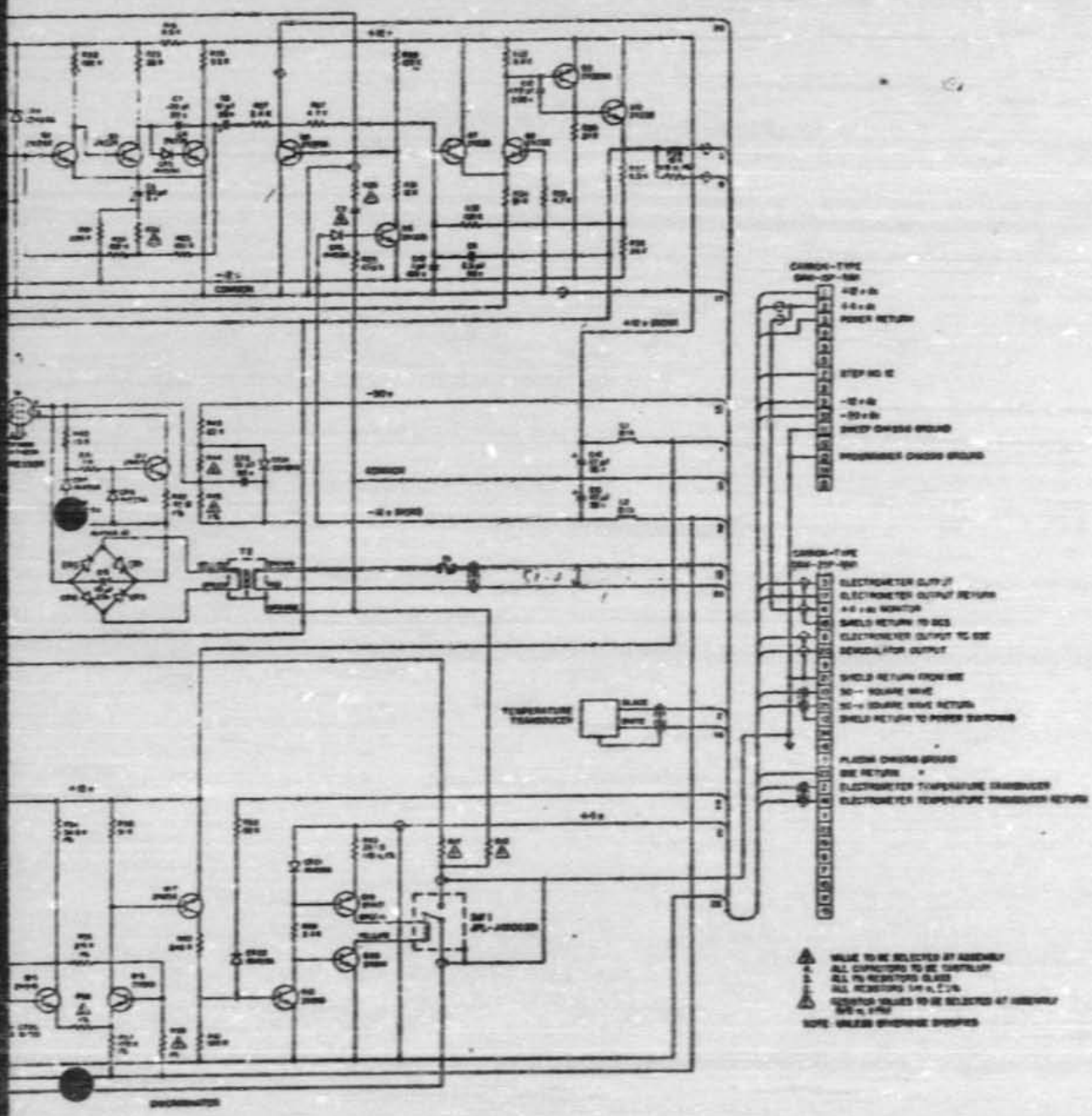

Fig. 14. Mariner 2 electrometer schematic diagram

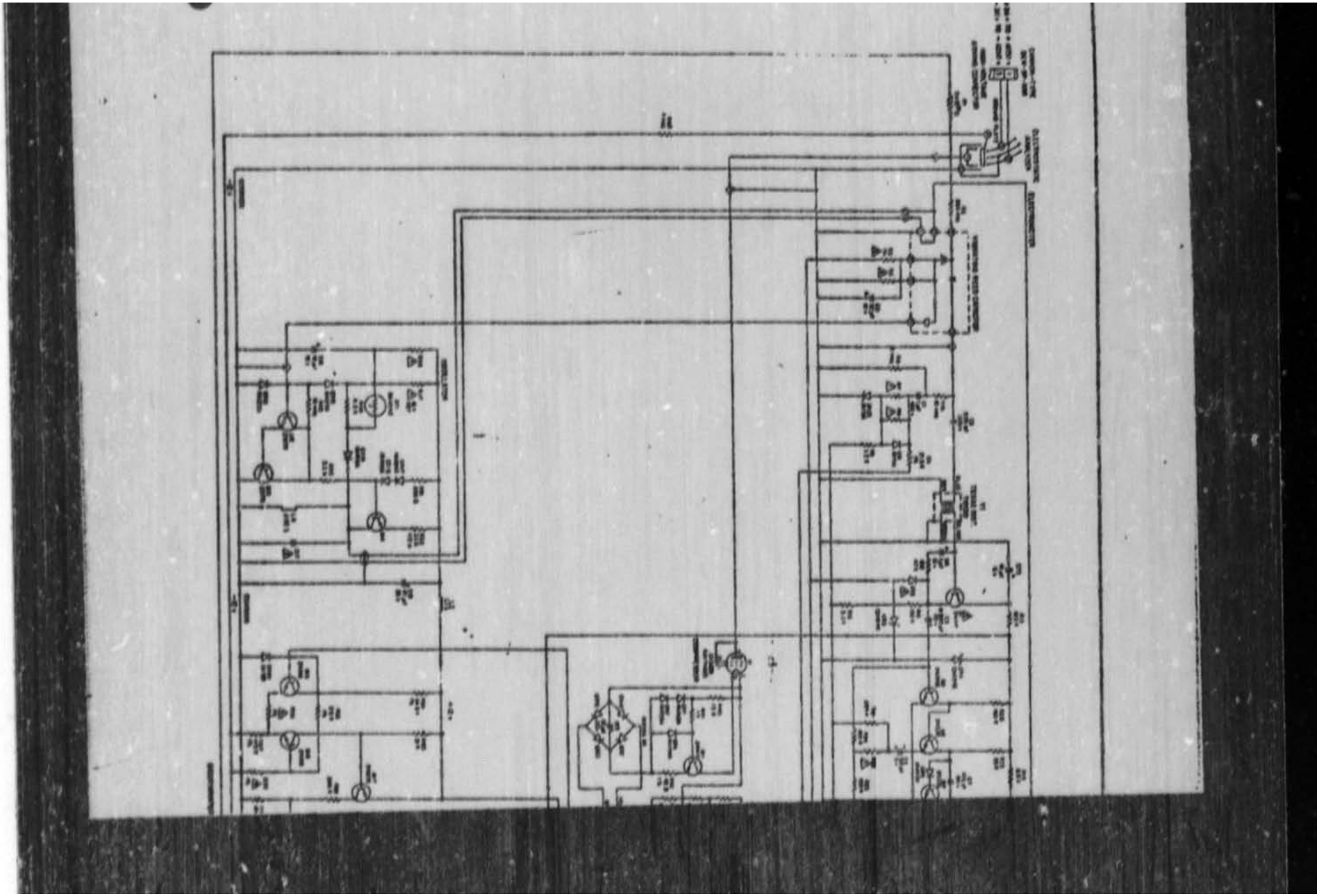

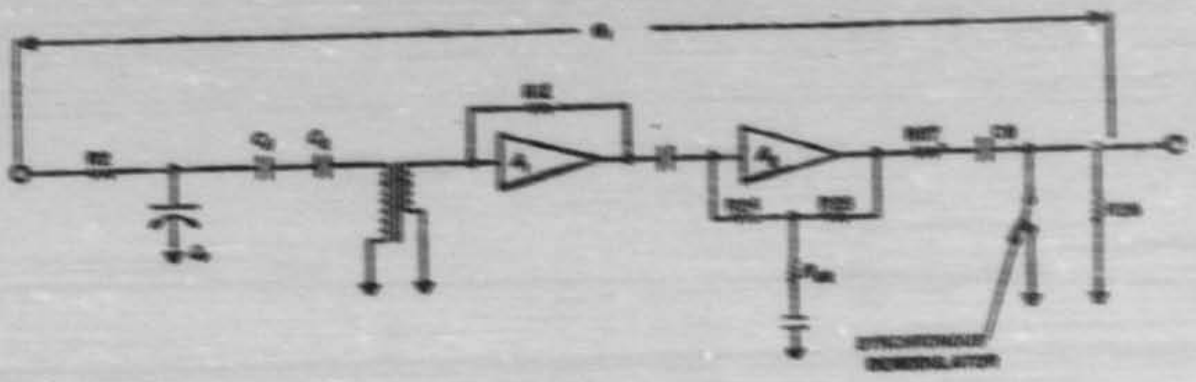

Fig. 17. Simplified diagram of carrier section

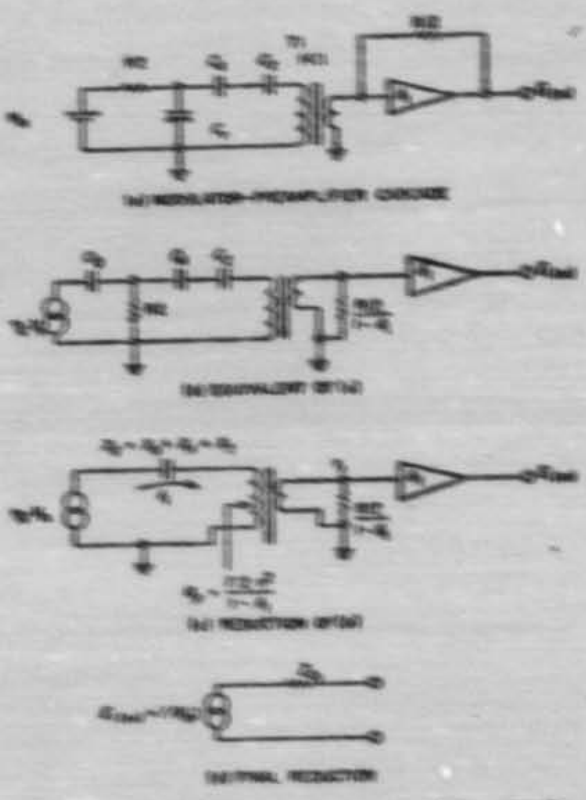

Fig. 18. Reduction of modulator–preamplifier circuit to Thevenin equivalent circuit

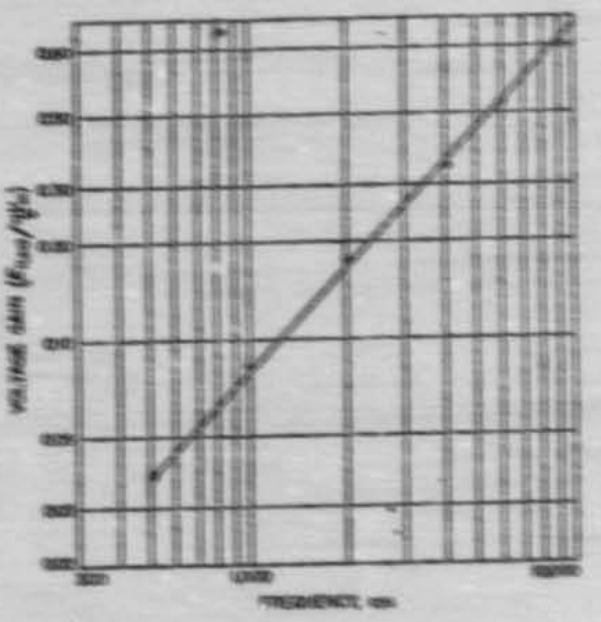

Fig. 19. Plot of preamplifier gain vs. frequency

amplifier at dc is disconnected by the shunt capacitor C_3. The resultant circuit is shown in Fig. 18, together with its equivalent driving source.

The gain of an operational amplifier may be expressed in the following general form:

$$K = K_o\left(\frac{A\beta}{1 - A\beta}\right) \qquad (18)$$

where

β = portion of output returned to summing point

$A\beta$ = feedback factor

$-K_v$ = closed-loop gain with infinite feedback factor.

In the circuit of Fig. 10a

$$K_v = \frac{R_{in}R_{in} + R_{in}R_{in} + R_{in}R_{in}}{Z_{in}R_{in}} \qquad (10)$$

Using circuit values of

$$R_{in} = R_{in} = 10^{6}\,\Omega$$

$$R_{in} = 220\,\Omega$$

$$Z_{in} = 3 \times 10^{3}\ \text{at 2,250 cps}$$

$$A_v = -65 \times 10^{3}$$

and

$$Z_{in} = 15 \times 10^{3}\,\Omega$$

(both Z_{in} and Z_{in} are considered resistive), one obtains

$$K_v = 0.1 \times 10^{6}$$

$$\beta_v = 0.25 \times 10^{-6}$$

and

$$A_v\beta_v = -230.$$

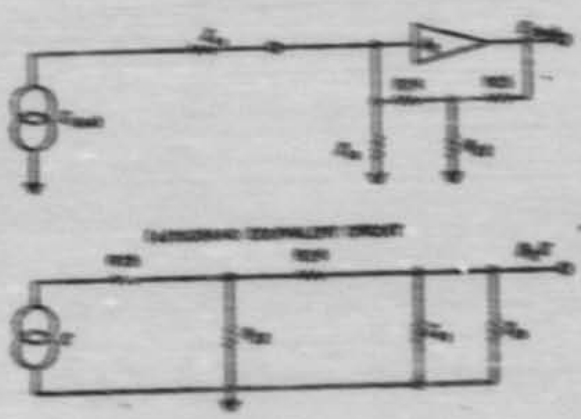

[illegible] TRIPLET CIRCUIT

[illegible] NETWORK FOR LOW-TRANSMISSION COUPLING

Fig. 10. Triplet amplifier

If $A_v\beta_v$ contained no phase shift, the triplet gain, as determined from Eq. (10), would be 0.24×10^{6}. Comparisons of measured and calculated values for carrier gains at 2,250 cps are shown in the following table.

Stage	Calculated gain	Measured gain
Preamplifier	420	420
Triplet amplifier	0.24×10^{6}	0.2×10^{6}
Cascade	1,260	440

Response of the entire cascade with respect to frequency is shown in Fig. 11. The low-frequency slope of 12 db/octave is composed of two equal contributions: one 6-db/octave rate from the capacitive source reactance to the transformer and another similar effect from

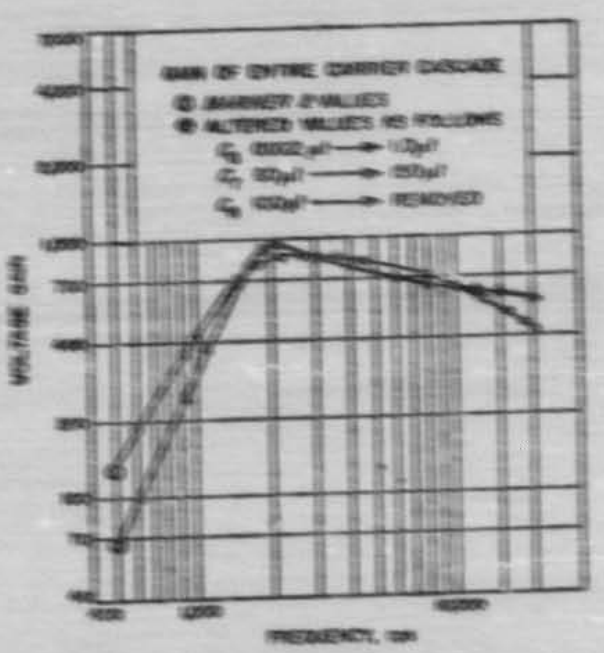

Fig. 11. Carrier-amplifier performance curves

the network coupling the preamplifier and the triplet. If the preamplifier output impedance Z_{in} were constant, one might expect a characteristic that would still be rising 6 db/octave at the carrier frequency. This impedance, because it is affected by the preamplifier source impedance, is actually rising with frequency at 2,250 cps and is the principal cause of flattening as seen in Fig. 11.

b. Demodulator. The ac signal from the carrier amplifier is connected to it by means of synchronous detection. The signal E_{ac} in the equivalent circuit of Fig. 22 represents the open-circuit output voltage of the triplet amplifier. The series element R_s is a composite of 2227 (see Fig. 17) and the output resistance of the triplet amplifier. The synchronous switching in this example is performed by the transistor Q2 while 2227, the input resistance to the dc filter amplifier, is closely approximated in its equivalent circuit by the ground-connected 2R. The physical series resistor that is part of R_s must be made large enough to limit the maximum chopped current in the diode switch (I_s in Fig. 22c) and prevent the triplet amplifier from cutting off on its positive swing. On the other hand, this resistor must not be made so large as to seriously attenuate the signal to the dc amplifier. Interposition of a voltage step-up transformer between the triplet and the demodulator would have the effect of multiplying the component of R_s due to triplet output resistance by the square of the turns ratio. To preserve high detection efficiencies it then becomes necessary to elevate the impedance levels in the amplifier following the demodulator.

Maximum detection efficiency is produced at drive-to-signal phasings of 0 and 180 deg. At intermediate phasings, efficiencies are described by the cosine of the drive-signal phase angle. Two important aspects of demodulator performance that will be discussed here are the efficiency and the low-pass frequency response of the idealized capacitive-coupled demodulator as characterized by the circuit of Fig. 22a. In both cases a 180-deg chopping duration, phased for maximum efficiency, will be assumed.

The output developed across the synchronous switch is made up of two components, signal and pedestal, both of which are attenuated by the factor $R_c/(R_c + R_s)$. The pedestal is attributable to a dc voltage retained by the coupling capacitor as though it were the output filter of a rectifier system.

To determine the value of the output pedestal and finally of the aggregate output, it is first necessary to determine the steady-state voltage developed across the capacitor. The voltage across the capacitor, e_c, at the end of one cycle of signal demodulation may be written

$$e_c = e_{c_0} + \frac{1}{C}\int_{t_0}^{t_1} i_{c_1}\,dt + \frac{1}{C}\int_{t_1}^{t_2} i_{c_2}\,dt \qquad (24)$$

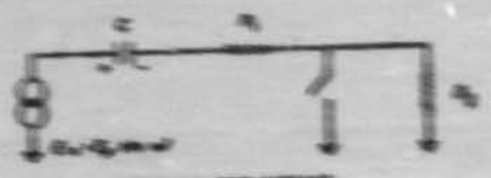

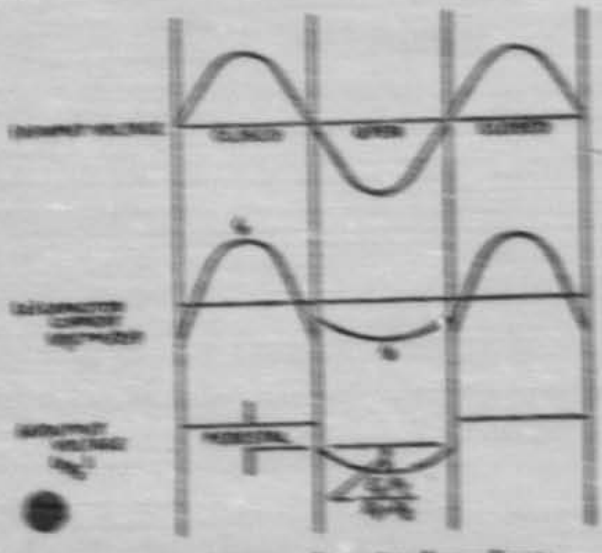

Fig. 22. Demodulator and associated waveforms

where

e_{c_0} = capacitor voltage at start of cycle

i_{c_1} = capacitor current during switch closure

$$= \frac{E_{ac}\sin\omega t - e_{c_0}}{R_s}$$

i_{c_2} = capacitor current during switch opening

$$= \frac{E_{ac}\sin\omega t - e_{c_0}}{R_c + R_s}$$

The assumption made in writing the current equations is that e_c does not significantly change in value during the cycle. If the system has reached equilibrium, e_c must

equal to e_{c_1} at the end of the cycle, and Eq. (34) may be rewritten

$$\Delta e_{c_1} = \int_{\frac{T}{2}}^{\frac{T}{2}+t_1} i_{c_1}\,dt + \int_{\frac{T}{2}+t_1}^{T} i_{c_2}\,dt = 0. \tag{35}$$

Substituting i_{c_1} and i_{c_2} in Eq. (35) and integrating, the steady-state capacitor voltage e_{c_1} may be written

$$e_{c_1} = \frac{2E_{c_1}}{\pi}\left[\frac{R_1}{2R_1 + R_2}\right]. \tag{36}$$

The average half-cycle output voltage may then be determined by adding the average half-cycle pedestal and signal voltages, dividing by 2, and multiplying by the positive attenuation as follows:

$$e_{o_1} = \frac{1}{2}\left(\frac{R_1}{R_1 + R_2}\right)\left[\frac{2E_{c_1}}{\pi}\left(\frac{R_1}{2R_1 + R_2}\right) + \frac{2E_{c_1}}{\pi}\right]$$

$$= \frac{2E_{c_1}}{\pi}\,\frac{R_1}{2R_1 + R_2}. \tag{37}$$

Since input modulator efficiency was described as the ratio of rms voltage to dc input voltage (Eq. 10), it becomes convenient in completing the gain calculation for the carrier section to define the demodulator efficiency η_d in inverse form, i.e.,

$$\eta_d = \frac{e_{o_1(rms)}}{E_{c_1(rms)}}$$

$$= \frac{2}{\pi}\sqrt{\frac{R_1}{(2R_1 + R_2)}}$$

$$= \frac{2\sqrt{2}R_1}{\pi(2R_1 + R_2)}. \tag{38}$$

In the circuit of Fig. 19

$$R_1 = R_2 = 4.7\text{K}$$

$$R_1 \text{ or } R_2 = R_1 + \frac{R_1}{1 - A_v R_1}$$

$$= 2.4\text{K} + \frac{2.3\text{K}}{200} = 4.5\text{K}$$

and

$$\eta_d = 38.8\%.$$

The dc voltage gain of the entire carrier section may thus be written

$$E_{c_1} = \eta_d G_{dc} e_{in}. \tag{39}$$

The laboratory model on which many of these tests were run, like the flight electronics, had its carrier gain adjusted with R_{1A} to a nominal value of 25. Using the measured value of G_{dc} (810) and the calculated value of η_d for the sake of illustration, the dynamic capacitor conversion efficiency producing the requisite gain of 25 is calculated to be 12%.

It is interesting to note that when a signal suddenly appears at the output of the triple amplifier, only the signal component is transmitted at first. The pedestal component, however, builds up in accordance with the charging of the capacitor. The effect on the carrier envelope or on the average demodulated signal, in a low-pass sense, is that of a network producing a phase-lag doublet. This variation of e_{o_1} vs. frequency and the attendant low-pass phase shifts are discussed in the following paragraphs.

The general expression for incremental capacitor voltage in a system that has not reached equilibrium is given in Eq. (25), except that e_{in} is not zero. Substituting i_{c_1} and i_{c_2} in Eq. (35), the incremental building across the capacitor during one cycle may be written

$$\Delta e_{c_1} = \frac{e_{in}}{sC}\left[\frac{1}{R_1} + \frac{1}{R_1 + R_2}\right]$$

$$+ \frac{2E_{c_1}}{sC}\left[\frac{1}{R_1} - \frac{1}{R_1 + R_2}\right] \text{ volts/period} \tag{40}$$

or

$$\frac{\Delta e_{c_1}}{dt} = \frac{e_{in}}{sC}\left(\frac{2R_1 + R_2}{R_1(R_1 + R_2)}\right)$$

$$+ \frac{E_{c_1}}{sC}\left[\frac{R_2}{R_1(R_1 + R_2)}\right] \text{ volts/second.} \tag{41}$$

If the time required for the capacitor voltage to build up is long compared with a carrier signal period, Eq. (21) may be written in the following differential form:

$$\frac{dv_c}{dt} = \frac{-v_c}{2CR_A} + \frac{E_p}{\pi CR_B} \tag{22}$$

where

v_c = capacitor voltage at t sec after introduction of a sine wave signal having a peak voltage E_p

$$R_A = \frac{R_1(R_1 + R_2)}{2R_1 + R_2}$$

$$R_B = \frac{R_1(R_1 + R_2)}{R_2}.$$

Rewriting Eq. (22) in operational form,

$$pv_c(p) + \frac{1}{2R_AC}v_c(p) = \frac{E_p}{p\pi R_BC}$$

and

$$v_c(p) = \frac{E_p}{\pi R_BC}\frac{1}{p}\frac{1}{p + \frac{1}{2R_AC}} \tag{23}$$

where p = Laplace operator.

The average demodulated voltage may be similarly written in operational form (see Eq. 17) as follows:

$$v_{R_2}(p) = \frac{1}{2}\frac{R_2}{R_1 + R_2}\left(v_c(p) + \frac{2E_p}{p\pi}\right). \tag{24}$$

Combining Eq. (23) and (24), the demodulated output is reduced to the following form:

$$v_{R_2}(p) = \frac{E_pK}{\sqrt{2}\,p}\eta_0(p) \tag{25}$$

or

$$v_{R_2}(p) = \frac{E_{(rms)}}{p}\left[\eta_{dc}\left(\frac{p\tau_1 + 1}{p\tau_2 + 1}\right)\right] \tag{26}$$

where

η_{dc} = dc or steady-state demodulation efficiency

$$\tau_1 = R_1C$$

$$\tau_2 = 2R_AC = \frac{2CR_1(R_1 + R_2)}{2R_1 + R_2}.$$

In the demodulation circuit of Fig. 16,

$$\tau_1 = 4.2 \times 10^3 \times 10^{-4}$$

$$= 4.2 \times 10^{-1}\ \text{sec}$$

and

$$\tau_2 = 2 \times 10^{-4}\,\frac{4.2(8.9) \times 10^3}{13.1 \times 10^3}$$

$$= 5.7 \times 10^{-4}\ \text{sec}.$$

The pole and zero corner frequencies are then, respectively,

$$f_2 = \frac{1}{2\pi\tau_2} = 2.8\ \text{cps}$$

and

$$f_1 = \frac{1}{2\pi\tau_1} = 3.8\ \text{cps}.$$

The maximum phase shift, as calculated at $\sqrt{f_1 f_2} = 3.24$ cps, is 9 deg lagging. Maximum-efficiency detectors of this design (90%) will produce 1-octave pole-zero doublets with maximum associated phase lags of about 20 deg. As in other phase contributions, the modest amount presented by this demodulator need not present a problem unless, of course, it occurs unexpectedly at gain crossover, using up most of the margin.

c. *DC Amplifier.* The dc amplifier, which is the final element in the electrometer and comprises transistors Q7, Q8, Q9, and Q10, provides the following functions:

1. Supplementary gain for required loop tightness,
2. Suitably wide output dynamic range,
3. Demodulation ripple filtering, and
4. Low output impedance.

Consider the gain requirement. The dc gain between modulator and demodulator was designated to be 33. The section following the demodulator must also provide a dc gain of 35 if the arbitrary standard of tightness,

the zero-frequency feedback factor, is to be about 1,000. The filter capacitor, located across the amplifier in this design, must be chosen so as to satisfy a variety of conditions. It must reduce the ripple component at the output of the electrometer to within tolerable limits for external measuring equipment. This is most often a level low enough to preclude problems due to ripple feedback to the modulator. This capacitor should not, however, be made so large as to produce a serious voltage rate-limiting problem. Such a problem is often caused by a combination of (1) limited dynamic range in the carrier amplifier and (2) too large a filter capacitor. Since this capacitance is an important term in one of the corner frequencies for the low-pass loop transmission characteristic, it must also be scrutinized from the viewpoint of loop stability.

The filter-amplifier is depicted in a somewhat simplified form in Fig. 23a. The input E_0 is the average demodulated signal developed across the shunt switch (Q5) when the switch is loaded by R_{in}. The resistive T feedback network performs, as its principal function, the zero-signal level adjustment of the output, which must be above zero to accommodate the log diode characteristic. Two successive approximations to the circuit shown in Fig. 23a are shown in Fig. 23b and 23c. The nominal voltage gain of the filter-amplifier as calculated from the diagram in Fig. 23c may be written

$$K_0 = \frac{G_{v_0}}{1 + p\,\tau_0} \qquad (27a)$$

where

$$G_{v_0} = \text{dc gain} = \frac{R_{22}\left(\frac{R_{21} + R_{11}}{R_{21}}\right) + R_{22}}{R_{11}}$$

and

$$\tau_0 = \left[R_{22}\left(\frac{R_{21} + R_{11}}{R_{21}}\right) + R_{11}\right] C_{21}. \qquad (27b)$$

Characteristic feedback factors of 30 for this amplifier make the equivalent circuit and the resulting gain calculation accurate to within about 3%. Using values from Fig. 18,

$$G_{v_0} = 37.5$$

and

$$\tau_0 = 0.435 \text{ sec.}$$

The rate limit of the electrometer is the slope of the integrated output of the filter amplifier produced by the maximum signal available from the carrier amplifier. Maximum values for positive and negative demodulated voltages will be somewhat different because of asymmetrical current-handling capabilities in the output stage of the triplet amplifier on negative and positive swings. In the actual transfer characteristic as shown in Fig. 24, the maximum average positive demodulator voltage of 1.2 v establishes an amplifier charging rate limit of

$$\frac{dE_0}{dt} = \frac{E_0}{R_{21} C_{21}} = -100 \text{ v/sec.}$$

This permits the amplifier to negotiate a negative 5-v step in 50 msec if no other factors are involved.

In most applications, where the output of a sensitive device such as this electrometer must be protected against electrostatic coupling of external power and signal transients, it is imperative to furnish the amplifier with a suitably low output impedance. Over-all electrometer

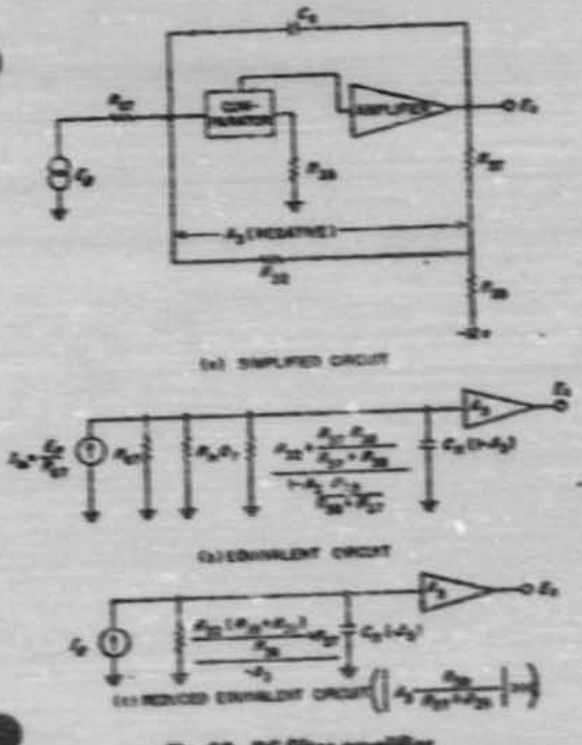

Fig. 23. DC filter amplifier

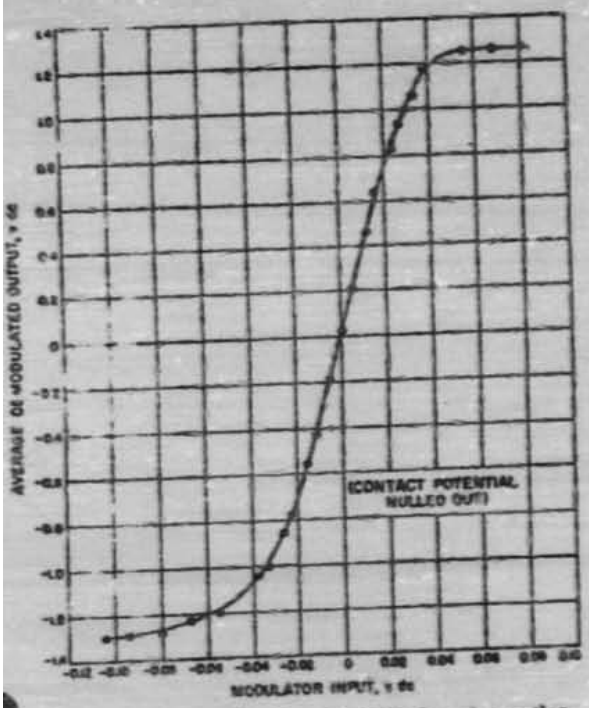

Fig. 24. Static transfer characteristic of carrier section

feedback does not necessarily ensure wide-band protection, because at low input-current levels the dynamic feedback resistance is high, and unity-gain crossover for the loop feedback factor occurs at low frequencies. The result is a total absence of impedance degeneration above a few cycles per second. For this reason, local feedback in the filter-amplifier is required to provide low-output impedance independent of the over-all loop. The emitter-follower, Q10, for instance, may have an output impedance of 300 ohms, further degenerated by the local feedback to about 10 ohms. The dc impedance of 10 ohms is further reduced at frequencies where C_{11} produces increased local feedback. The static output impedance, as previously suggested, is also enhanced by the dc feedback factor of the entire loop, which reduces the filter-amplifier impedance by 1,000 to a small fraction of an ohm.

4. Offset Stability

There are three main contributions to drift at the electrometer input. These are

1. Variation in dynamic capacitor contact potential,
2. Variation in balance of the dc amplifier comparator, and
3. Variation of the demodulator offset.

Contact potential drift in the modulator appears directly at the electrometer input. Changes in modulator reference potentials are similarly reflected directly at the input. As a precaution against inverse-polarity leakage currents, the modulator is referenced so that a nominal negative potential appears at the summing point. Leakage produced by input resistance will therefore cause a small error current, of the same polarity as positive-ion input current, to flow in the feedback element.

The comparator stage of the dc filter-amplifier is a relatively coarse device. The drift in the differential stage composed of Q7 and Q8 is characteristically about −50 mv between −20 and +70°C, yielding an average temperature coefficient of −0.8 mv/°C. If the gain of the carrier section between the modulator and demodulator were assumed constant at 35 over this temperature range, the drift at the summing point attributable to the dc amplifier instability would be 1.4 mv.

The demodulator transistor (Q5) is likewise coarse in performance. A 2N329A PNP alloy transistor is used in the normal configuration for its superior current gain, thereby forsaking the stability of the inverted connection. In an application such as this, one may consider the zero-signal closed-switch offset potential as the principal source of instability. This offset is expressed as follows (Ref. 17):

$$e_s = \frac{KT}{q} \ln \frac{1}{\alpha_i} \quad (28)$$

where

α_i = inverse emitter-to-collector current gain

e_s = collector-to-emitter voltage with zero collector current.

It is estimated that drifts in e_s attributable to temperature and alpha changes will not exceed 10 mv. The full-cycle average drift, 5 mv, would correspondingly produce a 0.14-mv shift at the electrometer input. The combined demodulator–dc amplifier drift reflected to the electrometer input would therefore be small compared with the modulator contact potential drifts, which fall in the 5- to 10-mv range.

C. Feedback Stability

This section will first describe theoretical considerations in the analysis of the electrometer as a feedback amplifier. The equations for loop transmission (feedback factor) will be presented under conditions of zero and fixed secondary damping feedback. A table of dominant time constants versus input current will illustrate the consequences of using a nonlinear or non-discrete primary feedback element. Both theoretical and measured curves of loop transmission are presented, after which closed-loop frequency and transient responses are shown.

1. Open-Loop Frequency Response

The electrometer transfer characteristic may be written

$$E_o = I_{in} Z_f \left(\frac{A\beta}{1 - A\beta} \right) \tag{29}$$

where

A = forward dc amplifier gain

β = portion of output returned to summing point

Z_f = feedback impedance.

The amplifier, as is implied in Eq. (29), is dependent upon the feedback factor $A\beta$ for such important characteristics as static accuracy, speed of response, and loop stability. Trying to satisfy conditions for loop stability presents an unusual problem, in that R_f, one of the principal parameters in the calculation of $A\beta$ (see Fig. 25a), varies in excess of 7 decades.

Since the feedback resistance varies as an inverse function of the feedback current, the secondary feedback, or damping, must also be nonlinear. No single condition of feedback will satisfy requirements for both loop stability and speed of response at all currents within the measurable range of the instrument. A nonlinear attenuator composed of R7, R8, R11, and zener diode CR1 provides a two-point compensation characterized by zero damping at low currents, fixed damping at high currents, and a transition corresponding to about one current decade. The use of C_A in the dual role of damping element and carrier-frequency coupling capacitor was suggested by an earlier commercial application (Ref. 18).

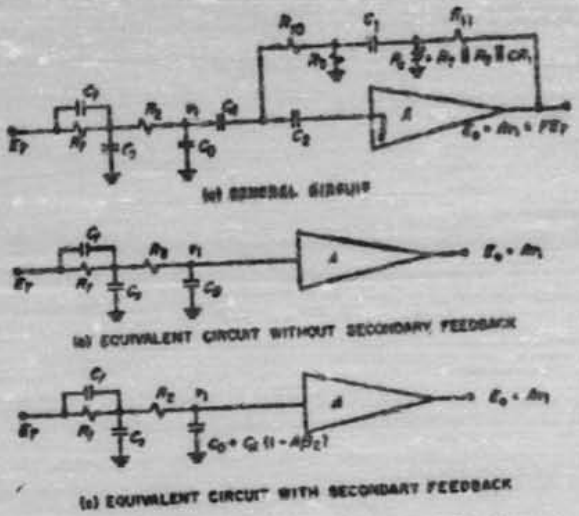

Fig. 25. Equivalent circuits for determining loop transmission

a. Theoretical Considerations. At low currents where secondary feedback is effectively disconnected, the loop transmission as determined from the circuit of Fig. 25 is given by

$$F = \frac{A(1 + p\tau_f)}{p^2(R_f R_2 C_2 C_B + \tau_f C_B R_2) + p(R_f[C_B + C_o + C_f] + C_B R_2) + 1} \tag{30}$$

where

$\tau_f = R_f C_f$

$C_B = C_o + (C_A C_2)/(C_A + C_2)$

C_o = collector-to-shield capacitance.

The amplifier gain may be described principally by the filter-amplifier and demodulator time constants in such a manner that

$$A = \frac{A_o(1 + p\tau_2)}{(1 + p\tau_1)(1 + p\tau_2)} \tag{31}$$

where

A_o = dc gain

τ_1 = demodulator pole time constant (see Eq. 28)

τ_2 = demodulator zero time constant (see Eq. 22)

τ_3 = filter-amplifier time constant (see Eq. 27b).

The polynomial in the denominator of Eq. (30), when written in the form

$$ap^2 + bp + c$$

can be approximately factored into

$$+\left(\frac{a}{b}p+1\right)\left(\frac{b}{c}p+1\right)$$

when

$$\frac{4ac}{b^2} \ll 1.$$

Over the range of input currents where secondary feedback is disconnected, this condition is satisfied in the following form:

$$\frac{R_1}{R_2}\left\{\frac{G_2(G_1+G_2)}{[(G_0+G_1+G_2)+G_2(R_1/R_2)]^2}\right\} \ll 1.$$

The loop transmission F may therefore be written in the following factored form:

$$F = \frac{[A_0(1+p\tau_0)(1+p\tau_2)]}{[(1+p\tau_1)(1+p\tau_2)(1+p\tau_3)(1+p\tau_4)]} \quad (32)$$

where

$$\tau_1 = \tau_2 = G_1R_1$$

$$\tau_3 = R_1(G_0+G_1+G_2)+G_2R_1$$

and

$$\tau_4 = \frac{R_1G_2(G_1+G_2)}{(G_0+G_1+G_2)+G_2(R_1/R_2)}.$$

An feedback current is raised to the order of 10^{-6} amp, upward migration of the corner frequency determined by τ_3 produces sufficient phase shift at gain crossover to result in oscillatory behavior. The addition of secondary feedback at lower current before this condition is reached produces a new set of dominant time constants.

Consider the effect of the limited amplifier bandwidth on the gain-sensitive capacitance in Fig. 20a. If the amplifier response is approximated exclusively by filter cutoff so that

$$A = \frac{A_0}{1+p\tau_0}$$

the loop transmission is then given by

$$F = \frac{A_0(1+p\tau_2)}{(1+p\tau_0)(1+p\tau_1')(1+p\tau_2')}. \quad (33)$$

The expressions for τ_1' and τ_2' are identical with the τ_1 and τ_2 terms of Eq. (32) except that G_0 is replaced by the gain-sensitive capacitance

$$G_0 + G_0\left(1 - \frac{A_0\beta_0}{1+p\tau_0}\right)$$

where

$$\beta_0 = \frac{R_1}{R_1+R_{11}}$$

and

$$R_2 >> \frac{R_1R_{11}}{R_1+R_{11}}.$$

If G_1 is assumed to be infinite and if the pole in the β_0 network (produced by the lag network comprising R_{11}, G_0, G_1, and G_2) is neglected ($\tau_0 = 3$ msec), the loop transmission (Eq. 33) may then be reduced to

$$F = \frac{A_0(1+p\tau_2)}{(1+p\tau_1')(1+p\tau_2')(1+p\tau_3')} \quad (34)$$

where

$$\tau_1' = -\frac{\tau_0}{A_0\beta_0}\left[\left(\frac{G_0+G_1}{G_2}\right)+\left(\frac{R_1}{R_1+R_{11}}\right)\left(\frac{G_0+G_1}{G_2}\right)\right] \quad (35)$$

$$\tau_2' = \tau_2 - A_0\beta_0C_0(R_1+R_2)+(R_1+R_2)(G_1+G_2)+R_2(G_1+G_2)$$

$$\approx \tau_2 - A_0\beta_0C_0(R_1+R_2) \quad (36)$$

and

$$\tau_c' \simeq \frac{R_c R_f}{R_c + R_f}(C_c + C_d). \tag{37}$$

The dominant pole in Eq. (34) is produced by τ_c. The principal effect of the amplifier time constant, τ_a, is to add directly to $-A_a \beta_c C_c (R_c + R_d)$. Corner frequencies produced by τ_c' and τ_a occur sufficiently beyond gain crossover as to produce gain margins no less than 15 db over the range of currents for which this secondary feedback is effective.

A consequence of using ac coupling in the secondary feedback that was overlooked in the initial design is the peak that occurs in the loop transmission. While there was no harmful effect in this case, it is evident that this coupling time constant can provide large lagging phase shifts as illustrated in some of the gain and phase curves. Consider the effect of the ac coupling in the secondary loop as embodied in the dominant time constant of Eq. (34). The loop transmission may then be written

$$F \simeq \frac{A_a}{1 + p\tau_c'} \tag{38}$$

where

$$\tau_c' = \tau_c - A_a \beta_c C_c (R_c + R_d) \frac{p\tau_c}{1 + p\tau_c}$$

$$= \frac{\tau_c + p\tau_a\tau_c}{1 + p\tau_c}$$

and

$$\tau_c = C_c R_c.$$

Substituting for τ_c' in Eq. (38)

$$F = \frac{A_a(1 + p\tau_c)}{1 + p(\tau_c + \tau_a) + p^2\tau_a\tau_c}. \tag{39}$$

The location of the poles of Eq. (39) in the p plane are as follows:

$$p_1, p_2 = \frac{(\tau_c + \tau_a)}{2\tau_a\tau_c}\left[1 \pm \left(1 - \frac{4\tau_a\tau_c}{(\tau_c + \tau_a)^2}\right)^{1/2}\right]. \tag{40}$$

For the condition where

$$\frac{4\tau_a\tau_c}{(\tau_c + \tau_a)^2} \gg 1,$$

which is applicable in this case, Eq. (40) may be rewritten

$$p_1, p_2 \simeq \frac{-(\tau_c + \tau_a)}{2\tau_a\tau_c} \pm j\frac{1}{(\tau_a\tau_c)^{1/2}}. \tag{41}$$

The frequency at which F (Eq. 39) peaks is now determined by the imaginary component of Eq. (41), i.e.,

$$f_{max} = \frac{1}{2\pi(\tau_a\tau_c)^{1/2}}.$$

For bias currents of 10^{-10} and 10^{-9} amp where $\tau_a = 2$ sec, the peaking frequencies are calculated to be 0.035 and 0.037 cps, respectively.

Table 5 presents a listing of all dominant time constants and their variation with bias current. The asymptotic loop responses resulting from the tabulated corner frequencies for the cases of secondary feedback out and in are shown in Fig. 26 and 27, respectively.

b. Experimental Results. To correlate actual performance with predicted behavior and to verify adequacy of phase margins, a set of tests was performed on a laboratory electrometer using the experimental arrangement of Fig. 25. The signal generator was placed in the feedback loop so that the feedback would still stabilize the dc operating point and that output levels would be determined by the equivalent series generator voltage, i.e.,

$$E_o = V_g\left(\frac{F}{1 - F}\right) \tag{42}$$

where

$$V_g = E_g - F E_g.$$

The open-loop amplitude and phase responses were obtained by taking oscilloscope pictures of the waveforms on both sides of the floating signal generator, which also supplied scope trigger pulses. The dc bias current in the tube was determined by resistors connected between a 1-v battery and the electrometer input. This resulted in a 30% reduction in A_a and in a small modification to the responses of F vs. the frequency that would have been obtained with perfect current sources. A 50-pf capacitor

Table 3. Nominal time constants and corner frequencies

(a) Secondary feedback out

Bias current, amp	Time constant, sec						Corner frequency, cps					
	τ_1	τ_2	τ_3	τ_4	τ_5	τ_6	f_1	f_2	f_3	f_4	f_5	f_6
10^{-7}	0.542	0.107	0.434	0.855	0.149	0.0373	0.3	3.0	0.37	30	0.59	39
10^{-8}	↓	↓	↓	0.97	1.19	↓	↓	↓	↓	3.3	0.1	↓
10^{-9}				0.3	10.9					0.33	0.01	
10^{-10}				3.0	106					0.033	0.001	

(b) Secondary feedback in

Bias current, amp	Time constant, sec					Corner frequency, cps				
	τ_1	τ_2	τ_3	τ_4	τ_5	f_1	f_2	f_3	f_4	f_5
10^{-7}	3×10^{-3}	8.9×10^{-4}	7.8×10^{-4}	9.3	3.9	3.3×10^{2}	2.9×10^{2}	330	1.7×10^{-2}	0.0795
10^{-8}	3×10^{-3}	3.7×10^{-4}	1.78×10^{-4}	10.3	↓	230	43	89	1.1×10^{-2}	↓
10^{-9}	0.003	9.2×10^{-4}	3.84×10^{-4}	30		33	10.3	26	3.9×10^{-3}	
10^{-10}	0.03	11 $\times 10^{-4}$	3.13×10^{-4}	400		3.3	10.4	24	3.3×10^{-4}	
10^{-11}	0.3	11 $\times 10^{-4}$	3.13×10^{-4}	4,000	↓	0.33	10.4	24	3.3×10^{-5}	↓

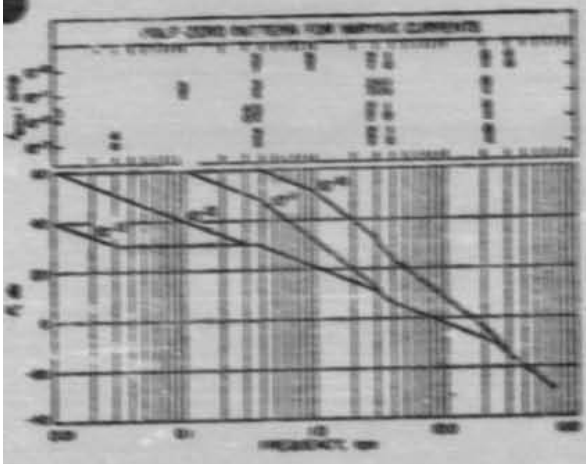

Fig. 26. Asymptotic loop transmission response without secondary feedback

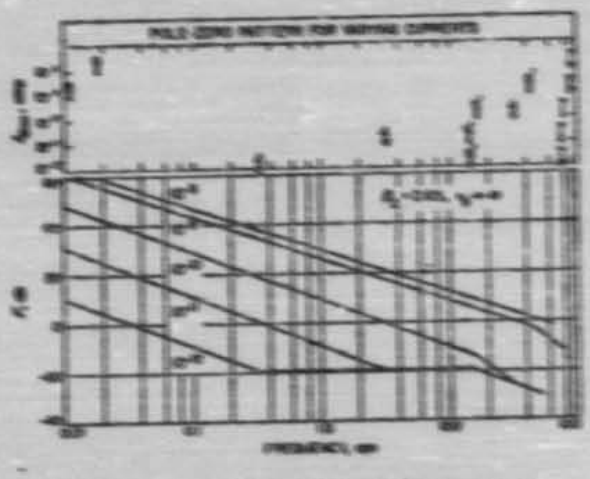

Fig. 27. Asymptotic loop transmission response with secondary feedback

with a leakage resistance greater than 10^{10} ohms simulated the capacitance between the collector and its electrostatic shield. An R-C filter at the amps input reduced the 60-cps signals generated in the loop by the large flux generator, as a result, measurements above 30 cps were somewhat unreliable. For bias currents greater than or equal to 2^{-10} amp, the secondary feedback was removed by disconnecting S10. Figures 22 to 24 show gain and phase shift of the amplifier measured at frequencies from 0.01 to 300 cps for bias currents between 10^{-8} and 10^{-10} amp.

The laboratory electrometer used for these tests contained several components whose values were different

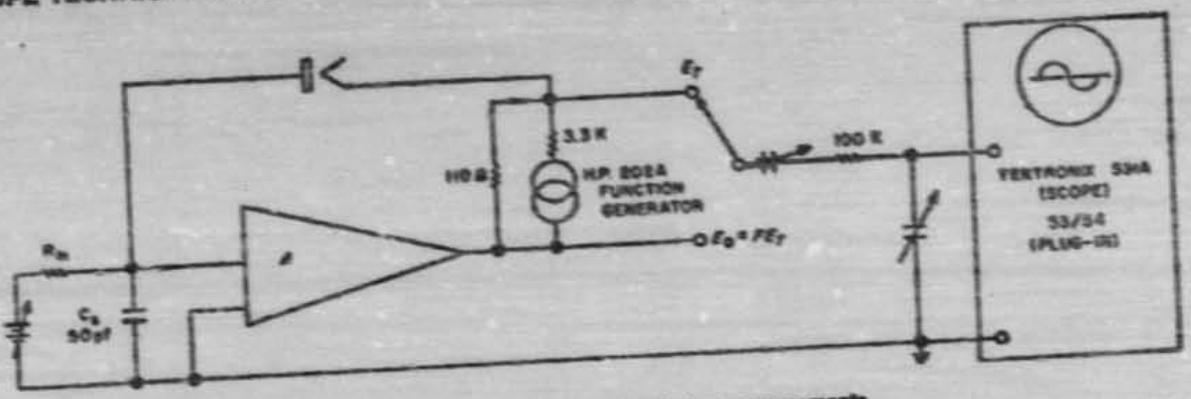

Fig. 28. Test setup for loop transmission measurements

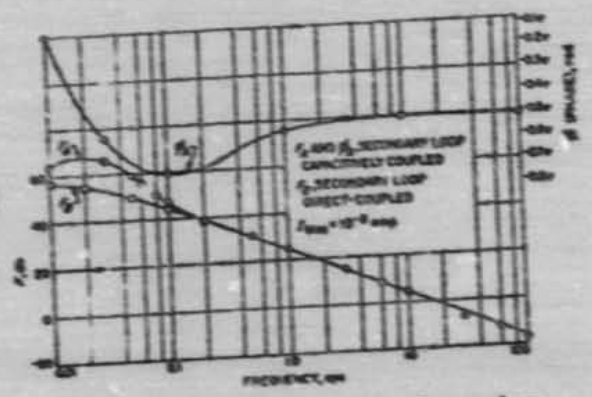

Fig. 29. Gain and phase curves with secondary feedback in (I_{bias} = 10^{-4} amp)

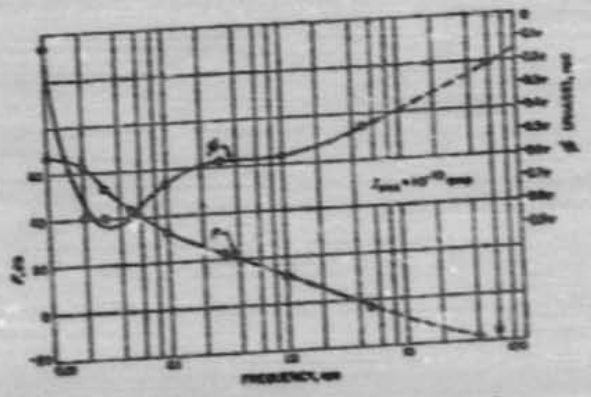

Fig. 31. Gain and phase curves with secondary feedback in (I_{bias} = 10^{-12} amp)

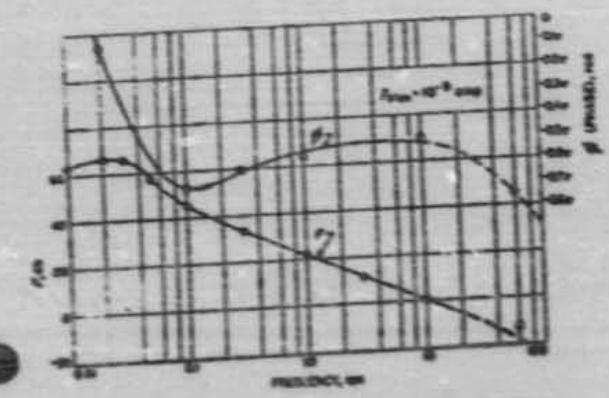

Fig. 30. Gain and phase curves with secondary feedback in (I_{bias} = 10^{-8} amp)

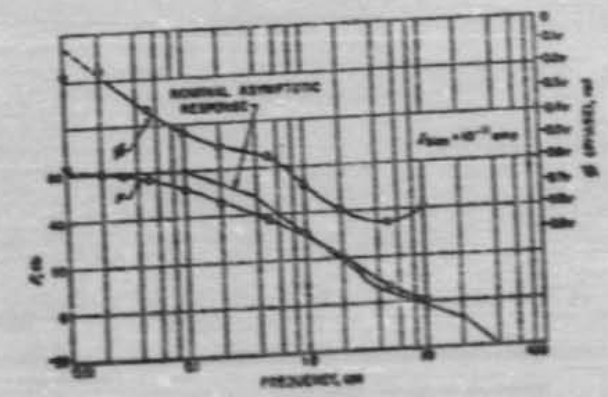

Fig. 32. Gain and phase curves with secondary feedback out (I_{bias} = 10^{-12} amp)

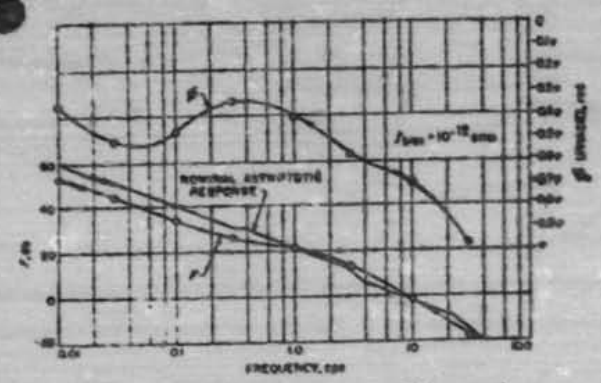

Fig. 33. Gain and phase curves with secondary feedback out ($I_{bias} = 10^{-13}$ amp)

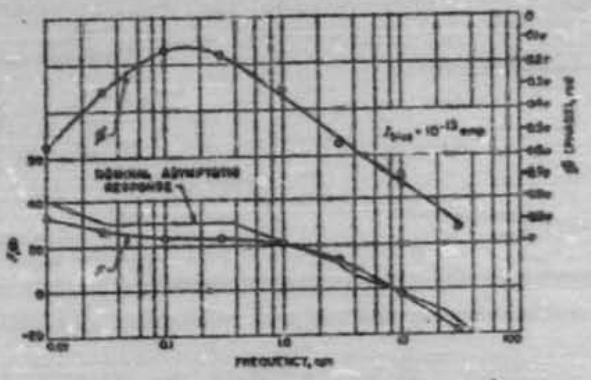

Fig. 34. Gain and phase curves with secondary feedback out ($I_{bias} = 10^{-11}$ amp)

from the nominal flight-unit values or had changed since those components were installed. Since there was some variance between measured responses and nominal curves, comparison was then made between measured component values and values providing the best fit to the experimental curves (see Table 6).

Table 6. Component values

Component	Value		
	Nominal	Measured	Best fit
			Assumed
C_a, pf	30	150	130
C_b, pf	220	—	220
C_c, pf	1	—	1
R_a, K	130	150	130
R_b, K	6.8	9.1	9.1
R_c, K	24	24	24
R_d, K	21.3	21.3	21.3
R_e, K	60 (max.)	60 (max.)	60 (max.)
R_f, meg	2	2	2
R_i, Ω	$1/10\ I_{bias}$	$\approx 1/10\ I_{bias}$	$1/10\ I_{bias}$
			Calculated
C_s, pf	30	63	154
C_L, pf	70	60	59
C_m, pf	2.5	0.96	0.93
C_f, pf	3	3	3.3
R_m, meg	200	160	220
A_v	−1000	—	−1000

The best-fit component values agree reasonably well with the measured values except for C_s, where the dispersion is not fully understood at this time. Most notable departures from expected values were in the cases of the filter capacitor C11 and the dynamic capacitor rest capacitance, C_s. The filter capacitor, a bipolar tantalum unit, may have deteriorated with age. The dynamic capacitor, a non-flightworthy developmental model, had apparently acquired a reduced reed-to-anvil spacing.

Of the six bias conditions for which curves have been drawn, minimum margin occurs with a bias current of 10^{-11} amp. (Fig. 32). In this curve, the rolloff rate at gain crossover (10 cps) is about 8 db/octave with a −144-deg phase shift, although the phase shift in this case does reach a pre-crossover maximum of −153 deg at 6 cps. Deviations in the capacitances C_s and C_s reduced the corner frequency f_s from a nominal 22 cps to less than half its standard value. This placed f_s near gain crossover, thereby reducing margins in the laboratory instrument, though not to intolerably small levels. The flight instruments were generally adjusted for transition between secondary feedback states at about 5×10^{-13} amp.

2. Closed-Loop Performance

When the electrometer is driven by a current source, its transfer impedance may be expressed in the following modified form of Eq. (29):

$$Z_T = \frac{-E_o}{I_{in}} = Z_f \left[\frac{1}{1-(1/F)}\right]. \qquad (43)$$

If the loop transmission characteristic is approximated at gain crossover (f_{go}) by a 6 db/octave rolloff rate, the transfer impedance is then given by

$$Z_f = \frac{Z_g}{(1 + p\tau_1)(1 + p\tau_{go})} \qquad (44)$$

where

$$\tau_{go} = \frac{1}{2\pi f_{go}}$$

Table 7 lists the time constants of Eq. (44) and their associated frequencies as a function of bias current. The gain-crossover frequency with secondary feedback (f'_{go}) is also listed.

Families of closed-loop frequency responses are shown in Fig. 35 and 36 for secondary feedback in and out, respectively. Electrometer biasing was similar to that used in Fig. 32, and a signal current was inserted into the summing point by a function generator connected in series with a suitably large resistor. The only parameter significantly different from the ones used in the loop transmission tests was the modulator rest capacitance (C_r), which was 50 pf for the dynamic capacitor used in this case.

Peaking that occurs at lower currents in Fig. 35 is directly attributable to phase shifts associated with poles in loop transmission characteristics that are not sufficiently removed from gain crossover. The overshoots associated with transient response to these characteristics were not observed in flight instruments, since secondary feedback transition occurred at about 5×10^{-13} amp.

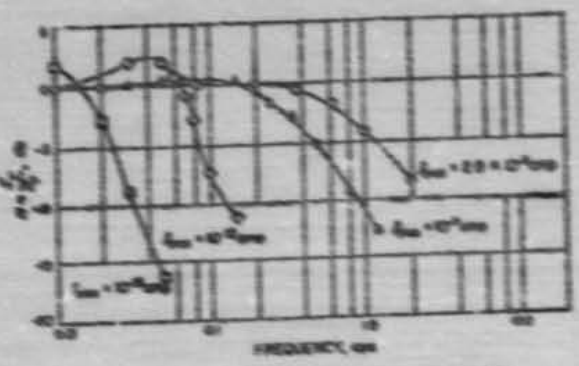

Fig. 35. Closed-loop frequency response with secondary feedback

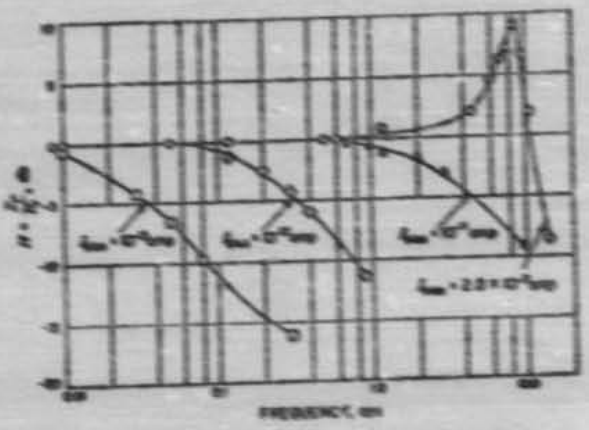

Fig. 36. Closed-loop frequency response without secondary feedback

Table 7. Dominant time constants and corner frequencies for nominal closed-loop response

Bias current, amp	Time constants, sec			Corner frequency, cps		
	τ_1	τ_{go}	τ'_{go}	f_1	f_{go}	f'_{go}
10^{-9}	8×10^{-3}	[illegible]	0.0954	3.7×10^{3}	—	17
10^{-10}	8×10^{-2}	[illegible]	0.514	370	—	31
10^{-11}	0.803	[illegible]	0.933	37	—	3.5
10^{-12}	0.15	0.213	0.47[a]	3.7	0	0.35
10^{-13}	0.5	0.318	4.7[a]	0.37	0	0.033
10^{-14}	5	0.813	47[a]	0.037	0	0.0035

[a] Secondary feedback assumed as three seventy for available time constant, see τ'_{go} values.
[b] Secondary feedback noticeably disconnected at three seventy values listed; denote theoretical values that would be obtained if secondary feedback were connected.

NATIONAL AERONAUTICS AND SPACE ADMINISTRATION

Technical Report No. 32-991

Average Properties of the Solar Wind as Determined by Mariner II

Marcia Neugebauer
Conway W. Snyder

JET PROPULSION LABORATORY
CALIFORNIA INSTITUTE OF TECHNOLOGY
PASADENA, CALIFORNIA

November 1, 1966

NATIONAL AERONAUTICS AND SPACE ADMINISTRATION

Technical Report No. 32-991

Average Properties of the Solar Wind as Determined by Mariner II

Marcia Neugebauer
Conway W. Snyder

Approved by:

C. J. Mackin, Jr.

R. J. Mackin, Jr., Manager
Physics Section

JET PROPULSION LABORATORY
CALIFORNIA INSTITUTE OF TECHNOLOGY
PASADENA, CALIFORNIA

November 1, 1966

CONTENTS

TABLES

FIGURES

ABSTRACT

This Report summarizes the properties of the positive-ion component of the solar wind observed during the four months of the *Mariner II* flight to and past Venus in 1962. The protons' average velocity and temperature were approximately 500 km/sec and 1.7×10^5 °K, respectively. Several streams of hot, high-velocity plasma were observed to recur at 27-day intervals, with peak velocity and temperature values of ~ 830 km/sec and 9×10^5 °K. One of these streams existed for probably at least 18 months. Between streams, the velocity dropped to a low of 307 km/sec, while the temperature was ~ 3×10^5 °K. Near 1 AU, the average density was approximately 5 protons/cm³. The density was usually highest at the leading or western edge of each stream, with a maximum value of ~ 80 protons/cm³. Otherwise, the density varied inversely with the plasma velocity. The ions' velocity, temperature, and density were calculated from ~ 35,000 energy/charge spectra by fitting the data to isotropic Maxwell-Boltzmann distributions in a reference frame moving away from the Sun at the solar-wind velocity. A model in which the protons and alpha particles have equal thermal velocities gives a better fit to the observed spectra than a model having equal temperatures. The spectra usually had high-energy tails, which became more pronounced at the higher plasma velocities. The velocity, temperature, and high-energy tail were not strongly dependent on distance from the Sun, whereas the density varied approximately as the inverse square of this distance.

I. INTRODUCTION

This Report is a summary of the average properties of the positive-ion component of the solar wind as determined by the electrostatic spectrometer on *Mariner II*.

Various plasma parameters such as velocity, density, and temperature have been calculated from the measured spectra and averaged over periods of either 3 hr (up to 49 complete spectra) or 24 hr. In later reports, these parameters will be related to properties of the interplanetary magnetic field on both a 3-hr or daily-average basis, and, for selected intervals, on as fine a time scale as the data allow.

II. TRAJECTORY OF *MARINER II* AND SOLAR CONDITIONS

Mariner II was launched on August 27, 1962, on a trajectory passing close to Venus. Usable data were obtained from the positive-ion spectrometer on board the spacecraft almost continuously from 1725 UT, August 29, through December 18, 1962, between 2013 UT, October 31, and 2137 UT, November 8, the scientific instruments on board were not operating. About 10 hr of data were obtained per day from December 17 through 1725 UT, December 30, when a failure occurred in a spacecraft reference-frequency circuit.

The *Mariner II* plasma data pertain to a period of declining solar activity during which no solar flare greater than class 2 was reported. The Zurich final relative sunspot numbers ranged from 0 to 98 with an average daily value of 36.3. Much of the geomagnetic activity for this period can be attributed to *M*-region storms. The geomagnetic indices K_p (3-hr) and A_p (daily) ranged from 0 to 7+ and 1 to 58, respectively, with the average daily A_p equal to 18 (Ref. 1).

Because the first plasma measurements were made when the spacecraft was 721,000 km from the Earth and the Sun–Earth–probe angle was 75.7 deg, no information on the properties of the Earth's magnetosphere or bow shock was obtained. The near-Venus observations were reported in an earlier paper (Ref. 2).

Table 1 summarizes the spacecraft trajectory. The orientation of the spacecraft was controlled by an attitude-stabilization system, which kept the entrance aperture of the spectrometer pointed to within 0.1 deg of the center of the Sun. During the first six days, the spacecraft slowly rolled about the Sun–probe line; thereafter, the Sun–probe–Earth plane remained fixed in the spacecraft.

III. INSTRUMENTATION

The configuration of the positive-ion spectrometer is shown in Fig. 1, and a block diagram is given in Fig. 2. The principal components of the spectrometer were (1) a cylindrical electrostatic analyzer, which separated positively charged ions according to their energy per unit charge (E/Q), (2) a programmer and a high-voltage sweep amplifier, which applied the proper balanced potentials to the plates of the analyzer, and (3) an electrometer, which measured the current from the charge collector at the output of the analyzer. The spectrometer was designed, built, and tested principally by C. Josias, J. L. Lawrence, Jr.[1], and H. R. Mortz at the Jet Propulsion Laboratory; it is described in greater detail in the Report by Josias and Lawrence (Ref. 3).

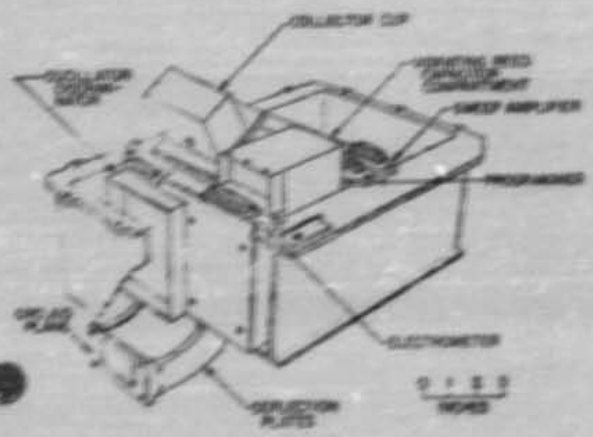

Fig. 1. *Mariner II* positive-ion spectrometer

The electrostatic analyzer was constructed of gold-plated magnesium, the interior was coated with gold black to minimize the amount of ultraviolet light that could enter the charge-collector region. The deflecting plates were 120 deg in length, and were separated by 1.3 cm. The entrance aperture was 5.0 cm² in area and rectangular in shape to provide approximately equal

[1] C. Josias is now President and J. L. Lawrence, Jr., Vice President of Analog Technology Corporation, Pasadena, California.

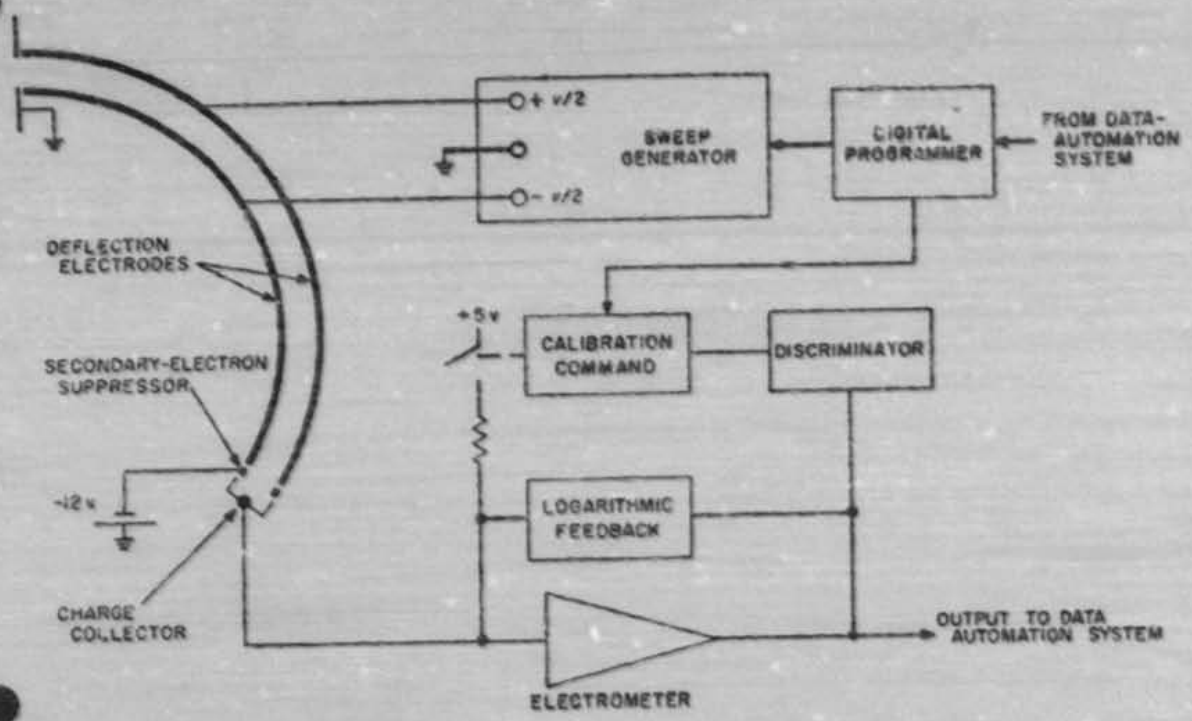

Fig. 2. Block diagram of *Mariner II* positive-ion spectrometer

Table 1. Summary of *Mariner II* trajectory

Date	Event	Distance from Sun, × 10^6 km*	Solar latitude, deg*	Earth-Sun-probe angle, deg*	Sun-Earth-probe angle, deg	ϕ, roll angle, deg*	Tangential velocity, km/sec*	Radial velocity, km/sec*	Distance from Earth, × 10^6 km*
August 29	First data	150.9	6.9	0.3	73.7	Rolling	26.6	−1.2	0.7
September 3	Attitude stabilized	150.3	7.4	0.7	72.4	17.4	26.8	−1.6	1.9
September 23	Start of solar rotation 1768	146.0	7.8	2.2	52.6	20.5	27.6	−3.4	6.9
October 7	Maximum Earth-Sun-probe angle	141.2	7.7	2.5	36.3	26.9	28.6	−4.3	10.3
October 20	Start of solar rotation 1769	135.6	7.0	2.1	20.5	40.6	29.7	−5.3	14.4
October 31	Earth overtaken	130.1	6.1	1.7	11.6	90.0	31.0	−6.0	18.8
November 16	Start of solar rotation 1770	121.6	4.1	4.4	19.3	29.4	33.2	−6.3	28.3
December 13	Start of solar rotation 1771	108.0	−1.4	18.5	37.4	4.8	37.8	−4.6	53.4
December 28	Perihelion	101.4	−4.0	30.2	43.4	3.0	40.0	0.0	77.1
December 30	Last data	105.5	−4.4	32.6	44.3	3.0	40.0	+0.7	81.7

Presented graphically by Coleman, Ref. 4.

*The angle ϕ is defined in Section III; a related angle has been plotted by Coleman, Ref. 4.

angular acceptance for charged particles in two perpendicular planes. The theoretical angular and E/Q transmission functions in the plane of analysis (i.e., the fraction of a uniform beam of ions that reaches the collector as a function of energy and angle of incidence) are shown in Fig. 3.

The spectrometer was mounted on the spacecraft with the axis of the cylindrical deflecting plates parallel to the probe–Earth vector R_e (Fig. A-3, Appendix A). The angle ϕ, given in Table 1, is the angle between the vectors $R_s \times v_s$ and $R_s \times R_e$, where R_s is the probe–Sun vector, and v_s is the spacecraft velocity. This angle was very nearly equal to the angle between the Sun–probe–Earth plane and the ecliptic.

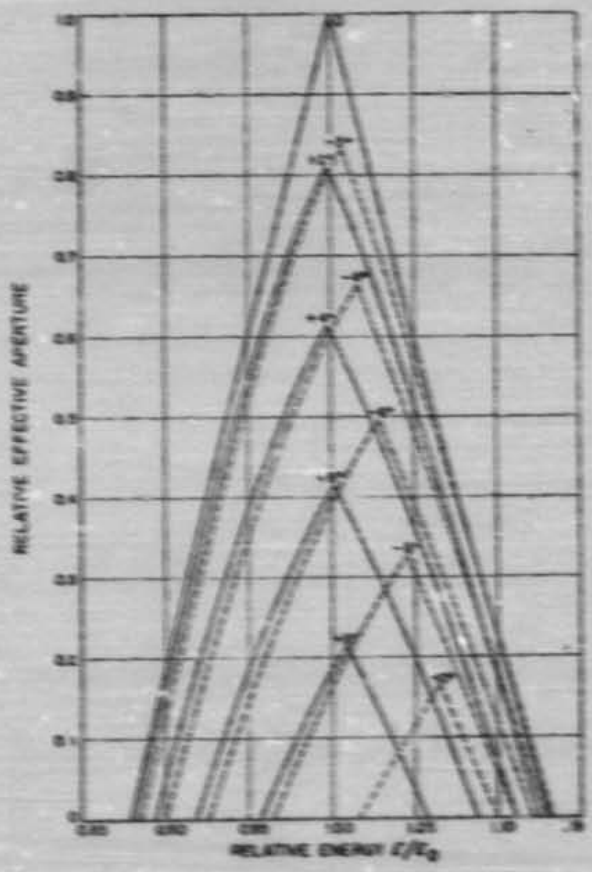

Fig. 3. *Mariner II* electrostatic-analyzer transmission functions

To obtain an E/Q spectrum of the solar-plasma ions, the deflecting voltage on the analyzer plates was changed by the programmer at intervals of about 18 sec in a sequence of ten ascending values. The voltages assumed for this analysis are given in Table 2. Laboratory measurements showed that the variation of these voltages with variations in instrument temperature amounted to ± 0.7% or less over the range − 9 to + 66°C. Because a sensor in the instrument indicated temperatures between 29 and 77°C during the mission, no temperature corrections to the voltages were made.

Table 2. E/Q, proton velocity, and alpha-particle velocity corresponding to the center of each spectrometer channel

Channel	E/Q, v	Proton velocity, km/sec	Alpha velocity, km/sec
1	251	210	149
2	346	288	182
3	516	304	223
4	751	379	268
5	1124	464	328
6	1614	340	398
7	2479	695	488
8	3688	840	594
9	5508	1026	725
10	8224	1259	384

After 10 spectral measurements, a zero reading and a calibration reading (using a standard current of 10^{-10} amp) were taken with the plates connected to guides. The calibration permitted correction of the data for temperature variations in the electrometer, and for shifts in the analog-to-digital converter. The complete sequence of twelve measurements was repeated every 3.696 min.

Table 3. Time intervals for the *Mariner II* plasma spectrometer

Function	Time, sec
Time from start of one spectrum to start of the next	330
Average time to obtain a five-point spectrum	72
Average time between measurements in adjacent channels	18
Average time to obtain a single current measurement (peak)	~0.1

The electrometer, which utilized a dynamic-capacitor modulator to assure long-term stability, was capable of measuring currents from 10^{-9} to 10^{-13} amp, and its output was an accurately linear function of the logarithm of the input current over all but the lowest 1/2 decade of this 7-decade range (Ref. 3). The output dc voltage was converted by the spacecraft data-automation system into a digital reading with a quantization interval of 1/10 decade.

The electrometer time constant was a function of the magnitude of the measured current. At the 10^{-10} or 10^{-11} amp levels usually observed at the peak of a plasma spectrum, the relevant time constant was ~0.1 sec. The analog-to-digital conversion process, which occured about 18 sec after the change in plate voltage, required only about 1 msec (Ref. 3). Table 3 summarizes the several time intervals that were involved in this experiment.

IV. METHOD OF SPECTRAL ANALYSIS

Of the approximately 40,000 spectra telemetered to Earth from *Mariner*, 35,189 have been included in this analysis. All spectra for which any one of the 12 current readings was either missing or failed to pass a parity check have been omitted. Those spectra for which the current in any channel was several orders of magnitude different from both the preceding and the following several current measurements in that channel have also been omitted. Even if such an anomalous current measurement were correct, the calculated plasma properties probably would be incorrect because of the assumed time-independence of the spectrum. In general, the plasma spectra changed very slowly relative to the 3.7 min between successive spectra, for only about 10% of the current readings for a given channel changed by more than two digital steps from one spectrum to the next.

Many of the spectra were similar to that shown in Fig. 4, where the logarithm of the measured current is plotted against the channel number, or against the approximate logarithm of E/Q. The currents in the five other E/Q channels were very small and usually of negative polarity, the result, presumably, of electrons released from the suppressor electrode by the action of sunlight reflected down the deflection plates. This negative current was always below 10^{-12} amp, and frequently five to ten times smaller than this value for all energy channels. Because the peak positive-ion currents were usually in the range 10^{-10} to 10^{-11} amp, the positive-ion data have not been corrected for photoelectric effects.

If it is assumed that the positive-ion component of the solar plasma consisted of protons and alpha particles with isotropic Maxwell-Boltzmann distributions in a reference frame moving radially away from the Sun, then the peak of the alpha-particle distribution function would be at a value of E/Q equal to twice the value of E/Q at the proton peak, or approximately 1.74 spectrometer channels above the proton peak. Thus the left peak in each spectrum has been interpreted as a proton flux, and the right peak as a flux of alpha particles moving

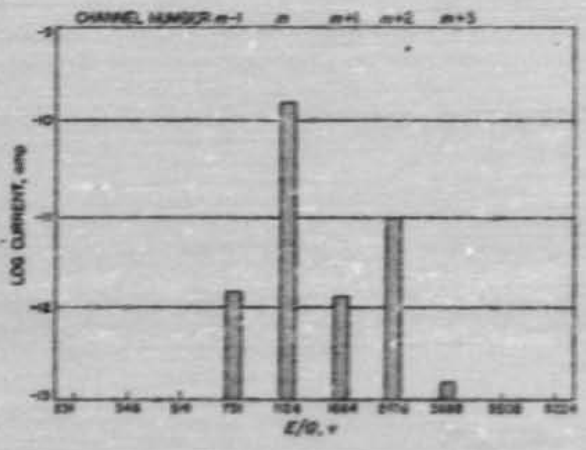

Fig. 4. Sample spectrum obtained by the *Mariner II* positive-ion spectrometer

with approximately the same bulk velocity as the protons. Equal bulk velocities for the two components should be assured by the influence of the fairly irregular interplanetary magnetic field.

A spectrum similar to that in Fig. 4 was analyzed as follows:

1. The currents in channels $m-1$, m (the "peak channel"), and $m+1$ were provisionally assumed to be due to protons only. By fitting a Maxwell-Boltzmann velocity distribution to these three measurements, the width of this proton peak and its location relative to the center of channel m were determined. The width determined the parameter

$$\theta_p = 2kT_p/M_pv^2$$

where k is the Boltzmann constant, T_p is the proton temperature, M_p is the proton mass, and v is the plasma flow velocity.

2. This proton spectrum was then mathematically extended to channel $m+2$. The difference between the measured current in channel $m+2$ and this predicted proton current was assumed to be due to alpha particles.

3. The alpha-particle spectrum was determined from the alpha-particle current in channel $m+2$, and from the assumptions that the alpha particles and protons had equal flow velocities and appropriately related thermal-velocity distributions as discussed later.

4. An extension of the alpha-particle spectrum to channel $m+1$ gave the expected alpha-particle current in this channel.

5. After correction of the proton current in channel $m+1$, the calculations of steps one through four were repeated to obtain iterations of the proton spectrum until the iteration process either converged, or the calculated alpha-particle current in channel $m+1$ became greater than the total measured current in this channel. For this analysis, the final answer was considered to be known when the proton current in channel $m+1$ agreed with its value in the previous iteration within a factor of $10^{0.03} = 1.0715$, which corresponded to 0.3 of the instrument's digitization levels.

6. If a consistent set of proton and alpha-particle spectra could be obtained, the following plasma properties could be determined:

   a. The plasma bulk velocity v, which depends on the position of the proton peak relative to the center of channel m, on the value of θ_p (not a strong dependence), and on the velocity at the center of channel m (Table 2).

   b. The quantity T_p, which is determined by the values of θ_p and v. Although T_p is merely a measure of the velocity dispersion, it is convenient to define the term as "proton temperature."

   c. The proton and alpha-particle densities, n_p and n_α, which are determined by appropriate integrations over the final spectra.

   d. The parameter h, which is the logarithm of the ratio of the measured current to the predicted current in channel $m+3$, was calculated. The value of h is a measure of how well the assumed model fit the data.

Appendix A describes this spectral analysis procedure in more detail, and includes some of the mathematical shortcuts and approximations used in the actual analysis. Appendix B is a discussion of the uncertainties occurring in the calculated plasma parameters v, T_p, n_p, n_α/n_p, n_pmv^2, etc.

Of course, not all the measured spectra looked like Fig. 4. In general, any variation from this example could be classified in one or more of the following four categories:

1. With no current in channel $m+3$, there were four spectral points from which to calculate the four parameters v, T_p, n_p, and n_α for an assumed relationship between T_α and T_p. Because the parameter h could not be calculated, there was no way of telling how well any assumed model fit the data.

2. When channel $m+2$ had no current, higher channels had no current either. This type of spectrum might be expected when the composition changed to a state with relatively few alpha particles, when the apparent plasma density was so low that the currents in all channels were not as far above the sensitivity threshold as usual, when the alpha-particle peak fell midway between channels and, simultaneously, the alpha-particle temperature was relatively low, and when, if ever, the effective arrival direction of the alpha particles was at an appreciably greater angle to the Sun–probe line than were the protons. For these spectra, the proton velocity was calculated as usual. If the proton

peak was above the center of channel m, the proton temperature and density were then calculated. If, however, the proton peak was below the center of channel m, there may have been an appreciable alpha-particle contribution to the current in channel $m+1$; the values of n_p and T_p, therefore, were not calculated for that spectrum. Obviously, values could not be obtained for the parameters n_α and k.

3. If currents were observed in channel $m-2$ or in channel $m+4$, the extra values were not used in the analysis. Fewer than 1% of the observed spectra were of this type.

4. No current was observed in channel $m-1$, or no current was observed in channel $m+1$, if either n_p or n_α was unusually low, or if the proton peak was quite far above the center of channel m so that channels m and $m+1$ had almost equal currents. In such cases, the upper limits of δ_p and T_p were obtained by assuming an actual current in the "missing" channel ($m-1$ or $m+1$) just at the electrometer's threshold of sensitivity; the spectral analysis then proceeded as outlined above. Lower limits for δ_p and T_p were obtained by assuming that n_p for this spectrum could not have been more than 3 standard deviations greater than the average n_p for a 15-hr period centered on the 3-hr period containing the spectrum in question. All spectra of this type were, of course, omitted from the calculation of the average n_p and its standard deviation. In addition to n_p, neither n_α nor k could be calculated for these spectra. The two values of v corresponding to the upper and lower limits of δ_p seldom differed by more than 2%. If there was no measurable current in either channel $m-1$ or channel $m+1$, the lower limits of δ_p and T_p were set equal to zero, and the velocity was assumed to equal the velocity at the center of channel m.

The spectral-analysis procedure described above and in Appendix A was applied to each of two models of the solar wind: (1) the equal-temperature model assumed that the protons and alpha particles were in thermodynamic equilibrium with each other (in the moving reference frame) at a temperature T; (2) the equal-thermal-velocity model assumed that the proton and alpha particles were separately in thermodynamic equilibrium, with the alpha-particle temperature T_α four times greater than the proton temperature T_p, giving the two types of ions identical, isotropic velocity distributions in the moving reference frame.

The analyses of the 35,139 spectra can be grouped as follows:

1. 22,477 spectra had unreasonably small currents in either channel $m-1$, channel $m+1$, or both; therefore, only upper and lower limits were found for δ_p and T_p, while n_p, n_α, and k could not be calculated at all.

2. 12,282 spectra were successfully analyzed with the equal-thermal-velocity model of the solar wind to obtain v, δ_p (and therefore T_p), n_p, and n_α. There was also a measurable current in channel $m+2$ allowing the calculation of k. The equal-temperature model calculations converged for almost all of these spectra, but for only seven spectra did the equal-temperature model give a smaller absolute value of k than did the equal-thermal-velocity model. Apparently, then, the equal-thermal-velocity model better represents the state of the plasma than does the equal-temperature model.

3. 4,228 spectra were successfully analyzed with the equal-thermal-velocity model to obtain v, δ_p (and T_p), n_p, and n_α, but they did not have a current in channel $m+2$ large enough to permit the calculation of k. The results of the equal-thermal-velocity model for this group have been used for the data presentations in the rest of this paper.

4. 1,089 spectra were such that the analytical procedure did not converge for the equal-thermal-velocity model, and the results of the equal-temperature calculations are used in the data presentations that follow. Of these spectra, 86% had a measurable current in channel $m+2$, and k was calculated.

5. 4,138 spectra were such that neither model of the solar wind could be successfully applied, either because the calculations did not converge, or because there was no measurable current in channel $m+2$. If the proton peak for one of these spectra was above the center of channel m, the "proton-only" approximations for v, δ_p, T_p, and n_p were used. However, if the proton peak was below the center of channel m, the proton-only approximation for v was used, but this spectrum was not included in the average values of δ_p, T_p, and n_p.

It is important to note in connection with groups 3 and 4 that the calculated values of v, δ_p, T_p, and n_p are relatively insensitive to the choice of model. However, the width of the alpha-particle spectrum, and, therefore, the values of n_α and k, are strongly model-dependent.

V. RESULTS AND DISCUSSION

A. Velocity

The 3-hr averages of plasma velocity are shown in Fig. 5, where the time base was chosen to show the 27-day recurrence features associated with solar rotation. It is apparent that during this 4-month period the interplanetary plasma consisted of a series of long-lived, high-velocity streams separated by slower plasma. The 27-day recurrence pattern, the association of these streams with M-region geomagnetic storms, and the high correlation of the bulk velocity with the geomagnetic-activity indices K_p or A_p have been discussed in earlier papers (Refs. 5, 6, and 7). These conclusions still follow from the velocity profiles based on the more sophisticated calculations presented here.

While some of the high-velocity streams showed structures that were fairly symmetric, other observed velocity profiles were steeper on the leading or western edge than on the trailing edge (i.e., the velocity increased more rapidly than it decreased). Good examples of this behavior were observed in the streams with peak velocities observed on September 13, October 8, October 28, and November 21. This sort of profile is not unexpected for a reasonably symmetric source on the Sun (with the highest velocity at the center of the source), because the higher-velocity plasma tends to overtake the slower plasma ahead of it. At distances of 0.7 to 1.0 AU, however, the structure had not yet steepened into a shock front[2]. A high-velocity stream may eventually develop a shock front or a series of shocks at distances from the Sun appreciably greater than 1 AU.

The average daily-average velocity for the period August 29 through December 30, 1962, was 504 km/sec. The 3-hr averages ranged from 319 to 771 km/sec. The lowest and highest velocities sustained for at least three consecutive spectra occurred on November 18 when the velocity was between 305 and 308 km/sec for five spectra (18 min), and on December 20 when the velocity was between 815 and 842 km/sec for three spectra (11 min). From the velocity minima on November 13–14, November 18–20, November 28–29, December 7–8, and December 9–10, it would seem that the quiet, between-stream, solar-wind velocity was in the range 320 to ~ 340 km/sec. Subsequent observations of solar-wind velocities as low as ~ 250 km/sec by *IMP*, *OGO*, and *Velo* satellites[3], however, seem to contradict this conclusion. Perhaps the difference in minimum velocity reflects the difference in phase of the 11-yr solar cycle.

Scarf (Ref. 9) has calculated a quiet solar-wind velocity of 290 km/sec from a model in which there is uninhibited thermal conduction and viscous flow between 2 and 17 solar radii, followed by an adiabatic continuum flow region between 17 and 75 solar radii, with collisionless flow beyond 75 solar radii. Using a two-fluid model of the solar wind, Sturrock and Hartle (Ref. 10) calculated a velocity of 270 km/sec at 1 AU. These theoretically predicted velocities are not very different from the lowest observed velocities.

The averages of the plasma velocity over each solar-rotation period were also calculated in an attempt to separate the effect of variations in solar activity from the effect of Mariner's varying distance from the Sun. No clear radial variation of plasma velocity between 0.7 and 1.0 AU emerges from the calculations, as shown in Fig. 6. This result is consistent with theoretical predictions (Refs. 9, 11, 12, and 13). The basic inadequacy of the 27-day averaging method for determining the radial variations of plasma properties is apparent from Fig. 5; the high-velocity peaks were much less pronounced in the last half of solar rotation 1770 than in the four other rotations under consideration. The conclusion that plasma velocity is independent of radial variation comes as well from the constancy of the between-stream velocity minima noted above, which occurred at Sun–spacecraft distances between 0.824 and 0.732 AU.

B. Density

The number density of protons could be calculated for only 18,632 spectra, or 53% of the spectra for which velocity could be calculated. The resulting 3-hr and daily-average values of proton density and their relation to plasma velocity are shown in Figs. 5 and 7. It can be seen from Fig. 5 that the density generally reached a maximum on the leading edge of a high-velocity stream before maximum velocity was reached (September 12,

[2]The velocity change across the shock front observed on October 7 (Ref. 8) was from ~370 to ~450 km/sec, which was only a small fraction of the total velocity increase on October 7 and 8.

[3]Personal communication from H. S. Bridge, J. H. Wolfe, and I. Strong, 1966.

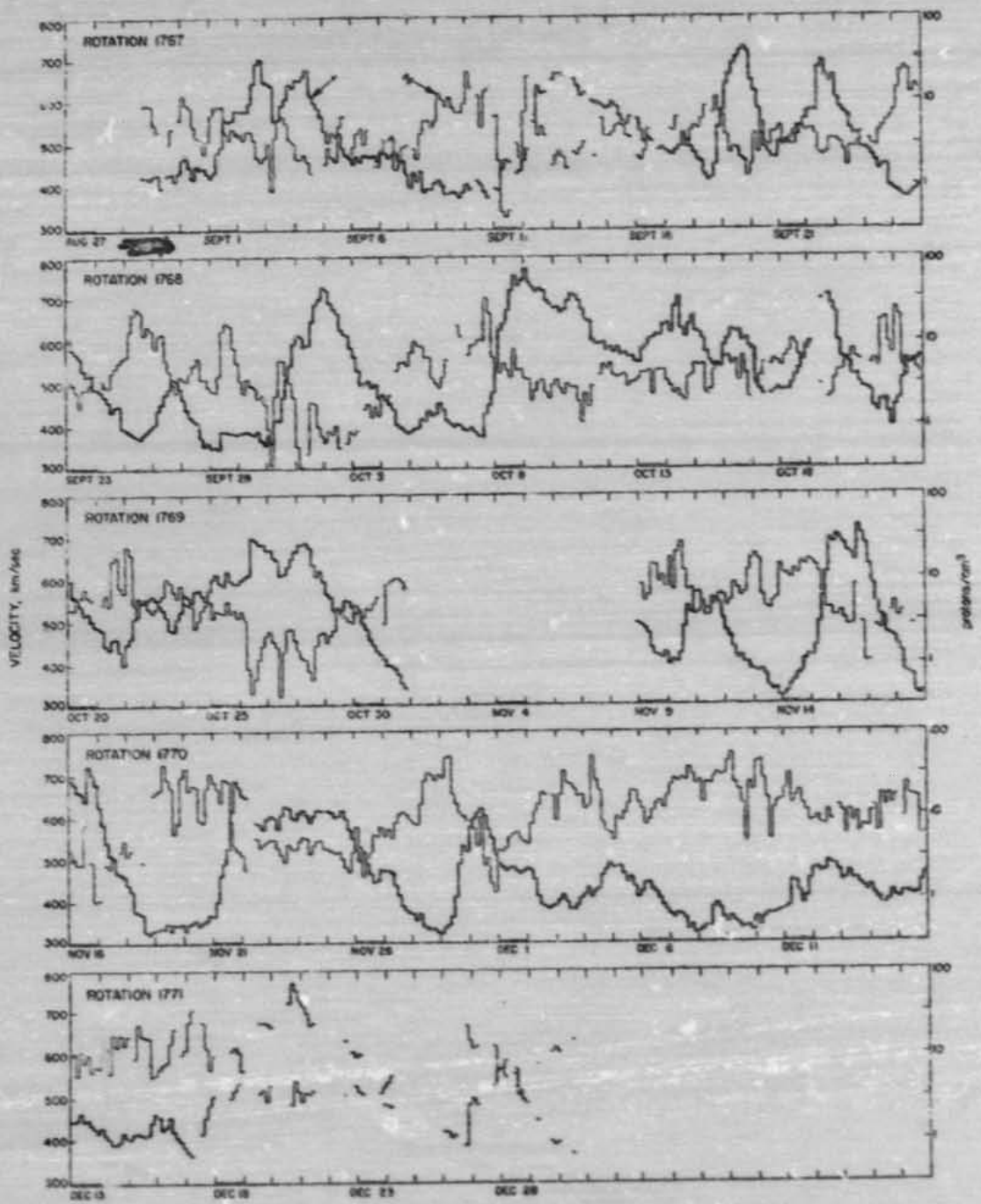

Fig. 5. Three-hr average values of v and n_e (logarithmic scale) vs. time

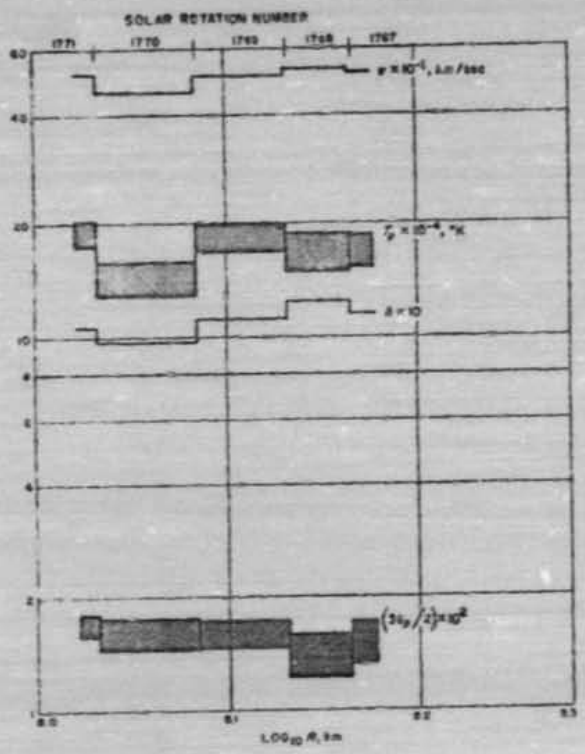

Fig. 6. Twenty-seven-day averages of the daily averages of v, T_p, $3\theta_p/2$, and h vs. distance from the Sun

September 30, October 7, November 10, and November 29 of Fig. 5 are good examples). The calculated density usually was very low (often less than 1 proton/cm³) in the center of a high-velocity stream, as observed on September 4, September 13, September 19, October 2, October 26, October 28, and November 16.

The 3-hr average values of density ranged from 0.44 protons/cm³ on September 11 to 54 protons/cm³ on December 9. (In Fig. 5, there are four 3-hr intervals with n_p between 0.31 and 0.42 protons/cm³, but each of these intervals contained only two or three spectra for which density could be calculated; the average values, then, were perhaps not representative.) The lowest density maintained for at least three consecutive spectra was observed on September 11 when there were between 0.081 and 0.094 protons/cm³ for four spectra. The highest density was observed between high-velocity streams on December 9 when there were between 70 and 85 protons/cm³ for three spectra.

It is also apparent from Fig. 5 that the proton density generally increased with time as *Mariner II* approached perihelion. Further analysis of this effect is based on Fig. 8, in which the 27-day averages of the daily averages of the proton density n_p, of the proton flux $n_p v$, and of the momentum flux, or energy density associated with the bulk motion $v^2 (M_p n_p + M_\alpha n_\alpha)/2$ are shown as a function of solar distance. The slopes for an inverse-square relation are also given in this figure. Despite the large effects of the varying nature of the high-velocity streams from one solar rotation to the next, the dependence of the plasma parameters on the inverse square of the distance from the Sun can perhaps be detected.

This inverse-square relation was used to normalize the daily-average values of proton density to 1 AU (Fig. 7). The average of the normalized daily averages for the four months of these observations was 5.4 protons/cm³. Figure 7 also shows a rough inverse proportionality between the logarithm of the normalized density and the plasma velocity. Thus the density was much more variable than the velocity, and such parameters as mass flux, momentum flux, and energy flux were roughly correlated with density and showed little correlation with velocity or the K_p index.

For comparison with near-Earth observations, the average daily averages (not normalized) during solar rotation number 1767 when *Mariner II* was between 1.01 and 0.97 AU from the Sun were:

$$n_p = 5.0 \text{ protons/cm}^3$$

$$n_p v = 2.4 \times 10^8 \text{ protons/cm}^2 \text{ sec}$$

$$v^2 (M_p n_p + M_\alpha n_\alpha)/2 = 1.2 \times 10^{-3} \text{ ergs/cm}^3$$

Both density and flux for the between-stream periods were consistently greater by factors between 2 and 6 than the values predicted by Scarf's (Ref. 9) quiet solar-wind model.

As discussed in Appendix A, the shapes of the measured spectra and, therefore, the calculated values of velocity and temperature were relatively insensitive to the plasma's angle of incidence. As seen in Fig. 3, however, the absolute values of the measured currents, and thus the calculated proton density depended strongly on the angle of incidence. The calculations presented here were based on the assumption of a radial velocity corrected for aberration due to the spacecraft's motion. The

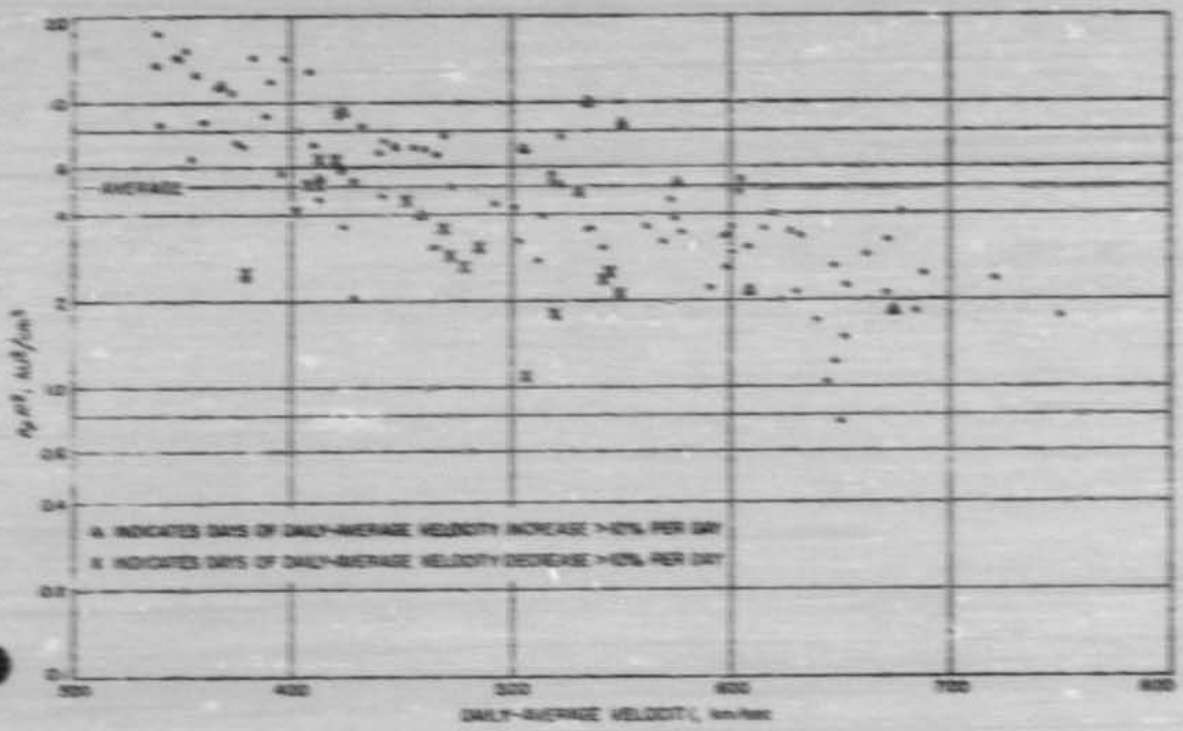

Fig. 7. Daily average of $n_p R^2$ vs. the daily average of v

velocity could never have been very different from radial, because no current would have been observed at all for a net velocity (solar wind plus spacecraft) more than ~ 10 deg from the solar direction. However, smaller transverse velocity components that would significantly affect the density calculations cannot be ruled out. The present calculations, for example, would underestimate the true proton density on the leading edge of a high-velocity stream if the type of refraction discussed by Davis (Ref. 14) were significant. Furthermore, any tangential velocity component deriving from the probable corotation of the plasma close to the Sun would tend to cancel out the effect of the spacecraft motion, and the densities presented here would be higher than the true densities.

According to E. F. Lyon*, the direction of the velocity vector (determined to an accuracy of a few degrees) was consistent with a radial flow for about 90% of IMP-I's period of observation of the solar wind. Therefore, the calculations of long-time averages of proton density and the general trends of the density's temporal variations are probably reliable, although undetectable errors may have been present about 10% of the time.

The calculated values of proton density were also based on the assumption of an isotropic velocity distribution in the reference frame that moved with the plasma. If, for an extreme example, there were no thermal motion at all in the transverse directions, the calculated densities presented here should be decreased by a factor of 1.5 to 2.

C. Temperature

The upper and lower limits of the 3-hr averages of the proton temperature are shown in Fig. 9 where the time base was chosen to show the 27-day recurrence features associated with solar rotation. This plot of temperature vs. time generally follows the plot of bulk velocity vs. time (i.e., the high-velocity streams were hotter than the surrounding plasma).

*Oral communication at European Space Research Institute Conference, May 1968.

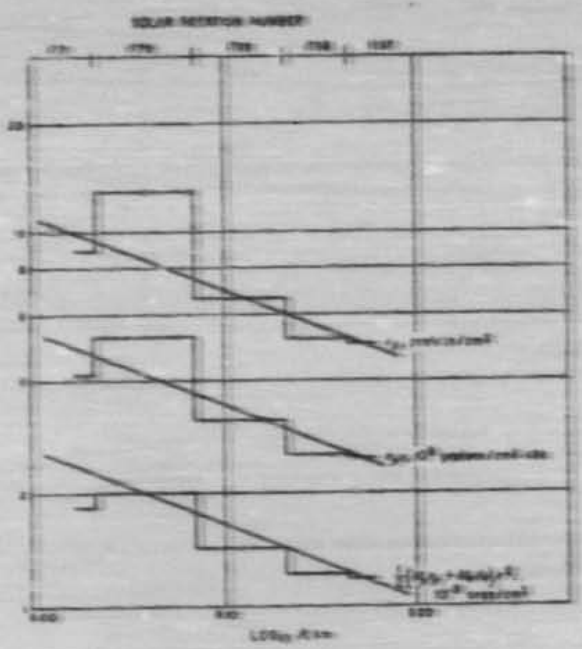

Fig. 8. Twenty-seven-day averages of the daily averages of n_p, $n_p v$, and $v^2(M_p n_p + M_\alpha n_\alpha)/2$ vs. distance from the Sun

As a high-velocity stream overtook the spacecraft, the temperature usually increased more rapidly than did the velocity, and reached its maximum value several hours to half a day before maximum velocity was reached (examples are shown in Fig. 2 for September 12, September 19, October 7 and November 29).

The 3-hr averages of proton temperature ranged up to 8.0×10^5 °K on October 28. The highest temperature observed for at least three consecutive spectra was between 9.0 and 9.1×10^5 °K maintained for three spectra on December 17.

The average daily-average value of T_p for the entire experiment was between 1.51 and 1.85×10^5 °K (lower and upper limits). Thus the temperature of the interplanetary protons was, on the average, about a factor of 10 lower than the temperature at the base of the corona, and, occasionally, between the high-velocity streams, was cooler than the corona by a factor of about 50.

The 27-day averages of the daily averages of the upper and lower limits of T_p are plotted vs. distance from the Sun in Fig. 8. There was no obvious radial dependence. This conclusion is further verified by noting that the 3-hr temperature averages reached about the same minimum values of $\sim 3 \times 10^4$ °K for each of the between-stream periods found on the basis of bulk velocity.

Scarf's calculations of a model quiet solar wind based on assumptions of thermal conduction and viscous flow followed by adiabatic expansion[*] predict a temperature of 2.2×10^5 °K at 1 AU, while Sturrock and Hartle's two-fluid model of the solar wind (Ref. 10) predicts a positive-ion temperature of 2800 °K at 1 AU. These minimum temperatures correspond to the absence of any plasma heating by interactions with magnetic or electric-field fluctuations. Hence the observations of temperature by *Mariner II* may be evidence for appreciable heating of positive ions in the solar wind by field-particle interactions.

The ratio of proton thermal-energy to flow-energy densities,

$$3\theta_p/2 = (3kT_p/2)/(M_p v^2/2)$$

has also been studied. Figure 10 is a plot of the daily averages of the upper and lower limits of $3\theta_p/2$ vs. the daily-average velocity; the dependence on the time derivative of v is apparently more important than any dependence on velocity v. This behavior is probably understandable in terms of the instabilities, turbulence, and perhaps small shocks created at the leading edge of a stream when a high-velocity plasma overtakes the slower plasma in its path.

On December 17, the 3-hr averages of $3\theta_p/2$ reached a maximum of 0.053, while the maximum value maintained for at least three consecutive spectra was between 0.104 and 0.115. The actual minimum values of $3\theta_p/2$ could not be determined with this instrumentation.

The averages of the daily-average values of the lower and upper limits of $3\theta_p/2$ for the entire flight were 0.013 and 0.017, respectively. The 27-day averages of $3\theta_p/2$ are shown in Fig. 8.

The energy density of proton random motions was never more than a small fraction of the energy density of bulk motion. Preliminary comparisons of the *Mariner II* plasma and magnetic-field data indicate that the energy

[*] Personal communication, 1965.

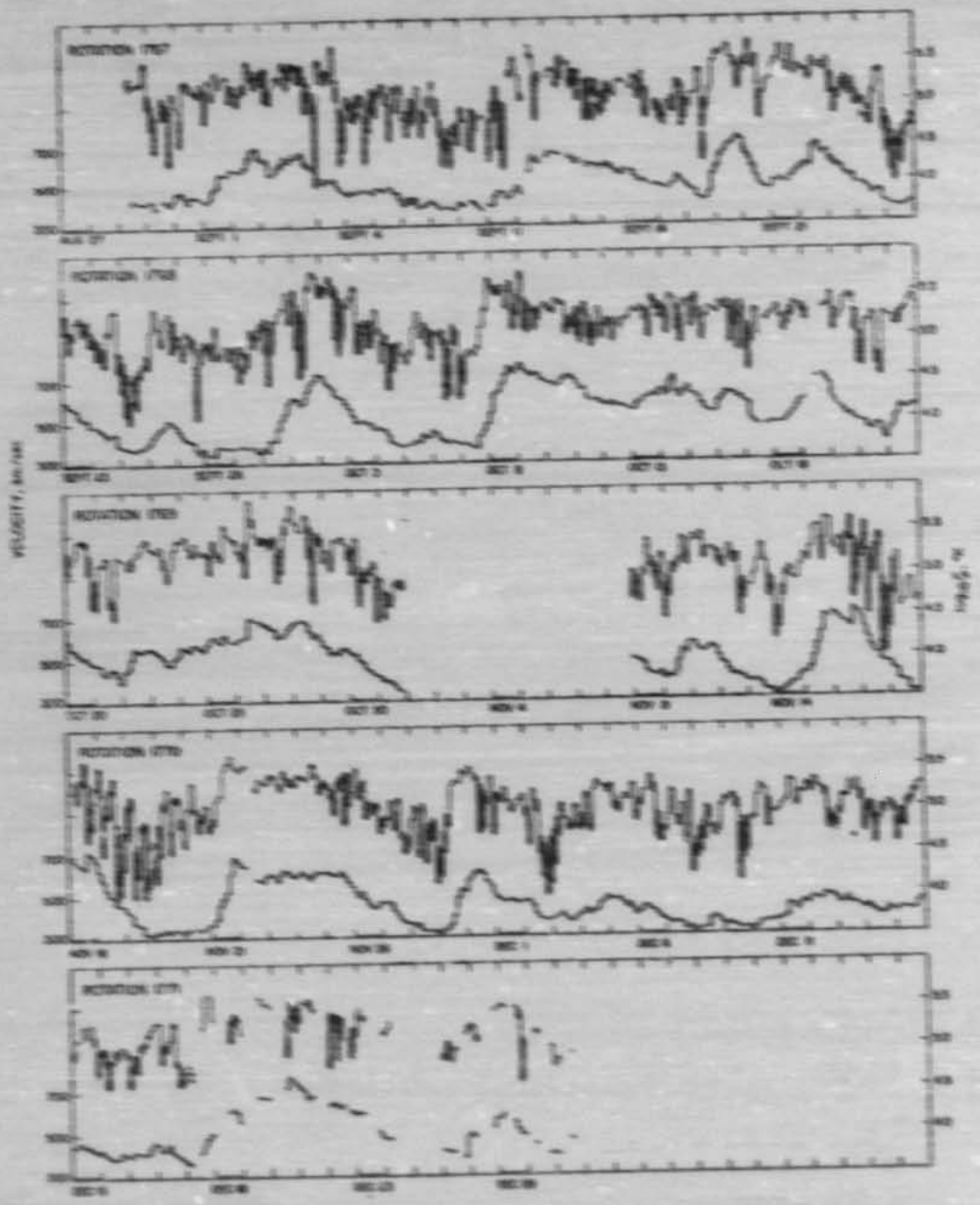

Fig. 9. Three-hr average values of ϵ and T_e (logarithmic scale) vs. time (temperature limits have not been chosen below 10°K)

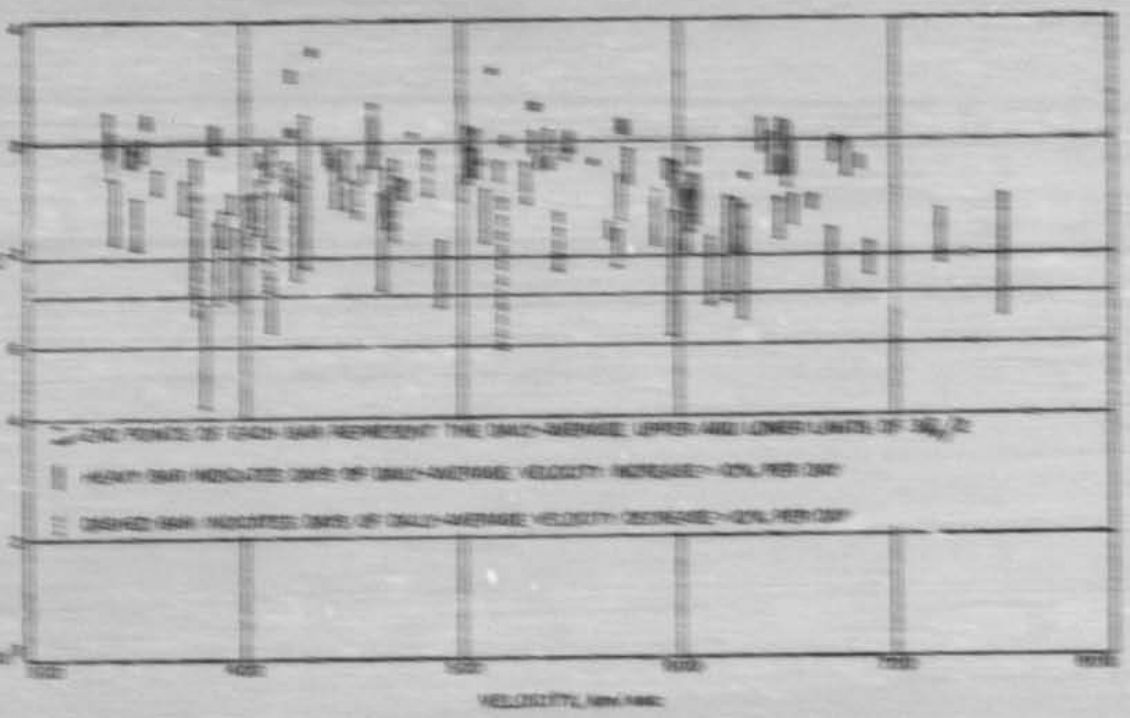

Fig. 12. Daily-average value of the ratio B_y/B_z vs. the daily-average solar-wind velocity

density of the complanetary magnetic field was generally comparable to the thermal-motion energy density (Ref. 13). Thus, for problems involving only the momentum flux or energy density of the solar wind, use of the bulk-motion energy density alone would be a fair approximation; the electron energy density is probably not large (Ref. 19).

D. The Definition of T_e

Whether the parameters T_e and N_e calculated from the spread in orbital velocity are properly called temperature and a measure of thermal motions is questionable. The possibility that the observed velocity spread was really due to superposition of small, non-thermal motions on gain large, turbulent, wave motion, or other collective motions cannot be ruled out.

It is possible, however, to put an upper limit on the wavelength of any of the collective motions present. Because the instrument was sensitive to the general peak was approximately 60 sec, and because the current in a given channel usually changed little, if at all, from one spectrum to the next, there could not have been any large-amplitude motions present that changed appreciably over the distance swept out by the spacecraft in 60 sec in a reference frame moving with the solar wind. The limiting wavelength in such case is thus approximately 30 km for an average solar wind of 500 km/sec. If, for example, the calculated T_e actually represented waves moving through a hot, cold plasma at a velocity of V_{ph}, the frequency of these waves would have been greater than $V_{ph}/30$ km. For $n_e = 30/cm^3$ and an interplanetary field strength of 3×10^{-5} gauss, V_{ph} is about 30 km/sec; the wave frequency, then, must have been greater than ~ 1 cps.

At better fit to the measured spectra can be obtained by assuming that the ions particles had the same thermal velocity, rather than the same temperature, as the proton; this fact has at least two possible interpretations:

1. Collective motions were not of major importance, and the temperature of each type of ion was determined by such an individual interaction as collisions

from shock fronts moving through the plasma. (Ion-field interactions are expected to play an important role because the proton self-collision mean free path (Ref. 17) for a plasma with $T_p = 1.85 \times 10^5$ °K and $n_p = 5/cm^3$ is 2.7 AU.)

2. The velocity distributions were due to such motions as those found in transverse hydromagnetic (Alfvén) waves, in which the protons and alpha particles moved with a magnetic-field line, and therefore had the same velocities.

From a study of the correlations of plasma velocity and magnetic field observed by *Mariner II*, P. J. Coleman, Jr.,* found that the ratio of the power in velocity fluctuations to the power in magnetic-field fluctuations was independent of frequency in the range 1 to 116 cycles/day. On the basis of observations by *Mariner IV* and *OGO*, Coleman then extrapolated the magnetic-fluctuation spectrum to higher frequencies, and assumed that this ratio of powers remained constant at these higher frequencies; he found that the rms velocity for all oscillations with a frequency greater than 116 cycles/day was 4 km/sec. Because the thermal velocity was an order of magnitude greater than 4 km/sec, a temperature due to collective motions must have been the result of motions in which the magnetic field did not participate.

There are several possible sources of collective motions in the interplanetary medium:

1. Turbulent flow might be expected on the basis of the Reynolds number $nM_p cD/\mu$, (where D = scale size $\approx 10^{13}$ cm, and μ = viscosity $\approx 1.2 \times 10^{-16} T^{1/2}$ gm/cm sec), the value of which is about 10^5 in the relatively cool, dense plasma between streams. However, because the upper limit of the eddy sizes under consideration ($\sim$ 50 km) is 10^5 times less than the mean free path, and is approximately equal to the proton gyro radius for a thermal proton in the moving reference frame, it is not clear that the ordinary Reynolds number is a useful parameter.

2. Because the mean free path at 1 AU is so very large, because only the two degrees of thermal motion perpendicular to the radial direction are cooled by adiabatic expansion, and because collisions are too infrequent to restore isotropy, an anisotropic thermal velocity distribution might be expected. This anisotropic pressure could lead to either the hose or the mirror instability, depending upon the direction and strength of the interplanetary magnetic field (Ref. 18).

3. Both the two-stream and Kelvin-Helmholtz instabilities (Ref. 19), and collision-free shocks might be generated on the leading (western) edge of the high-velocity streams where hot, high-velocity plasma overtakes cooler, slower gas. At least one example of such a shock was observed by *Mariner II* (Ref. 8); the observable (low frequency) fluctuations in both the magnetic field and plasma were greatly enhanced behind this shock. The *Mariner II* data have also shown that these lower-frequency fluctuations, as exhibited by the standard deviations in velocity and the magnetic field (Ref. 20), were generally increased at the leading edges of the high-velocity streams.

Thus, because it seems likely that turbulent or wave motions would be generated in the interplanetary plasma, the answer to the question of whether T_p was primarily a measure of thermal or of collective motions depends on both the rate of creation of these disturbances, and on the rate of their dissipation into thermal energy through field-particle interactions. In either case, it is probably true that the values of T_p observed between 0.7 and 1.0 AU often depended in large part on disturbances generated in or propagating through the interplanetary medium, rather than on thermal conduction from the inner corona alone.

E. Nonthermal Ions

The parameter h was defined as $\log_{10}[I_{m+1}\text{(measured)}/I_{m+1}\text{(calculated)}]$. A positive value of h therefore implies the presence of more ions with a large value of E/Q than predicted by a fit of Maxwell-Boltzmann distributions of protons and alpha particles (where $T_\alpha = 4T_p$) to the currents measured in channels $m-1$, m, $m+1$, and $m+2$. If the possible contributions of any ions with mass/charge ratios greater than that for alpha particles are ignored, h can be considered a measure of any high-energy tail on the proton and alpha-particle distribution functions. It is only a semiquantitative measure of such a tail, however, because the ratio of measured to calculated currents was taken not at a fixed value of E/Q relative to the peak of the distribution function, but at a value of E/Q equal to 3.30 times the value of E/Q at the center of the channel with the largest current. Furthermore, it was not possible to separate the relative contributions of protons and alpha particles to the apparent tail.

*Personal communication, 1966.

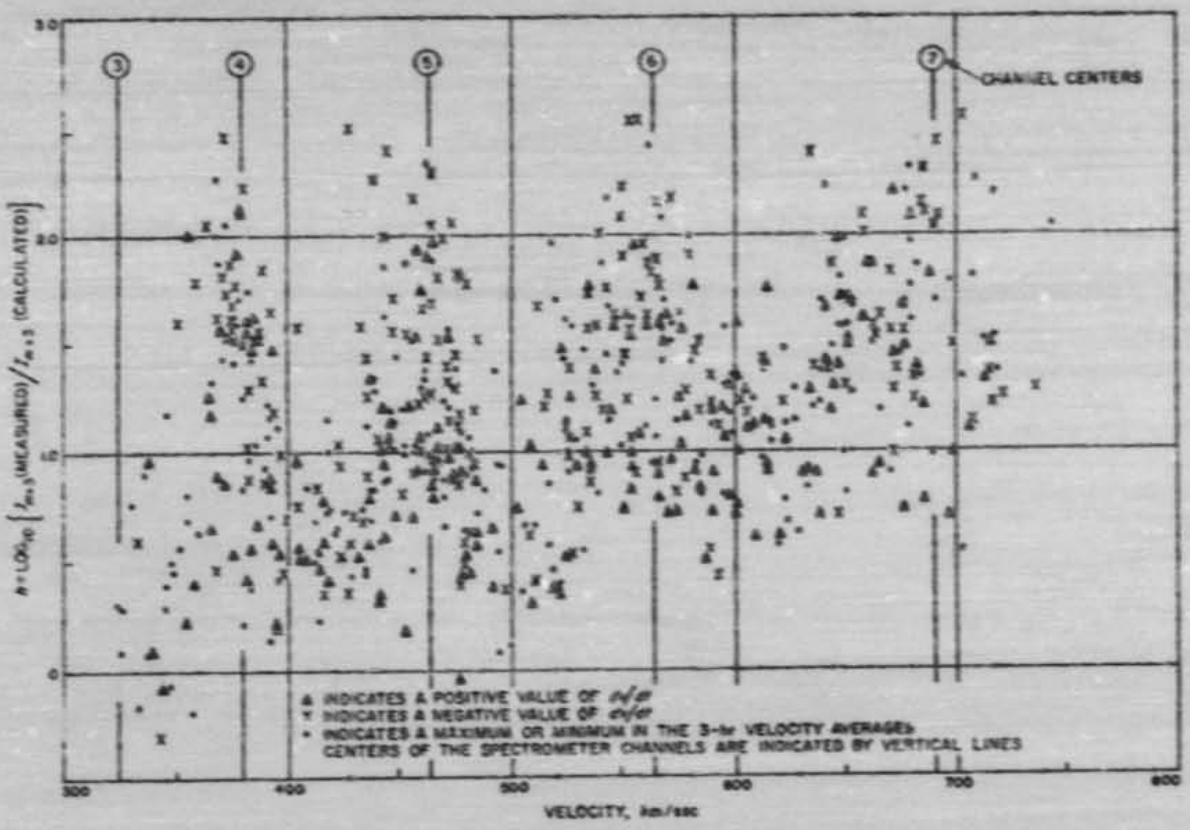

Fig. 11. Three-hr averages of the high-energy-tail parameter h vs. the 3-hr averages of plasma flow velocity

Figure 11 shows the distribution of 3-hr averages of h with the 3-hr averages of plasma velocity. The values of h showed some velocity dependence; in general, the high-energy tail was more pronounced when the velocity was high rather than low. Figure 11 also shows that h occasionally reached fairly high positive values, corresponding to about 300 times the expected current in channel $m+3$. The fact that h was seldom negative (except at velocities less than $-$ 360 km/sec) can be interpreted as evidence that an excess of high-energy ions was almost always present. The observation of a high-energy tail is in agreement with observations of the solar wind by *IMP-2* and *Vela 2A* (Ref. 21).

A significant high-energy tail often developed suddenly during the rising-velocity phase of a stream and then disappeared very slowly. For example, three consecutive spectra observed about 3 hr after the shock front seen on October 7 (Ref. 8) are shown in Fig. 12, where the dashed curves represent a rough fit of the proton and alpha-particle spectra to the currents in channels 4 through 7. There had been no current observed in channel $m+3$ for about 8½ hr preceding this time, and, after this time, large values of h were observed almost continuously for about a week. (Frame 63:115 shows one of the very few 7-point spectra obtained.) The sudden increase in h shown in Fig. 12 coincided with a change in direction of the interplanetary magnetic field of close to 180 deg. Some details of such correlations will be discussed in a later paper.

According to Fig. 11, h was generally greater on the trailing edge (negative dv/dt) than on the leading edge (positive dv/dt) of a high-velocity stream. The sudden appearance of a high-energy tail on the leading edge followed by the tail's slow decay (often over many days,

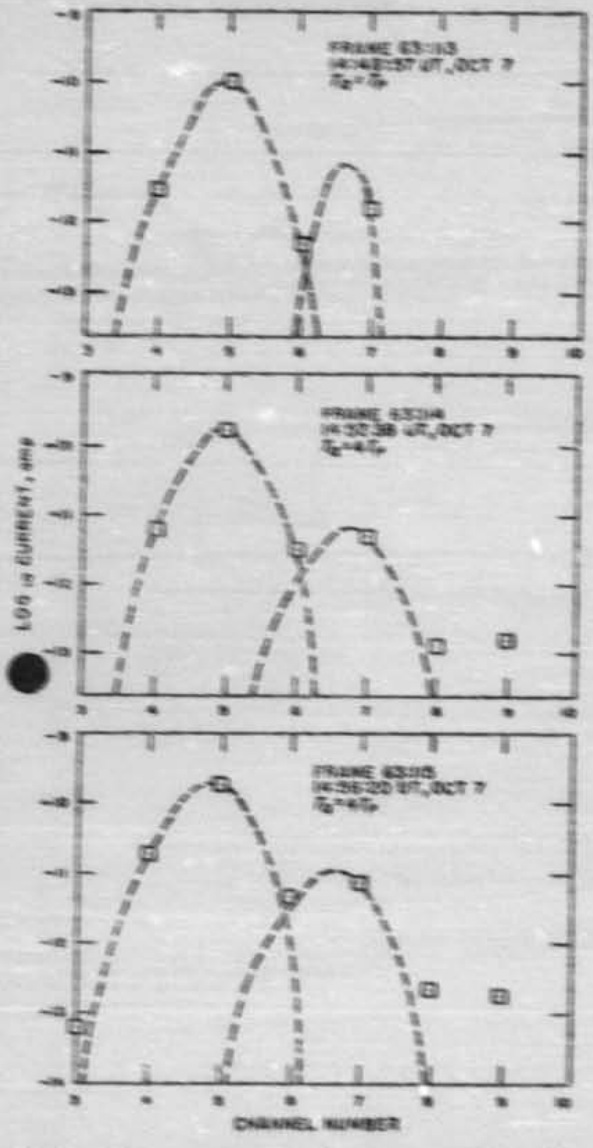

Fig. 12. Three consecutive positive-ion spectra obtained on October 7, 1962

is partially responsible for this effect. Also, larger values of k on the trailing edge of a stream often occurred in regions of low proton temperature and low values of k_{max} (calculated), rather than in regions of unusually high values of I_{max} (measured) similar to that shown in Fig. 11.

In Fig. 11, the quasi-periodic structure in phase with the spacing of the spectrometer channels probably arose from a combination of these effects:

1. As the proton peak occurred at higher values of E/Q relative to the center of channel m, the measurement of k was made at values of E/Q closer to the alpha-particle peak, where the fractional deviation from a Maxwell-Boltzmann distribution was smaller.

2. As the proton peak occurred at lower values of E/Q relative to the center of channel m, the current in channel $m+2$ was more likely to be unmeasurably small so that k could not be calculated.

3. If the proton peak was far above (or far below) the center of channel m, an unmeasurably small current in channel $m-2$ (or $m+1$) was likely, preventing the calculation of k.

The 27-day averages of the daily averages of k are plotted vs. distance from the Sun in Fig. 6. The k plot looks very much like an exaggerated version of the v plot, except that a slight increase of k with increasing distance from the sun might be inferred. If this increase is real, it may be explained on the basis of an increase in the occurrence of acceleration mechanisms in shocks and neutral sheets as the velocity profiles of the streams steepen.

F. Alpha-Proton Ratio

The calculated ratio of alpha-particle density to proton density, n_α/n_p, is almost certainly in error for a spectrum with a large high-energy tail. Therefore, only those spectra for which $|k| \leq 0.3$ (i.e., for which the observed spectrum fit the assumed model within 3 digitization levels) have been included in this study of the ratio n_α/n_p. Of the 24,147 spectra for which a value of k could be calculated, only 1,223 (5.6%) fit the model to this extent. Figure 13 is a plot of the daily value of N_α/N_k vs. the daily-average velocity. N_α is the number of spectra with $|k| \leq 0.3$, and N_k is the number of spectra for which a value of k could be calculated. It is evident that most of the "good-fit" spectra were observed during periods of low plasma velocity. This relation is consistent with the dependence of k on velocity discussed in the previous section.

Figure 14 shows the daily-average values of n_α/n_p plotted vs. the daily-average velocity for those days on

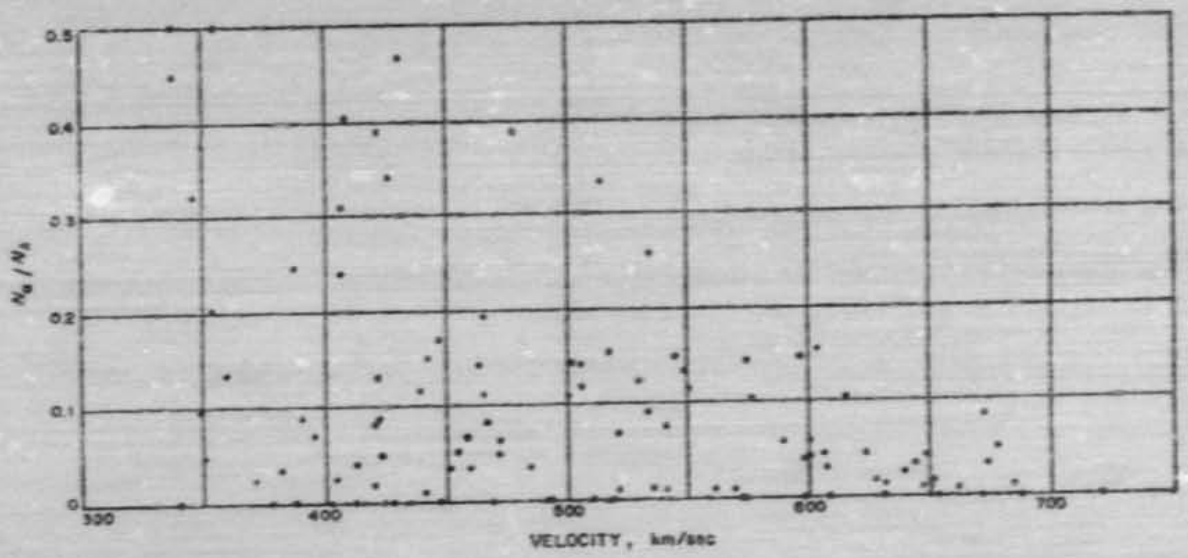

Fig. 13. Three-hr value of N_α/N_h vs. the 3-hr average solar-wind velocity

which $N_\alpha/N_h \geq 0.10$. There was no obvious dependence of n_α/n_p on either the velocity or its time derivative.

The average value and standard deviation of n_α/n_p for all the 1,213 spectra with $|h| \leq 0.3$ were 0.046 ± 0.038.

From a combination of spectroscopic and solar-cosmic-ray observations, Biswas and Fichtel (Ref. 22) determined the solar photospheric ratio of n_α/n_p to be ~ 0.09. The discrepancy between a solar ratio of 0.09 and the ratio observed by *Mariner II* may be due to the fact that the *Mariner II* values of n_α/n_p were heavily biased by low velocity conditions. A steady-state composition on the Sun could be maintained if greater amounts of helium were carried away from the Sun either in high-velocity streams, or in the plasma ejected from solar flares, or as solar cosmic rays.

The calculated values of n_α/n_p are strongly dependent on the underlying assumptions concerning the angle of incidence (assumed radial velocity), the relative alpha-particle and proton temperatures (assumed $T_\alpha = 4T_p$), and the relative alpha-particle and proton velocities (assumed $v_\alpha = v_p$). If a set of assumptions better than those used for this analysis result from future experiments of higher resolution, a recalculation of n_α/n_p from the *Mariner II* data using this set could give results quite different from those presented here.

Figure 15 is a plot of the mean value of n_α/n_p for each solar rotation vs. the logarithm of distance from the Sun. Because of the very large scatter about the mean values, it is not possible to reach any definite conclusions about the radial variation of the ratio n_α/n_p. However, since the general appearance of the spectra did not change between 1.0 and 0.7 AU, the ratio v_α/v_p (assumed = 1.00) could not have changed by as much as 20 or 30%. Because the quantity $(n_\alpha v_\alpha)/(n_p v_p)$ cannot be a function of distance from the Sun (assuming the same, if any, departure from a spherically symmetric flow for the two kinds of ion), it is unlikely that n_α/n_p changed by as much as 20 or 30% between 0.7 and 1.0 AU.

G. Persistence of High-Velocity Streams

The recurrent high-velocity streams discussed in this paper are probably earlier observations of the "quasi-stationary corotating structures" in Wilcox and Ness's analysis (Ref. 23) of *IMP-1* data. Besides magnetic-field data, Wilcox and Ness also presented their analysis of the solar-wind plasma data communicated to them by Lyon and Bridge. The *Mariner II* and *IMP-1* plasma experiments revealed similar relations between plasma velocity and the geomagnetic index K_p, and between plasma velocity and density; the density was a maximum about one day before the velocity peak, a minimum abou

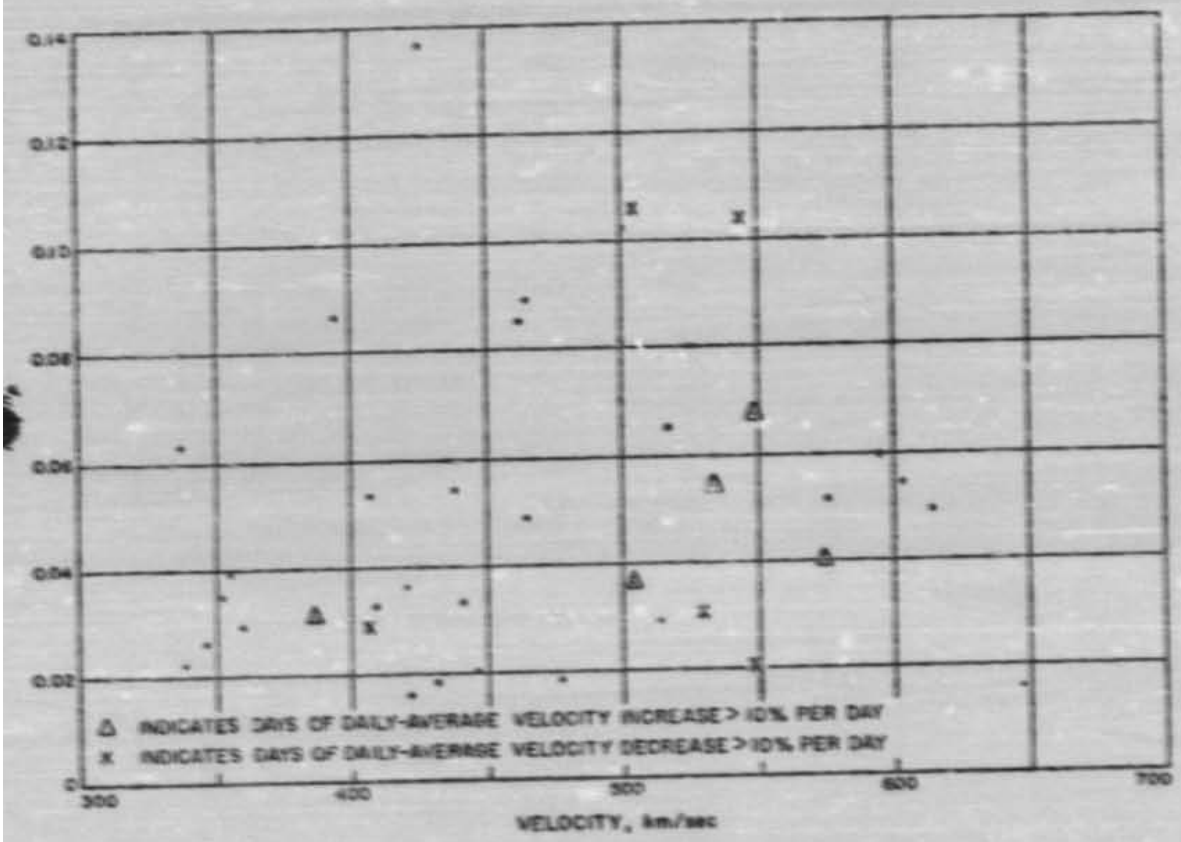

Fig. 14. Daily-average alpha-proton density ratio n_α/n_p vs. daily-average solar-wind velocity for those days on which $N_\alpha/N_p > 0.1$

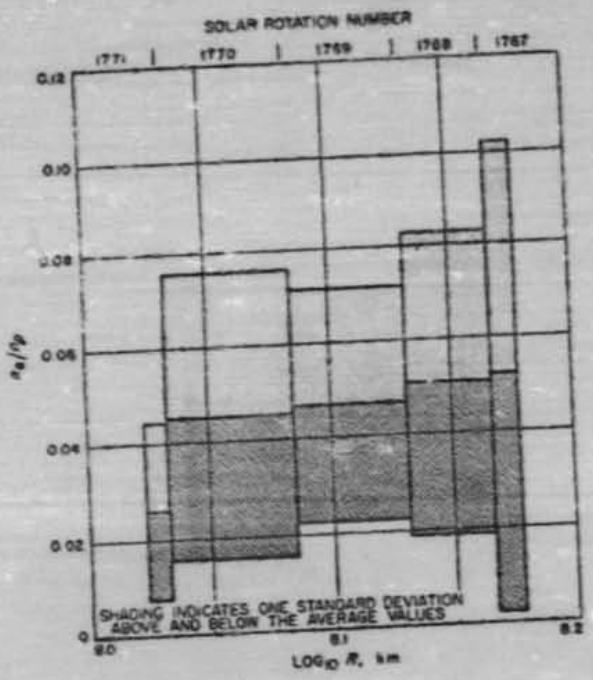

Fig. 15. Mean values of n_α/n_p for each solar rotation vs. the logarithm of distance from the Sun

two days after the velocity peak, and then increased while the velocity continued to decrease.

In particular, geomagnetic data indicate that the very long-lived *M*-region stream occurring roughly from the sixth through the twelfth days of each solar-rotation cycle was probably observed by both *Mariner II* (August–December, 1962) and *IMP-I* (November, 1963–February, 1964). Comparison of Wilcox and Ness's report (Ref. 23) with those of Davis, Smith, Coleman and Sonett (Ref. 20) and Coleman (Ref. 4) indicates that the interplanetary magnetic-field lines in this stream were pointing outward from the Sun during both the *Mariner* and *IMP* observations. Furthermore, Wilcox and Ness (Ref. 23) reported that Fan, Gloeckler, and Simpson's detector on *IMP-I* observed a recurrent counting-rate increase of protons with a few Mev of energy associated with this recurrent structure; Van Allen, Frank and Venkatesan (Ref. 24) reported particle fluxes above the galactic cosmic-ray background within a day of the peak velocity for each of the five appearances of this stream during the *Mariner II* experiment. Some of the particles observed by Van Allen, Frank, and Venkatesan could have been either protons with energy greater than 0.5 Mev, or electrons with energy greater than 40 kev; at other times, the particles could be identified as protons. Thus, although there were obvious changes in the detailed structure of this stream from one solar rotation to the next, many of its basic features were perhaps unchanged over a period of at least 18 months.

The other streams observed by *Mariner II* are probably the same kind of phenomenon as, but not the direct ancestors of the other quasi-stationary structures discussed by Wilcox and Ness (Ref. 23).

REFERENCES

1. Lincoln, J. V., "Solar and Geomagnetic Data," *J. Geophys. Res.*, vol. 67, pp. 5341–5342, 1962; vol. 68, pp. 581–585, 1155–1156, 1767–1768, and 2335–2342, 1963.

2. Neugebauer, M., and Snyder, C. W., "Solar-Wind Measurements Near Venus," *J. Geophys. Res.*, vol. 70, pp. 1587–1591, 1965.

3. Josias, C., and Lawrence, J. L., Jr., *An Instrument for Measurement of Interplanetary Solar Plasma*, Technical Report 32-492, Jet Propulsion Laboratory, Pasadena, Calif., May 1, 1964.

4. Coleman, P. J., Jr., *Irregularities in the Interplanetary Magnetic Field*, Ph.D. thesis, University of California, Los Angeles, Calif., 1966.

REFERENCES (Cont'd)

5. Snyder, C. W., Neugebauer, M., and Rao, U. R., "The Solar Wind Velocity and Its Correlation with Cosmic-Ray Variations and with Solar and Geomagnetic Activity," *J. Geophys. Res.*, vol. 68, pp. 6361–6370, 1963.

6. Snyder, C. W., and Neugebauer, M., "Interplanetary Solar-Wind Measurements by Mariner 2," *Space Res.*, vol. 4, pp. 89–113, 1964.

7. Moor, K., Jr., and Dessler, A. J., "Comment on the Paper by Conway W. Snyder et al., 'The Solar Wind Velocity and Its Correlation with Cosmic-Ray Variations and with Solar and Geomagnetic Activity,'" *J. Geophys. Res.*, vol. 69, p. 2846, 1964.

8. Sonnett, C. P., et al., "Evidence for a Collision-Free Magnetohydrodynamic Shock in Interplanetary Space," *Phys. Rev. Lett.*, vol. 13, pp. 153–156, 1964.

9. Scarf, F. L., *Lecture Notes on Plasma and Space Physics*. ASEE-NASA Summer Faculty Institute, 1965.

10. Sturrock, P. A., and Hartle, R. E., "Two-Fluid Model of the Solar Wind," *Phys. Rev. Lett.*, vol. 16, pp. 628–631, 1966.

11. Scarf, F. L., "The Origin of the Solar Wind," in *The Solar Wind*, pp. 199–212. Edited by R. J. Mackin, Jr., and Marcia Neugebauer. Jet Propulsion Laboratory, Pasadena, Calif. 1966. (Distributed through Pergamon Press, New York.)

12. Parker, E. N., "Dynamics of the Interplanetary Gas and Magnetic Fields," *Astrophys. J.*, vol. 128, pp. 664–676, 1958.

13. Parker, E. N., *Interplanetary Dynamical Processes*. Interscience Publishers, New York, 1963.

14. Davis, L., Jr., "Models of the Interplanetary Fields and Plasma Flow," in *The Solar Wind*, pp. 147–157. Edited by R. J. Mackin, Jr., and Marcia Neugebauer. Jet Propulsion Laboratory, Pasadena, Calif., 1966. (Distributed through Pergamon Press, New York.)

15. Neugebauer, M., and Snyder, C. W., "Mariner-2 Measurements of the Solar Wind," in *The Solar Wind*, pp. 3–21. Edited by R. J. Mackin, Jr., and Marcia Neugebauer. Jet Propulsion Laboratory, Pasadena, Calif., 1966. (Distributed through Pergamon Press, New York.)

16. Lyon, E. F., "Explorer-18 Plasma Measurements," in *The Solar Wind*, pp. 295–314. Edited by R. J. Mackin, Jr., and Marcia Neugebauer. Jet Propulsion Laboratory, Pasadena, Calif., 1966. (Distributed through Pergamon Press, New York.)

17. Spitzer, L., Jr., *Physics of Fully Ionized Gases*. Second Edition. Interscience Publishers, New York, 1962.

18. Parker, E. N., "Kinetic Properties of Interplanetary Matter," *Planetary Space Sci.*, vol. 9, pp. 461–475, 1962.

19. Dessler, A. J., and Fejer, J. A., "Interpretation of K_p Index and M-Region Geomagnetic Storms," *Planetary Space Sci.*, vol. 11, pp. 505–511, 1963.

20. Davis, L., Jr., et al., "Interplanetary Magnetic Measurements," in *The Solar Wind*, pp. 25–50. Edited by R. J. Mackin, Jr., and Marcia Neugebauer. Jet Propulsion Laboratory, Pasadena, Calif., 1966. (Distributed through Pergamon Press, New York.)

REFERENCES (Cont'd)

21. Wolfe, J. H., Silva, R. W., and Myers, M. A., "Preliminary Results from the Ames Research Center Plasma Probe Observations of the Solar-Wind–Geomagnetic Field Interaction Region on Imp-II and OGO-I," Space Research VI (to be published).

22. Biswas, S., and Fichtel, C. E., "Nuclear Composition and Rigidity Spectra of Solar Cosmic Rays," Astrophys. J., vol. 139, pp. 941–950, 1964.

23. Wilcox, J. M., and Ness, N. F., "Quasi-Stationary Corotating Structure in the Interplanetary Medium," J. Geophys. Res., vol. 70, pp. 5793–5805, 1965.

24. Van Allen, J. A., Frank, L. A., and Venkatesan, D., "Small Solar Cosmic-Ray Events Observed with Mariner 2," Trans. Am. Geophys. Union, vol. 45, p. 80, 1964.

APPENDIX A

Method of Calculation of Plasma Parameters from Measured Spectra

I. VELOCITY AND TEMPERATURE

For a given spectrum, the peak channel, m, was usually the channel in which the largest current was observed. However, there were two exceptions to this general rule. (1) Because of the relatively wide spacing of the non-overlapping E/Q windows, the channel nearest the alpha-particle peak occasionally had a larger measured current than did any of the proton channels. Such occurrences were fairly obvious, and the appropriate proton channel could be easily selected as the peak channel. (2) If the actual proton peak was approximately midway between two adjacent spectrometer channels, these two channels had almost equal currents. When the currents in the two channels were within one digitization level (i.e., within a factor of $10^{0.1}$) of being equal, the channel at the lower value of E/Q was chosen to be the peak channel.

Let I_m denote the current in the peak channel, while I_{m-1} is the current in the adjacent channel at a lower value of E/Q. Similarly, I_{m+1} is the current in the channel just above the peak channel. The quantities R and Q are defined as follows:

$$R = \log_{10}(I_m/I_{m-1}) \tag{A-1}$$

$$Q = \log_{10}(I_m/I_{m+1}) \tag{A-2}$$

Figure A-1 shows the relation between R, Q, ν, and θ for an isotropic Maxwell-Boltzmann distribution (in a reference frame moving radially away from the Sun with velocity v) for a single type of ion, where $\nu = v/v_m$ = plasma bulk velocity relative to the velocity at the center of the peak channel, and $\theta = 2kT/M_p v_m^2$. The dotted and lined areas in Fig. A-1 show the range of values of R and Q that correspond to selected values of ν and θ, respectively, for a large range of values of angle of incidence.

The straight lines of constant ν and constant θ in Fig. A-1 represent the following convenient set of approximations:

1. The average logarithmic value of the spacing of the channels was selected to make Fig. A-1 independent of the value of m.

2. The lines of constant ν and constant θ were assumed to be independent of the angle between the normal to the detector aperture and the velocity vector of the plasma bulk motion.

3. The lines of constant θ can be represented by the equation:

$$\theta = 0.03228\,(R + 0.028Q)^{-1.366}. \tag{A-3}$$

4. The lines of constant ν can be represented by the equation:

$$g(\nu) = (R - 0.3)/(Q + 0.3), \tag{A-4}$$

where the function $g(\nu)$ is shown in Fig. A-2.

The size of the errors in ν and θ resulting from the use of the approximations given in listings 2, 3, and 4 above can be estimated from the differences between the straight lines and the shaded areas in Fig. A-1. Each of these four approximations can be justified on the basis that errors arising from their use are usually less than, or of the same order as the uncertainties arising from the digitization of the current measurements. The effects of these quantization uncertainties are discussed in more detail in Appendix B.

The parameter P is defined by

$$P = \log_{10}(I_m/I_{m+1}) \tag{A-5}$$

and a set of relations similar to Eqs. (A-3) and (A-4) can be found for $\theta(R,P)$ and $\nu(R,P)$. By elimination of P between $\theta(R,Q)$ and $\theta(R,P)$, the following equation is obtained for the expected relation between R, Q, and P for a Maxwell-Boltzmann distribution of a single type of ion:

$$P = 0.66\,(R + 0.028Q)^{-0.366} - 0.783R \tag{A-6}$$

The calculation of ν and θ for a given spectrum proceeded as follows: for the first iteration, it was assumed that only protons contributed to the currents in channels $m-1$, m, and $m+1$; the measured values of I_{m-1}, I_m, and I_{m+1} were used to calculate R and Q from

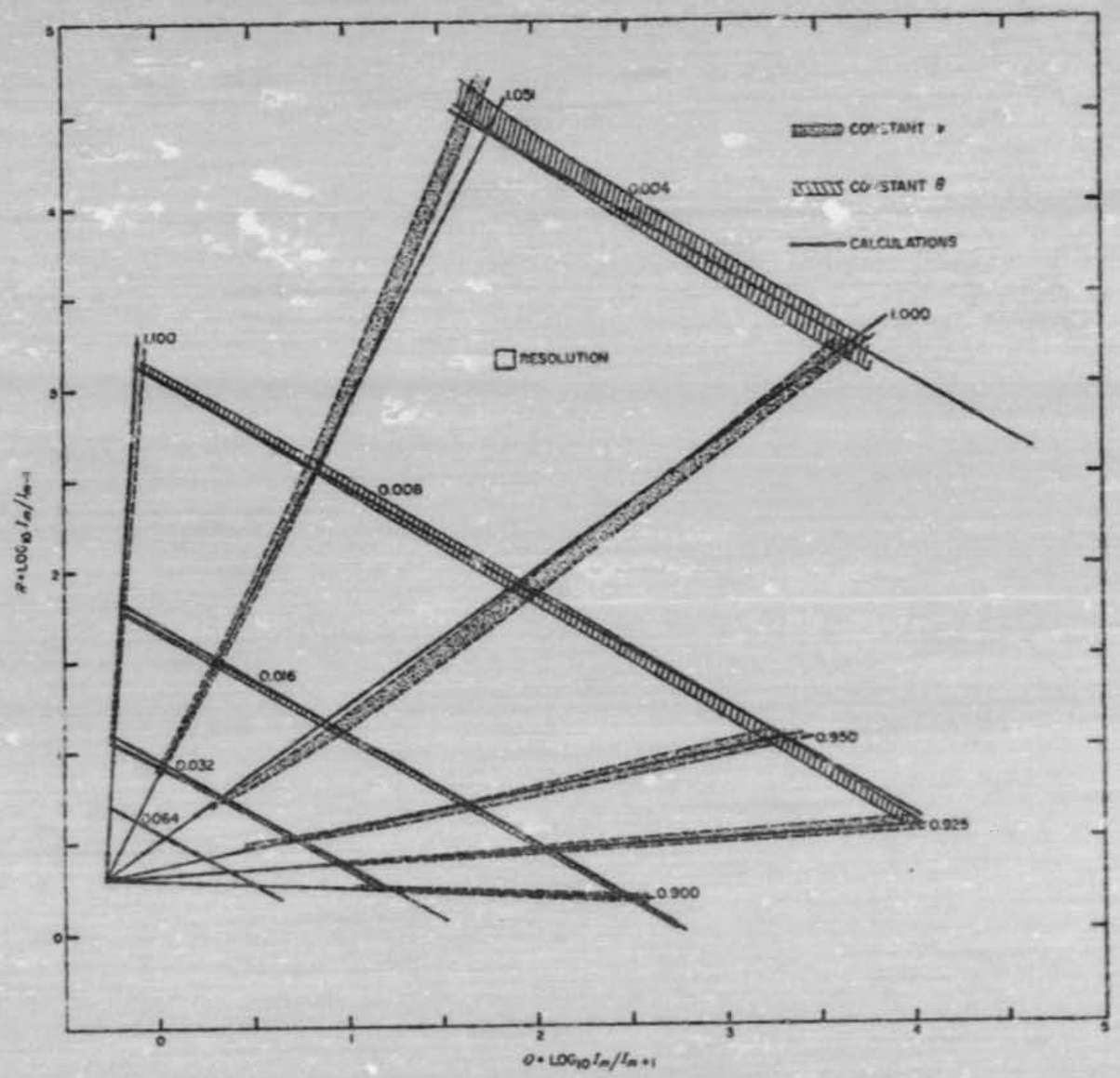

Fig. A-1. Contours of constant ν and constant θ as a function of the currents in channels $m-1$, m, and $m+1$ for a single type of ion

Eqs. (A-1) and (A-2); R and Q were used in Eqs. (A-3) and (A-4) to obtain first approximations to ν and θ; P was determined from Eq. (A-6). Then, according to Eq. (A-5), the proton contribution to the current in channel $m+2$ was $I_m \times 10^{-P}$; the remainder of the current in channel $m+2$ was assumed due to alpha particles.

If $\nu \geq 0.947$, and if the alpha particles had the same bulk velocity as the protons, then the alpha-particle peak would have been nearest channel $m+2$; if the alpha-particles had the same thermal velocity as the protons, then the value of θ would have been the same for the two kinds of ions. If $r = \log_{10}(I^o_{m-1}/I^o_{m+1})$ and

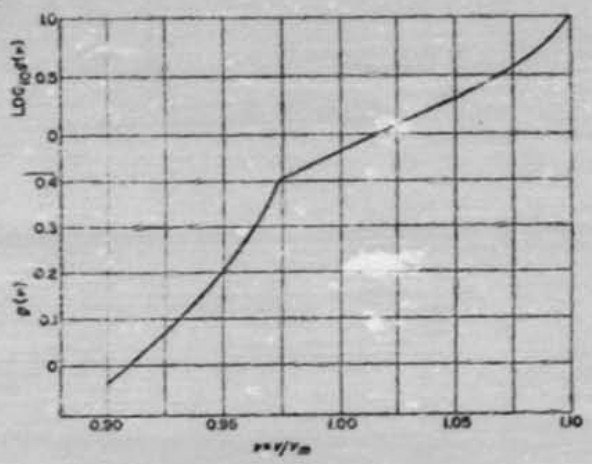

Fig. A-2. The function $g(v)$ vs. v

$Q = \log_{10}(I^a_{m-1}/I^a_{m+1})$, where the superscript a refers to the alpha-particle contribution, then, from Eq. (A-3), the assumption that $\theta_a = \theta_p$ can be written in the form:

$$r + 0.608q = R + 0.608Q, \qquad \text{(A-7)}$$

while Eq. (A-4) gives

$$g(0.950v) = (r - 0.3)/(q + 0.3) \qquad \text{(A-8)}$$

The factor 0.950 in Eq. (A-8) is the ratio of the proton velocity at the center of channel m to the alpha-particle velocity at the center of channel $m+2$. Elimination of q from Eqs. (A-7) and (A-8) gives

$$r = \frac{g(0.950v)\,(R + 0.608Q + 0.1824) + 0.1824}{0.608 + g(0.950v)} \qquad \text{(A-9)}$$

The alpha-particle contribution to the current in channel $m+1$ is then given by

$$I^a_{m-1} = I^2_{m+2} \times 10^{-r} = 10^{-r}(I_{m+2} - I_m \times 10^{-p}) \qquad \text{(A-10)}$$

A correction can now be made to the assumption that all protons contributed to the current in channel $m+1$, and the whole calculation is repeated with a new value of Q:

$$Q' = \log_{10}[I_m/(I_{m+1} - I^a_{m+1})]$$

The iteration is considered to be sufficiently converged when successive values of Q agree within a factor of $10^{\pm 0.03}$ (i.e., within 0.3 digitization levels). For some of the *Mariner II* spectra, the iteration does not converge before I^a_{m+1} becomes greater than I_{m+1}. For many of these spectra, however, convergence can be obtained if one assumes that the protons and alpha particles had equal temperatures rather than equal thermal velocities. In this case, $\theta_a = \theta_p/4$, and the procedure for finding v and θ is similar to that outlined above.

If $v < 0.947$, the equations used must be modified slightly because the alpha-particle peak is nearer channel $m+1$ than channel $m+2$. Specifically, for the equal-thermal-velocity model, r is eliminated between Eq. (A-7) and an equation similar to Eq. (A-8) to obtain

$$q = \log_{10}(I^a_{m+1}/I^a_{m-1})$$

$$q = \frac{R + 0.608Q - 0.3 - 0.3g(1.159v)}{0.608 + g(1.159v)} \qquad \text{(A-11)}$$

where, in this case, 1.159 is the ratio $v_{m+2}/v_{m+1,a}$. Then the correction to be subtracted from I_{m+1} is

$$I^a_{m+1} = I^a_{m+2} \times 10^q = (I_{m+2} - I_m \times 10^{-p})10^q \qquad \text{(A-12)}$$

The velocity must be corrected for the radial component (v_r) of the spacecraft's velocity to obtain the plasma velocity relative to the sun, v_s:

$$v_s = v\,v_m + v_r \qquad \text{(A-13)}$$

During the course of the *Mariner II* mission, v_r changed from -1.2 to -6.3 to $+0.7$ km/sec.

The proton temperature is given by:

$$T_p(^\circ\mathrm{K}) = 60.57\,v^2 v_m^2 \theta_p \qquad \text{(A-14)}$$

for v_m in units of km/sec.

II. PROTON DENSITY

Although the shape of the observed spectrum, and therefore the calculated values of the plasma's velocity and temperature, is relatively insensitive to the angle of incidence of the plasma flow, the absolute values of the measured currents, and therefore of both the plasma density and flux, are very sensitive to direction. If we assume that the plasma flows radially away from the Sun, then the angle of incidence on the spectrometer aperture is a known function of the spacecraft's velocity, of the spacecraft's orientation in space, and of the plasma velocity calculated in the previous section.

Since the spectrometer's aperture always faced the Sun, a coordinate system is defined in which the z axis is radially away from the Sun and parallel to the spectrometer normal. The x and y axes are chosen so that the xz plane is the analysis plane (Fig. A-3). Then, according to the model chosen (i.e., an isotropic Maxwell-Boltzmann distribution at temperature T in a coordinate system moving radially away from the Sun with velocity v_0), the current measured in channel j is related to the properties of the plasma, to the spacecraft's trajectory, and to the spectrometer's transmission function by the equation:

$$I_j = (QA)\int\int\int N(v_x, v_z)\,\epsilon(v_x, v_z)\,(v + v_0) \left(\frac{M}{2\pi kT}\right)^{3/2} \exp\left[-M\left(v_x^2 + v_y^2 + v_z^2\right)/2kT\right] dv_x\,dv_y\,dv_z \qquad (A\text{-}15)$$

where Q is the charge on each ion (considering, now, only a single type of ion), A is the aperture area (510 cm^2), N is the transmission function (or transparency factor) in the yz plane, and ϵ is the transmission function in the xz plane.

The transverse transmission function N can be written as:

$$N = 0 \qquad \text{for } v_{y_0} \le -v_{y_0} - \frac{v + v_0}{3.69}$$

$$N = 1 + \frac{3.69\,(v_{y_0} + v_0)}{v + v_0} \qquad \text{for } -v_{y_0} - \frac{v + v_0}{3.69} \le v_{y_0} \le -v_{y_0}$$

$$N = 1 - \frac{3.69\,(v_{y_0} + v_0)}{v + v_0} \qquad \text{for } -v_{y_0} \le v_{y_0} \le -v_{y_0} + \frac{v + v_0}{3.69}$$

$$N = 0 \qquad \text{for } -v_{y_0} + \frac{v + v_0}{3.69} \le v_{y_0}$$

where v_{y_0} is the y component of the spacecraft's velocity v_0.

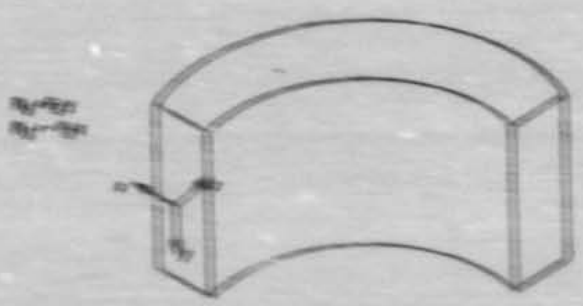

Fig. A-3. Coordinate system used in data analysis

The variation of ϵ with energy and angle of incidence in the analysis plane is shown in Fig. 3. The w_y integration in Eq. (A-15) can be done analytically, and the other two integrations have been done numerically to obtain a simplified form for Eq. (A-15):

$$I_j = Q A n_0 v_{xj} f(\phi, s, \theta, \epsilon) \qquad \text{(A-16)}$$

where ϕ is the roll angle, given in Table 1, and $s = v_{sw}/v_{xj}$, the component of the spacecraft's velocity in the xy plane relative to the ion velocity at the center of channel j.

The function $f(\phi, s, \theta, \epsilon)$ is illustrated in Fig. A-4 for the case $\phi = 30°$, $s = 0.0755$, and in Fig. A-5 for the case $\phi = 30°$, $\theta = 0.008$. Since the dimensions of the analyzer were chosen so that the angular apertures in the xz and the yz planes were approximately equal, $f(\phi, s, \theta, \epsilon)$ is not very sensitive to variations in ϕ. In fact, no correlation has been found between the calculated plasma properties and the angle ϕ during the six days that the spacecraft rolled about the probe–Sun vector. Figure A-1 and Eqs. (A-3) and (A-4) were derived by using sets of figures such as Figs. A-4 and A-5.

The proton density n_p is found from the measured spectra by rewriting Eq. (A-16) in the form:

$$n_p = \frac{I_m \times 10^{-6}}{\delta e\, v_{xm} f(\phi, s, \theta, \epsilon)} \ (\mathrm{cm}^{-3}) \qquad \text{(A-17)}$$

for I_m the current in the peak channel, in amp, and v_m in km/sec. The value of $f(\phi, s, \theta, \epsilon)$ was computed by first rounding off the actual value of ϕ to the nearest 15° and then performing a three-dimensional, logarithmic interpolation for the dependent variables s, θ, and ϵ.

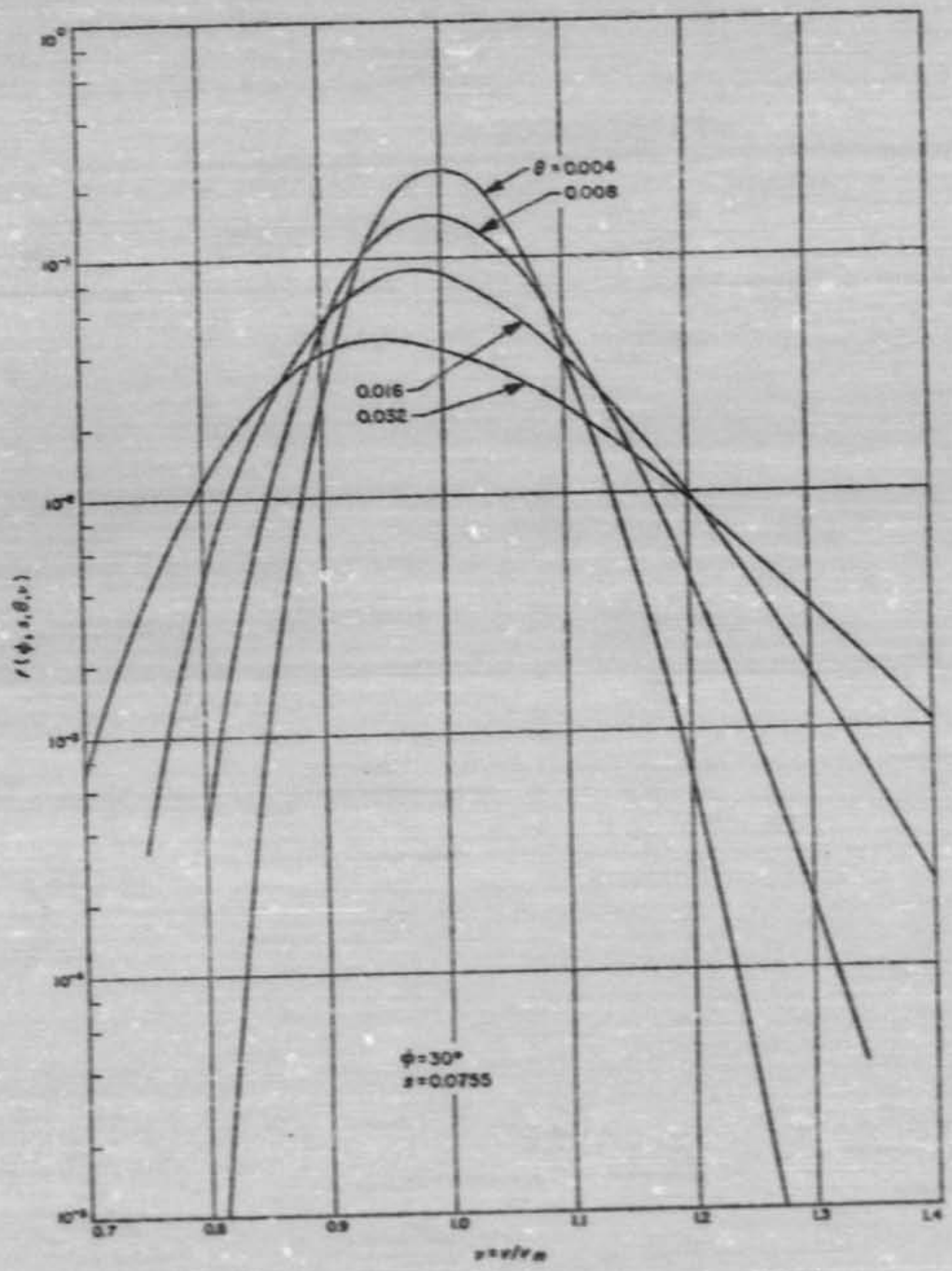

Fig. A-4. $f(\phi, s, \beta, \nu)$ vs. ν as a function of β for $\phi = 30°$ and $s = 0.0755$

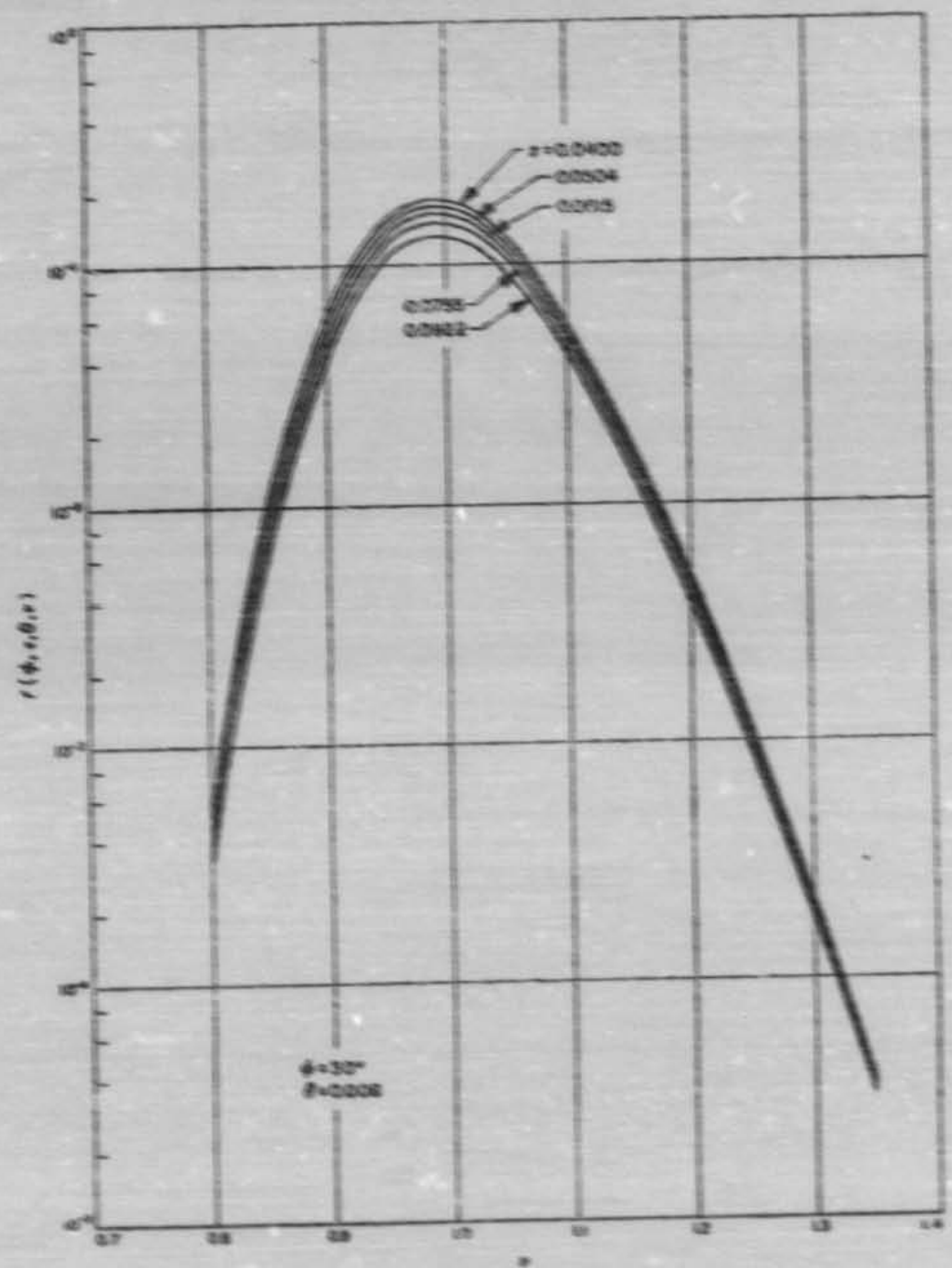

Fig. A-5. $f(\phi, \varepsilon, \theta, \rho)$ vs ρ vs ε function of ε for $\phi = 30°$ and $\beta = 0.008$

III. ALPHA-PROTON DENSITY RATIO

Equation (A-16) can be written for the alpha-particle current in channel $m+2$, the proton current in channel $m+1$, and the proton current (or the total current) in channel m, respectively, as:

$$I^{\alpha}_{m+2} = 2Q\Delta\cos_{\alpha}f(\phi, 0.950\pi, \theta, 0.950\nu)$$

$$I^{p}_{m+1} = Q\Delta\cos_{p}f(\phi, 0.674\pi, \theta, 0.674\nu) = I_{m+1} - I^{\alpha}_{m+2}$$

$$I_{m} = Q\Delta\cos_{p}f(\phi, \pi, \theta, \nu)$$

These equations can be combined to yield:

$$n_{\alpha}/n_{p} = \frac{f(\phi, \pi, \theta, \nu)\,(I_{m+1}/I_{m}) - f(\phi, 0.674\pi, \theta, 0.674\nu)}{2f(\phi, 0.950\pi, \theta, 0.950\nu)} \qquad \text{(A-18)}$$

Equation (A-18) is for the equal-thermal-velocity model in which the value of θ is the same for the protons and alpha particles. If a spectrum fits an equal-temperature model better, then equation Eq. (A-18) should be modified to give:

$$n_{\alpha}/n_{p} = \frac{f(\phi, \pi, \theta, \nu)\,(I_{m+1}/I_{m}) - f(\phi, 0.674\pi, \theta, 0.674\nu)}{2f(\phi, 0.950\pi, \theta/4, 0.950\nu)} \qquad \text{(A-19)}$$

where θ refers to the value for protons.

IV. SUPERTHERMAL-PARTICLE PARAMETER

The parameter h was defined as:

$$h = \log_{10}\frac{I_{m+2}\,(\text{measured})}{I_{m+2}\,(\text{calculated})}$$

It can be assumed that the proton contribution to the current in channel $m+3$ is negligible compared to the alpha-particle contribution.

If $\nu \geq 0.947$,

$$I_{m+2}\,(\text{calculated}) = I^{\alpha}_{m+2}\,10^{q} = (I_{m+2} - I_{m}10^{p})\,10^{q}$$

where, for the equal-thermal-velocity model,

$$q = \frac{(R + 0.608Q) - 0.3g(0.950\nu) - 0.3}{g(2.850\nu) + 0.608}$$

whereas, for the equal-temperature model,

$$q = \frac{3.193(R + 0.608Q) - 0.3g(0.950\nu) - 0.3}{g(0.950\nu) + 0.608}$$

If $\nu < 0.947$,

$$I_{m+2}\,(\text{calculated}) = (I_{m+2} - I_{m}10^{p})10^{q}$$

where, for the equal-thermal-velocity model,

$$q = \frac{R + 0.503Q - 0.3g(1.139\nu) - 0.3}{g(1.139\nu) + 0.608}$$

$$p = 0.44(R + 0.608Q)^{1.305} - 4.762(R + 0.608Q) + 2.895q$$

whereas, for the equal-thermal-velocity model,

$$q = \frac{3.193(R + 0.608Q) - 0.3g(1.139\nu) - 0.3}{g(1.139\nu) + 0.608}$$

$$p = 19.73(R + 0.608Q)^{1.305} - 15.51(R + 0.608Q) + 2.895q$$

The final, iterated values of ν and Q are used to calculate q and p from these equations.

APPENDIX B

Accuracy of Calculated Parameters

The principal approximations used in fitting the *Mariner II* plasma data to the chosen models were:

1. Digitization of current measurements: this is probably the most important source of uncertainty in the calculated parameters. The velocity depends on the ratio $(R - 0.3)/(Q + 0.3)$; R and Q are defined in Appendix A. For all the observed combinations of R and Q, the largest possible uncertainty in v is $\Delta v/v = 0.02$. For a typical spectrum with $\theta_p = 0.01$, $\Delta v/v \leq 0.007$. The digitization errors in the parameters θ_p, n_p, and n_α/n_p are shown as functions of θ_p in Fig. B-1. The curves in this figure correspond to the largest possible fractional uncertainty for most of the observed spectra for the equal-thermal-velocity model; it is possible, however, to find spectra for which certain combinations of one-half-step perturbations make the difference, especially at large values of θ_p, between convergence or lack of convergence of the iterative calculation. Because the fractional error in velocity is small, $\Delta T_p/T_p \simeq \Delta\theta_p/\theta_p$, $\Delta(n_p m_p v^2)/(n_p m_p v^2) \simeq \Delta n_p/n_p$, etc.

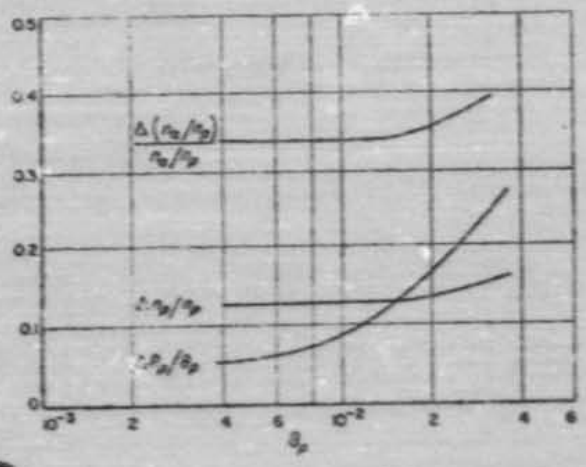

Fig. B-1. The largest possible fractional uncertainties in θ_p, n_p, and n_α/n_p arising from the 0.1-decade digitization of the current measurements

2. Spacing of E/Q channels: the ratio v_{n+1}/v_n ranged from 1.207 to 1.228. A value of 1.220 was assumed for this analysis, resulting in velocity errors of 1% or less. The resultant percentage errors in θ_p, n_p, n_α/n_p, etc., are much smaller than the percentage uncertainties due to the digitization of the current measurements.

3. Edge effects, scattering of ions, etc., neglected in calculation of the transmission function: the theoretical transmission function used for this analysis (Fig. 3) was based on the assumption of a purely radial electric field with absorption or neutralization of all ions that hit the analyzer electrodes. Figure B-2 compares the curves of constant ν and constant θ of this assumed transmission function with similar curves for the extreme case of a square transmission function for which:

$$\delta = 1 \text{ if } -0.15 \leq \frac{w_2}{v_n} \leq +0.15; \text{ otherwise, } \delta = 0$$

$$\epsilon = \alpha\beta, \text{ where}$$

$$\alpha = 1 \text{ if } -0.15 \leq \frac{w_2}{v_n} \leq +0.15; \text{ otherwise, } \alpha = 0$$

$$\beta = 1 \text{ if } 0.95 \leq \frac{v + w_2}{v_n} \leq 1.05; \text{ otherwise, } \beta = 0$$

For an average spectrum with $\theta_p \simeq 0.01$, the error in the calculated values of ν and θ_p arising from the lack of a precise knowledge of the resolution function is probably no greater than the uncertainty arising from the digitization of the current measurements.

4. Spacecraft potential: in interplanetary space, the spacecraft potential is probably between zero and a few volts negative. A 10-volt potential would amount to a 2.5% shift in the effective velocity of channel 1, and a 0.06% shift in the velocity of channel 10. If the spacecraft had had a very large potential of either sign, the alpha-particle peak would

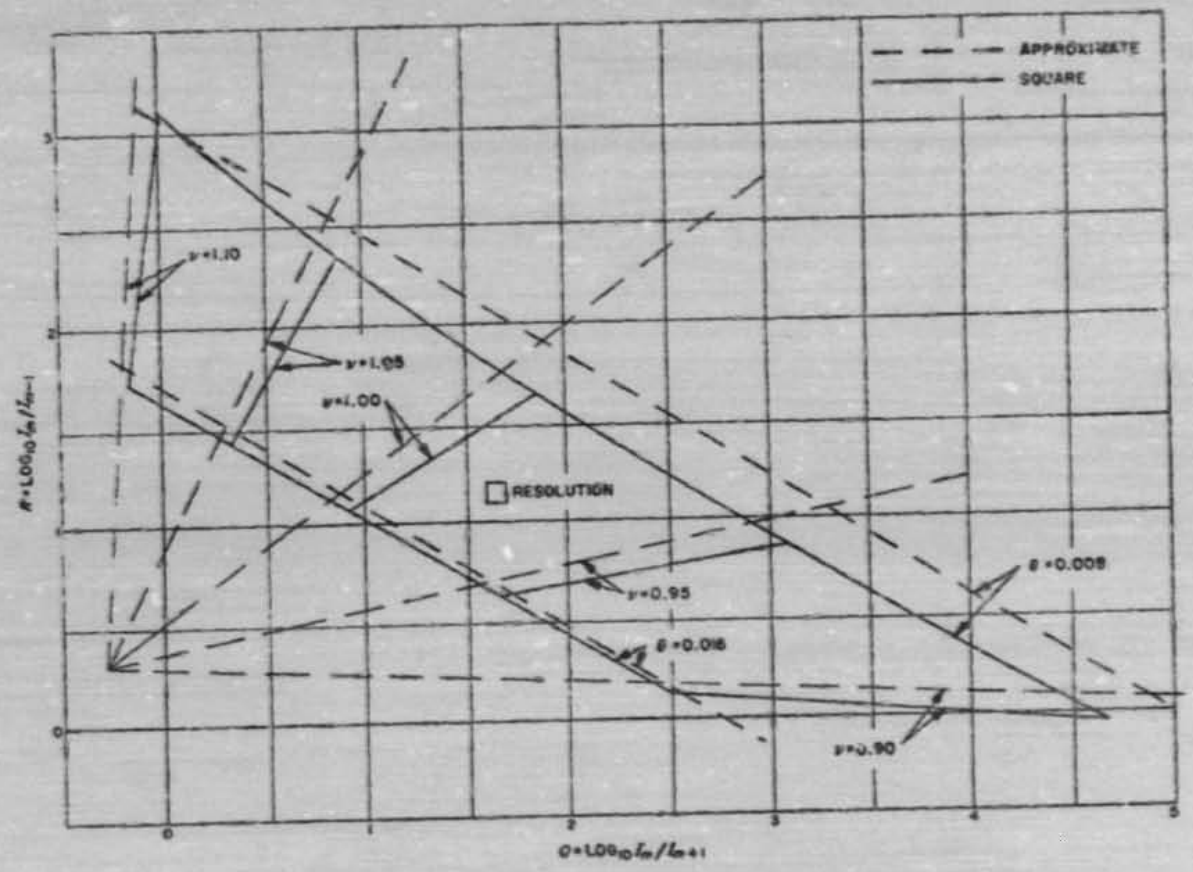

Fig. B-2. Contours of constant ν and constant θ as a function of the currents in channels $m-1$, m, and $m+1$ for an approximate and a square transmission function

not have been observed at a value of E/Q approximately twice that of the proton peak; spacecraft potential, therefore, was neglected.

5. Other approximations used, all of which gave errors less than the digitization uncertainties:

   a. ν and θ assumed independent of ϕ and z.

   b. ν and θ in simple relation to R, Q, and P.

   c. Quantization, rather than interpolation of ϕ, in calculation of n_p.

   d. Convergence of iteration considered satisfied when successive values of Q change by ≤ 0.03.

ACKNOWLEDGEMENT

The data analyzed in this Report could not have been obtained without the extraordinary efforts of C. Josias, J. Lawrence, Jr., and H. R. Mertz in designing, constructing, and testing the electronic equipment. We are also indebted to Kurt Heftman, Truman Cox, Patricia Conklin, and Margot Masin for their help in data handling and reduction.

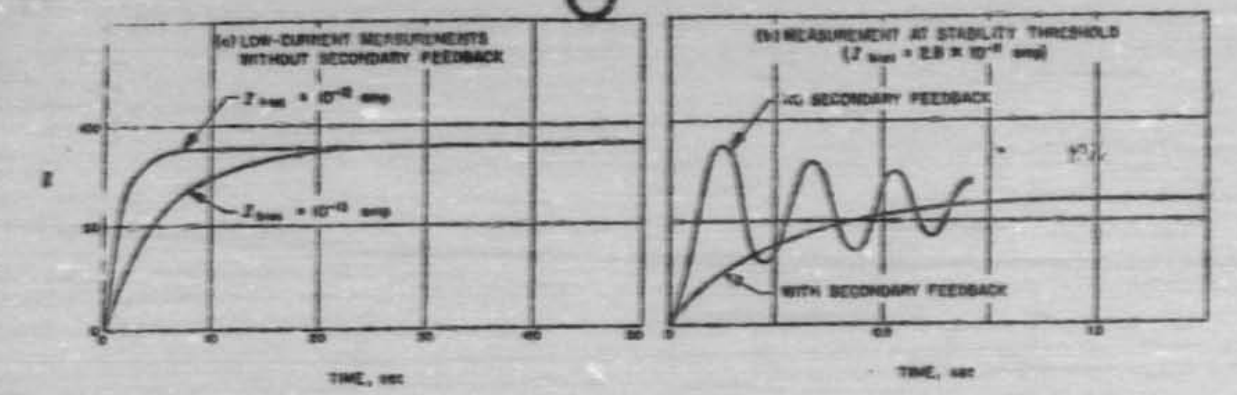

Fig. 37. Closed-loop transient response

The peaks are removable, however, by direct coupling of the secondary feedback. This is considered a generally advisable procedure for this configuration providing that capacitor C_s has a sufficiently large leakage resistance.

Closed-loop transient responses (Fig. 37) were recorded by changing the sine-wave signal used in the previous closed-loop tests to a square wave. Care was taken to keep the signal amplitude down to swings of not more than a quarter of a decade from quiescent levels, lest nonlinearities in the feedback tube mask the true small-signal performance.

Although this electrometer is fast enough for *Mariner 2* sampling rates (one sample per 17 sec), the interelectrode capacitance of the feedback element may make this system too sluggish for other applications requiring faster low-current response. Speed-of-response capabilities for this amplifier may be put in a better perspective, however, by inspecting its performance with a more universally used feedback component such as a carbon resistor. A current threshold of 10^{-13} amp, for example, may be obtained with a feedback resistor of 10^{11} ohms. If gain crossover for this new system were comparable to the values in Table 7 ($\tau_{gc} = 0.018$ sec), the closed-loop speed of response would reflect the lower time constant of the new feedback element. Assuming a distributed capacitance of 0.5 pf across the resistor, the feedback time constant τ_s becomes 0.05 sec. This value of τ_s, indeed, becomes the e^{-1} response time for the electrometer, because τ_{gc} is small enough to not affect the composite response. If the filter-induced rate limit for the electrometer described in this Report (100 v/sec) were applied to this hypothetical case, rate limiting would occur for input step currents above 5×10^{-11} amp. A maximum-range signal of about 10 v ($I_{in} = 10^{-12}$ amp) would therefore require about 100 msec to reach 90% of full amplitude.

For the case of a particular feedback resistor, electrometer transient responses to signal currents below rate-limit level may be considered uniformly linear. What makes quantitative comparison of the log diode system difficult is that dominant time constants for log feedback are based upon bias currents and not necessarily on absolute values of transient current. It is also very possible in actual spectrometer applications that the log diode system will come to rest somewhere between the lower end of the useful diode characteristic and the discriminator threshold. Tube capacitance must then be charged before the tube becomes conductive, whereas resistive feedback provides a constant conductance and a fixed starting point.

In applications requiring the speed of response and zero stability afforded by a feedback resistor, one may then tailor the loop transmission characteristic to the specific requirements of the resistor. The technique of secondary damping feedback described in this Report may then be applied, when needed, in a more efficient manner by the inclusion of a fixed damping factor (β_s). In a similar fashion, commutated feedback resistors may also be efficiently used with synchronous switching of discrete optimized feedback networks.

D. Dynamic Reed Capacitor Development

Dynamic capacitors of the type used in the *Ranger* and *Mariner* solar plasma instruments (Fig. 38 and 39) originated over 15 years ago (Ref. 16), and have been employed in various commercial electrometers. Since the

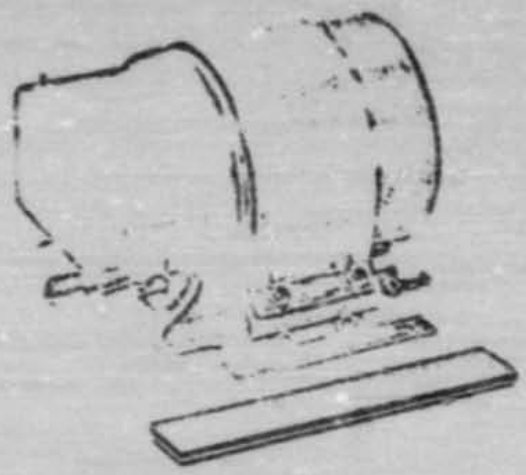

Fig. 38. Dynamic capacitor on mounting base

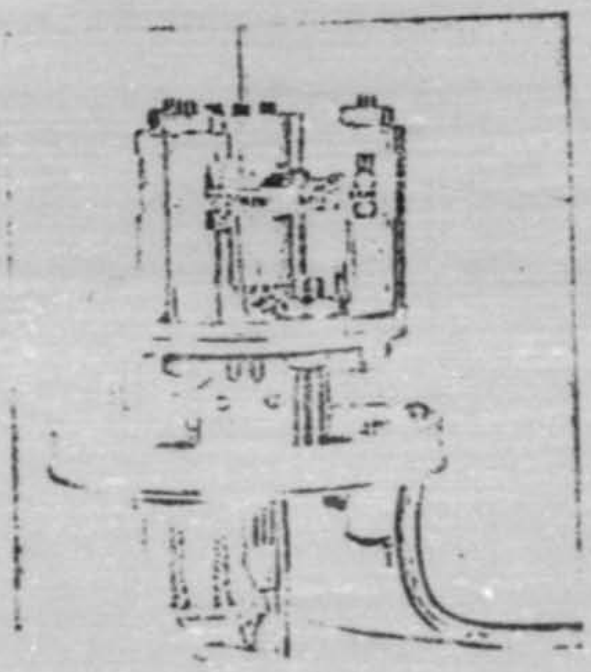

Fig. 39. Uncased dynamic capacitor

instrument demanded a lightweight, low-power device that could withstand the rigorous vibrational and thermal environment imposed by the spacecraft, a special design was required. In January 1960, a development contract for the vibrating reed capacitor was let to the Applied Physics Corporation of Monrovia, California.

Evaluation of the first six prototypes and communication with Applied Physics resulted in the following target specifications:

1. Reed resonance at 25°C: 2,398 ± 8 cps.
2. Resonant frequency shift between 0 and 70°C: 15 cps max.
3. Conversion efficiency at 2,400 cps and 25°C: 8 to 10%.
4. Resonant Q: 150 max.
5. Drive voltage at 2,400 cps: 6.8 v rms.
6. Drive coil power: 75 mw max.
7. Reed-to-anvil rest capacitance: C_s = 70 pf max.
8. Coupling capacitance: 50 ± 3 pf.
9. Contact potential: 0 ± 50 mv dc max.
10. Temperature coefficient of contact potential: 70 μv/°C max.
11. Weight: 0.6 lb max.
12. Unit evacuation pressure: $< 10^{-4}$ Torr.
13. Input resistance: $> 10^{14}$ ohms.

The choice of reed resonance at approximately 2,400 cps was based on (1) the ability to drive the reed directly from the 2,400-cps spacecraft supply and (2) the small size of the reed, which resulted in an over-all structure of minimum dimensions. The values of rest and coupling capacitance were influenced by such factors as conversion efficiency, loop transient response, and the source impedance presented to the subsequent transistor electronics.

The over-all structure of the reed capacitor suggested a cylindrical or can-type enclosure. The can was evacuated in order to obtain high compliance of the reed with a minimum expenditure of drive power for a given conversion efficiency. In addition, since anticipated uses of the converter would require extended periods of operation (one to two years) in the vacuum of space, and since gradual loss of an atmosphere of inert gas in a modulator would catastrophically alter the reed characteristics, the evacuated can appeared doubly attractive.

However, as development progressed, the effect of the evacuated can on the contact potential specification

became painfully obvious. Temperature cycling of the evacuated modulator caused outgassing of most of the materials inside the device and resulted in contamination of the reed and anvil, with an accompanying increase in contact potential and its thermal coefficient. This problem was ultimately solved by high-temperature vacuum annealing of most components internal to the can and by elimination of all internal organic materials and internal solder connections.

Early in the program, the need for a reed-tracking oscillator was considered; that is, a device that would sense the drift in reed resonant frequency due to age and temperature change and would synchronously drive the phase-sensitive demodulator in the electrometer amplifier. The behavior of the capacitor resonant characteristic vs. temperature for the early prototypes (Fig. 40) was monitored, and several units were installed in a breadboard electrometer. Loop-gain and phase-margin tests were performed vs. temperature in this test fixture, with both the reed and the demodulator driven from a fixed 2.4-kc signal (see the discussion on the demodulator). Analysis of these data indicated that the change in amplifier loop gain, owing to changes in demodulator efficiency (caused by phase shift between the reed output signal and the demodulator drive signal), would not seriously degrade the amplifier performance. Because of this fact and the limited period for development of the instrument, it was decided in September 1960 to drop the tracking oscillator approach and start production on units to be driven at 2.4 kc, a point slightly above the natural resonant frequency. By operating the reed in this manner with the specified Q and the allowable resonant frequency drift, it appeared that the amplifier loop-gain stability requirements would be reasonably easy to satisfy. Troubles developed shortly thereafter when attempts at simultaneous control of parameters such as resonant frequency, frequency drift, mechanical Q, and conversion efficiency led to a poor yield of production modulators. To meet the demands of the *Ranger 1* and *2* system schedules, it then became a necessary part of the reed acceptance procedure to run each modulator in an electrometer breadboard and select the optimum phase compensation network for the demodulator for that particular assembly. Since the production reed characteristics were not uniform, this optimum phase shift network had to be selected by examining the gain and carrier phase characteristics of the electrometer over the operating temperature range (−10 to +80°C) and selecting a compromise value which would ensure electrometer stability at all temperatures.

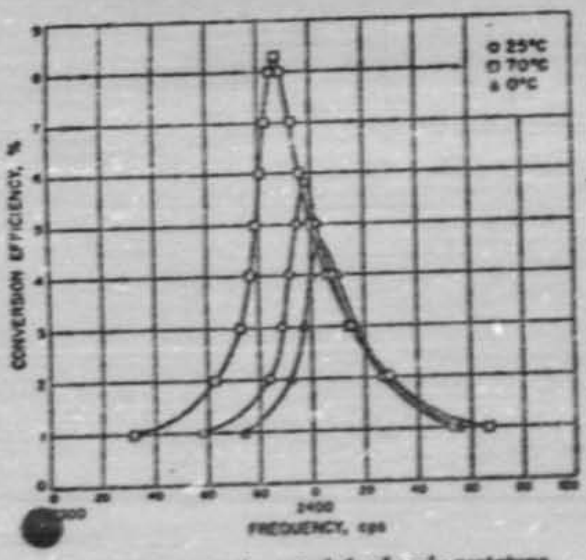

Fig. 40. Resonant characteristic of early prototype dynamic capacitor vs. temperature

This complicated evaluation procedure subsequently led to a new contract with the Applied Physics Corporation in April 1961, which resulted in a capacitor with a piezoelectric crystal mounted on the reed. Since the crystal, which was made of lead titanate, gave maximum output at reed resonance, it provided a stimulus signal for a regenerative coil drive system, which could also synchronously drive the demodulator. The frequency stability of mechanical resonance in this capacitor was also markedly improved by changing the reed material from stainless steel 303 to a constant-modulus alloy, Ni-SPAN-C. The mechanical assembly drawing (Fig. 41) illustrates the rugged construction of the unit, which passed vibrational tests far surpassing the actual launch vibration environment.

The center post forms one element of the coupling capacitor with respect to the stator assembly and also acts as an input terminal to the stationary element of the variable capacitor, the anvil. The construction design ensures that both the variable and coupling capacitors are guarded, in order to provide capacitor stability and minimize leakage current paths. Although the center post was initially designed to house an input resistor that provided isolation of the source and input terminal capacitance from the reed–anvil capacitance, it was decided to accept a small decrease in open-circuit conversion efficiency (owing to additional shunt capacitance) and to place the

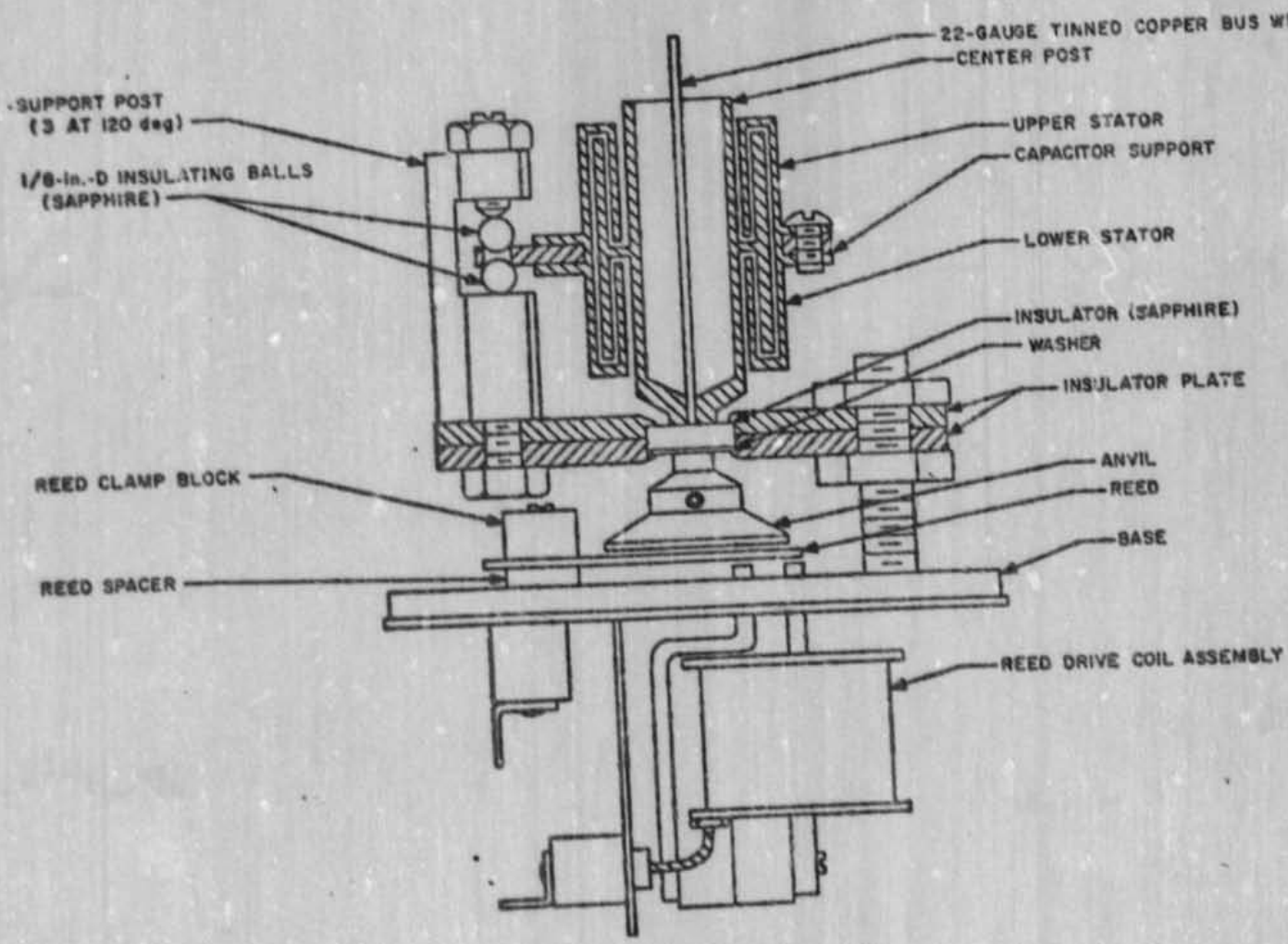

Fig. 41. Dynamic capacitor assembly

resistor outside the assembly in order to reduce possible sources of contamination. The *Mariner 2* unit (with an coil shield to reduce the effects of magnetic fields from the reed assembly) was 3.25 in. long by 2.00 in. in diameter and weighed 0.8 lb.

Since the absolute value of the coupling capacitor is not critical in an electrometer of this type, an improved version of the unit was later developed which utilized small-area, closely spaced, parallel plates for the coupling capacitor and afforded a 3/4-in. reduction in length and a resultant weight saving. A sapphire input terminal increased the input resistance to more than 10^{16} ohms. The superior short time constant of strain currents exhibited by this material has made practicable the design of electrometers for long-term, space use with a null stability of 10^{-16} amp over the temperature range of −50 to +90°C.

IV. THE DEFLECTION VOLTAGE SYSTEM

The electrostatic deflection system for the *Ranger* and *Mariner* plasma instruments consisted of three elements: a digital programmer, a high-voltage sweep amplifier, and the electrostatic deflection plates. The programmer received timing pulses from the spacecraft DAS and supplied precise analog currents to the high-voltage sweep amplifier. The output voltage of the sweep amplifier was then impressed across the electrostatic deflection plates so that particles of a particular charge sign and energy proportional to that deflection voltage were focused through the deflection plate assembly onto the Faraday charge collection cup. Mechanization of the *Ranger* and *Mariner* deflection systems was practically identical except that the *Mariner* sweep amplifier was somewhat simpler since only positive ions were to be measured.

A. Electrostatic Deflection Plates

The *Ranger* and *Mariner* deflection plate systems (Figs. 4 and 8 respectively) were designed according to dimensions supplied by the JPL experimenters, M. M. Neugebauer and C. W. Snyder. Each unit consisted of a set of curved parallel plates separated by ground rails to eliminate fringing effects between the plates. A rectangular plate at ground potential was located at both the entrance and exit of the deflection plates for the same reason. Inside the entrance to the Faraday cup, but shielded from the particle beam by the rectangular ground plane, was a suppressor electrode which prevented secondary emission of electrons from the Faraday cup due to collision of incident particles. All metal parts were gold-plated magnesium with the exception of the entrance ground plane, which for reasons of spacecraft passive temperature control was made of polished aluminum.

The energy E_c required for a constant radius of curvature for normally incident particles was equal to 2.74 times the deflection voltage on *Ranger* and 4.0 times the deflection voltage on *Mariner*. Differential deflection voltage (outer to inner plate) vs. energy level is shown in Tables 2 and 3 for the *Ranger* and *Mariner* systems, respectively.

Evaluation of a prototype instrument in a particle accelerator revealed a troublesome phenomenon. Ultraviolet photons in the Lyman-Alpha region emitted by the particle source reflected down the bright gold walls of the deflection plates and then reflected off the charge collection cup. This indirectly illuminated the negatively biased suppressor electrode and caused a release of photoelectrons. The photoelectron current collected at the Faraday cup and measured by the electrometer was on the

order of 10^{-16} amp or three orders of magnitude above the electrometer threshold.

The problem of darkening the gold-plated parts to reduce the reflected light was complicated by the fact that any material utilized had to be a good electrical conductor. Following a method described for increasing the efficiency of infrared detectors (Ref. 19), it was decided to coat the deflection plates and Faraday cup with gold-black. Gold was evaporated off a tungsten filament onto the gold-plated magnesium surfaces in a low-pressure atmosphere of hydrogen. The hydrogen decreased the mean free path and the temperature of the gold molecules emanating from the filament so that they accumulated on the surfaces of interest in a loose molecular structure. The resultant surface was extremely black to ultraviolet as well as visible wavelengths. Although the black surface could be easily rubbed off, evaluation over a temperature range of −30 to +150°C and exposure to a vibrational energy spectrum much greater than that anticipated on the spacecraft failed to indicate any changes in the surface absorbtivity.

Subsequent evaluation of the gold-blacked system with an ultraviolet source whose estimated intensity was equal to three times that emitted by the Sun revealed that the resultant background current was on the order of 10^{-16} amp (measured with a commercial electrometer) and well below the flight electrometer threshold. Gold-black was applied on later instruments using nitrogen in lieu of hydrogen, but in either case the process was an extremely laborious one, owing to the difficulty in obtaining a uniform, nonspecular coating over the large surface area. Platinum-black, which is a commercial plating process, was evaluated late in the *Mariner* program and proved to be as effective as the gold-black. The platinum-black method was dropped, however, owing to the limited development time, when it was discovered that there was a corrosive action between the platinum-black plating solution and the magnesium plates as a result of the porosity of the gold plate.

In a redesign of the deflection plates for the *Mariner* system, the sector angle of the deflection plates was increased from 90 to 220 deg to increase the number of reflections necessary for a beam of photons to reach the suppressor grid, and the resultant background electron current dropped to less than 10^{-16} amp. Experience with the *Ranger* instrument at AMR, where the humidity was very high, dictated the use of insulators such as Teflon and Diall FS-4, a glass-filled diallyl phthalate, in lieu of materials such as nylon that were hygroscopic and absorbed water in the humid environment, and thus drastically lowered important insulation resistances. Other engineering improvements in the *Ranger* design were the use of improved ground rails to reduce the number of critical high-voltage insulators, reduction of the over-all number of parts to simplify mechanical construction, and redesign of the collector cup, which reduced the number of insulator leakage paths and provided a substantial decrease (60%) in collector cup capacitance.

2. *Digital Programmer*

The digital programmer receives a timing pulse from the DAS at fixed intervals, and at each interval gates a precise analog current into the high-voltage sweep amplifier to generate a discrete deflection voltage. At the end of every measurement interval, a reset pulse, which resets the binary counters to the zero state, is received from the DAS. This procedure insured synchronism of the measurement interval with the frame coding of the DAS data format and was used in lieu of an energy level identification signal which would have required more information bits.

The *Ranger* and *Mariner* programmers were essentially identical except for the number of energy levels and the data interval time. The *Ranger* system provided twelve discrete outputs and also a thirteenth step, which was identical with Step 1. This provision was to ensure that the entire system would stabilize before DAS readout if the electrometer input went from a large positive-ion current in Step 12 (2,600 v) to an electron current in Step 1 (−40 v). The measurement sequence for the *Ranger* system is shown in Table 1. The *Mariner* sequence was similar except that the time interval was approximately 17 sec and there were 20 energy levels plus a reset and calibration interval (Table 3).

A block diagram of the *Ranger* programmer (Fig. 42) can be correlated with the *Mariner* programmer schematic (Fig. 45). Reset gate circuitry (transistors Q28 through Q30) was incorporated into one of the *Ranger* programmers to allow synchronization of all the sweep voltages in the absence of the DAS in a systems test operation. Transistors Q16 through Q23 formed a four-stage counter which was triggered by the DAS timing pulse through pulse amplifier and shapers Q24 and Q25. The flip-flops used were flown on *Pioneer III* and *IV* (Ref. 20) and were used here because of the proven design reliability. The outputs of the counter were examined by a multiple AND gate diode matrix using the standard binary-to-decimal conversion technique. Transistor gates

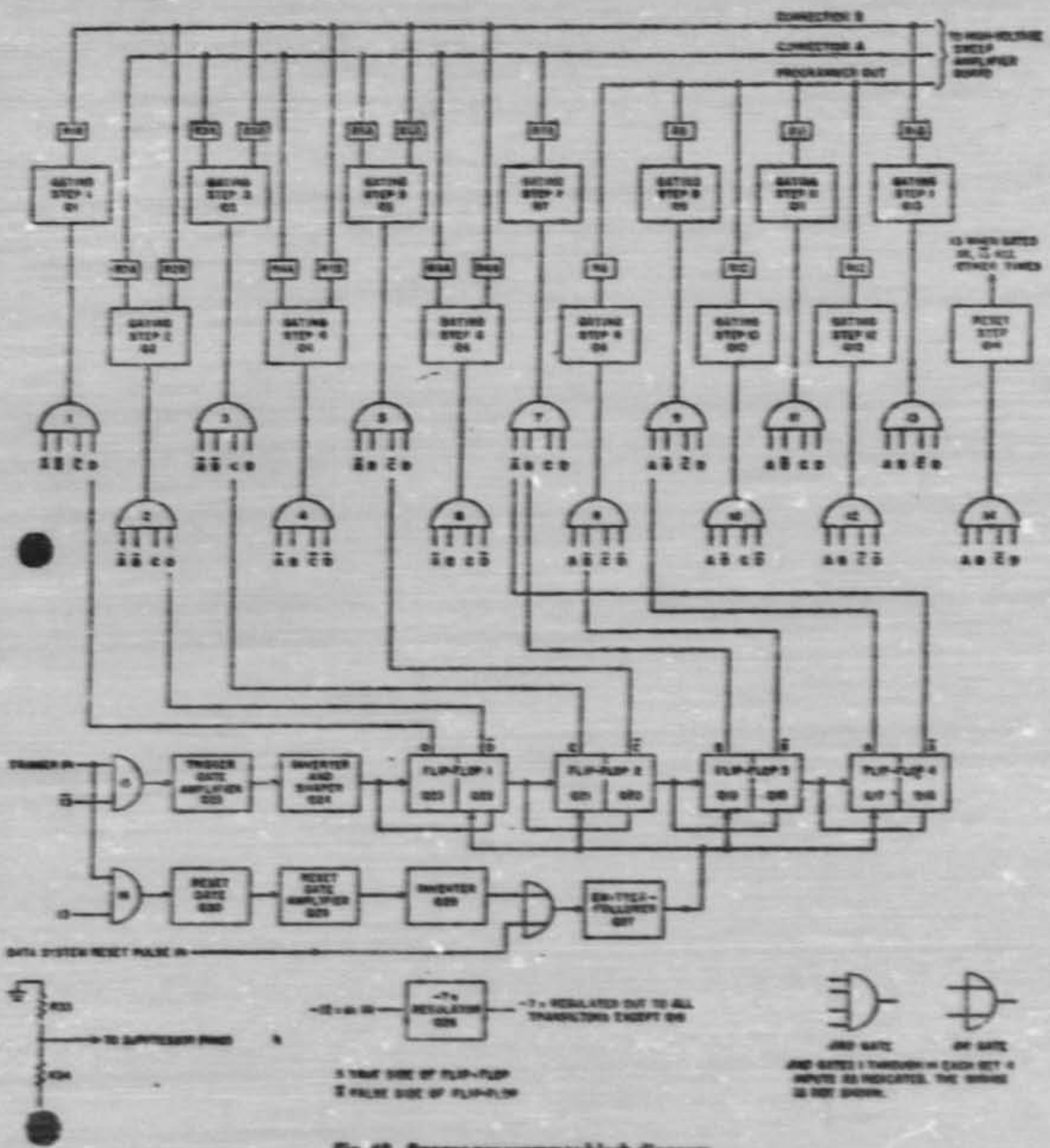

Fig. 42. Ranger programmer block diagram

Q1 through Q13 (Q1 through 10 on *Mariner 2*) switched a regulated reference voltage to resistive weighting networks to form the sweep amplifier analog input currents. On *Mariner*, no input voltage was gated to the sweep amplifier in Step 11 (Q11), as will be explained, and Step 12 (Q12) provided gating for the electrometer calibration reed-switch coil.

Since the programmer output circuitry is direct-coupled and since it was desired to keep the sweep analog input currents stable within a few percent over the specified operating temperature range (−20 to +80°C), an effort was made to compensate for the temperature variations of diodes in the signal path. Figure 44 shows the compensation technique used to stabilize the sweep analog input currents. The compensated zener diode (CR110) is a selected precision reference with temperature coefficient of better than 0.004%/°C at a bias current of slightly less than 1 ma. Diodes CR111 and CR112 buck out the offset and temperature variation of the base emitter diode of Q15 and the blocking diode (CR1) associated with the gate transistor (Q1). A resistive divider (R82, R88, and R85) is used to adjust the absolute value of the input voltage, and after a series of temperature runs, a silicon resistor (R88) is selected to compensate for the attenuation of the divider on the temperature coefficients of diodes CR111 and 112 and for the general temperature coefficient mismatch of all components involved. The diodes (CR2) connected from the gating transistor collector to ground clamp the cutoff voltage of the *OFF* gates, limiting the back voltage on the blocking diodes and thus minimizing the total leakage current errors from those gates that are off. Resistors R_a, R_b, and R_c are designed for the proper transfer impedance for a particular sweep amplifier input current, and in addition are constrained so that the resistance seen by the individual blocking diodes is identical. As a result, the current through the individual blocking diodes is almost independent of signal current, the voltage rise across all diodes is the same and, therefore, the voltage appearing at the input resistor on any step will be approximately the same (about 7.0 v).

Another advantage of the resistive T networks is that although the transfer impedance varies greatly (almost two decades) through a cycle, the effective β network of the sweep amplifier feedback loop remains a constant, and consequently the loop gain ($A\beta$) of the sweep amplifier remains constant. The following figures illustrate the change in voltage at the input of the resistor network on Step 1 at the initial setting and at temperature extremes on a typical flight programmer:

Temperature °C	Error, %	ΔE_{in}, mv
+80	−0.961	+21
+25	−0.984	+19
−20	−0.987	

Since these deviations are only a −0.3% and a −0.27% change from the 25°C value, they are considered satisfactory, as the allowable deviation of any deflection voltage about the 25° value was ±5%. In more recent programmer designs, use of a reference zener diode with a tightly controlled absolute value has eliminated the need for the resistive divider and the resultant thermal tracking problems.

C. High-Voltage Sweep Amplifier

The high-voltage sweep amplifiers used on *Mariner* and *Ranger* were identical except that the *Ranger* system used two subsidiary amplifiers for stable generation of the low-voltage steps. (For comparison of ranges, see Tables 2 and 3.) Figure 45 illustrates the logic arrangement of the *Ranger* sweep system. The main sweep amplifier portion of the block diagram is identical for both systems. The large dynamic range required by the *Ranger* system (−20 to +1,000 v, one side to ground) suggested the use of a transformable ac system. In order to avoid the effects of various drifts arising in dc input stages and thus achieve reasonable thermal gain stability (<10%) in the low-voltage steps, a carrier-type operational amplifier was considered. Subsequent investigation of the carrier approach revealed that the most critical part of this design would be the chopper itself. Although much had been written about the static offset parameters of chopper transistors, very little was known or had been published about the mechanics of dynamic offset parameters such as switching spikes. In addition, thermal and long-term stability of leakage currents in the choppers then available was poor, owing to the lack of surface treatment found in present-day choppers. Although this design approach was recently achieved through the advances in (1) chopper transistor technology, (2) use of wide-band amplifiers with low hangover and blocking characteristics, and (3) duty-cycle action between modulator and demodulator to cancel the switching spikes, it was not a feasible approach at the time of the *Ranger* development. Instead, a direct-coupled operational amplifier, with a balanced differential output, was used for generation of voltage steps of +32 to +1,000 and −32 to −1,000 v, and a pair of three-stage, direct-coupled, feedback-biased operational amplifiers generated voltage

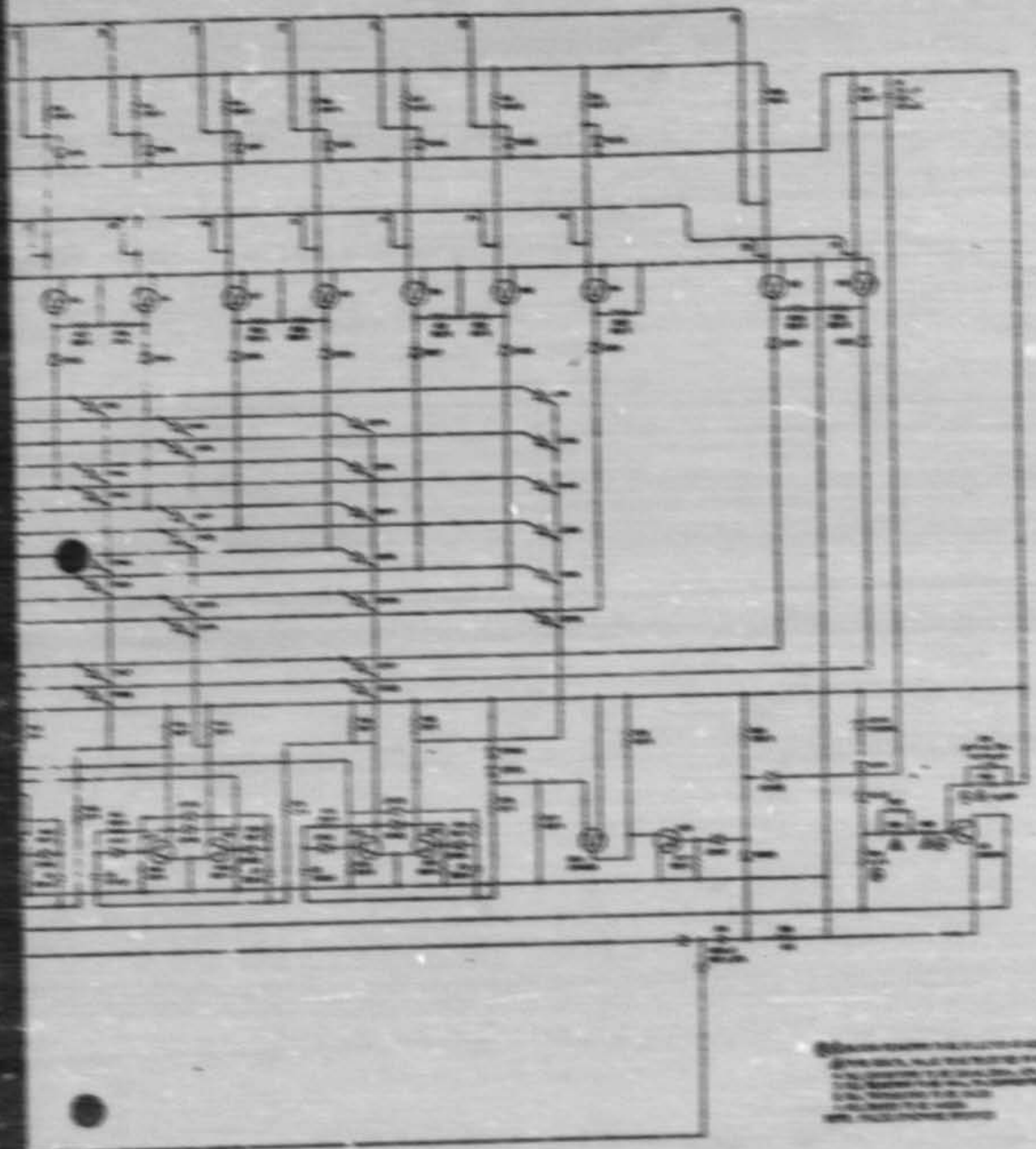

[illegible]

Fig. 43. Motor Sympressor schematic diagram

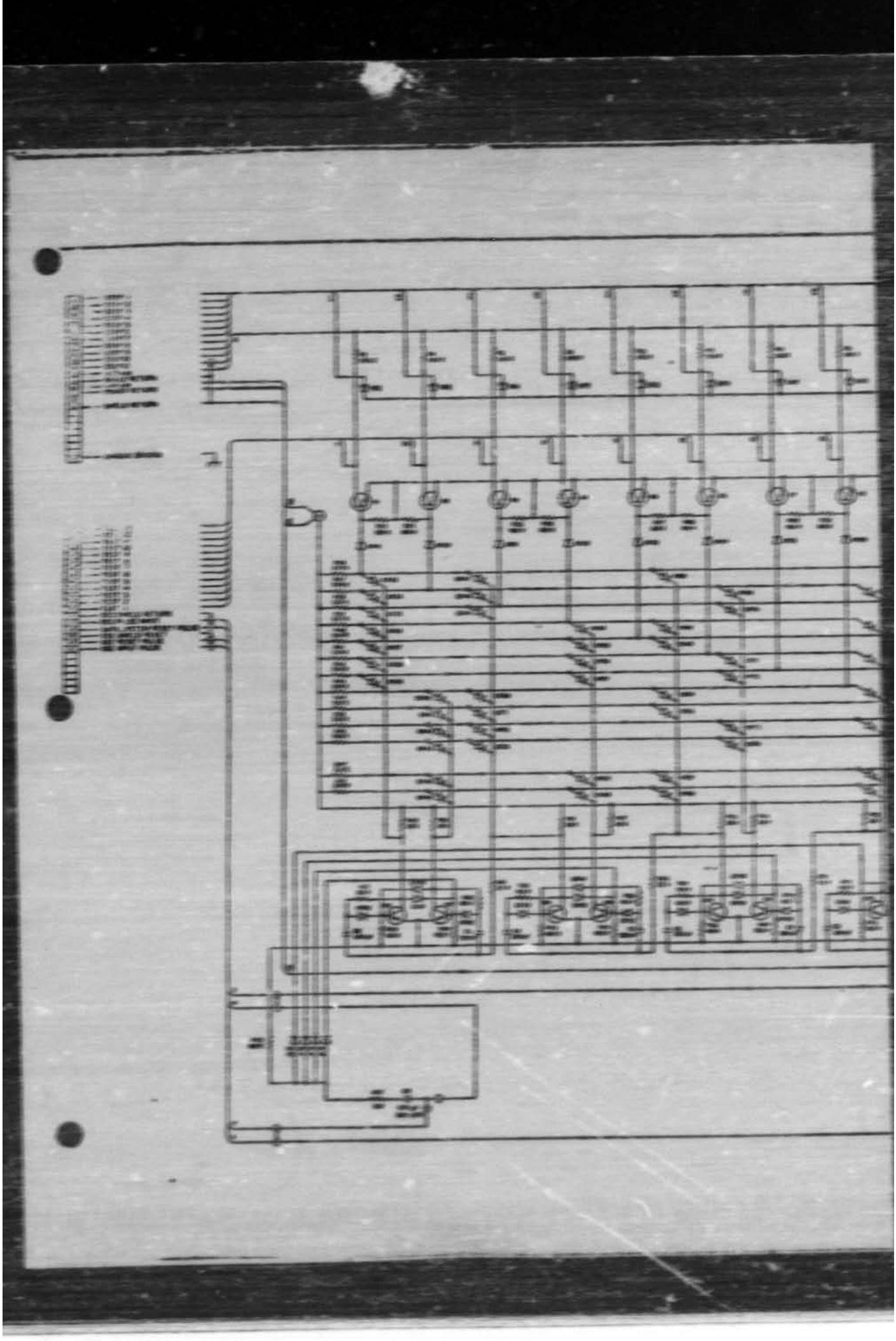

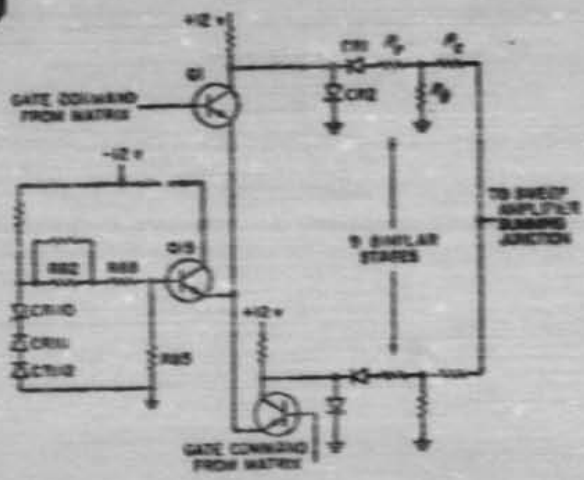

Fig. 44. Partial schematic diagram of programmer reference and sweep amplifier input

steps of −20 to +10 and +20 to −10 v (Fig. 46). A temperature-compensated diode isolation circuit was utilized so that the deflection plates were clamped to the subsidiary amplifiers for the low-voltage steps and to the main sweep amplifier for the high-voltage steps. Use of forward biased diodes (CR6 and CR7) in series with the outputs of the subsidiary amplifiers provided adequate temperature compensation for the voltage variation of the blocking diodes (CR7 and 8, CR12 and 16). During the subsidiary amplifier portion of the sweep cycle, the normally positive output of the main sweep amplifier was allowed to cut off, leaving the junction of R33 and R34 at approximately −30 v, thus clamping the positive or outer deflection plate to the subsidiary amplifier. With the exception of the polarities involved, the inner deflection plate sweep circuit worked in a similar manner.

The main sweep amplifier used on *Ranger* and *Mariner* (Fig. 47) was a direct-coupled operational amplifier which relied on a balanced differential input stage for null stability. The input stage (Q1 and Q2) is followed by a stage of voltage gain (Q3) succeeded by two stages of power gain (Q4 and Q5) which drive a transistor-saturable-core oscillator. The oscillator drives a balanced voltage-doubler network (CR16, 17, 18, 19, and C4, C5 on the positive side) such that output voltages of equal magnitude and opposite polarity, which are proportional to the oscillator input drive voltage, are obtained. An opposite-polarity bucking voltage is placed in the charging paths of both sides of the balanced voltage in such a way that each single-ended output voltage of the sweep amplifier is equal to the algebraic sum of the bucking voltage and the output voltage doubler. For a given deflection voltage, the closed-loop system then forces the static inverter output to a value equal to the given voltage plus the bucking voltage magnitude. This allows the saturable-core oscillator to operate with reasonable efficiency at the lower deflection voltages, increases the frequency of oscillation at the lower deflection voltages so that fairly small capacitors can be used for high-voltage ripple filtering, and conveniently allows the high-voltage amplifier to operate with a null output without danger that the loop will open because of static inverter cutoff.

The balanced, half-wave rectifier that was used for the offset voltage on *Ranger* had a 26-v rms, 2,400-cps, sinusoidal, spacecraft power supply. Some difficulty was experienced in designing an efficient voltage step-up transformer at this frequency because of the large excitation losses and the small secondary current demand. It was determined that *Mariner 2* would use a 100-v peak-to-peak, 2,400-cps, 5-μs rise time, square-wave power supply in order to provide greater spacecraft conversion efficiency. To ease the complexity of the step-up transformer design problem, a balanced half-wave voltage doubler was adopted. On the *Mariner* system, the negative bucking voltage in the positive output side was generated by C2 and C8 and by CR46 and CR14.

Inspection of Fig. 47 reveals that the amplifier feedback loop is single-ended so that the system error signal is provided by the positive output side alone. This design approach assumes reasonable thermal tracking of both sides of the static-inverter voltage doubler and demands that the outputs of the bucking supply be of equal magnitude in order to obtain a symmetrical output of the over-all sweep amplifier. This is reasonable since the negative-output side is a mirror image of the positive output about the ground center line. During operation of the system in the space environment, all charged particles that enter the deflection system and are not focused onto the collection cup impinge on the deflector plates and form a current that must be absorbed by the power supply. An electron current that is absorbed on the positive plate and that is larger than the idling current through R49 minus the feedback current will develop a voltage across R49 sufficiently large to keep diode CR48 reverse-biased during its normal charging cycle. As the current increases, the bucking voltage across R49 increases. Since the negative bucking voltage is inside the amplifier feedback loop, the system would force the static inverter output upward to maintain the

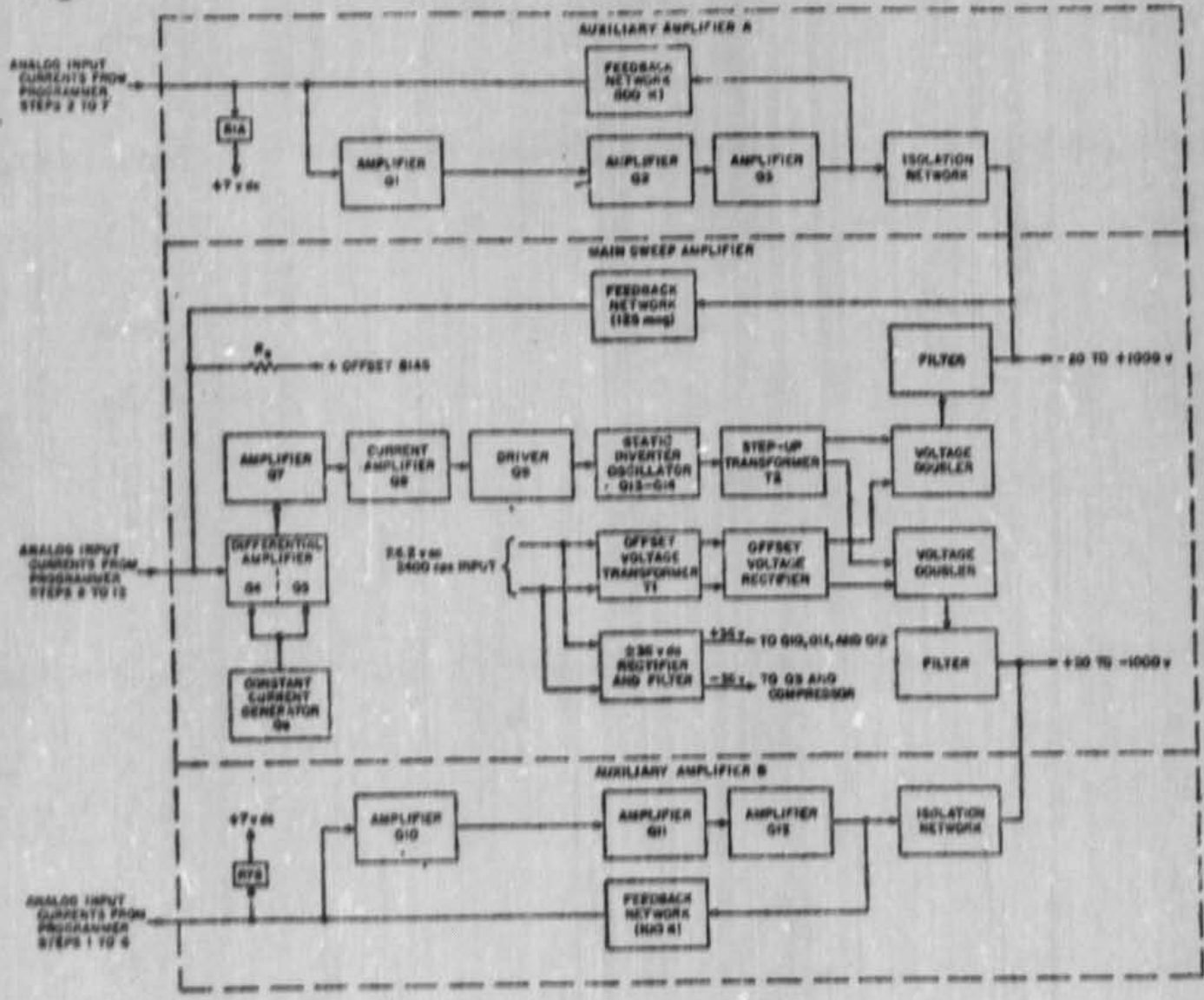

Fig. 45. Ranger high-voltage sweep amplifier block diagram

Fig. 14. Receiver Subassembly Diagram

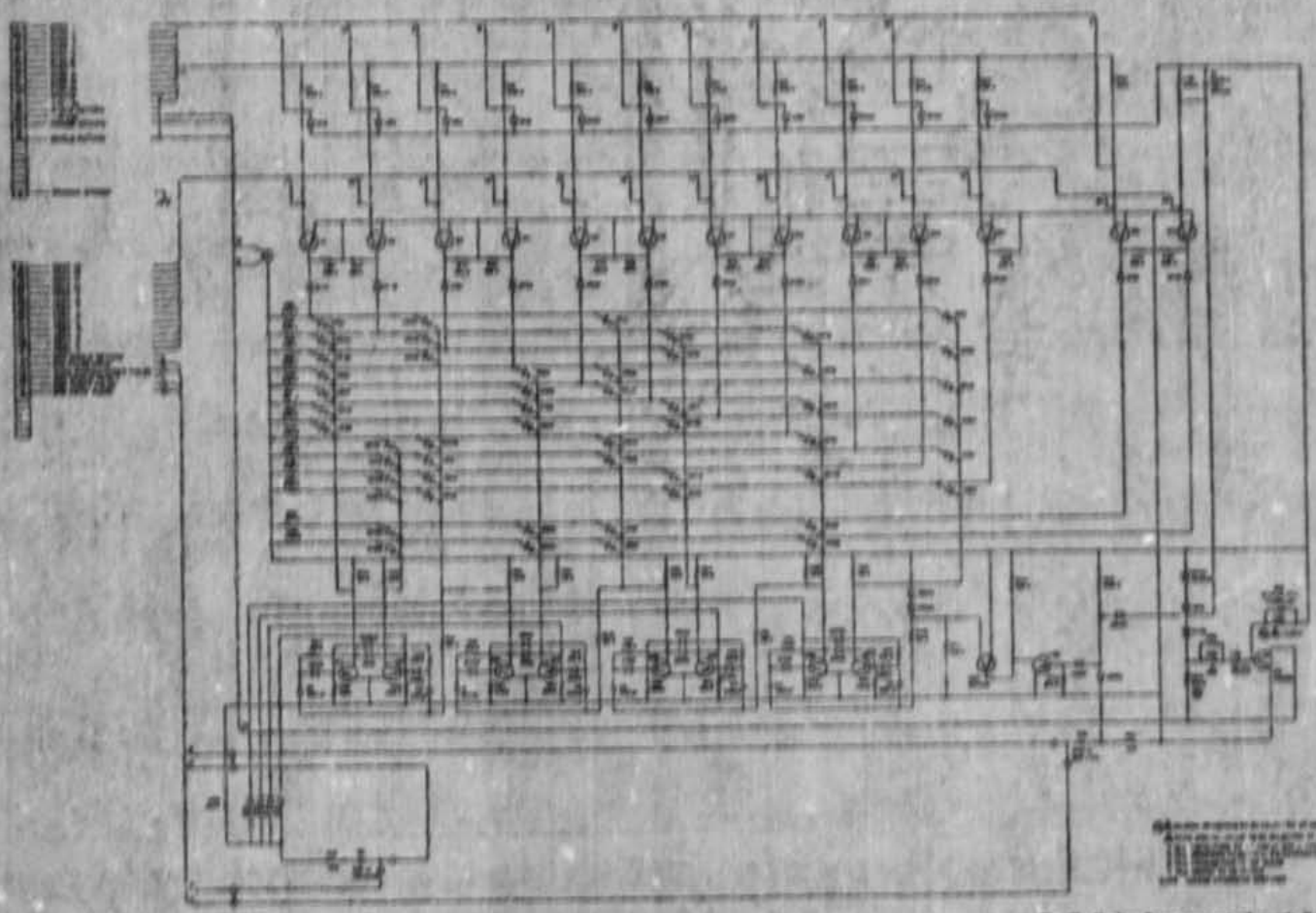

Fig. 43. Mariner 3 programmer schematic diagram

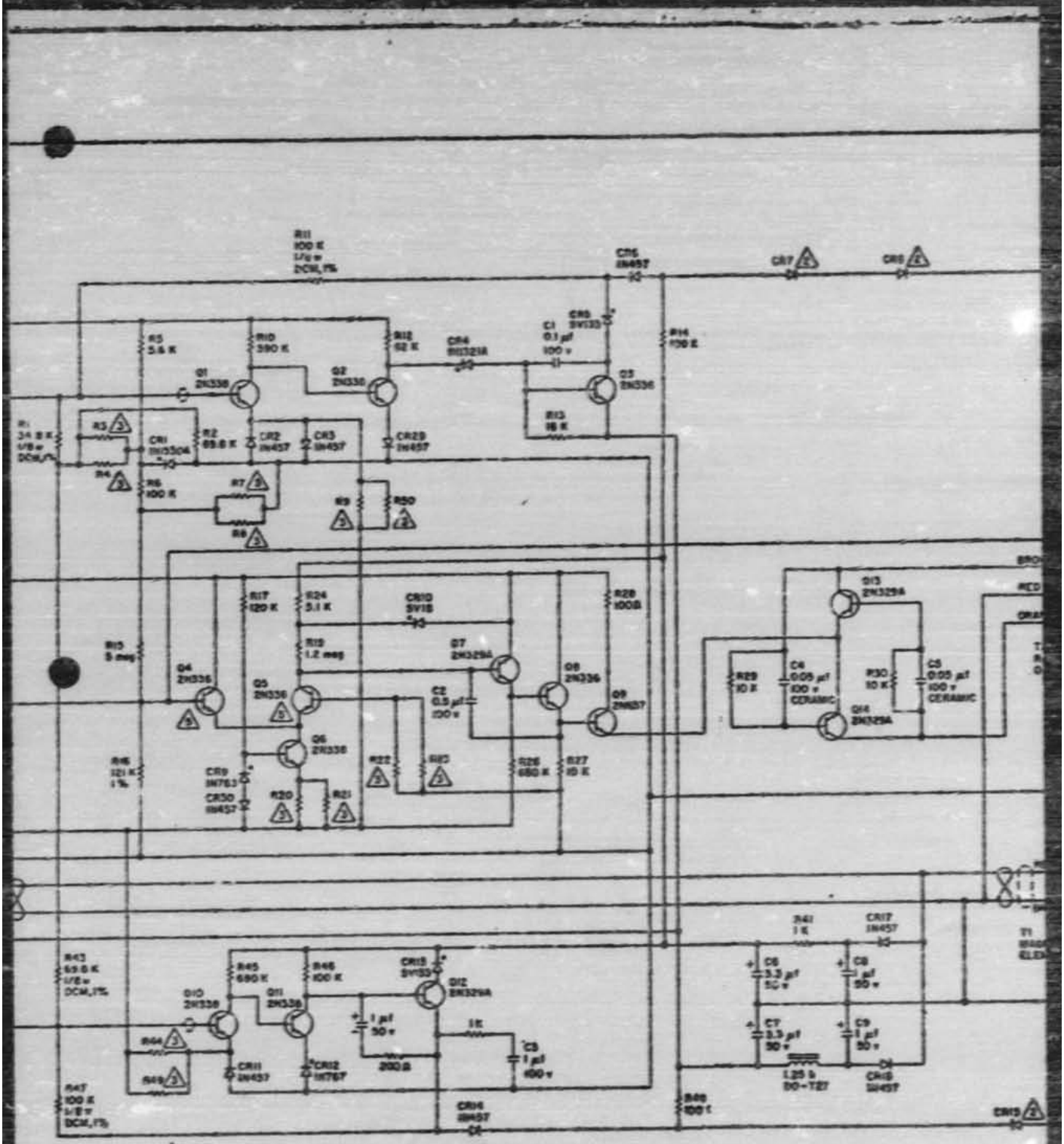

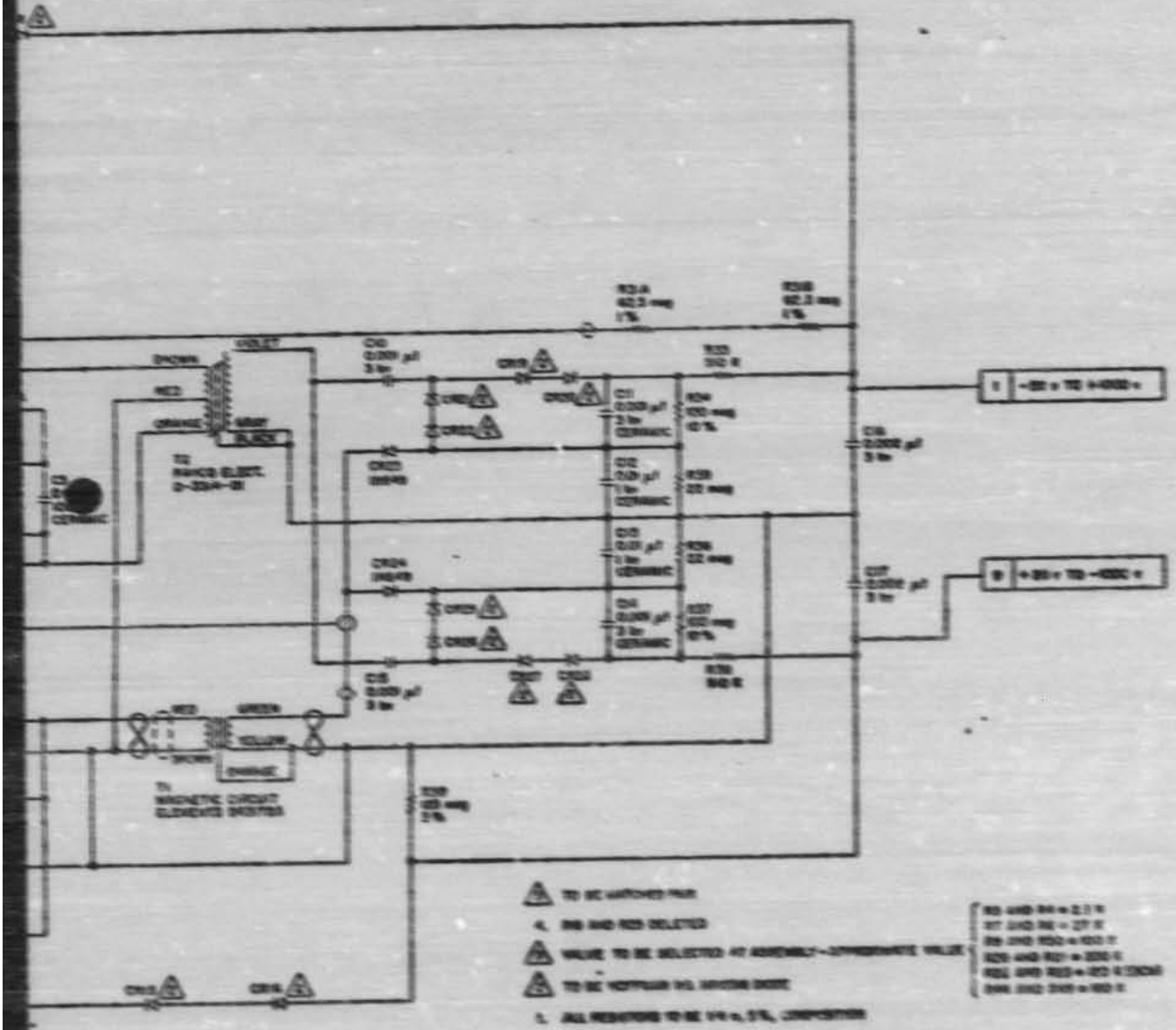

Fig. 46. Ranger ramp amplifier schematic diagram

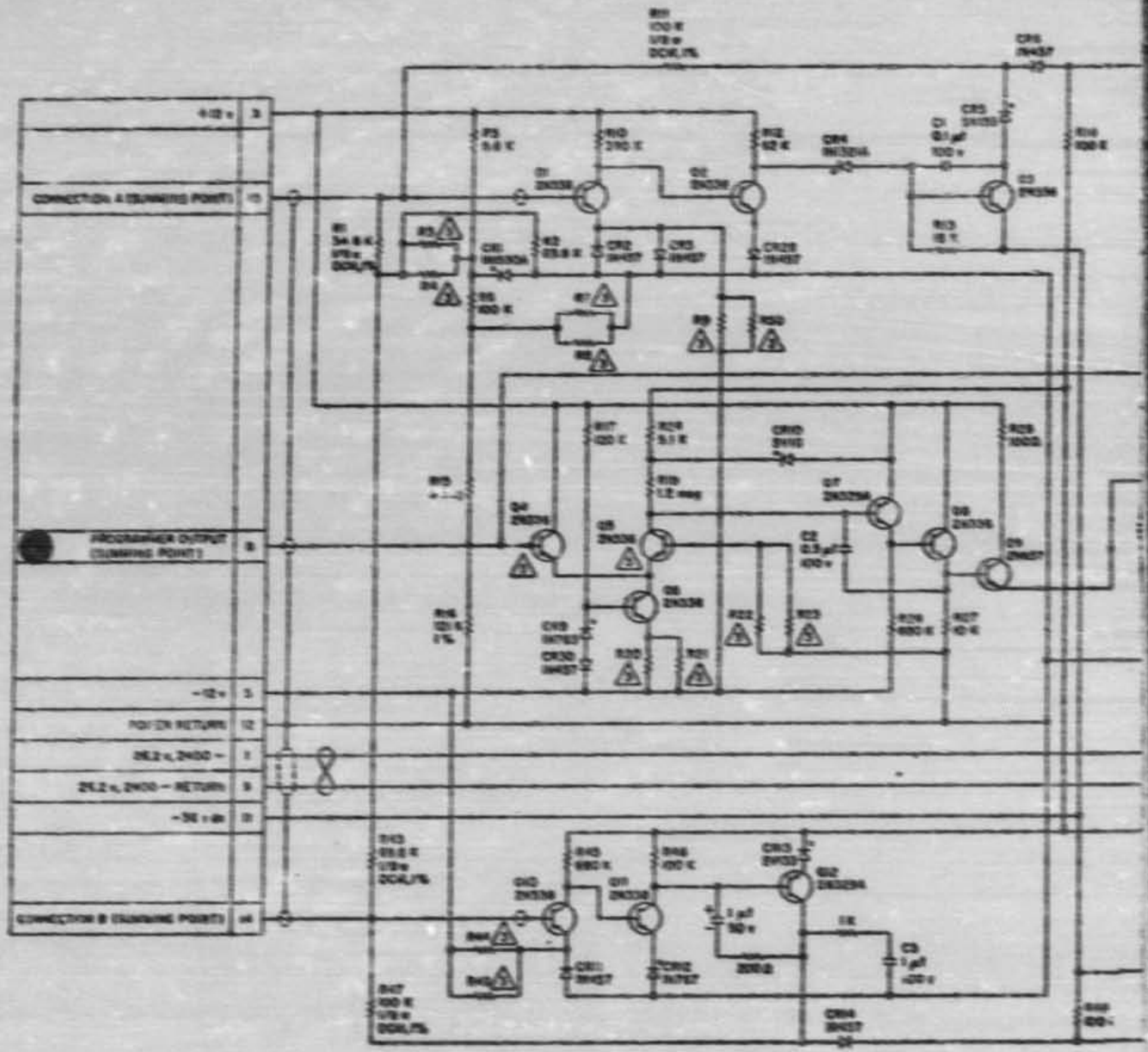

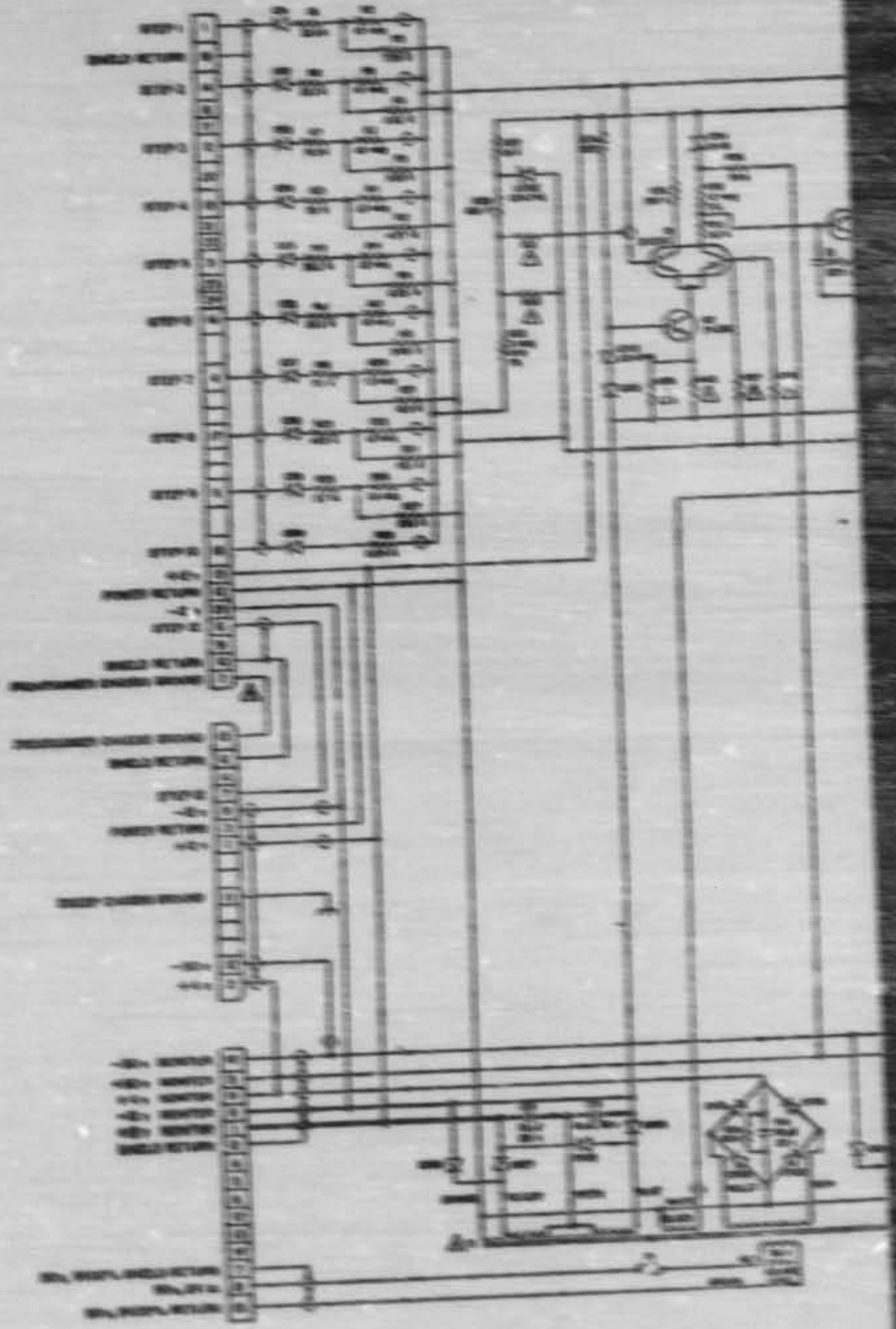

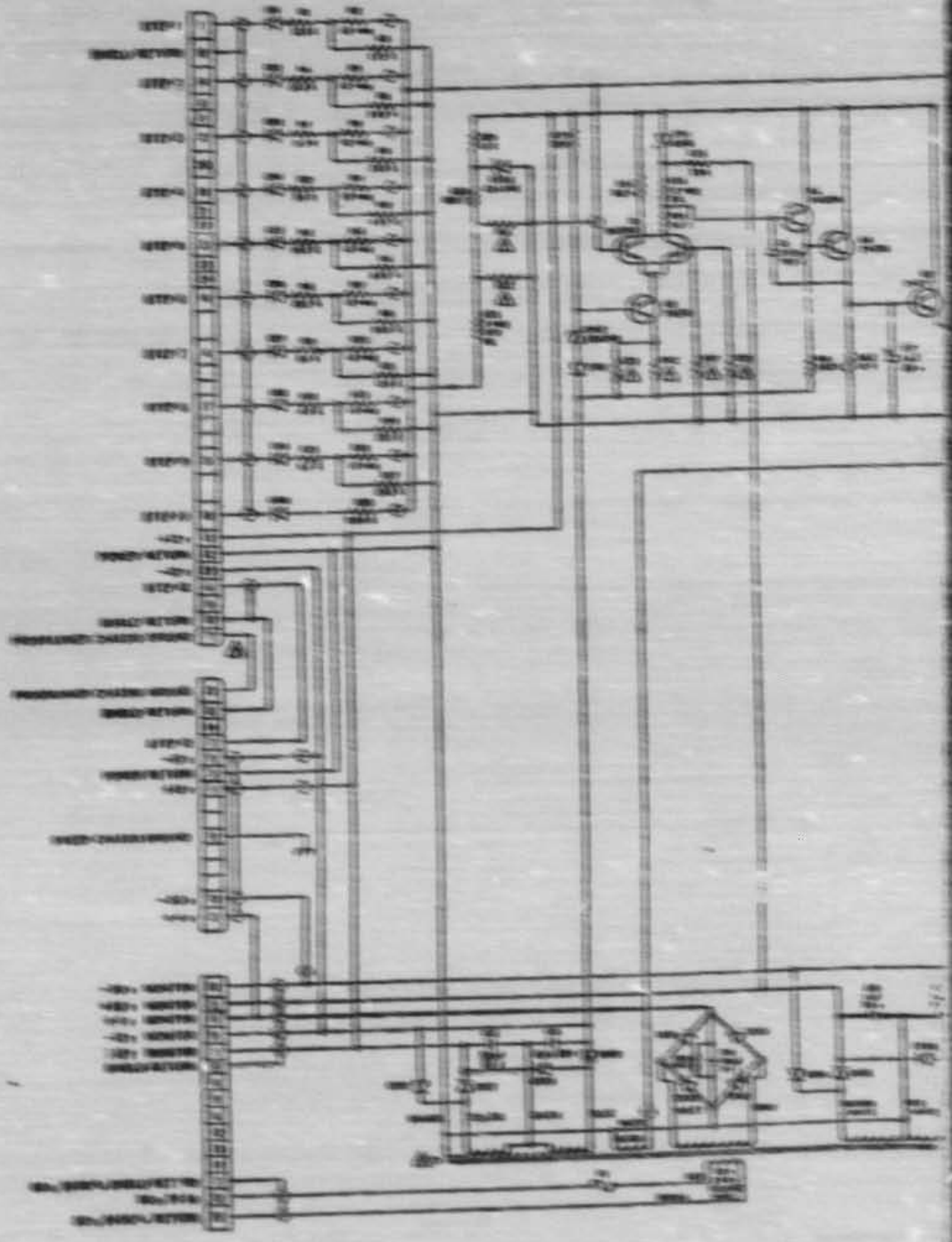

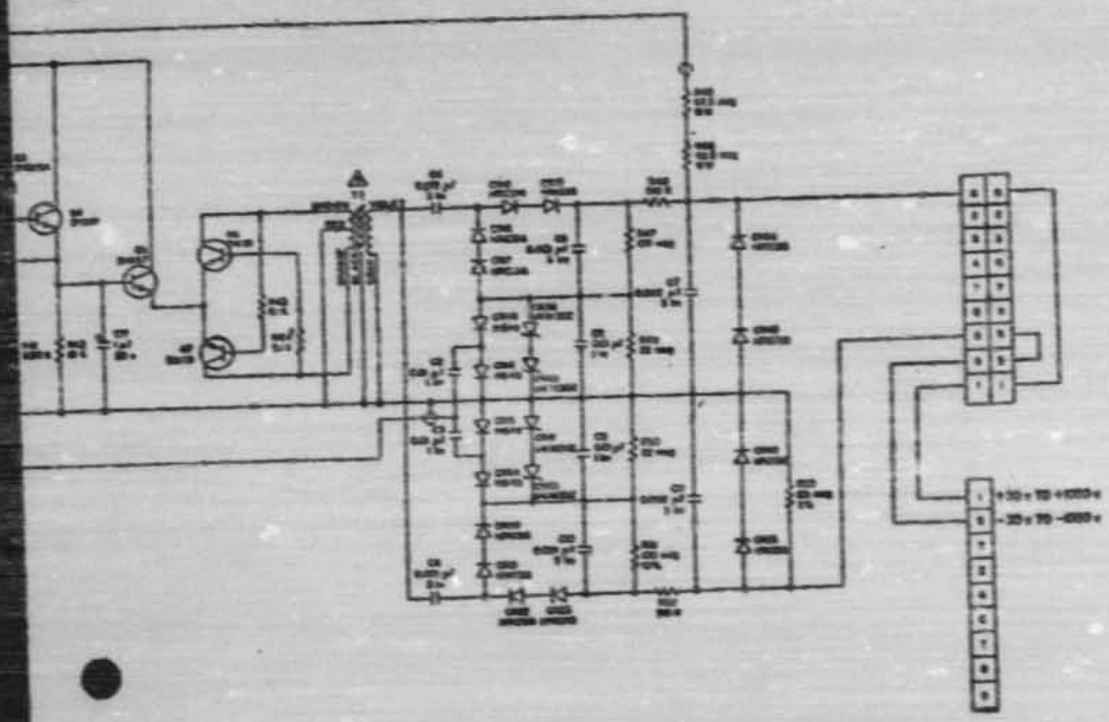

Fig. 47. *Mariner* sweep amplifier schematic diagram

given positive deflection voltage. Accordingly, the negative output of the static inverter increases and, since its offset voltage will remain constant, a nonsymmetrical system output will result. Zener diodes CR39 and 40, whose total threshold is slightly above the normal offset potential, limit voltage buildup on R49 to the zener breakdown voltage and so tend to keep the offset voltage symmetrical. At the +30-v output, either side of the system could sustain an injected loading current of 100 μa with less than a 1-v unbalance.

Positive-ion current on the positive plate has a similar, though inverse, effect. In this case, the idling current of interest is delivered to R47 by the voltage-controlled oscillator and is a variable given by

$$\frac{E_o - E_{\text{breaking}}}{R47} + \frac{E_o}{R_f}.$$

Inverse current in excess of this value will develop a voltage across R47 that will reverse-bias diodes CR18 and CR19. At the +30-v output, the outer plate could sustain an inverse or unloading current of 2.5 μa before disconnecting rectifier diodes CR18 and CR19.

Diodes CR24 and 42 (CR43 and 25 on the negative side) clamp the output of the system to a small potential during the instrument reset and calibration periods. During Steps 11 and 12 in the *Mariner* scan cycle, all negative signal currents to the sweep amplifier are disconnected, and a fixed positive-input reference (which will be discussed below) forces the system outputs to the opposite polarity. The diodes then become forward biased, clamping the output, and the error signal increases and forces the static inverter to cut off. The offset supply then keeps the diodes in this condition, and charged-particle loading of the deflection plates can alter the resultant voltages only within the limitations of the conduction characteristics of the diodes. The resultant deflection voltage (−1.4 v dc) corresponds to electron energies of 5.6 ev and thus assures negligible interference with calibration current injected into the electrometer during the twelfth step.

Capacitor C1, which is bootstrapped about transistors Q3 and Q4, in combination with the Thevenin impedance looking from the junction of the capacitor with the base of Q3, provides the dominant pole that rolls off the open-loop response at 6 db per octave. This pole occurs at approximately 0.04 cps as illustrated in a measured loop-transmission characteristic (Fig. 48). The zero frequency $A\beta$ is greater than 200, which is more than adequate for 1% transfer function accuracy. This curve was obtained by placing an isolated dc or sinusoidal source in series with the positive output and the feedback resistor in the same manner as described in the electrometer evaluation. Care was exercised during the test to ensure that the output signal was a symmetrical sinusoid throughout the measurement. This waveshape is essential since a signal that tends to rapidly drive the positive output to a less positive value will be rate-limited by the output filter networks. The feedback loop will rapidly force the static inverter to a smaller value, the charge retained on the filter capacitor C5 will reverse-bias diodes CR18 and 19, and the loop will intermittently open; the resultant output will then be distorted owing to rate limiting. Since the deflection voltages consistently increased in magnitude during the measurement cycle and the system was always in a linear mode, this distortion did not occur. The rise time for a step-function input that drives the output from +5 to +50 v is 70 msec. Since the electrometer was allowed to settle out for one interval between the 1,050-v step and the calibration interval, the decay time of approximately 400 msec offered no problem.

The ultimate null stability of the sweep amplifier depends on the tracking characteristic of the balanced differential input stage. Changes in differential input currents and imperfect tracking of the base-emitter diode voltages of the comparator transistors are the most significant factors in the cause of output voltage drift. Current drift effects in the input stage are minimized by making the Thevenin equivalent resistance of the input networks (R1 through R33, Fig. 47) and feedback resistors (R45, 46) equal to the parallel combination of the reference base resistors (R37, 38). Assuming balanced collector currents and β-tracking of the comparator transistors, input current changes due to β variation cause common-mode signals and are not a significant factor in output drift. To ensure common-mode stability, a thermally compensated constant-current source consisting of Q2, CR12, CR13, and R39 and 40 is used. This thermal stabilization is essential, as any change in the current source must be absorbed by the input transistor of the comparator stage and will then cause input drift currents, since the output or referenced side has a regulated collector load. Diode CR12 is a low-temperature coefficient reference zener, and diode CR12 is used to compensate the base-emitter diode variation of Q2 in such a way as to maintain a constant voltage across R39 and R40, and hence a constant current. The current source proved to be stable to within 3% at a collector current of 30 μa over a 100°C temperature range. In the

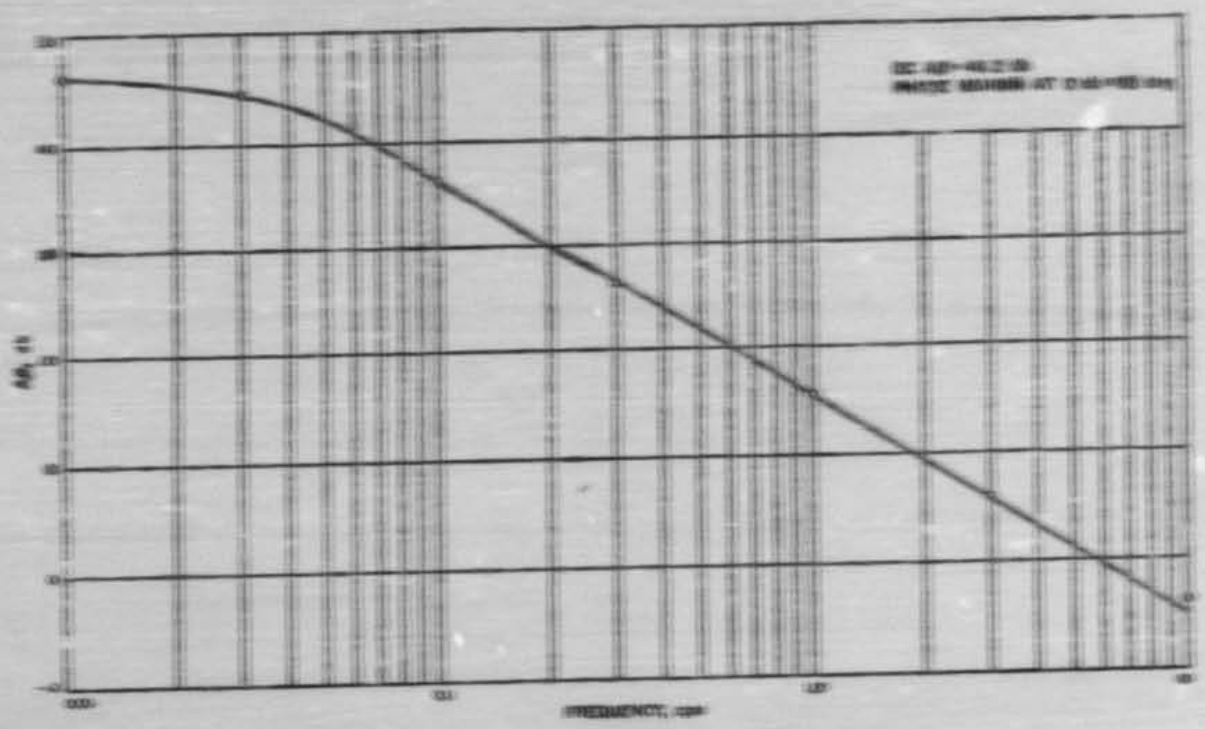

Fig. 48. *Mariner* sweep amplifier loop transmission response

initial adjustment procedure, the parallel combination of resistors R39 and 40 was selected for balanced comparator collector currents of approximately 15 μa. In order to avoid variations in the collector current of the comparator output stage owing to base-emitter voltage variation of the subsequent PNP transistor (Q35) across the collector load resistor, a semi-stable current source was formed by R35, zener diode CR33, and collector load resistor R36. Resistors R58 and R55 were added to the *Mariner* design to equalize the collector operating voltages and thus achieve balance of the collector leakage currents.

The comparator transistors used in the early Ranger designs were 2N338 transistors and were carefully selected for matching characteristics; that is, the various values of V_{BE} and the current gains were matched at collector currents of 15 μa. In addition, collector leakage currents were matched at a V_{CB} value of 12 v. Although this procedure was successful, the long-term results were not always so, since individual units tended to degrade with time. The advent of the passivated planar transistor in the fall of 1960 provided a solution to this problem. A special unit was obtained which contained two 2N1613 transistors in a single TO-5 case (Fairchild FSP-2). This unit had a higher β and a leakage current lower by an order of magnitude than that of the available 2N338's. The common heat sink also contributed markedly to improved thermal tracking of the comparator stage. By the completion of the *Mariner* development, the superior 2N2060 was available as a standard (and cheaper) component. The irony of electronic design is that when a project reaches the production phase, having taken up to a year in development depending on the complexity of the task and the available manpower, components inevitably become available which make the present design obsolete since they permit vast simplification or increased performance.

Because of the small available input voltages, the large dynamic output range, and the necessity to avoid excessive power dissipation in the feedback network, the feedback attenuation

$$\frac{R_a}{R_a + R_b}$$

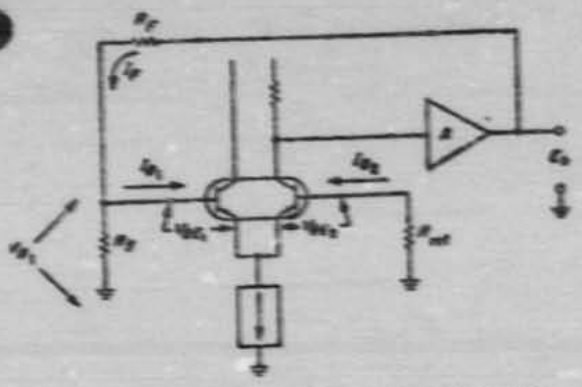

Fig. 49. Main sweep amplifier equivalent circuit

where

R_s = Thevenin equivalent resistance of all input and bias networks

R_f = sweep amplifier feedback resistance

became very small and thus magnified the effects of drift in the input stage. The effects of comparator current and base-emitter voltage drifts on the output may be studied with the aid of Fig. 49. In this equivalent circuit, the input networks have been replaced by their equivalent resistance R_s. It may be shown that

$$V_{s_1} = (I_f - I_{b_1}) R_s$$

and

$$V_{s_1} = V_{BE_1} - V_{BE_2} - I_{b_2} R_{ext}$$

so that

$$I_f = \frac{I_{b_1} R_s - I_{b_2} R_{ext} + \delta V_{BE}}{R_s}$$

where

$$\delta V_{BE} = V_{BE_1} - V_{BE_2}.$$

The output voltage is given by

$$E_o = I_f R_f + V_{s_2}.$$

Assuming

$$V_{s_2} << I_f R_f$$

then

$$E_o = (I_{b_1} R_s - I_{b_2} R_{ext} + \delta V_{BE}) \frac{R_f}{R_s}$$

and

$$\frac{\partial E_o}{\partial T} = \left(\frac{\partial I_{b_1}}{\partial T} R_s - \frac{\partial I_{b_2}}{\partial T} R_{ext} + \frac{\partial (\delta V_{BE})}{\partial T} \right) \frac{R_f}{R_s} \quad (45)$$

assuming

$$\frac{\partial R_s}{\partial T} = \frac{\partial R_{ext}}{\partial T} = 0.$$

Since R_s = 111 K and R_f = 125 meg, it is seen that the algebraic sum of the voltages around the comparator base-emitter loop that are due to input drift current and improper diode voltage tracking is reflected to the output by a factor of about 1,000. It is realized that the incremental variation of base currents and base-emitter voltages is not a linear function over a wide temperature range. Equation (45) is generalized, therefore, in terms of the total change of these parameters over a large temperature excursion.

For

$$\frac{\Delta E_o}{\Delta T} \to 0$$

$$\Delta I_{b_1} R_s - \Delta I_{b_2} R_{ext} = - \Delta (\delta V_{BE}). \quad (46)$$

From this result, it can be shown that the small base-emitter tracking errors can be compensated by the differential base current drift by variation of resistor R_{ext} with respect to R_s. For a representative 2N2060 at I_b = 15 μa, variations of these parameters from −25 to +75°C are as follows:

$$\Delta I_{b_1} = 0.10\ \mu a$$

$$\Delta I_{b_2} = 0.14\ \mu a$$

$$\Delta (\delta V_{BE}) = 2.8\ mv.$$

Substituting these parameters in Eq. (46),

$$0.10 \times 10^{-6} \times 111 \times 10^3 - 0.14 \times 10^{-6} \times R_{ext} = -2.8 \times 10^{-3}$$

and

$$R_{ext} = 97\ K.$$

Table 6. Output voltage vs. temperature for Gauge sweep system

Gauge test step	Voltage, V			Gauge test step	Voltage, V		
	[illegible]°C	[illegible]°C	[illegible]°C		[illegible]°C	[illegible]°C	[illegible]°C
Position				Position			
1	[illegible]	[illegible]	[illegible]	1	[illegible]	[illegible]	[illegible]
2	[illegible]	[illegible]	[illegible]	2	[illegible]	[illegible]	[illegible]
3	[illegible]	[illegible]	[illegible]	3	[illegible]	[illegible]	[illegible]
4	[illegible]	[illegible]	[illegible]	4	[illegible]	[illegible]	[illegible]
5	[illegible]	[illegible]	[illegible]	5	[illegible]	[illegible]	[illegible]
6	[illegible]	[illegible]	[illegible]	6	[illegible]	[illegible]	[illegible]
7	[illegible]	[illegible]	[illegible]	7	[illegible]	[illegible]	[illegible]
8	[illegible]	[illegible]	[illegible]	8	[illegible]	[illegible]	[illegible]
9	[illegible]	[illegible]	[illegible]	9	[illegible]	[illegible]	[illegible]
10	[illegible]	[illegible]	[illegible]	10	[illegible]	[illegible]	[illegible]
11	[illegible]	[illegible]	[illegible]	11	[illegible]	[illegible]	[illegible]
12	[illegible]	[illegible]	[illegible]	12	[illegible]	[illegible]	[illegible]

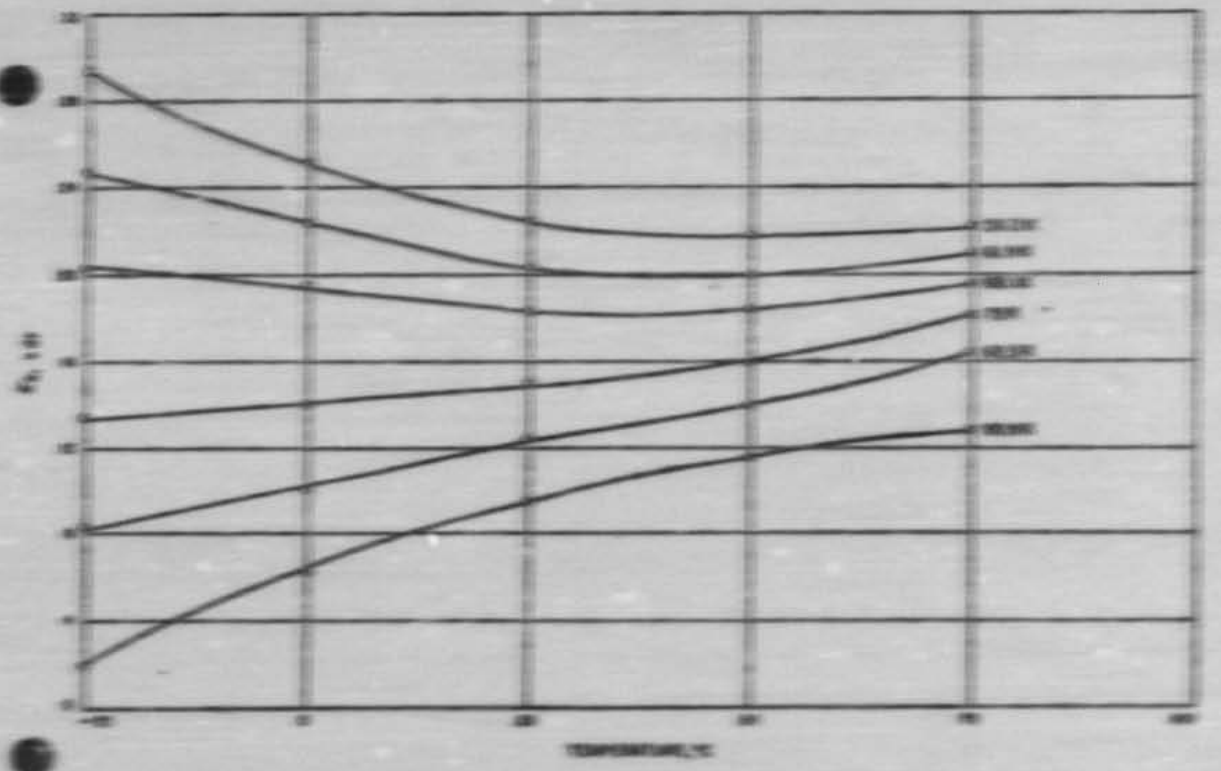

Fig. 33. Thermal drift characteristics vs. reference base resistor for typical Kistler sweep amplifier

After the comparator collector currents are balanced in the sweep amplifier alignment procedure, the output voltage is recorded vs. temperature for different values of R_{set}. A family of curves that depicts the test result for a typical *Mariner* sweep amplifier is shown in Fig. 50. It is seen that the flattest output characteristic over the 100°C temperature range was provided by a 68.1-K resistor. This corresponds to an average equivalent input drift of 20 μv/°C. Since this adjustment resulted in a stable output offset, a reference base resistor of the proper value was installed, the precise analog current was gated in on the first step (corresponding to 30 v output), and a regulated input bias current was adjusted to give the correct output voltage. The regulated bias voltage is supplied by reference zener diode CR38 with an adjustable voltage divider R30 through R32, and the bias current is produced by R33. The temperature test is then rerun to prove the validity of the adjustment.

For a typical *Ranger* sweep amplifier (the *Mariner* design was similar) the output voltage is given vs. temperature and energy-level step in Table 8. The *Mariner 2* sweep amplifier calibration is presented in the next section, which describes preflight performance.

V. THE *MARINER 2* FLIGHT INSTRUMENT

A. Preflight Calibrations

Four solar plasma instruments were built in preparation for the two 1962 launchings to Venus. Construction on the third unit, which was to fly aboard *Mariner 2*, was completed on February 9, 1962. Flight acceptance environmental tests were conducted between February 25 and March 5, 1962, during which time temperature, vibration, and vacuum-temperature performances were monitored. Between March 5 and May 8, 1962, the flight instrument was alternated with other plasma units for spacecraft systems tests. When not on the spacecraft, each unit was returned to the laboratory for routine calibrations and performance checks. The history of each unit as recorded in its log book provided an abbreviated yet effective instrument life test and burn-in record.

Vacuum-temperature tests were once again performed on May 5, 1962, and shortly afterward unit No. 3 was shipped with other spacecraft elements to AMR. Final laboratory calibration was performed on August 5, 1962, followed on the next two days by the last spacecraft systems test. The last useful data observed were electrometer calibrations taken in the explosive-safe area on August 14, 1962, prior to the move to the launching pad. The next message from the instrument did not occur until August 29, 1962, about 2½ days after launch, when *Mariner 2* scientific instruments were turned on.

The curves and tables presented here describe the preflight performance of various parts of the *Mariner 2* solar plasma instrument. Figure 51, for instance, shows the result of final adjustment to the electrometer secondary feedback. Part of the logging operation, which started after completed construction of each unit, consisted of monitoring important instrument performance parameters and power supply levels in addition to the customary calibrations. Table 9 presents results of characteristic measurements taken in the 4-month period prior to launching. The mechanical resonance of the dynamic capacitor is measured by the frequency of its feedback-driven oscillator. The importance of this measurement is that large increases in frequency with time are indicative of leaks in the modulator vacuum seal, which suggest damping effects such as reduction in conversion efficiency and alteration in mechanical Q. Acceptance standards for frequency stability were based upon statistical data obtained from *Ranger* instrument modulators. During this period of time, loop gain variations were within +1.8 and −3.7 db of the nominal

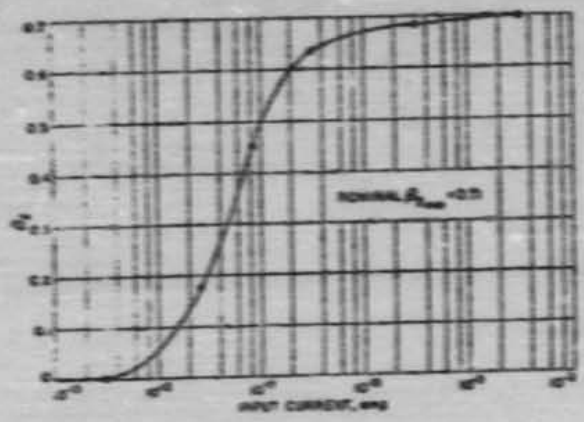

Fig. 51. Portion of secondary feedback connected (β_2) vs. input current

...put error signal potentials were, therefore, about +2 mv for the tabulated values at input currents ... amp. As a result, if −2-mv corrections are made to tabulated values of V_{cm}, one has a thermal and temporal history of modulator contact potential. In most of the formal thermal tests of each flight unit, the instrument's temperature stabilized near that of the chamber wall or near the ambient temperature, depending upon which was controlled. Wherever possible, chassis temperatures were recorded. Where results are listed for tests at atmospheric pressure with no chassis temperatures recorded (e.g., spacecraft systems tests), it is safe to assume a chassis temperature within a few degrees centigrade of the recorded ambient temperature. The final temperature listed in Table 9 (these values also appear in Tables 10 and 11) were somewhat different from the previous test values, because the instrument and its handling fixture were attached to a Plexiglas wall of a reliable vacuum chamber at AMR, and no internal thermal control was provided.

The curves of Fig. 52 provide the basic temperature calibration for the electrometer system, but for final adjustment they must be normalized to the last temperature calibration (columns 2 and 3 of Table 10). The effective translational drift of calibrations between May 8 and August 5, 1962, was about 8 mv.

During each spacecraft systems test a fixture attached to the plasma instrument permitted remote sequencing of electrometer calibration currents. During these tests, outputs from both the electrometer and the analog-to-digital converter of the spacecraft science Data Conditioning System (DCS) were monitored. The results of these measurements on the last systems test (August 7, 1962) are listed in columns 4 to 7 of Table 10. Differences between readings taken on ground support equip-

Table 9. Preflight electrometer performance

Date	Modulator frequency f_c, cps	Loop gain A_1	V_{cm} at $i_{in} = 10^{-9}$ amp, mv	Temperature*, °C	Pressure, Torr
5/8/62	2,259.7	1,150	−26.3	+24	1 atm
(JPL)	2,259.4	1,150	−26.1	+28	10^{-6}
	2,259.3	450	−25.6	−9	2×10^{-6}
	2,261.1	1,170	−25.8	+68	2×10^{-6}
	2,258.8	1,130	−25.4	+24	10^{-6}
↓	2,259.1	1,110	−29.7	+23	1 atm
6/29/62	2,260.5	1,080	−25.2	A+25°	1 atm
(AMR)	2,260.9	720	−27.6	A−20	↓
↓	2,262.0	910	−25.5	A+70	
	2,260.1	1,051	−22.8	A+25	↓
8/5/62	2,260.8	1,110	−28.8	+28	1 atm
(Final at AMR)	2,260.7	1,350	−23.7	+40	1.3×10^{-6}

* Unless otherwise noted, all temperatures are those at the instrument chassis.

* A denotes ambient temperature.

Table 10. Final preflight electrometer calibrations

I_{in}, amp	Final instrument calibration[a] E_{in}, v		Final spacecraft systems test[b]				Equivalent spacecraft calibration,[c] referenced to	
			GSE readout, E_{in}, v	DCS readout, steps		Corresponding step center value, v	GSE ground data, v	Data system, v
	Air atmospheric pressure[d]	In vacuum[e]		Digital output in octal numbers	Digital output in decimal numbers			
10^{-6}	1.831	1.835	1.812	115	77	1.810	1.813	1.818
10^{-7}	2.139	2.175	2.106	133	91	2.115	2.117	2.158
10^{-8}	2.373	2.380	2.252	144	100	2.250	2.257	2.263
10^{-9}	2.618	2.624	2.394	156	110	2.390	2.401	2.407
10^{-10}	2.854	2.861	2.430	173	121	2.844	2.838	2.846
10^{-11}	3.092	3.095	2.840	202	130	3.023	3.072	3.078
10^{-12}	3.319	3.324	—[f]	—	—	—	3.301	3.307
10^{-13}	3.561	3.543	—	—	—	—	3.519	3.525
10^{-14}	3.833	3.860	3.832	173	121	2.844	3.837	3.843

[a] At AMR laboratory, 8/2/62.

[b] At JPL, 8/7/62. Ambient temperature, 23°C; pressure, 1 atm.

[c] Transducer calibration of 8/2/62. Ambient temperature, 23°C; pressure, 1.2×10^{-6} Torr. This calibration assumes chassis temperature equal to ambient temperature during systems test.

[d] Instrument temperature, 28°C.

[e] Instrument temperature, 40°C; pressure, 1.2×10^{-6} Torr.

[f] Calibrations on the spacecraft were generally suspect at or below 10^{-12} amp because of humidity effects, and therefore were not usually taken.

[g] Internal calibration.

ment (CSE) and those taken in the laboratory are attributable principally to ground reference differentials between measurements. Verification of these grounding differentials was obtained by comparison of CSE-based readings with direct measurements at the output of the instrument compartment (case 1 of the 6-case *Mariner* hexagonal structure). The calibration in column 8 was produced by a −8-mv translation of column-3 data, normalizing it to +23°C, and another −14-mv translation of the same data to account for ground-reference differentials, a total of −23 mv discrepancy.

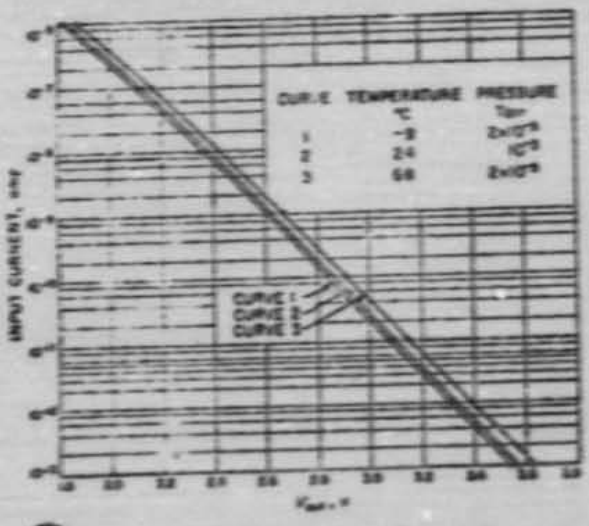

Fig. 52. Vacuum–temperature electrometer calibrations, May 8, 1962

The nominal scale-factor and linearity of the analog-to-digital converter in the DCS were verified by measurement of step-crossings in subsystems tests prior to the final tests on August 7, 1962. The nominal voltage at step center was given by

$$V_{sc} = 0.0235\,N \qquad (47)$$

where N represents the number of quantizing steps. Assuming nominal scale factor and linearity for this part of the data system, a crude 7-point statistical average was taken of the differences between the GSE voltages and the center values of the recorded DCS steps. Although offsets also exist between GSE-based voltages and those appearing at the input to the DCS, a single

Table 11. Preflight deflection voltage calibration*

Step	Deflection plate voltage, v, for indicated conditions															
	JPL calibration, 5/8/62												Final AMR calibration, 8/3/62			
	+24°C, 1 atm		+26°C, 10^{-3} Torr		−9°C, 2×10^{-6} Torr		+68°C, 2×10^{-6} Torr		+24°C, 10^{-6} Torr		+23°C, 1 atm		+28°C, 1 atm		+48°C, 1.5×10^{-6} Torr	
	Outer	Inner	Outer	Inner	Outer	Inner	Outer	Inner	Outer	Inner	Outer	Inner	Outer	Inner	Outer	Inner
1	29.4	29.1	29.5	29.1	29.1	29.2	30.3	31.2	29.5	29.5	29.5	29.5	27.5	28.1	28.1	27.7
2	43.9	43.6	43.9	43.6	43.4	43.5	44.7	45.5	44.0	43.95	44.0	44.0	41.5	41.3	42.5	41.6
3	65.5	65.2	65.6	65.2	64.8	65.0	66.3	67.0	65.6	65.6	65.7	65.6	62.4	62.1	64.0	62.6
4	96.5	96.2	96.5	96.1	95.4	95.7	97.1	97.6	96.5	96.5	96.6	96.4	91.7	91.6	93.3	91.3
5	142	142	143	142	141	141	143	143	143	143	143	142	138	138	141	138
6	211	211	211	211	209	209	212	212	212	211	212	211	205	205	208	206
7	314	314	314	313	311	311	314	313	314	314	314	314	306	305	308	306
8	468	467	468	467	463	464	467	466	468	467	468	467	456	455	459	457
9	699	699	700	698	692	693	698	696	699	699	699	699	683	682	686	685
10	1,051	1,051	1,052	1,051	1,038	1,038	1,053	1,051	1,052	1,052	1,052	1,051	1,027	1,026	1,032	1,031
11	−0.7	+0.8	−0.7	+0.7	−0.9	+0.9	−0.5	+0.5	−0.7	+0.7	−0.7	+0.7	−0.8	+0.7	−0.7	+0.7
12	−0.7	+0.8	−0.7	+0.7	−0.9	+0.9	−0.5	+0.5	−0.7	+0.7	−0.7	+0.7	−0.8	+0.7	−0.7	+0.7

* Outer and inner plate voltages are positive and negative, respectively, unless otherwise indicated.

composite calibration characteristic can now be listed, based upon the nominal characteristic of the analog-to-digital converter (Eq. 47). This is accomplished in column 9 of Table 9 by a +6-mv translation of GSE-based calibration.

Table 11 contains preflight calibrations of deflection voltages. Scale-factor differences between readings taken on May 8 and those taken on August 3, 1962 (27¢), are very likely produced by the different measurement equipment used at JPL and at AMR. Probes having nominal attenuations of 100 to 1 were used with electrometer-type voltmeters, whose analog outputs were recorded on a digital voltmeter. The offset shift can be accounted for in probe calibration.

B. Flight Performance

Mariner 2, the second of a series of spacecraft designed and developed by JPL, was launched on August 27, 1962, at 1:53:14 Eastern Standard Time (EST) from AMR by the National Aeronautics and Space Administration. (*Mariner 1*, launched on July 22 from AMR, had been destroyed after approximately 290 sec of flight because of a deviation from the planned flight path.) The *Mariner 2* spacecraft (Fig. 7) was identical with *Mariner 1* and had the same mission.

1. General Flight Data

Of six scientific instruments carried by the spacecraft, two were used in close-range infrared and microwave measurements of the planet Venus and four performed experiments during the flight and in the vicinity of Venus and collected and transmitted information on interplanetary phenomena.

The flight to Venus lasted approximately 109 days, during which time an over-all flight distance of about 180 million miles was traversed. At Venus encounter, the spacecraft communicated its scientific data to Earth over an interplanetary distance of 36 million miles.

Radio signals from the *Mariner* spacecraft were heard for the last time by the JPL Deep Space Instrumentation Facility station in Johannesburg, South Africa, at the conclusion of its acquisition period at 2:00 a.m. EST on January 3, 1963. At that time the spacecraft was 53.9 million miles from the Earth and 5.6 million miles beyond Venus and had traveled 223.7 million miles since launch on August 27, 1962. During the 129 days between launching and the final loss of radio contact with the spacecraft, interplanetary or cruise science instruments operated for a total of 118.2 days, and data produced by these instruments were actually recorded by the tracking stations for approximately 104.1 days. Information on cruise science experiments was recorded without interruption for one period of 38.3 days and for three other periods of more than 9 days.

2. Instrument Performance

The *Mariner 2* solar plasma instrument operated successfully throughout the entire flight, in both the cruise and encounter modes.

The digital programmer that commutated different inputs to the high-voltage sweep amplifier operated normally. There was no measurement of deflection plate voltage, although plasma energy spectra do indirectly corroborate the presence of appropriate voltages. Future instrumentation should unquestionably provide at least a coarse direct monitor of deflection plate voltage.

Electrometer performance is probably best summarized by calibration history and by signal range and fluctuation patterns. Cruise science was turned on by an Earth-transmitted command on August 28, 1962 (day 241), at 16:13 GMT, about 2½ days after liftoff. The spacecraft was then Sun-oriented, rotating approximately once every 120 min about its roll axis. Earth acquisition took place on day 246, at which time the steerable directional antenna was optically pointed towards the Earth and the spacecraft roll motion stopped. (A chronology of important spacecraft events such as this is shown in Table 12; see also Ref. 11.) The first calibration change took place 6 hr after the Earth-reacquisition sequence that followed a midcourse correction. The calibration output (programmer step 12) dropped one DCS step (23.5 mv/step) in an unexplained fashion (see Table 13). On day 251, another downward shift of two DCS steps occurred. On day 315, the calibration value began increasing, and by planet encounter it had returned to 120. The expected shift for the entire flight was between two and three steps increase. Therefore, at least part of the increase in calibration value after day 315 can be explained by expected changes due to temperature. The three-step increase after day 315 denotes a shift of between 47 and 94 mv, and vacuum-temperature histories account for 36 mv.

In comparing these shifts with other spacecraft events, it was noted that the science temperature measurement for the magnetometer shifted about 1.2 DCS steps on day 251. The engineering temperature measurements did not record a similar shift. Since the magnetometer temperature is measured on a seven-bit channel, this

Table 12. Spacecraft events affecting cruise science[a]

No.	Event	Day	Cruise-science OFF time[b]		
			days	hr	min
1	Liftoff	229	2	9	20
2	Cruise science on	241			
3	Earth-acquisition sequence	243			20
4	Midcourse maneuver sequence	247–248		1	44
5	Earth-reacquisition sequence	248			35
6	Reacquisition sequence loss of orientation	251			30[c]
7	Reacquisition sequence loss of orientation	272			30[c]
8	Power failure	304	8	6	22
9	Power failure	319		—	
10	Planet encounter mode	348			
11	Spacecraft's last signal	363			

[a] Ref. 21.
[b] Total elapsed time was 131 days, 17 min; cruise-science ON time was 118 days, 4 hr, 13 min.
[c] Estimated.

Table 13. Electrometer calibration history

Day	Temperature range, °F	Calibration step	Duration of calibration, days
242–248	85–89	120	6
248–281	89–100	119	33
281–281	100	118	11 hr
281–315	100–122	117	34
315–325	122–133	118	10
325–337	133–146	119	12
337–001	146–175[a,b]	120	23

[a] Temperatures are listed in degrees Fahrenheit, the same units used in instrument temperature transducer calibrations.
[b] Maximum telemeterable temperature was 132°F. Maximum readings during this period were estimated.
[c] Maximum heating occurred near perihelion, December 21, 1962 (day 347).

shift, if attributable to translational effects in common data elements such as a ground reference, would correspond to a 2.4-step decrease on the eight-bit plasma channel. During this time, the threshold of the discriminator in the electrometer assembly was being regularly exceeded by effects of negative background current. A table of discriminator thresholds obtained from electrometer data maxima revealed a two-step downward shift concurrent with the change in electrometer calibration. The simultaneous downward shifts of plasma calibration, discriminator threshold, and magnetometer temperature measurements suggest translational or offset effects between at least these two instruments and the staircase generator of the analog-to-digital converter in the DCS. If nominal calibration current is assumed during the flight (actual internal test-current variations about the adjusted value at 23°C are ±8% at temperatures of −10 and +70°C, respectively), preflight temperature-vacuum calibrations can then be normalized to the equivalent step center value of the flight calibration with an uncertainty of ±11.75 mv. The uncertainty may be appreciably reduced by interpolation between points on a plot of step-crossings vs. time, especially where the resultant curve is a monotonic function of time.

To extract meaningful data from the instrument with negative or very-low-value positive input currents, one should consider the electrometer operation between the discriminator threshold and the low-current end of the static characteristic. Negative background current may be caused by sunlight reflecting down the blackened, curved deflection plates and liberating electrons from the suppressor electrode. It may also be caused by energetic electrons reaching the collector cup after having been scattered from the walls of the analyzer deflection plates at least twice. This background current fluctuated throughout the flight and on occasion was observed to be as high as -10^{-14} amp. The minimum net positive current needed to charge the capacitance of the electrometer feedback compressor from the discriminator threshold to the proper point on the static characteristic is calculated to be 5×10^{-15} amp when the voltage excursion is 2 v, the time interval is 20 sec, and the diode capacitance is 5 pf. All net positive currents above 5×10^{-15} amp may be taken directly from the static characteristic. An integration calculation may be used for average positive currents of less than 5×10^{-15} amp when the electrometer feedback capacitance is in a highly discharged state. The integration scale factor for this condition is 5×10^{-15} amp per DCS step per measurement time interval. An electrostatic transient caused by the reed switch coil in sequencing from calibration to energy level No. 1 usually leaves the electrometer output near the discriminator threshold at the end of Step 1. The ability of a 3×10^{-15} amp current to restore the output to its steady-state value within 20 sec is illustrated in the transient record of Fig. 53. Transients occurring in higher steps are produced by the coupling of minute amounts of energy from the deflection system to the electrometer (sometimes by test cables).

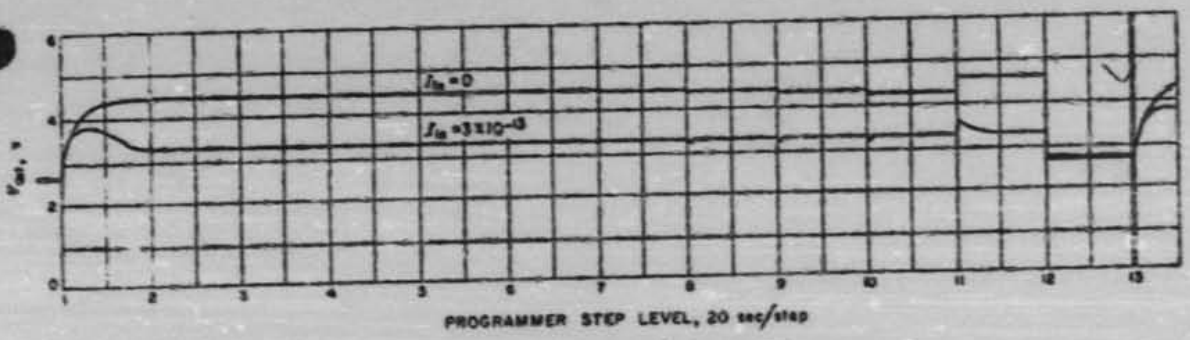

Fig. 53. Electrometer transient response

In the encounter mode, odd-step sampling intervals are reduced to approximately 1/6 of the cruise intervals. In this condition, the minimum current required to charge the electrometer to its correct steady-state value in odd steps, when the feedback capacitance is in the maximum discharged state, is six times the cruise threshold or 3 × 10^{-12} amp. However, worst-case conditions did not generally apply during actual planet encounter, and most odd-step data were therefore directly usable with no corrections required. Step-1 readings were different from cruise-mode readings owing to the switch coil transient, but even there the results were very predictable.

3. Scientific Results

The solar plasma experiment required 3.7 min to acquire a complete energy spectrum of the plasma and during the flight of *Mariner* 2, approximately 40,000 such spectra were obtained. Perhaps the most interesting new information to arise from the very large volume of data on interplanetary fields and particles is the demonstration that solar plasma flowing radially out from the Sun was detectable in every one of the 40,000 spectra obtained in the 4-month mission and is therefore presumably always present.

The solar wind has been explained theoretically as a continuous expansion of the solar corona. *Mariner* 2 results show that the velocity of this expansion (if such is the mechanism) undergoes frequent fluctuations. Approximately 20 occasions were seen when the velocity increased within a day or two by amounts of 20 to 100 percent (Ref. 22, 23, 24). Indeed, solar wind velocities observed during the flight varied from 200 to 500 mi/sec. The fluctuations correlate very well with the amount of magnetic disturbance observed on the Earth, and in several cases sudden and sharp increases in the density, velocity, and temperature of the plasma preceded the onset of sudden magnetic storms on the Earth. The time delay was attributable to the fact that *Mariner* was always inside the Earth's orbit, so that the outward-moving plasma cloud would generally reach the spacecraft first. The following interesting account of one such magnetic disturbance was published on December 7, 1962, before Venus encounter (Ref. 25):

> "There were six geomagnetic storms during the period August 29 through October 18. Figure 2 [not included] shows the plasma flux for the period of the geomagnetic storm which started at 2025 UT, October 7. One could see a sudden increase in plasma flux and energy at about 1547 UT, October 7, when the spacecraft was 8.55 × 10^6 km closer to the Sun than was the Earth. If it is assumed that this plasma front was advancing with spherical symmetry and constant velocity from the center of the Sun (at least for the region of space containing the spacecraft and the Earth), then the velocity of the front was 504 km/sec. This velocity corresponds fairly well to the measured plasma velocity spectrum in which more current was measured at 464 km/sec than at 379 or 563 km/sec.
>
> "The discontinuity, or plasma front, passed the spacecraft so quickly that the instrument with its 3.7 min time resolution could not resolve its structure, which must therefore be less than 112,000 km thick. The Mariner magnetometer data for this period could be interpreted as showing a front thickness of the order of 50,000 km."

During the flight, scientific data became available in several forms such as quick-look telemetry data, decommutated telemetry data, hand-tabulated copies of the decommutated data, and computer-plotted spectra. Table 14 shows a page of hand-collated data. On this occasion, currents above +10^{-11} amp were observed only in energy

Table 14. Manually collated plasma data beginning Sept. 24, 1962 (Day 267), 23:55 GMT[a]

[illegible]	Digitized output (input of [illegible] mv/cm for bottom / programmer step and corresponding E/Q											
	1 916 v	2 555 v	3 499 v	4 733 v	5 1,104 v	6 1,649 v	7 2,611 v	8 3,659 v	9 5,405 v	10 8,313 v	11 0 v	12
43013	239	243	130	153	153	138	183	189	163	164	160	119
43014	239	243	133	156	153	140	184	189	163	164	160	119
43015	239	243	131	153	153	140	184	189	163	164	161	119
43016	239	243	133	153	156	139	184	189	163	164	160	119
43017	239	243	133	154	156	139	184	189	163	163	159	119
43018	239	243	137	154	153	139	184	189	163	164	159	119
43019	239	243	137	154	156	139	183	188	162	163	159	119
43020	239	243	134	154	157	139	183	188	163	163	159	119
43021	239	243	134	154	158	137	184	189	163	164	159	119
43022	239	243	133	153	157	139	184	189	163	163	158	119
43023	239	243	243	153	158	137	183	188	163	163	158	119
43024	239	243	243	153	157	137	183	188	163	163	159	119
43025	239	243	243	153	155	137	183	188	161	163	158	119
43026	239	243	243	153	159	137	183	188	163	163	158	119
43027	239	243	243	153	158	137	183	188	163	163	158	119
43028	239	243	243	153	156	136	184	189	163	163	158	119
43029	239	243	243	153	159	137	183	189	161	164	158	119

[a] Approximate calibration

DCS step	Input current, amp
119	10^{-9}
139	10^{-8}
139	10^{-7}
149	10^{-6}

[b] Data was obtained with an internal reference source of 10^{-9} amp.

els 4, 5, and 6. Peak currents at that time were occurring in level 4 with a particle flux corresponding to a current of about 5×10^{-11} amp. Over the course of the experiment, net positive currents were observed in steps 3 to 10 with peaks occurring in steps 4 to 8. The largest current observed during the flight was about 4×10^{-10} amp. During these periods of intense solar activity, electrometer outputs at supposedly quiet adjacent energy levels gave evidence of an integrating-type discharge corresponding to currents of up to -10^{-10} amp.

NOMENCLATURE

Abbreviations

AMR	Atlantic Missile Range
DAS	Data Automation System
DCS	Data Conditioning System
GSE	Ground Support Equipment

Symbols

A	(1) area (2) amplifier gain
A_v	dc voltage gain of entire electrometer $A_v = G_1 G_2$
$A\beta$	feedback factor, loop gain, or loop transmission (F)
C	coupling capacitance
C_s	source capacitance (test capacitance)
C_2	coupling capacitor
C_a	vacuum dielectric coupling capacitor
C_e	equivalent capacitance
C_p	interelectrode capacitance
C_f	feedback capacitance
C_c	collector-to-shield capacitance
C_v	instantaneous value of dynamic capacitance
d	separation between plates
E	energy
$E_{o(ac)}$	open-circuit preamplifier output voltage
E_c	(1) contact potential (2) energy required for a trajectory with a constant radius of curvature for normally incident, singly charged particles
E_d	average demodulated signal
E_{oc}	open-circuit output voltage of the triplet amplifier, or equivalent input voltage to demodulator
E_o	output voltage
E_p	peak voltage
E_T	test voltage
F	loop transmission ($A\beta$)
F_0	dc loop transmission
f_0	resonant frequency
f_{gc}	gain crossover frequency
f'_{gc}	gain crossover frequency with secondary feedback
G_1	dc voltage gain of carrier section (modulator to demodulator)
G_2	gain of dc filter-amplifier
G_{ac}	ac voltage gain of carrier amplifier
H	transfer impedance normalized to feedback resistance R_f
I	total emission current
I_0	initial-velocity electron current
i_1	primary current in preamplifier input transformer

NOMENCLATURE (Cont'd)

i_c capacitor current during switch closure

I_B transistor base current

i_f capacitor current during switch opening

I_c circulating current

I_{co} collector cutoff current

I_F feedback current

I_f filament current

I_{in} input current to diode grid or diode plate

i_{in} transient or instantaneous value of input current

I_p dc plate current

j $\sqrt{-1}$

K (1) Boltzmann constant
(2) closed-loop gain

$-K_1$ closed-loop gain with infinite feedback factor

M slope of the semilog diode characteristic

N number of quantizing steps in analog-to-digital converter

p Laplace operator

Q (1) resonant selectivity $\left(\frac{\text{resonant frequency}}{\text{3-db bandwidth}}\right)$
(2) charge

q electron charge

Q_m mechanical Q

R2 input resistor to dynamic capacitor

R_A equivalent resistance during demodulation switch closure

R_B equivalent resistance during demodulation switch opening

R_c dynamic resistance of diode CR1 in parallel with R7 and R8

r_d dynamic resistance of a diode in its retarded field region

R_F sweep amplifier feedback resistance

R_f electrometer feedback resistance

R_{in} current-forming resistor connected to electrometer input

R_{sc} leakage resistance

R_p resistance seen at primary of preamplifier transformer

R_{ref} resistance in reference base of sweep amplifier differential comparator

R_s Thevenin equivalent resistance of all input and bias networks in sweep amplifier

S_{I_C} transistor collector stability factor. $S_{I_C} = \frac{\partial I_C}{\partial I_{co}}$
where I_C = collector current and I_{co} = collector cutoff current

T temperature in degrees Kelvin

t time

V_B (1) dc bias voltage
(2) transistor base voltage

V_{BE} transistor base-to-emitter voltage

V_{CE} transistor collector-to-emitter voltage

e_c voltage across coupling capacitor

e_{c_1} coupling capacitor voltage at start of cycle

$e_c(p)$ capacitor voltage as represented in complex (p) plane

V_o translational offset voltage

V_s series generator voltage in feedback loop

V_{in} dc input voltage to dynamic capacitor assembly

V_{nom} nominal voltage at center of analog-to-digital converter step

V_p plate voltage

e_{s_1} average demodulated output voltage

e_s voltage across secondary of preamplifier input transformer

X_c source reactance of modulator capacitance

X_d reactance of vacuum dielectric capacitor (C_d)

X_2 reactance of coupling capacitor C2

NOMENCLATURE (Cont'd)

X_p equivalent series reactance

Z_f feedback impedance

Z_{in} input impedance

Z_{o_1} preamplifier open-circuit output impedance

Z_T transfer impedance

α_i inverse short-circuit emitter-to-collector current gain

β (1) short-circuit base-to-collector current gain
(2) portion of output returned to summing point

β_s portion of output returned to secondary damping capacitor

ϵ_0 dielectric constant of free space

η_c conversion efficiency

η_d demodulation efficiency

η_{d_0} dc or steady-state demodulation efficiency

τ time constant

ω angular frequency

ω_n angular resonant frequency

REFERENCES

1. *Scientific Experiments for Ranger A-1 and A-2*, Technical Memorandum No. 33-4, Jet Propulsion Laboratory, Pasadena, California, March 16, 1960, pp. 9–17.

2. *Scientific Experiments for Ranger 1 and 2*, Technical Report No. 32-55, Jet Propulsion Laboratory, Pasadena, California, January 3, 1961, pp. 15–16.

3. Chamberlain, J. W., "Interplanetary Gas. II. Expansion of a Model Solar Corona," *Astrophysical Journal*, Vol. 131, 1960, pp. 47–56.

4. Parker, E. N., "Dynamics of the Interplanetary Gas and Magnetic Fields," *Astrophysical Journal*, Vol. 128, 1958, pp. 664–676. See also: Parker, E. N., "The Hydrodynamic Treatment of the Expanding Solar Corona," *Astrophysical Journal*, Vol. 132, 1960, pp. 175–183.

5. Biermann, L., "Solar Corpuscular Radiation and the Interplanetary Gas," *Observatory*, Vol. 107, 1957, pp. 109–110. See also: Biermann, L., "Physical Processes in Comet Tails and Their Relation to Solar Activity," *Mémoires de la Société Royale des Sciences de Liège*, Vol. 13 (Series 4), 1953, pp. 291–301.

6. Coleman, P. J., Jr., Davis, L., and Sonett, C. P., "Steady Component of the Interplanetary Magnetic Field: Pioneer V," *Physical Review Letters*, Vol. 5, 1960, pp. 43–46.

7. *The Ranger Program*, Technical Report 32-141 (reprinted from *Astronautics*, Vol. 6, No. 9, September 1961, pp. 22–52), Jet Propulsion Laboratory, Pasadena, California.

8. "Lunar Program," Space Programs Summary No. 37-11, Vol. I, Jet Propulsion Laboratory, Pasadena, California, October 1, 1961, pp. 3–4.

9. Bonetti, A., Bridge, H. S., Lazarus, A. J., Lyon, E. F., Rossi, B., and Scherb, F., "Explorer X Plasma Measurements," *Space Research III*, North-Holland Publishing Co., Amsterdam, 1963, pp. 540–542.

10. Bridge, H. S., Lazarus, A. J., Rossi, B., Scherb, F., Lyon, E. F., and Dilworth, C., "Explorer X Interplanetary-Plasma Observations," *IGY Bulletin No. 55*, National Academy of Sciences, January 1962.

REFERENCES (Cont'd)

11. Neugebauer, M., *The Detection of the Plasma Component of Magnetohydrodynamic Waves in Space*, Technical Memorandum No. 33-93, Jet Propulsion Laboratory, Pasadena, California, June 12, 1962, pp. 10–11.

12. *Scientific Experiments for Mariner R-1 and R-2*, Technical Report No. 32-315, ed. by R. C. Wyckoff, Jet Propulsion Laboratory, Pasadena, California, July 15, 1962, pp. 24–27.

13. Chao, S. K., "Logarithmic Characteristic of Triode Electrometer Circuits," *Review of Scientific Instruments*, Vol. 30, No. 12, December 1959, pp. 1087–1092.

14. Chance, B., Hughes, V., Sayre, D., and Williams, F. C., *Waveforms*, Massachusetts Institute of Technology Radiation Laboratory Series, Vol. 19, McGraw-Hill Book Co., Inc., New York, 1949.

15. Sloughter, D. W., "Reed Drive Oscillator for a Vibrating-Reed Electrometer," *Research Summary No. 36-12*, Vol. 1, Jet Propulsion Laboratory, Pasadena, California, January 2, 1962, pp. 11–13.

16. Palevsky, H., Grenchik, R., and Swank, R. K., "Design of Dynamic Condenser Electrometers," *Review of Scientific Instruments*, Vol. 18, No. 5, May 1947, pp. 298–314.

17. Ebers, J. J., and Moll, J. L., "Large-Signal Behavior of Junction Transistors," *Proceedings of the IRE*, Vol. 42, Part 2, December 1954, pp. 1761–1772.

18. *Cary Model 31–31V Vibrating Reed Electrometer Instruction Manual*, Applied Physics Corporation, Monrovia, California.

19. Harris, L., McGinnies, R. T., and Seigel, B. M., "The Preparation and Optical Properties of Gold Blacks," *Journal of the Optical Society of America*, Vol. 38, 1948, p. 582.

20. Josias, C. S., "Radiation Instrumentation Electronics for the Pioneer III and IV Space Probes," *Proceedings of the IRE*, Vol. 48, April 1960, p. 735.

21. *Flight Performance Report by Spacecraft Data Analysis Team*, Engineering Planning Document No. 149, Jet Propulsion Laboratory, Pasadena, California, February 22, 1963.

22. *Mariner Mission 1962*, Engineering Planning Document No. 129, Jet Propulsion Laboratory, Pasadena, California, April 12, 1963.

23. Snyder, C., Neugebauer, M., and Rao, U. R., *The Solar-Wind Velocity and its Correlation with Cosmic-Ray Variations and with Solar and Geomagnetic Activity*, Technical Report No. 32-514, Jet Propulsion Laboratory, Pasadena, California, October 15, 1963. Also published in the *Journal of Geophysical Research*, Vol. 68, No. 24, December 15, 1963, pp. 6361–6370.

24. Snyder, C., and Neugebauer, M., "Interplanetary Solar-Wind Measurements by Mariner II," to be published in *Space Research IV*, North-Holland Publishing Co., Amsterdam.

25. Snyder, C., and Neugebauer, M., "The Mission of Mariner 2: Preliminary Observation—Solar Plasma Experiment," *Science*, December 7, 1962, pp. 1095–1096.

Binary 62-041A-06A A

INSTRUCTIONS FOR READING AND INTERPRETING THE RAW DATA TAPE

Tape density - 800 bpi.

DCUS blocked format.

Each record contains data from 1 subframe (6 subframes = 1 frame) and can be read with the following FORTRAN IV statement:

READ ( ) TIME, DAY, FC, PL1, PL2

where:

TIME is the time at the start of the subframe and is coded hhmmss, (i.e., hours, minutes, seconds)

DAY is the day number, where Jan. 1, 1962, is day 1.

FC is frame count. Except in cases of missing data, FC should remain unchanged for 6 consecutive subframes (=1 frame). FC is generated by an on-board counter continuously cycled from 0 to 255.

PL1 is the first plasma data word in the subframe.

PL2 is the second plasma data word in the subframe.

A complete 12-point plasma spectrum is constructed by taking the 12 readings per frame consecutively. For example, the readout for the first energy channel is PL1 in the first subframe (first record with a given value of FC), the second energy channel is PL2 in the first subframe, the third energy channel is PL1 in the second subframe, etc.

Following the last subframe of good data, an "END" is written on the tape in BCD in the position of the word TIME. There is also an eof after the "END."

A FORTRAN IV program which reads the tape, combines the subframes into frames, and prints out all complete frames (one line per frame) is attached together with a copy of the first page of this printout.

```
                    FSD,F042000,28012-0,54198,A  IC     18JOB V13M16  7094 A    06/16/67          PAGE  1
      JL          - EFR   SOURCE STATEMENT  -  IFR(S)  -

                                                                                                  PLPR0000
      DIMENSION A(5), B(15)                                                                       PLPR0005
      DATA  END/3HEND/                                                                            PLPR0010
      DATA I/1/,PREFC/-9.9/                                                                       PLPR0020
C     PRINT TITLE AND HEADING.                                                                    PLPR0025    1
    1 WRITE(6,1000)                                                                               PLPR0030
 1000 FORMAT(1H1, 8X, 2HFC,8X, 3HDAY, 8X, 4HTIME,                                                PLPR0035
     1  6( 6X, 3HPL1, 3X, 3HPL2 ) ////)                                                          PLPR0040
      LINE = 5                                                                                    PLPR0045
C     INPUT A FIVE WORD RECORD FROM TAPE.                                                         PLPR0050
    2 READ (13) A                                                                                 PLPR0055    2
C     CHECK FOR END-OF-FILE.                                                                      PLPR0060
      IF(A(1).EQ.END) GO TO 7                                                                     PLPR0065
C     CHECK CHANGE IN FRAME NO. YES, START NEW LINE.                                              PLPR0070
      IF (A(3).NE.PREFC) GO TO 3                                                                  PLPR0075
C     CHECK FOR MORE THAN SIX SUB-FRAMES. YES, START NEW LINE.                                    PLPR0080
      IF (I.GE.13) GO TO 4                                                                        PLPR0085
C     FILL OUTPUT BUFFER WITH DATA. (PL1 + PL2)                                                   PLPR0090
      B(I) = A(4)                                                                                 PLPR0095
      B(I+1) = A(5)                                                                               PLPR0100
      I = I+2                                                                                     PLPR0105
      GO TO 2                                                                                     PLPR0110
C     CHECK FOR FIRST TIME THROUGH PROGRAM.                                                       PLPR0115
    3 IF(PREFC.EQ.-9.9) GO TO 5                                                                   PLPR0120
C     PRINT LINE.                                                                                 PLPR0125   19
    4 WRITE(6,1001)                (B(J),J=1,15)                                                  PLPR0130
 1001 FORMAT( 7X, F6.0, 5X, A6, 5X, A6, 6( 5X, F4.0, 2X, F4.0))                                   PLPR0135
      LINE = LINE + 1                                                                             PLPR0140
C     SAVE DATA FROM NEW FRAME.                                                                   PLPR0145
    5 B(1) = A(3)                                                                                 PLPR0150
      B(2) = A(2)                                                                                 PLPR0155
      B(3) = A(1)                                                                                 PLPR0160
      B(4) = A(4)                                                                                 PLPR0165
      B(5) = A(5)                                                                                 PLPR0170
C     FILL THE REST OF ARRAY B WITH MINUS ZEROS.                                                  PLPR0175
      DO 6 K=6,15                                                                                 PLPR0180
    6 B(K) = -0.0                                                                                 PLPR0185
      PREFC = A(3)                                                                                PLPR0190
      I = 6                                                                                       PLPR0195
C     CHECK FOR FULL PAGE.                                                                        PLPR0200
      IF(LINE.GE.58) GO TO 1                                                                      PLPR0205
      GO TO 2                                                                                     PLPR0210
C     TERMINATE REPORT.                                                                           PLPR0215   39
    7 WRITE(6,1002)                                                                               PLPR0220
 1002 FORMAT( 14H RUN FINISHED.  )                                                                PLPR0225
      RETURN                                                                                      PLPR0230
      END
```

Figure 1.0-4

PROGRAM DOCUMENTATION

MAR 2

MARINER 2 DATA SET

Programmer: Jewell Chase

Date: 3 March 1968

Prepared by:

Wolf Research & Development Corporation
Bladensburg, Maryland

Prepared for:

National Space Science Data Center
Space Sciences Directorate
GSFC
NASA

Under Contract NAS 5-8060

Programs to Print and Plot 62-041A-06A

I. ABSTRACT

This program lists Mariner II data off line and also on the S-4020 plotter.

II. IDENTIFICATION

A. Source Language

Fortran IV - manual references C28-6392.

B. Required Peripheral Equipment

1. One tape unit (A2) for on-line card reader
2. One tape unit (A3) for off-line printer
3. One tape unit (A6) for program input tape
4. One tape unit (A7) for 4020 output

C. Computer

IBM 7094/II

D. Operating System

February 14, 1966. Goddard Space Flight Center System Tape.

E. Subroutines required

1. Sysgo (34)

   a. labeled common SYSEOF

2. Sysgo (35)

   a. labeled common AWAERR

F. Storage requirements

see figure #1

III. DESCRIPTION

This program reads the Mariner II, Plasma Spectrometer data tape and outputs a listing of the data. A print out is generated on the 4020 for microfilm or hard-copy output. Asterisks (*) are printed to flag invalid parameters.

IV. PROGRAM SETUP

A. Input requirements

1. Cards - none

2. Tapes

a. tape unit A-6

1. parity --odd
2. density - 556 BPI
3. label - none
4. format - see figure #2
5. disposition - retain & file

B. Output description

1. Printer output

see figure #3

2. Tape

a. tape unit A-7. SC-4020 output tape

1. parity - odd
2. density - 556 BPI
3. label - none
4. format - same as computer printout. Figure #3
5. disposition - submit for microfilm or hard copy.

C. Control Cards - see standard set-up for NSSDC, see deck setup, figure #4.

D. Run time estimate

5 minutes

E. Restrictions - none

V. PROGRAM MAINTENANCE

A. Flow chart

see figure #5

B. Operating system used at GSFC is OS/MVS version 4 - ISPF version 2. Version 12 manuals are not available from IBM, therefore all manual references are to version 15 manuals. There are significant differences between versions.

C. Symbol List and Description

SYMBOL	DESCRIPTION
A	name of input array
IA	same as A (equivalenced)
ID1	programmers name (alphanumeric)
ID2	contract code number (alphanumeric)
ID3	building code (alphanumeric)
ID4	telephone extension (alphanumeric)
ILINE	line counter
JC1	symbol to flag the data (blank)
JC2	symbol to flag the data (*)
JDO	counter for data point occurrences
JFL	array to hold data flags (* or blanks)

Figure #1

02/14/66

IBLDR

MEMORY MAP

SYSTEM	00000 THRU 03765
FILE BLOCK ORIGIN	03766

NUMBER OF FILES - 5

1. UNIT03
2. UNIT06
3. UNIT07
4. UNIT36
5. 4020 OUTPUT FILE

FILE LIST ORIGIN	04062
PRE-EXECUTION INITIALIZATION	04074
CALL ON OBJECT PROGRAM	04133
OBJECT PROGRAM	04140 THRU 24000

1.	DECK 'MAR 2 '		04140
2.	DECK 'FSEL '	*	05575
3.	DECK 'SYSGO '	*	06072
4.	DECK 'SYSNO '	*	06132
5.	DECK 'FCNV '		06211
6.	DECK 'FIOB '		10706
7.	DECK 'FIOS '		11377
8.	DECK 'FSLBI '		11637
9.	DECK 'FSLDI '		11702
10.	DECK 'FXEM '		11751
11.	SUBR '.IBSYS'		00000

BINARY TAPE FORMAT FOR ONE RECORD

Symbol	Word Number	Description
A(1,1) to A(21,1)	1 - 21	Day number at start of frame
A(1,2) to A(21,2)	22- 42	Time in seconds from the beginning of the day
A(1,3) to A(21,3)	43 - 63	Frame count
A(1,4) to A(21,4)	64 - 84	Descriptive flag
A(1,5) to A(21,5)	85 - 105	Plasma velocity in Km/Sec corresponding to the upper limit temperature
A(1,6) to A(21,6)	106 - 126	Plasma velocity in Km/Sec corresponding to the lower limit temperature
A(1,7) to A(21,7)	127 - 147	Upper limit of the temperature in 10^5 o k.
A(1,8) to A(21,8)	148 - 168	Lower " " " " "
A(1,9) to A(21,9)	169 - 189	Proton density in protons/cm^3.
A(1,10) to A(21,10)	190 - 210	Rates of alpha-particle density to proton density, Na/Np
A(1,11) to A(21,11)	211 - 231	10h
A(1,12) to A(21,12)	232 - 252	15-hour value of (np + 3σ)

Figure #1

02/14/66

1BLDR

MEMORY MAP

SYSTEM	00000 THRU	03765
FILE BLOCK ORIGIN		03766

NUMBER OF FILES - 5

1. UNIT03
2. UNIT06
3. UNIT07
4. UNIT36
5. 4020 OUTPUT FILE

FILE LIST ORIGIN		04062
PRE-EXECUTION INITIALIZATION		04074
CALL ON OBJECT PROGRAM		04133
OBJECT PROGRAM	04140 THRU	24000

1.	DECK	'MAR 2 '	04140
2.	DECK	'FSEL ' *	05575
3.	DECK	'SYSGO ' *	06072
4.	DECK	'SYSNO ' *	06132
5.	DECK	'FCNV '	06211
6.	DECK	'FIOB '	10706
7.	DECK	'FIOS '	11377
8.	DECK	'FSLBI '	11637
9.	DECK	'FSLDI '	11702
10.	DECK	'FXEN '	11751
11.	SUBR	'.IBSYS'	06000
12.	SUBR	'.IOEX '	00702
13.	SUBR	'.JBCON'	03720
14.	SUBR	'.LXCON'	12412
15.	SUBR	'.IODEF'	13065
16.	SUBR	'.IOCSF'	13307
17.	SUBR	'.LXSL '	16615
18.	SUBR	'.FPTRP'	17073
19.	SUBR	'XIT '	17303
20.	SUBR	'FOUT '	17304
21.	SUBR	'FIOH '	17646
22.	SUBR	'FWRD '	20707
23.	SUBR	'FRDB '	20736
24.	SUBR	'UN03 '	20770
25.	SUBR	'UN06 '	20774
26.	SUBR	'UN07 '	20775
27.	SUBR	'UN36 '	20776
28.	SUBR	'FEET '	20777
29.	SUBR	'FRWT '	21075
30.	SUBR	'FSLI '	21212
31.	SUBR	'CAMRAV' *	21256
32.	SUBR	'FRAMEV' *	21311
33.	SUBR	'HOLLV ' *	21354

02/14/66

IBLDR

34.	SUBR 'PLOT..'	*	21401
35.	SUBR 'RITE2Q'		22474
36.	SUBR 'SCOUTQ'		22752
37.	SUBR 'SCPOOL'	*	23151
38.	SUBR 'UN61 '		23211
39.	SUBR 'VCHARV'	*	23212
40.	SUBR 'TABL1Q'		23460

(* - INSERTIONS OR DELETIONS MADE IN THIS DECK)

INPUT - OUTPUT BUFFERS 24001 THRU 77776

77777 THRU 77777

UNUSED CORE

BINARY TAPE FORMAT FOR ONE RECORD

Symbol	Word Number	Description
A(1,1) to A(21,1)	1 - 21	Day number at start of frame
A(1,2) to A(21,2)	22- 42	Time in seconds from the beginning of the day
A(1,3) to A(21,3)	43 - 63	Frame count
A(1,4) to A(21,4)	64 - 84	Descriptive flag
A(1,5) to A(21,5)	85 - 105	Plasma velocity in Km/Sec corresponding to the upper limit temperature
A(1,6) to A(21,6)	106 - 126	Plasma velocity in Km/Sec corresponding to the lower limit temperature
A(1,7) to A(21,7)	127 - 147	Upper limit of the temperature in 10^5 o k.
A(1,8) to A(21,8)	148 - 168	Lower " " " " "
A(1,9) to A(21,9)	169 - 189	Proton density in protons/cm^3.
A(1,10) to A(21,10)	190 - 210	Rates of alpha-particle density to proton density. Na/Np
A(1,11) to A(21,11)	211 - 231	10 h
A(1,12) to A(21,12)	232 - 252	15-hour value of (np + 3σ)

JC	JT	JFC	JG	VA	VB	TA	TB	D
241	62876	20	1	414.1	414.1	1.527	1.527	10.
241	63117	21	1	405.9	405.9	2.033	2.033	11.
241	63320	22	1	394.5	394.5	2.058	2.058	9.
241	63542	23	1	409.9	409.9	2.397	2.397	10.
241	63763	24	1	445.8	445.8	2.032	2.032	5.
241	63985	25	1	450.7	450.7	1.749	1.749	8.
241	64206	26	1	452.4	452.4	1.612	1.612	4.
241	64428	27	31	415.5	415.7	1.098	0.239	6.
241	64650	28	1	426.3	425.3	2.201	2.201	14.
241	64871	29	7	424.1	424.1	2.201*	2.201*	14.
241	65094	30	7	422.5	422.5	2.201*	2.201*	14.
241	65315	31	31	415.7	415.7	1.000	0.365	9.
241	65538	32	1	414.5	414.5	1.436	1.436	10.
241	65759	33	1	410.9	410.9	2.196	2.196	12.
241	65981	34	1	404.6	404.6	2.206	2.206	9.
241	66203	35	1	401.6	401.6	1.892	1.892	7.
241	67754	42	1	421.0	421.0	2.864	2.864	11.
241	67976	43	31	415.6	415.7	1.047	0.295	7.
241	68198	44	7	424.1	424.1	2.864*	2.864*	7.
241	69307	49	7	422.2	422.2	2.864*	2.864*	7.
241	69528	50	1	444.8	444.8	1.939	1.939	6.
241	70194	53	1	442.7	442.7	2.235	2.235	7.
241	70415	54	1	431.7	431.7	2.200	2.200	8.
241	70637	55	1	436.4	436.4	2.101	2.101	7.
241	78398	90	2	408.4	408.4	5.822	5.822	8.
241	78842	92	31	414.8	415.7	1.355	0.149	2.
241	79507	95	2	409.8	409.8	5.142	5.142	9.
241	79729	96	1	397.4	397.4	1.075	1.075	9.
241	84164	116	7	424.1	424.1	1.075*	1.075*	9.
241	84385	117	7	426.0	426.0	1.075*	1.075*	9.
241	84606	118	7	424.1	424.1	1.075*	1.075*	9.
241	84828	119	7	427.8	427.8	1.075*	1.075*	9.
241	85051	120	7	425.8	425.8	1.075*	1.075*	9.
241	85272	121	7	426.0	426.0	1.075*	1.075*	9.
241	85660	123	7	425.8	425.8	1.075*	1.075*	9.
241	86168	125	7	429.4	429.4	1.075*	1.075*	9.
242	142	127	7	422.3	422.3	1.075*	1.075*	9.
242	364	128	31	405.8	415.6	0.935	0.223	4.
242	586	129	7	437.7	437.7	1.075*	1.075*	4.
242	868	130	1	451.2	451.2	1.545	1.545	5.

* INVALID PARAMETER

VB	TA	TB	D	R	M	DX
414.1	1.527	1.527	10.746	0.0281	0.83	-0.000*
405.9	2.033	2.033	11.180	0.0325	1.03	-0.000*
394.5	2.058	2.058	9.845	0.0384	2.97	-0.000*
409.9	2.397	2.397	10.908	0.0616	-1.66	-0.000*
445.8	2.032	2.032	5.047	0.0318	12.34	-0.000*
450.7	1.749	1.749	4.214	0.0314	14.45	-0.000*
452.4	1.612	1.612	4.868	0.0250	15.87	-0.000*
415.7	1.098	0.239	6.196*	0.0309*	4.80*	17.086
425.3	2.201	2.201	14.291	0.0312	11.35	-0.000*
424.1	2.201*	2.201*	14.291*	0.0312*	11.35*	-0.000*
422.5	2.201*	2.201*	14.291*	0.0312*	11.35*	-0.000*
415.7	1.000	0.365	9.677*	0.0186*	6.57*	16.609
414.5	1.436	1.436	10.504	0.0276	2.12	-0.000*
410.9	2.196	2.196	12.947	0.0219	2.01	-0.000*
404.6	2.206	2.206	9.373	0.0196	3.07	-0.000*
401.6	1.892	1.892	7.824	0.0443	1.32	-0.000*
421.0	2.864	2.864	11.967	0.0360	6.40	-0.000*
415.7	1.047	0.295	7.738*	0.0190*	6.19*	16.609
424.1	2.864*	2.864*	7.738*	0.0190*	6.19*	-0.000*
422.2	2.864*	2.864*	7.738*	0.0190*	6.19*	-0.000*
444.8	1.939	1.939	6.156	0.0413	8.63	-0.000*
442.7	2.235	2.235	7.148	0.0401	5.97	-0.000*
431.7	2.200	2.200	8.192	0.0463	8.69	-0.000*
436.4	2.101	2.101	7.337	0.0354	7.39	17.086*
408.4	5.822	5.822	8.310	0.0571	-2.88*	-0.000*
415.7	1.355	0.149	2.589*	0.1370*	-0.63*	15.731
409.8	5.142	5.142	9.150	0.0474	-1.40*	-0.000*
397.4	1.075	1.075	9.210	0.0281	8.60	16.609*
424.1	1.075*	1.075*	9.210*	0.0281*	8.60*	-0.000*
426.0	1.075*	1.075*	9.210*	0.0281*	8.60*	-0.000*
424.1	1.075*	1.075*	9.210*	0.0281*	8.60*	-0.000*
427.8	1.075*	1.075*	9.210*	0.0281*	8.60*	-0.000*
425.8	1.075*	1.075*	9.210*	0.0281*	8.60*	-0.000*
426.0	1.075*	1.075*	9.210*	0.0281*	8.60*	16.609*
425.8	1.075*	1.075*	9.210*	0.0281*	8.60*	-0.000*
429.4	1.075*	1.075*	9.210*	0.0281*	8.60*	-0.000*
422.3	1.075*	1.075*	9.210*	0.0281*	8.60*	-0.000*
415.6	0.935	0.223	4.190*	0.0226*	12.55*	14.095
437.7	1.075*	1.075*	4.190*	0.0226*	12.55*	-0.000*
451.2	1.545	1.545	5.957	0.0205	13.32	17.086*

VALID PARAMETER

4

1 2

SOURCE DECK

7/8 EOF

BINARY DECK SYSGO (35)

BINARY DECK SYSGO (34)

$IBFTC
SOURCE DECK MAR 2

JOB CONTROL CARDS

Description:

The cylindrical electrostatic analyzer separated positively charged ions according to their energy per unit charge. It consisted of a pair of curved concentric electrostatic deflection plates terminated by an isolated Faraday cup. The deflection plates were 120 deg in angular length, separated by a distance of 1.3 cm, with r(2)/r(1) = 1.134. The entrance aperture was 5.0 sq cm and retangular, such that the acceptance angles for particles in two perpendicular planes were approximately equal. Rough experimental checks with the theoretical angular and energy per charge transmission functions in the plane of analysis indicated no gross deviations from theory.

The deflection plates were separated by ground rails to control field fringing effects between the plates. Rectangular plates at ground potential were located at both the entrance and exit of the analyzer for the same reason. A suppressor electrode, located inside the entrance to the Faraday cup but shielded from the particle beam by the rectangular ground plane, prevented secondary emission of electrons from the Faraday cup due to the collision of incident particles.

All metal parts were gold-plated magnesium with the exception of the entrance ground plane which for purposes of spacecraft passive temperature control, was made of polished aluminum. The interior of the analyzer was coated with gold black to minimize the amount of ultraviolet light entering the charge collector region.

A high-voltage sweep generator applied a balanced potential to the analyzer plates. This potential was changed by a digital programmer at intervals in an ascending sequence of ten values. After the ten spectral measurements, a zero current reading and then a calibration reading (using a standard current of 1.0 x 10 ** -10 amperes) were taken with the plates connected together. The complete sequence of twelve measurements was repeated every 3.696 min (every 2.016 min near Venus).

The charge measuring portion of the electronic system used an electrometer amplifier, a logarithmic compressor, and a discriminator circuit. The logarithmic compressor, located in the amplifier feedback loop, was a thermionic diode (Raytheon CK 5886) operated in the retarded field region. The compressor provided the electrometer with an input positive current range of 10 ** -13 to 10 ** -6 amperes. The electrometer d.c. output voltage was converted by the spacecraft's Data Conditioning System (DCS), into a digital number with a quantization interval of 0.1 decade.

The discriminator circuit acted to prevent saturation of the amplifier, an event that could occur in the presence of small negative back ground currents. The discriminator was referenced at a pre-saturation voltage which varied throughout the flight. When this reference level was exceeded, an input current source was activated to return the amplifier to midrange voltage. The input current source also acted as a calibration current.

A complete description of the instrument is given by C. Josias and J. Lawrence, Jr. in JPL technical report no. 32-492.

DATA USERS' NOTE

MARINER II (1962 A-Rho 1)

SOLAR-WIND SPECTROMETER

BACKGROUND

The Mariner-II solar-wind spectrometer was designed by scientists at the Jet Propulsion Laboratory of the California Institute of Technology to investigate the positive-ion component of the solar wind in interplanetary space and near Venus.

Mariner 2 was launched on August 27, 1962, on a trajectory passing within 41,000 km of the center of Venus (at 2000 UT, Dec. 14, 1962) and then reaching a perihelion distance of 1.054×10^8 km on Dec. 28, 1962. No measurements were made closer to the Earth than 721,000 km. Besides the solar-wind spectrometer, Mariner II carried several complementary experiments which are listed in Table 1.

The spacecraft's orientation was controlled by an attitude stabilization system, which kept the entrance aperture of the solar-wind spectrometer pointed to within 0.1° of the center of the Sun. Until Sept. 3, the spacecraft slowly rolled about the Sun-probe line; thereafter, the Sun-probe-Earth plane remained fixed in the spacecraft.

EXPERIMENTERS

K. Naugebauer - Jet Propulsion Laboratory

C. W. Snyder - Jet Propulsion Laboratory

EXPERIMENT

The solar-wind spectrometer is shown schematically in Figure 1. Its principal components were:

(1) A cylindrical electrostatic analyzer, which separated positively charged ions according to their energy per unit charge (E/Q). The deflection plates were 120° in length, separated by 1.3 cm, with $r_2/r_1 = 1.134$, and had an entrance aperture of 5.0 cm^2, which was rectangular in shape, such that the angular acceptance for charged particles in two perpendicular planes was approximately equal. The theoretical angular and E/Q transmission functions in the plane of analysis are shown in Figure 2; rough experimental checks showed no gross deviations from theory.

(2) A programmer and a high-voltage sweep amplifier, which applied the proper balanced potential to the plates of the analyzer. This voltage was varied in an ascending sequence of 10 values. The values assumed in JPL's data reduction are given in Table 2, together with the relevant timing information. Further information on the stability and temperature variations of these voltage settings can be found in Refs. 1 and 2. After 10 spectral measurements, a zero reading and a calibration reading (using a standard current of 1.0×10^{-10} amp) were taken with the plates connected together. The complete sequence of twelve measurements was repeated every 3.696 minutes (every 2.016 minutes near Venus).

(3) An electrometer, which measured the current from the charge collector at the output of the analyzer. At currents above 5×10^{-13} amp, the electrometer output was an accurately linear function of the logarithm

of the input current. The output dc voltage was converted by the spacecraft data-automation system into a digital reading with a quantization interval of 0.1 decade. The relation between current I and digital number D is

$$\log_{10} I = -10 + 0.1\,(D_{12} - D) \qquad (1)$$

where D_{12} is the digital number corresponding to voltage-step 12. For currents below 5×10^{-13} amp, the electrometer response time must be considered. The method of estimating these low currents is described in Section V.B.2 of Ref. 2.

DATA

Timespan

See Table 3.

Format of Available Data

Two types of data are available: raw and reduced. Either type can be obtained as either microfilmed computer printout (tabular form) or in binary on a single 1/2-inch magnetic tape. Since only complete spectra without any parity errors are included, there are time gaps in the listings.

(1) Raw Data

The following information is given for each data frame (3.696 or 2.016 min):

Frame count (Cycles from 0 to 255)

Day number (Jan. 1 is day 1)

12 electrometer output numbers, one for each channel

(2) Reduced Data

The data have been reduced on the basis of a simple model of the solar wind in which both the protons and alphas flow radially away from the Sun with velocity v, and with densities N_p and N_a, and temperatures, T_p and T_a, respectively. The apparent aberration of the radial flow due to the spacecraft's motion has been taken into account. By temperature is meant a measure of the spread in radial velocity. It was further assumed that either $T_a = T_p$ or $T_a = 4\ T_p$, whichever equality better fit the observations for the spectrum (data frame) under consideration. A parameter h which determines how well the observations fit the model was also calculated whenever possible. See Reference 1 for a much more detailed discussion.

The following data and calculated parameters are given for each data frame (3.696 or 2.016 min):

Frame count (Cycles from 0 to 255)

Day number (Jan. 1 is day 1)

Time (at start of frame, in sec from start of day)

v (km/sec)

T_p (10^5 °K)

N_p (cm^{-3})

N_a/N_p

h

Flag

The flag is an indicator of the type of spectrum. It indicates whether $T_a = T_p$ or $4\ T_p$ and to which of the four categories of spectra

(described on page 4474, Ref. 1) the spectrum belongs. For spectra in category 4, both upper and lower limits of T_p, the two values of v corresponding to these limits of T_p, and the density extrema used in the calculation of these limits are also given.

Only those currents corresponding to D (Eq. 1) less than 155 were used in this analysis; i.e., low currents, for which the time constant of the electrometer should be taken into account, were considered unknown.

Since the spacecraft's position and velocity changed very slowly compared to the 3.696 minutes per spectrum, none of these data tabulations or tapes include trajectory information. This information is available and should be requested from NSSDC separately.

REFERENCES

1. Neugebauer, M., and C. W. Snyder, "Mariner-2 Observations of the Solar Wind. 1. Average Properties," J. Geophys. Res., 71, 4469-4484, 1966. This is an abbreviated version of the report: "Average Properties of the Solar Wind as Determined by Mariner 2," by M. Neugebauer and C. W. Snyder, Jet Propulsion Lab., Tech. Rept. TR 32-991, 1966.

2. Josias, C., and J. T. Lawrence, Jr., "An Instrument for Measurement of Interplanetary Solar Plasma," Jet Propulsion Lab., Tech. Rept. TR 32-492, 1964.

BIBLIOGRAPHY

Jet Propulsion Laboratory staff, Mariner Mission to Venus, McGraw-Hill, 1963.

Josias, C., and J. L. Lawrence, Jr., "An Instrument for Measurement of Interplanetary Solar Plasma," Jet Propulsion Lab., Tech.Rept. TR 32-492, 1964.

Josias, C., and J. Lawrence, Jr., "An Electrometer for Use in Scientific Space Instruments," IEEE Transactions on Nuclear Science, NS-13, NO. 5, 25-36, 1966.

Neugebauer, M., and C. W. Snyder, "Mariner 2 Observations of the Solar Wind: 1. Average Properties," J. Geophys. Res., 71, 4469-4484, 1966.

Neugebauer, M., and C. W. Snyder, "Average Properties of the Solar Wind as Determined by Mariner 2," Jet Propulsion Lab., Tech. Rept. TR 32-991, 1966.

Neugebauer, M., and C. W. Snyder, "Solar Wind Measurements near Venue," J. Geophys. Res., 70, 1587-1591, 1965.

Neugebauer, M., and C. W. Snyder, "Mariner 2 Measurements of the Solar Wind," in The Solar Wind, edited by R. J. Mackin, Jr., and M. Neugebauer, Pergamon Press, New York, 1966.

Neugebauer, M., and C. W. Snyder, "Solar Plasma Experiment," Science, 138, 1095-1096, 1962.

Snyder, C. W., and M. Neugebauer, "Interplanetary Solar-wind Measurements by Mariner 2," Space Res., 4, 89-113, 1964.

Snyder, C. W., M. Neugebauer, and U. R. Rao, "The Solar Wind Velocity and its Correlation with Cosmic-ray Variations and with Solar and Geomagnetic Activity, J. Geophys. Res., 68, 6361-6370, 1963.

Snyder, C. W., and M. Neugebauer, "The Relation of Mariner-2 Plasma Data to Solar Phenomena," in The Solar Wind, edited by R. J. Mackin, Jr., and M. Neugebauer, Pergamon Press, New York, 1966.

Snyder, C. W., "Mariner Solar Wind Measurement," AAS-NASA Symposium on the Physics of Solar Flares, edited by W. N. Hess, NASA SP-50, 1964.

Snyder, C. W., and M. Neugebauer, "Interplanetary Solar-wind Measurements by Mariner II," in Proceedings of the Plasma Space Science Symposium, edited by C. C. Chang and S. S. Huang, pp. 67-90, Gordon and Breech, 1965.

Wyckoff, R. C., "Scientific Experiments for Mariner R-1 and R-2, Jet Propulsion Lab., Tech. Rept. TR 32-315, 1962.

LIST OF FIGURES

Figure

LIST OF TABLES

TABLE 1

MARINER-II EXPERIMENTS

Experiment	Investigators and Affiliations	Operation
Magnetometer	P. J. Coleman, Jr., NASA L. Davis, Jr., Calif. Inst. of Technology E. J. Smith, Jet Propulsion Lab. C. P. Sonett, NASA	Interplanetary, near Venus
Solar-wind Spectrometer	M. Neugebauer, Jet Propulsion Lab. C. W. Snyder, Jet Propulsion Lab.	Interplanetary, near Venus
Ion-chamber with matching Geiger counters	H. R. Anderson, Jet Propulsion Lab. H. V. Neher, Calif. Inst. of Technology	Interplanetary, near Venus
Thin-window Geiger counter	L. Frank, State Univ. of Iowa J. A. Van Allen, State Univ. of Iowa	Interplanetary, near Venus
Dust Detector	W. M. Alexander, Goddard Space Flight Center	Interplanetary, near Venus
Infrared Radiometer	L. D. Kaplan, Jet Propulsion Lab. G. Neugebauer, Jet Propulsion Lab. C. Sagan, Univ. of Calif., Berkeley and Harvard College Observatory	Near Venus
Microwave Radiometer	A. H. Barrett, MIT J. Copeland, Army Ordnance Missile Command and Ewen-Knight Corp. D. E. Jones, Jet Propulsion Lab. A. E. Lilley, Harvard College Observatory	Near Venus

TABLE 2

E/Q CORRESPONDING TO CENTER OF EACH

CHANNEL AND TIMING OF MEASUREMENTS

Channel	E/Q Volts	Time after start of frame * Interplanetary	Near Venus
1	231	1.92	1.92
2	346	19.20	19.20
3	516	38.88	22.08
4	751	56.16	39.36
5	1124	75.84	42.24
6	1664	93.12	59.52
7	2476	112.80	62.40
8	3668	130.08	79.68
9	5508	149.76	82.56
10	8824	167.04	99.84
11	0	186.72	102.72
12	0**	204.00	120.00

*Frames with time labels of 49674 through 73751 sec on Dec. 14 (Day 348).

**Current calibration: 1.0×10^{-10} amp input to electrometer

TABLE 3

TIMESPAN OF DATA

Time and Date	Data Coverage	Minutes per Spectrum
1728 UT, Aug. 29—2015 UT, Oct. 31	Almost Continuous	3.7
2015 UT, Oct. 31—2132 UT, Nov. 8	None	-
2132 UT, Nov. 8 —1340 UT, Dec. 14	Almost Continuous	3.7
1340 UT, Dec. 14—2040 UT, Dec. 14	Almost Continuous	2.0
2040 UT, Dec. 14—2400 UT, Dec. 16	Almost Continuous	3.7
0000 UT, Dec. 17—1728 UT, Dec. 30	~ 10 hrs/day, except no data on Dec. 25	3.7

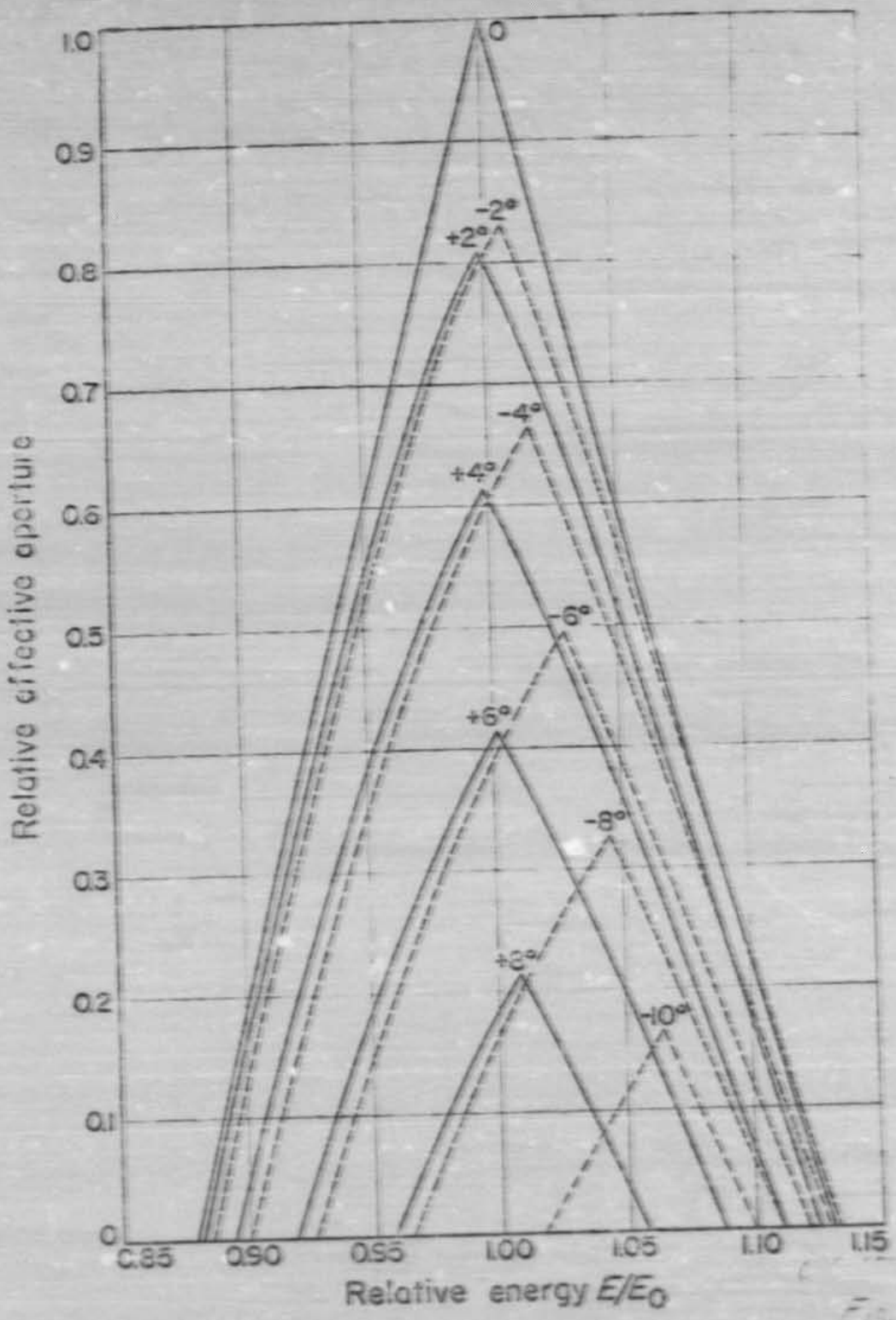
Relative effective aperture
1.0
0.9
0.8
0.7
0.6
0.5
0.4
0.3
0.2
0.1
0
0
-2°
+2°
-4°
+4°
-6°
+6°
-8°
+8°
-10°
0.85
0.90
0.95
1.00
1.05
1.10
1.15
Relative energy E/E_0

Fig. 2

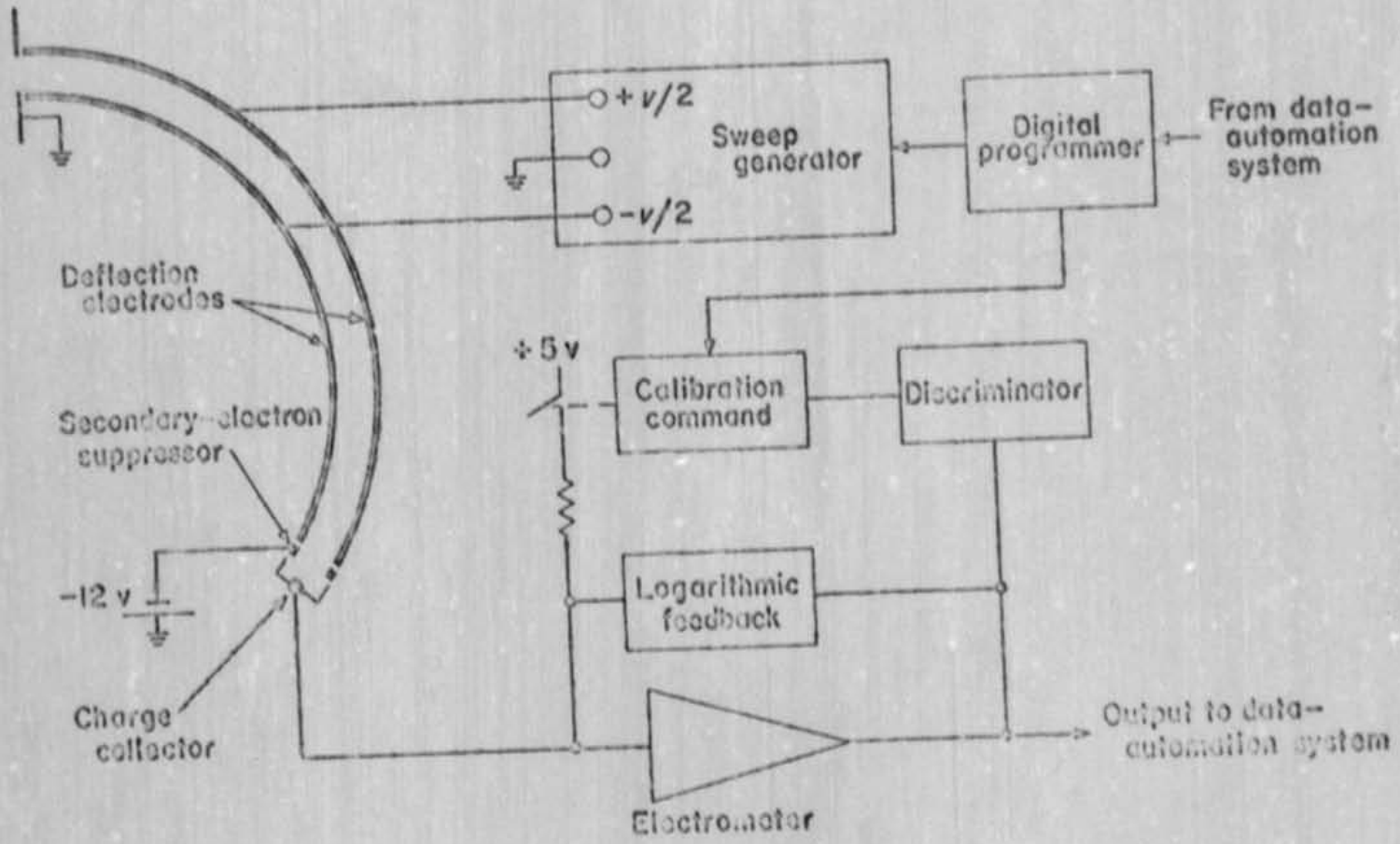
+v/2
Sweep generator
-v/2
Digital programmer
From data-automation system
Deflection electrodes
+5 v
Calibration command
Discriminator
Secondary-electron suppressor
-12 v
Logarithmic feedback
Charge collector
Output to data-automation system
Electrometer

Dump 48 42-041A-06A

FILE 0001 REC 0001 CH 2760

0001	000000000001	000000000060	000006200006	000005000001
0049	2107140CCC00	200006200006	000005000001	010703100205
0097	200006200006	000005000001	010702110300	000000020401
0145	000005000001	010703000006	000000020401	205500000000
0193	010703000403	000000020401	205500000000	210500000000
0241	000000020401	205500000000	210500000000	207740000000
0289	205520000000	210706000000	210710000000	200006200006
0337	210424000000	210400000000	200006200006	000005000001
0385	210424000000	200006200006	000005000001	010703030410
0433	200006200006	000005000001	010703040205	000000020401
0481	000005000001	010703040403	000000020401	205520000000
0529	010703050200	000000020401	205540000000	210706000000
0577	000000020401	205540000000	210430000000	210400000000
0625	205540000000	210404000000	210424000000	200006200006
0673	210434000000	210464000000	200006200006	000005000001
0721	210510000000	200006200006	000005000001	010703100205
0769	200006200006	000005000001	010703110002	000000020401
0817	000005000001	010703110310	000000020401	205560000000
0865	010704000105	000000020401	205560000000	210400000000
0913	000000020401	205560000000	210432000000	210450000000
0961	205560000000	210500000000	210505000000	200006200006
1009	210500000000	207740000000	200006200006	000005000001
1057	210712000000	200006200006	000005000001	010704030200
1105	200006200006	000005000001	010704030507	000000020401
1153	000005000001	010704040304	000000020401	205500000000
1201	010704050101	000000020401	205500000000	210476000000
1249	000000020401	205500000000	210500000000	207740000000
1297	205620000000	210704000000	210716000000	200006200006
1345	210714000000	210424000000	200006200006	000005000001
1393	210432000000	200006200006	000005000001	010704100105
1441	200006200006	000005000001	010704100503	000000020401
1489	000005000001	010704110211	000000020401	205620000000
1537	010705000006	000000020401	205640000000	210704000000
1585	000000020401	205640000000	210714000000	210424000000
1633	205640000000	207774000000	210432000000	200006200006
1681	210432000000	210454000000	200006200006	000005000001
1729	210504000000	200006200006	000005000001	010705030105
1777	200006200006	000005000001	010705030410	000000020401
1825	000005000001	010705040205	000000020401	205660000000
1873	010705050002	000000020401	205660000000	210402000000
1921	000000020401	205660000000	210432000000	210456000000
1969	205660000000	210500000000	210506000000	200006200006
2017	210500000000	207740000000	200006200006	000005000001
2065	210720000000	200006200006	000005000001	010705100404
2113	200006200006	000005000001	010705110201	000000020401
2161	000005000001	010705110510	000000020401	205700000000
2209	010705110510	000000020401	205700000000	210500000000
2257	000000020401	205700000000	210500000000	207740000000
2305	205720000000	210705000000	210720000000	200006200006
2353	210474000000	210402000000	200006200006	000005000001
2401	210424000000	200006200006	000005000001	011000030311
2449	200006200006	000005000001	011000030311	000000020401
2497	000005000001	011000040106	000000020401	205720000000
2545	011000040504	000000020401	205740000000	210706000000
2593	000000020401	205740000000	210514000000	210400000000
2641	205740000000	207770000000	210424000000	200006200006
2689	210424000000	210454000000	200006200006	000005000001
2737	210504000000	200006200006	000005000001	011000030311

FILE 0001 REC 0002 CH 2760

0001	000000000000	000000000060	000000020401	205740000000
0049	011000100105	000000020401	205740000000	210706000000
0097	000000020401	205760000000	210542000000	210400000000

Time	Opt	FC	OLI
19 39 56	249	20	226

```
FILE 0001 SEC 0002 CH 2760
0145 205760000000 207774000000 210426000000 200006200006 00
0193 210430000000 210460000000 200006200006 000005000001 01
0241 210540000000 200006200006 000005000001 011001010401 00
0289 200006200006 000005200001 011001020110 000000020401 20
0337 000005000001 011001020505 000000020401 206400000000 21
0385 011001070301 000000020401 206400000000 207774000000 21
0433 000000020401 206400000000 210432000000 210460000000 20
0481 205400000000 210500000000 210510000000 200006200006 00
0529 210500000000 207740000000 200005200006 000005000001 01
0577 210720000000 200006200006 000005000001 011001060306 01
0625 200006200006 000005000001 011001070103 000000020401 20
0673 000005000001 011001070500 000000020401 206410000000 21
0721 011001100207 000000020401 206410000000 210500000000 21
0769 000000020401 206410000000 210500000000 207740000000 20
0817 206420000000 210710000000 210715000000 200006200006 00
0865 210434000000 210402000000 200005200006 000005000001 01
0913 210432000000 200006200006 000005000001 011002010302 00
0961 200006200006 000005000001 011002020011 000000020401 20
1009 000005000001 011002020406 000000020401 206420000000 21
1057 011002030203 000000020401 206430000000 210704000000 21
1105 000000020401 206430000000 210436000000 210402000000 20
1153 206430000000 210434000000 210424000000 200006200006 00
1201 210436000000 210466000000 200006200006 000005000001 00
1249 210504000000 200006200006 000005000001 011002060207 00
1297 200006200006 000005000001 01100-110104 000000020401 20
1345 000005000001 011004110501 000000020401 206520000000 20
1393 011005000210 000000020401 206520000000 207774000000 20
1441 000000020401 206520000000 210430000000 210462000000 20
1489 206520000000 210500000000 210506000000 200006200006 00
1537 210500000000 207740000000 200006200006 000005000001 00
1585 210720000000 200006200006 000005000001 011005030307 00
1633 200006200006 000005000001 011005040101 000000020401 20
1681 000005000001 011005040410 000000020401 206530000000 20
1729 011005050205 000000020401 206530000000 210476000000 20
1777 000000020401 206530000000 210500000000 207740000000 20
1825 206540000000 210706000000 210722000000 200006200006 00
1873 210652000000 210404000000 200006200006 000005000001 00
1921 210424000000 200006200006 000005000001 011005100211 00
1969 200006200006 000005000001 011005110006 000000020401 20
2017 000005000001 011005110407 000000020401 206540000000 20
2065 011101050007 000000020401 206610000000 210712000000 20
2113 000000020401 206610000000 210676000000 210404000000 20
2161 206610000000 210400000000 210424000000 200006200006 00
2209 210426000000 210460000000 200006200006 000005000001 00
2257 210506000000 200006200006 000005000001 011101100101 00
2305 200006200006 000005000001 011101100410 000000020401 20
2353 000005000001 011101110205 000000020401 206520000000 20
2401 011102000002 000000020401 206520000000 207774000000 20
2449 000000020401 206520000000 210426000000 210462000000 20
2497 206620000000 210500000000 210506000000 200006200006 00
2545 210507000000 207740000000 200006200006 000005000001 00
2593 210726000000 200006200006 000005000001 011103000301 00
2641 200006200006 000005000001 011103010010 000000020401 20
2689 000005000001 011103010405 000000020401 206650000000 20
2737 011107020202 000000020401 206650000000 210476000000 20

FILE 0001 SEC 0003 CH 2760
0001 000000000003 000000000003 210506000000 200006200006 00
0049 210502000000 207740000000 200006200006 000005000001 00
0097 210730000000 200006200006 000005000001 011103040102 00
0145 200006200006 000005000001 011103040411 000000020401 20
0193 000005000001 011103050205 000000020401 206660000000 20
0241 011107060003 000000020401 206660000000 210476000000 20
```

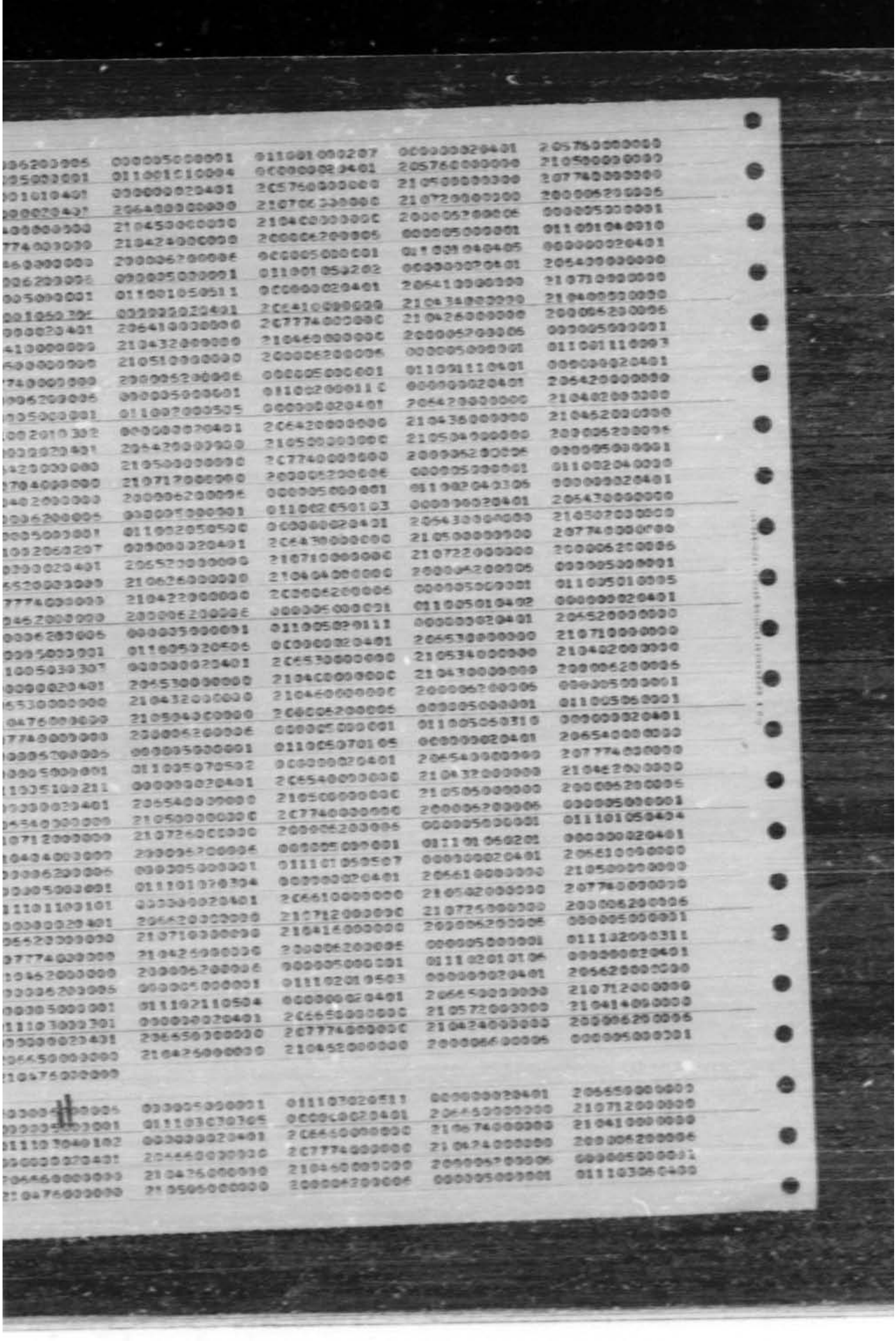

260	0300-0600	476.0	462.3	49	0.78	0.55	49	4.62	14	0.0
14										
260	0600-0900	472.7	473.3	49	1.00	0.98	49	4.46	47	0.0
47										
260	0900-1200	487.9	457.2	47	0.30	0.76	47	6.41	1	0.0
1										
260	1200-1500	431.9	459.6	47	1.11	0.74	47	0.	0	0.
0										
260	1500-1800	523.9	524.3	48	1.77	1.46	20	3.75	14	0.0
14										
260	1800-2100	503.9	508.9	48	1.58	0.52	30	2.81	1	0.0
1										
260	2100-2400	490.2	499.9	46	1.07	0.62	46	4.46	1	0.0
1										
261	0000-0300	427.8	460.9	47	0.99	0.88	47	5.01	35	0.
35										
261	0300-0600	462.3	462.3	48	1.19	1.19	48	4.70	48	0.
48										
261	0600-0900	455.0	455.0	48	1.23	1.23	48	6.10	48	0.
48										
261	0900-1200	424.9	425.7	49	2.40	2.27	44	8.52	35	0
35										
261	1200-1500	410.5	413.9	7	1.00	0.22	7	0.	0	0
0										
261	1500-1800	418.2	424.9	43	1.04	0.75	42	7.13	13	0
13										
261	1800-2100	448.1	448.4	47	1.42	1.39	45	10.93	41	0
41										
261	2100-2400	536.3	535.3	48	2.96	2.95	45	7.46	45	0
45										
262	0000-0300	675.9	678.5	48	3.79	3.65	48	5.67	43	
43										
262	0300-0600	636.7	636.8	48	3.77	3.59	19	3.86	17	
17										
262	0600-0900	662.1	662.1	49	4.12	4.12	22	2.42	22	
22										
262	0900-1200	685.8	685.8	32	4.60	4.60	32	2.83	32	
32										
262	1200-1500	699.5	699.5	1	3.30	3.30	1	2.70	1	
1										
262	1500-1800	714.1	721.8	44	3.12	2.54	44	2.12	31	
31										

.62	14	0.044	14	18.20	REC	184, LENGTH	108
.45	47	0.041	47	18.30	REC	185, LENGTH	108
.31	1	0.029	1	12.60	REC	186, LENGTH	108
.	0	0.	0	0.	REC	187, LENGTH	108
1.75	14	0.024	14	34.00	REC	188, LENGTH	108
2.81	1	0.060	1	8.50	REC	189, LENGTH	108
4.46	1	0.031	1	10.90	REC	190, LENGTH	108
5.01	35	0.036	35	14.40	REC	191, LENGTH	108
4.70	48	0.045	48	14.30	REC	192, LENGTH	108
6.10	48	0.036	48	17.90	REC	193, LENGTH	108
8.52	35	0.039	35	4.00	REC	194, LENGTH	108
0.	0	0.	0	0.	REC	195, LENGTH	108
7.13	13	0.023	13	13.50	REC	196, LENGTH	108
10.03	41	0.030	41	10.50	REC	197, LENGTH	108
7.46	45	0.029	45	9.40	REC	198, LENGTH	108
6.67	43	0.032	43	7.10	REC	199, LENGTH	108
3.96	17	0.053	17	8.50	REC	200, LENGTH	108
2.42	22	0.086	22	23.00	REC	201, LENGTH	108
2.83	32	0.072	32	7.70	REC	202, LENGTH	108
2.76	1	0.046	1	12.30	REC	203, LENGTH	108
2.12	31	0.056	31	11.00	REC	204, LENGTH	108

262 12	1800-2100	725.0	740.1	48	2.53	1.40	45	1.97	12	0.034
262 31	2100-2400	716.1	723.9	49	2.98	2.28	49	1.28	31	0.035
263 24	0000-0300	647.5	649.4	47	3.19	2.59	38	1.75	24	0.035
263 23	0300-0600	621.7	628.8	47	5.00	4.10	45	4.09	23	0.019
263 27	0600-0900	678.9	681.4	48	3.11	2.58	42	2.43	27	0.062
263 32	0900-1200	621.3	622.5	47	3.37	3.12	43	5.41	32	0.034
263	00- 00	4 .6	456.2	47	1.19	0.62	47	3.17	18	0 07

1.97	12	0.034	12	15.20	REC	205. LENGTH	108
1.28	31	0.036	31	11.40	REC	206. LENGTH	108
1.75	24	0.035	24	15.10	REC	207. LENGTH	108
4.09	23	0.019	23	5.30	REC	208. LENGTH	108
2.43	27	0.062	27	26.60	REC	209. LENGTH	108
5.41	32	0.034	32	7.40	REC	210. LENGTH	108
3.17	18	0 07		•	REC	211. LENGTH	108